UNIVERSITY OF SOUTHAMPTON

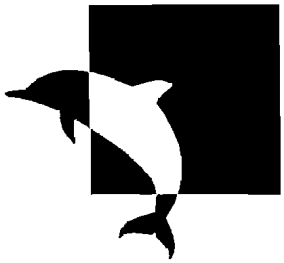

Towards Multiple Quantum Well Optically Pumped Far Infrared Lasers

by

Hock Aun TAN
BEng

A thesis submitted for the award of

Doctor of Philosophy

in the

OPTOELECTRONICS RESEARCH CENTRE
and the
DEPARTMENT OF ELECTRONICS AND COMPUTER SCIENCE

FACULTY OF ENGINEERING AND APPLIED SCIENCE

June 2003

Supervisor:

Professor Harvey N Rutt

UNIVERSITY OF SOUTHAMPTON

ABSTRACT

FACULTY OF ENGINEERING AND APPLIED SCIENCE
DEPARTMENT OF ELECTRONICS AND COMPUTER SCIENCE
and OPTOELECTRONICS RESEARCH CENTRE

Doctor of Philosophy

TOWARDS MULTIPLE QUANTUM WELL OPTICALLY PUMPED FAR INFRARED LASERS

by **Hock Aun TAN**

Optically pumped lasers based on GaAs/AlGaAs multiple quantum well (MQW) structures are a potential coherent source in the far infrared (FIR) wavelengths. The FIR (~ 30 to 300 μm) is a region within the electromagnetic spectrum that has seen relatively little development. No practical solid-state lasers have been possible in the FIR, which is also referred to as the terahertz (THz) wave, until the very recent demonstration of THz quantum cascade lasers. Other existing FIR lasers are either bulky, expensive, or require magnetic fields for operation. Hence, progress in the FIR depends on the availability of compact, miniature, and inexpensive FIR sources.

Optically pumped MQW lasers have advantages in simplicity of design, device processing, and lower free carrier loss, as compared to the electrically pumped lasers. Unlike traditional semiconductor lasers, the FIR MQW lasers involve only electron transitions between subbands of the conduction band. These subband energy levels in our stepped quantum well (QW) design can be tailored by selectively changing the thickness and alloy composition of the QW layers. However, electrons must first be confined to the subbands by doping of the MQW structure. Instead of placing the dopants at the middle of the barrier, the MQW is doped at the stepped well edge to minimise the parasitic distortion to the QW energy profile. FIR photoluminescence signal has been observed in a QW structure doped in the stepped well edge. Electron lifetime measurements were also conducted using a free electron laser (FELIX). Intersubband lifetimes of the order of few ps were obtained in the pump-probe experiment, which were longer than reported values for rectangular QWs. Moreover, a sub-ns slow decay due to multi-photon absorption was observed at high pump intensities. A rate equation model agreed well with the experimental result. A novel idea of stacking two MQW slabs face-to-face to improve the mode confinement of the laser system has been proposed. Possible errors in aligning the slabs were modelled, where the estimated increase in diffraction loss suggested that the stacking scheme is highly practical. Together with embedded heavily doped layers in the MQW structures, which utilise the surface plasmon guiding effects, a low modal loss and high mode confinement structure can be achieved. FIR optical signal systems were also studied, where detectors and optical materials required are different to those in the shorter wavelengths region. An optically pumped methanol gas laser was also built and tested for the work as an alternative FIR source.

Table of contents

List of figures

List of tables

List of publications and conference presentations

1. Rutt H N, Xin Z-J and Tan H A, 2000, 'Towards a Solid State Far Infrared Laser: Designs, Kinetics and Problems' in *Proceedings of Photonics 2000 TC-1*, Calcutta, India, pp. 187-190

2. Xin Z-J, Rutt H N, Tan H A, Wells J-P R and Bradley I V, 2000, 'Electron Lifetime Measurement in Stepped Quantum Wells for Far Infrared Lasers' presented in *Semiconductor and Integrated Optoelectronics (SIOE '2000)*, Aberdare Hall, Cardiff, Wales

3. Tan H A, Xin Z-J, Rutt H N, Wells J-P R and Bradley I V, 2001, 'Pump-probe measurements in asymmetric stepped quantum wells using FELIX', presented at *The Rank Prize Mini-Symposium on Applications of Free Electron Lasers*, Grasmere, United Kingdom

4. Tan H A, Xin Z-J, Rutt H N, Wells J-P R and Bradley I V, 2001, 'Pump-probe measurements in stepped quantum wells' in poster session of *The EPSRC III-V Semiconductor Facility Fifth Combined Users' and Industrial Liason Meeting*, University of Sheffield, Sheffield, United Kingdom

5. Tan H A, Xin Z-J, Rutt H N, Wells J-P R and Bradley I V, 2002: 'Intersubband lifetimes and free carrier effects in optically pumped far infrared quantum wells laser structures', *Semiconductor Science and Technology*, **17** (7) pp. 645-650

6. Tan H A, Xin Z-J and Rutt H N, 2002, 'Design and optimisation of optically pumped terahertz quantum well lasers', presented at *Semiconductor and Integrated Optoelectronics (SIOE '2002)*, Cardiff, Wales

7. Rutt H N, Xin Z-J and Tan H A, 2002: 'Design optimization of optically pumped terahertz lasers in stepped quantum wells', *Journal of Physics D: Applied Physics*, **35** (16) pp. 1907-1913

8. Tan H A, Xin Z-J and Rutt H N, 2003: 'Cavity modelling in stacked quantum well slabs for optically pumped lasers', *IEE Proceedings: Optoelectronics*, **150** (2) pp. 171-175

Acknowledgments

First of all, I want to thank my family in Malaysia for their support and encouragement throughout my studies here in the U.K. I wish them a healthy and happy life in the future, especially to my beloved parents.

Without the constant encouragement and guidance from Prof. HN Rutt, it would have been very different for this research work. Although having a busy schedule, he has never turned down a request for help when I approached him for advice, which I respect him for being a caring and responsible supervisor. It is thus very fortunate for me to have the opportunity to work with a very knowledgeable and helpful supervisor. I owed him in many aspects as a research student for the past few years.

Another person that I am greatly indebted to is Dr Z-J Xin (Johnson), who I must pay a sincere gratitude for his countless advice and assistance throughout this work. I gladly acknowledge the supplies of the MQW samples from the EPSRC III-V Semiconductor Facility in the University of Sheffield and the MBE group in the University of Glasgow. Without their samples, this project would not have been possible. Special thanks also to the FOM for allocating the valuable FELIX beam times for our measurements. The professional assistance from the FELIX staff are sincerely appreciated, especially Dr. AFG van der Meer, Dr. JPR Wells, and Dr. IV Bradley. I must also pay tributes to the technical and administrative staffs in the ORC and the ECS, especially W White and K Frampton for all their assistance that makes the research work possible. A note of appreciation also to Dr. PD Fairley, RJ Peaty, and other past and present members of the IRST group for all the happy time together. I would not have the chance to carry out the PhD studies if not for the research studentships from the Overseas Research Students Awards Scheme, and the financial support from the ORC. I also appreciate the undergraduate scholarship from MARA Malaysia that enabled me to come to Southampton at the first place. The financial assistance from the EPSRC is gladly appreciated both in funding this project and the trips to FELIX.

Lastly, I value the friendliness and kindness of the university community that make my stay here for the past few years a pleasant experience, and one that I will always remember. Not forgotten are all my friends here, in particular MH Ng, I wish them the very best of luck.

1 Introduction

The far infrared (FIR) is an electromagnetic (EM) wave region where relatively little work has been carried out compared to other regions such as in the visible, near-, and mid-infrared. Apart from some molecular spectroscopy [1-3], astronomy[4-6] and solid state physics [7], there are nearly no "real world" applications in this region. There is not even a clear definition of far infrared, but it is generally taken to be the region between ~30 to 300 μm in wavelength. Increasingly, this region is also referred to as the terahertz (THz) wave, corresponding to ~1 – 10 THz. Both the terminologies of FIR and THz wave will be used as interchangeable in the discussion of the wavelength region throughout this thesis.

1.1 FIR sources

In the mid-infrared region of ~5 – 30 μm, lead-salt semiconductor lasers [8] and quantum cascade (QC) lasers [9] are well established. Beyond 300 μm into the sub-millimetre region, the use of microwave technology becomes increasingly practical. Solid state devices have so far played a dominant role in all other EM wave regions. However, there is a so-called terahertz gap [10, 11] in the EM wave spectrum where solid state sources are notably absent. The fundamental reason for this phenomenon is the lack of a compact, tuneable, efficient and low cost coherent source. Current FIR lasers are either free electron lasers (FEL) [12-21], which cost millions of pounds and are massive central facilities, or carbon dioxide (CO_2) pumped pure rotational transition gas lasers [22, 23], which are large and offer a limited spectral choice. On the other hand, the hot hole p-type germanium (Ge) lasers [24] require operations in magnetic fields at liquid helium (He) temperature and thus unattractive for most applications. Hence, progress in this region depends crucially on the availability of practical FIR sources, especially room temperature semiconductor lasers.

1.2 Recent progress

In recent years, intensive research has been carried out on the possibility of developing FIR lasers based on intersubband radiation in quantum wells [9, 25-35]. This increase in interest follows the improved development of growing complex epitaxial layers and successful demonstration of laser emission utilising intersubband transitions [9, 25, 34]. Until recently, laser transitions with subband separation energy below the longitudinal

optical (LO) phonon energy in the host material (~36 meV in gallium arsenide (GaAs) and ~34 meV in indium gallium arsenide (InGaAs)) proved hard to achieve. For sometime, only electroluminescence [36-38] has been reported. A significant breakthrough was announced by Köhler et al [39] in 2002, where they have successfully demonstrated the first intersubband semiconductor THz emission (4.4 THz) with their quantum cascade laser (QCL) working at low temperature. This marks the first major step towards the realisation of practical FIR sources. Since then, a continuous wave (CW) QCL has been announced, which emits 0.4 mW optical power at wavelength of 66 μm with operation at T = 10 K [40]. However, room temperature devices have yet to be demonstrated. In addition, THz emissions from optically pumped impurity doped silicon (Si) lasers have also been reported [41, 42].

Both electrically and optically pumped intersubband devices have been proposed for the FIR lasers. In particular, the attempt to increase the laser wavelength of quantum cascade lasers to the THz region [43, 44]. Another approach is optically pumped quantum well (QW) lasers [31, 45], or the quantum fountain lasers [35, 46, 47], using for example a CO_2 gas laser as a pump source. The optically pumped QW lasers, without the need of injector layers and contact layer, have the advantage of simpler design and processing as compared to the electrically pumped QCL counterparts. Although requiring an external pumping source, optically pumped lasers have lower pump power threshold and internal losses due to free carrier absorption.

1.3 Optically pumped MQW lasers

Optically induced FIR lasers have advantages in efficiency, cost and size. Our work involves an attempt to develop a miniature, solid state sources for FIR region based on multiple quantum wells (MQW) in III-V semiconductors, specifically gallium arsenide/aluminium gallium arsenide ($GaAs/Al_xGa_{1-x}As$). The objective is the development of compact, near room temperature devices for future practical applications in security screening, space communication, quality control, spectroscopy and gas sensing. Unless specifically specified otherwise, the results and models presented in this thesis are the author's sole work.

In symmetric QW, a quantum selection rule states that photon-induced electron transitions are only possible between subbands with odd quantum number difference. However, this rule does not apply in an asymmetric QW, e.g. a stepped QW. Our

design for the FIR lasers will thus be based on 3-level stepped QWs, which is discussed in Chapter 2. The FIR laser relies on intersubband transitions of electrons for the emission of photons. In intersubband lasers, the emitted wavelengths correspond to the difference in the subband energies. Subband energies for a QW can be computed by self-consistently solving the Schrödinger and Poisson equations. Electrons need to be supplied and confined to the QWs for the intersubband transitions. This is achieved by selectively doping the QW structures in certain layers. Conventionally, for stepped QW and most QW structures, the dopants are placed in the middle of the barrier between two successive QWs. Nevertheless, at high doping densities, substantial electric potential may exist due to the separation between the dopants and the ionised electrons in the QW. Consequently, the energy profile of the QW can be distorted. This is highly undesirable, as the subband energies will be highly dependent on the doping concentration. A novel doping scheme is thus implemented, where the QW structure is doped in the stepped well edge to minimise the distortion due to the charge separation. These issues will be discussed in Chapter 2.

In a 3-level asymmetric QW lasers, population inversion is realised between the second excited subband where the electron is optically pumped from the ground subband, and the first excited subband. It is thus very important for us to understand the spectroscopy and kinetics of our MQW structure. The electron lifetimes in intersubband transitions of the MQW have been measured using pump-probe techniques at the Free Electron Laser for Infrared Experiments (FELIX) in the Netherlands. In Chapter 3, the experimental work on the electron lifetime measurements will be discussed. Intersubband lifetimes of the order of a few picoseconds were obtained for our MQW samples. These lifetimes were longer than obtained in rectangular QWs, which indicated a slower decay rate for our stepped QWs due to the smaller wavefunctions overlap. In addition, strong two-photon absorption (TPA) has been observed, leading to long-lived free carrier absorption in our sample. The two-photon absorption will represent a potential difficulty for our FIR laser. Fortunately, this TPA process can be avoided by suitable QW designs. A rate equation model has been utilised in the analysis of the data from the measurement. The model reproduces the essential characteristics of our pump-probe measurement. Fitted values using the model also show promising agreement with our experimental result. Evidence that FIR photoluminescence signals have been observed on a sample with the stepped well edge

doping scheme was presented. Observation of photoluminescence signals can provide a strong indication that the FIR lasers based on our design are indeed possible.

One of the well known difficulties in achieving laser action in the FIR is the issue of confining and guiding the THz laser emission in the active layers [37]. There is poor overlap between the laser mode (λ ~30 to 300 μm) and the active layers (a few micrometers). For optically pumped THz lasers, the pump wavelength is typically 10.6 μm since the CO_2 laser is normally the pump source although it may eventually be replaced by a mid-infrared QC laser. This inefficiency due to large difference between the modes and the active layer presents a technical challenge to find a way to guide the long wavelength emission, by utilising the current epitaxial growth techniques. The use of MQW, typically more than 50 periods, improves the confinement factor of the laser mode by increasing the total thickness of the active layer. However, the number of epi-layers that can be grown on a substrate is limited by the uniformity and morphology fluctuation from the growing process, as well as inhomogeneous line broadening issues [32, 48]. Typically, the epitaxial thickness grown by molecular beam epitaxy (MBE) is in the order of 10 μm for most modern growth facilities. On the other hand, the free carrier absorption loss, which is very serious in this long wavelength region, has to be minimised, as the loss is approximately proportional to the square of the wavelength λ. These issues have fundamentally hindered the success of lasing from various attempts to design a compact, solid state THz source. These issues will be discussed in Chapter 4. A novel idea is proposed, where two MQW slabs are stacked face to face to improve the mode confinement of the laser. Heavily doped layers can be embedded in the QW structures to act as surface plasmon guiding layers. A transfer matrix model is utilised to calculate the confined mode profiles and the corresponding losses. Alternatively, a metal layer can be coated on the surface of a single MQW slab, which is found to have a reasonable performance of mode confinement. Furthermore, the diffraction loss due to potential errors in aligning the slabs in the stacking scheme is estimated. This is modelled based on a Fresnel integral method.

In Chapter 5, issues associated with the FIR optical signals will be discussed. There are various types of detectors that have been developed for the FIR. An extrinsic semiconductor detector is chosen for the detection of the FIR signals in this work. A sensitive gallium doped germanium (Ge:Ga) photoconductive detector is ideal for detection at the wavelength range of our FIR lasers emission. This photoconductor

needs to be cooled to very low temperature for operations as a FIR detector. As the photoconductor is very sensitive and the very small detected signal needs to be first amplified. A preamplifier is thus designed to amplify this weak signal while minimising any noise effect. Several tests were carried out to measure the performance of this detector. A blackbody source was used as an FIR source for the purpose of testing the responsivity of the detector, as well as evaluating the preamplifier. The pulse response of the Ge:Ga detector was observed by utilising the greatly attenuated CO_2 pulse laser signal. Materials used in this work for FIR transmission and elimination of unwanted radiation are described. Pyroelectric detectors that are widely used in this work are also discussed. Furthermore, an optically pumped FIR gas laser is constructed as part of the experimental work. This gas laser is useful for analysing the performance of detectors, as well as an alternative FIR source.

Finally, a general conclusion is drawn in Chapter 6. A breakthrough has yet to be achieved in obtaining laser action from our MQW samples, although photoluminescence signals have been observed. Hence, there are still further improvements that need to be carried out in order to achieve the objective of an optically pumped MQW FIR laser. Brief discussion on the prospect of THz technology is included.

Some useful material for this work is included as appendices. Appendix 1 presents measured transmission spectra on a number of optical materials used in the mid and far infrared regions generally, and in particular this work. Appendix 2 describes some definitions and calculation regarding the blackbody emission, which includes the background radiation calculation for the pump-probe measurement, and analysis on detection of FIR emission by the Ge:Ga photoconductor. Appendix 3 presents additional measured transmission spectra for samples not discussed in the main text.

2 Quantum well design for FIR lasers

Traditionally, semiconductor lasers rely on the radiative recombination of excited electrons in the conduction band and holes in the valence band to generate the stimulated emission of light. A single recombination of electron and hole pair across the forbidden region or energy band gap of the active material emits energy in the form of a photon, where the frequency of the photon is proportional to the band gap energy. The relation between the photon energy E, and its wavelength λ, or frequency f, is given as:

$$E = hf = \frac{h\omega}{2\pi} = \hbar\omega = \frac{hc}{\lambda} \qquad (2.1)$$

where h is the Planck's constant, c is the speed of light in free space, ω is the angular frequency, and $\hbar$ is defined as $h/2\pi$. This type of lasers are sometime referred as interband lasers since the laser transition is across the band gap. Figure 2.1.a. illustrates the interband transition. Hence, the emission wavelengths of the interband lasers are determined by the energy band gap of the materials. For example, GaAs has an emission wavelength of 860 nm that corresponds to an energy band gap of 1.43 eV [49]. Furthermore, GaAs is a direct band gap material, where the maximum of the

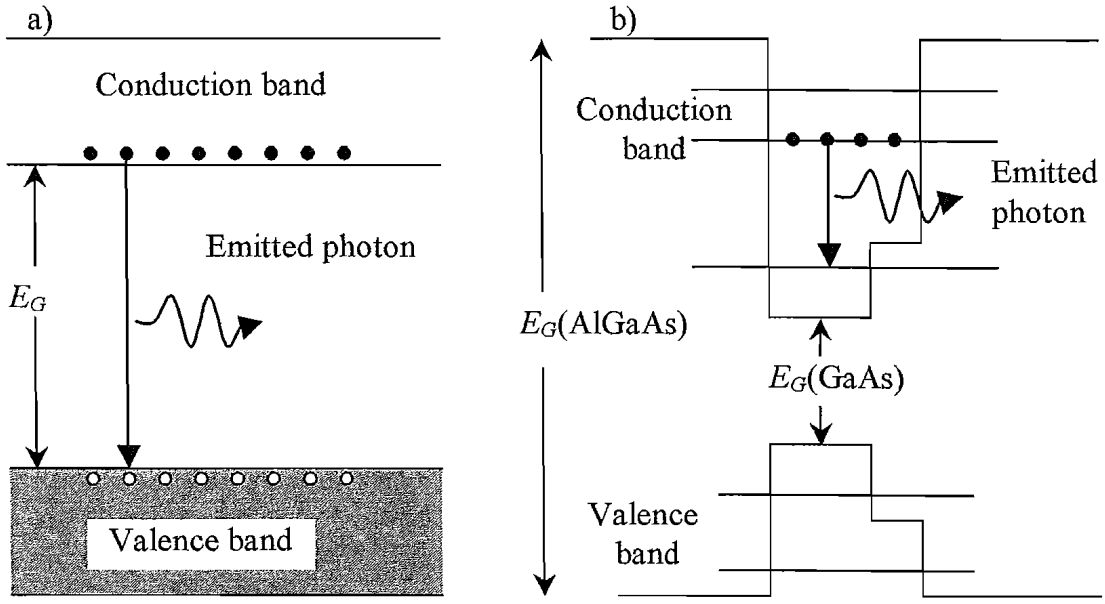

Figure 2.1. a) Interband transition across the energy band gap, E_G, involving an electron-hole pair. b) Intersubband transition involving only electrons between the confined subband energy levels. This diagram shows a stepped quantum well for the GaAs/AlGaAs system.

valence band occurs at the same propagation constant value k as the minimum of the conduction band. In contrast, indirect band gap materials, such as silicon (Si) have the valence band maximum and conduction band minimum at different k value. Consequently, radiative interband transitions are harder to achieve for indirect band gap materials than for direct band gap materials. Unlike interband lasers, our optically pumped FIR laser is based on electron transitions between closely separated subband energy levels within the conduction band, as shown in Figure 2.1.b. For this type of laser, the photon energy is determined by the spacing between the subbands.

In this chapter, the intersubband FIR laser design is discussed. Methods for calculating the energy levels of the QW structure will be introduced. The confined energy levels are chosen in order to realise the pump and FIR laser transitions effectively. Different ways of doping the QW structure to supply the electrons for the laser transition will also be described. An experimental method of determining the absorption band of photons across the energy subbands is discussed, utilising a spectrometer. Threshold gain of the laser and required pump intensity are then estimated. The chapter is concluded with a summary and general results of the QW design.

2.1 Intersubband QW lasers

In this section, the growth of QW structures for the FIR lasers will be explained. This is followed by the working principles of QW lasers, particularly the intersubband transitions. Then, the methods of pumping for the laser are discussed, where optical pumping is used for our system.

2.1.1 Epitaxial growth of the QW structure

Over the past decades, technological and engineering advances in epitaxial growth techniques have enabled the growth of very precise layers of semiconductor structures. The most important techniques include molecular beam epitaxy (MBE) and metal-organic chemical vapour deposition (MOCVD) [50, 51]. These techniques are now widely used to grow complex structures consisting of atomically flat layers of semiconductor materials. High surface uniformity and accurate control of thickness down to monolayer (~3 Å) thickness can be achieved using these techniques.

Our MQW structures are based on the GaAs/$Al_xGa_{1-x}As$ system, which are grown on GaAs substrate by MBE in facilities at the University of Glasgow [52] and the University of Sheffield [53, 54]. Both facilities are solid source MBE systems, capable

of growing As based III-V compound, e.g. GaAs, AlGaAs and InGaAs. In MBE, the QW structure is grown one monolayer at a time by evaporating the layer materials and the dopants from separate effusion ovens. Mechanical shutters are used to start and stop the molecular beam abruptly. The growing chamber is at high vacuum ($\sim 10^{-11}$ torr, 1 mbar = 0.75 torr) so that the atoms or molecules of evaporated elements remain as beams of atoms or molecules. There are no chemical reactions of the beams before the atoms or molecules reach the growing surface on the substrate. When the atoms or molecules reach the substrate, which is heated, they react and grow epitaxially. Typical growth rate for MBE is 1 μm/hour or ~ 1 monolayer per second. Furthermore, growth of the layers can be monitored by techniques which rely on the electron diffraction from the growth surface, i.e. the reflection high energy electron diffraction (RHEED) techniques. These techniques provide valuable real time feedback on the growth process in most MBE systems [50, 51, 55].

2.1.2 Formation of the QW structures

In general, a quantum well (QW) is formed when a material of lower band gap energy is grown in between two layers of materials with higher band gap energies. Quantum wells are formed in both the conduction and valence bands. In our QW structures, GaAs has an energy band gap of 1.42 eV compared to a higher energy band gap for $Al_xGa_{1-x}As$ [56, 57]. Due to the confinement, electrons or holes are unable to move freely in the growth direction. However, they can still move freely in the plane of the QW layers. As shown in Figure 2.2.a, a stepped QW is grown by having an intermediate layer of wider band gap material next to the GaAs lower well, in between even higher energy barrier materials. The energy band gap of $Al_xGa_{1-x}As$ is proportional to the Al content x. Hence, different compositions of x are used to form the stepped well and the barrier. Similarly, a triple quantum well structure (Figure 2.2.b), also known as parallel QW or coupled QW, can be grown by having one or more thin barriers in between the GaAs wells. In this case, electrons can tunnel through the thin barriers. The figure also shows the wave functions that correspond to the subband energy levels.

By having a layer thickness which is much smaller than the electron wavelength, electrons can be confined to a two dimensional plane [58]. The quantum confinement in quantum wells results in different energy levels being formed in the conduction band, normally referred to as the subband energy levels. By choice of material

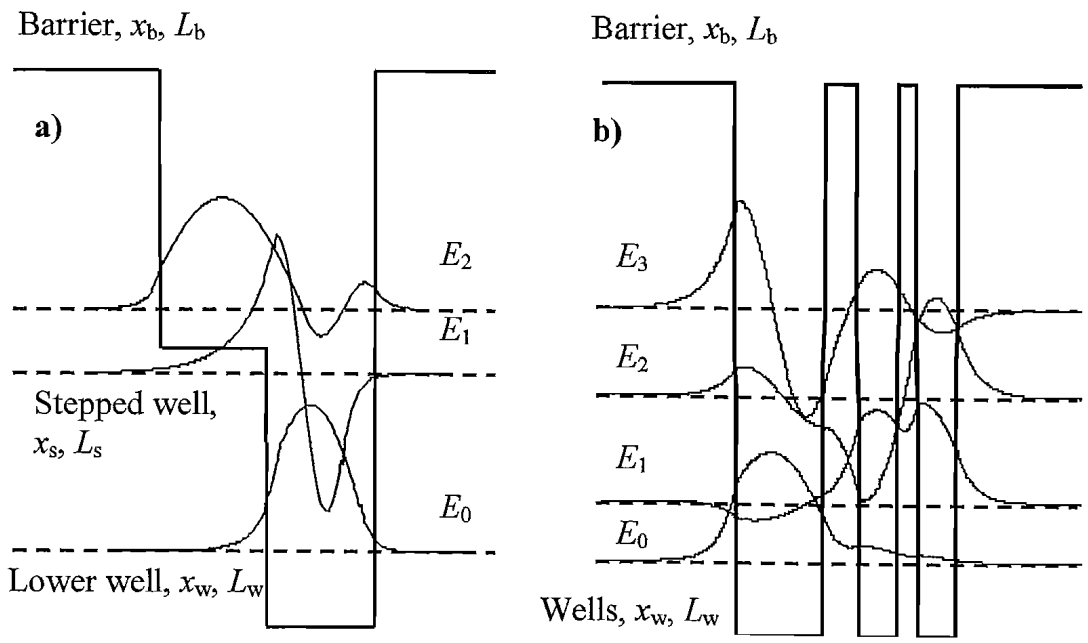

Conduction band diagrams, $Al_xGa_{1-x}As$

Figure 2.2. Confined subband energy levels and the corresponding electron wavefunctions in: (a) a single stepped quantum well, and (b) a coupled-well structures. The energy levels can be engineered by selecting the appropriate Al compositions and the widths of the stepped well, lower well, or the thin middle barrier layers.

composition and layer thickness, the subband energy levels can be engineered and determined. These energy levels can thus be chosen to ensure an effective laser system. Moreover, electrons that are needed for laser transitions have to be supplied to the QW structure by doping certain layers of the structure. As will be discussed later, the position and concentration of the dopants in the QW structures may also have a significant influence on the energy levels [59]. Therefore, a wide range of emission wavelength is possible by selectively choosing the QW parameters.

As the energy difference for emission in the FIR/THz region is small (very few tens of meV), realisation of interband lasers in this region will require materials with very narrow band gap energies, such as mercury cadmium telluride ($Hg_{1-x}Cd_xTe$) [60, 61]. HgCdTe is an alloy of HgTe and CdTe, where HgTe is a semimetal with a negative band gap (i.e. the conduction and valence bands overlapped). Therefore, a wide range of energy band gap can be covered by using this alloy material. Unfortunately, these narrow band gap materials are mostly difficult to process and fragile [62-65] compared to the available wide band gap materials, such as the III-V compound semiconductors. Wide band gap materials, which are technologically mature and well understood, can

be used to form the QW structures. The small energy difference between the confined subbands in QW thus appears as an ideal emission source for the FIR region [31, 36, 66]. In contrast to interband lasers, intersubband lasers transition only involve electrons in the conduction band. As there are no electron-hole pairs involved, intersubband lasers are also termed unipolar lasers [34, 35, 46].

2.1.3 Intersubband transitions

A quantum selection rule states that electrons can only make photon-induced transitions between subbands with odd quantum number difference in a symmetric quantum well [31, 67]. Due to the symmetry of this QW, wavefunctions overlap between energy levels with even quantum number difference is zero, which means no transition is theoretically possible between E_0 to E_2 in a 3-level laser system. Therefore, it is essential that asymmetry be introduced to the QW to break this rule. This asymmetry can be achieved by either introducing an electric field to the QW structure or in our case by using asymmetric QWs(AQW). In a 3-level asymmetric QW laser system, such as the stepped QW (SQW), population inversion is possible between the second excited subband (upper laser level) and the first excited subband (lower laser level). A comparison between stepped QW and coupled QW designs for FIR lasers has suggested that the former offers a lower pump threshold [31]. A low threshold system is necessary to ensure that the gain from the excitation of electrons can overcome the various losses associated with a laser system, such as the non-radiative scattering process. Our design for the optically pumped FIR lasers will thus be based on the SQW design. This 3-level laser scheme is analogous to a conventional optically pumped gas laser, where the upper pump and laser levels are shared. As discussed in [31], the mostly empty lower laser level in this scheme has the advantage of a low threshold. This is in contrast to the 3-level ruby laser [68], which has a high threshold since the lower pump and laser levels are shared.

In order to achieve population inversions in our 3-level system, it is desirable that the depopulation rate for the lower laser level is greater than the upper laser level, especially for CW lasers, i.e.

$$\tau_{21} > \tau_{10} \tag{2.2}$$

where τ_{21} and τ_{10} are the electron relaxation times from E_2 to E_1 and E_1 to E_0 respectively. This will ensure that electrons stay longer in E_2 than in E_1, in order for the

population in upper laser level to build up sufficiently. This condition is in turn related to the radiative and non-radiative transitions between the subbands. In particular, the laser transition ($E_2 \rightarrow E_1$) must favour a radiative transition to realise the laser emission.

For GaAs based structures, non-radiative scattering rate is dominated by the emission of LO (longitudinal optical) phonon when the energy separation between two subbands is larger than the LO phonon energy ($E_{LO} \sim 36$ meV in GaAs) [56]. On the other hand, if the energy separation is less than the LO phonon energy, then the electrons scattering is dominated by the interactions with the acoustic phonons. For the past decades, intersubband transition measurements have determined that the transition rate for the LO phonon assisted scattering is in the orders of under 1 ps to a few ps. In contrast, lifetimes measurement for energy separation that is smaller than the LO phonon energy suggested lifetimes of few tens to hundreds of ps [29, 69-73].

In order to achieve a high performance in a FIR laser, the subband energies need to be designed such that the wavefunction overlaps of E_0 with E_2, and E_2 with E_1 are large. This will ensure that the pump and laser transitions have high interactions with photons, thus increasing the laser efficiency [31]. The wave function overlap can be characterised by a dimensionless quantity, the oscillator strength, which is described as [74]:

$$F_{i\to f} = \frac{2m^*}{\hbar^2}\left(E_f - E_i\right)\left|M_{i\to f}\right|^2 \qquad (2.3)$$

where $M_{i\to f}$ is the dipole matrix element, m^* is the electron effective mass, E_f is the final state, and E_i is the initial state for the transition involved. The dipole matrix element is written as

$$\begin{aligned} M_{i\to f} &= \langle \psi_f | z | \psi_i \rangle \\ &= \sum_{Mesh} \psi_f^* z \psi_i \end{aligned} \qquad (2.4)$$

where ψ is the wave function and the operator * signifies the complex conjugate of the function. The oscillator strength is proportional to the overlap of the wave function between two energy levels where the transition is taking place. Consequently, high oscillator strength values are needed for the pump and laser transitions in our design to increase the efficiency of the laser system.

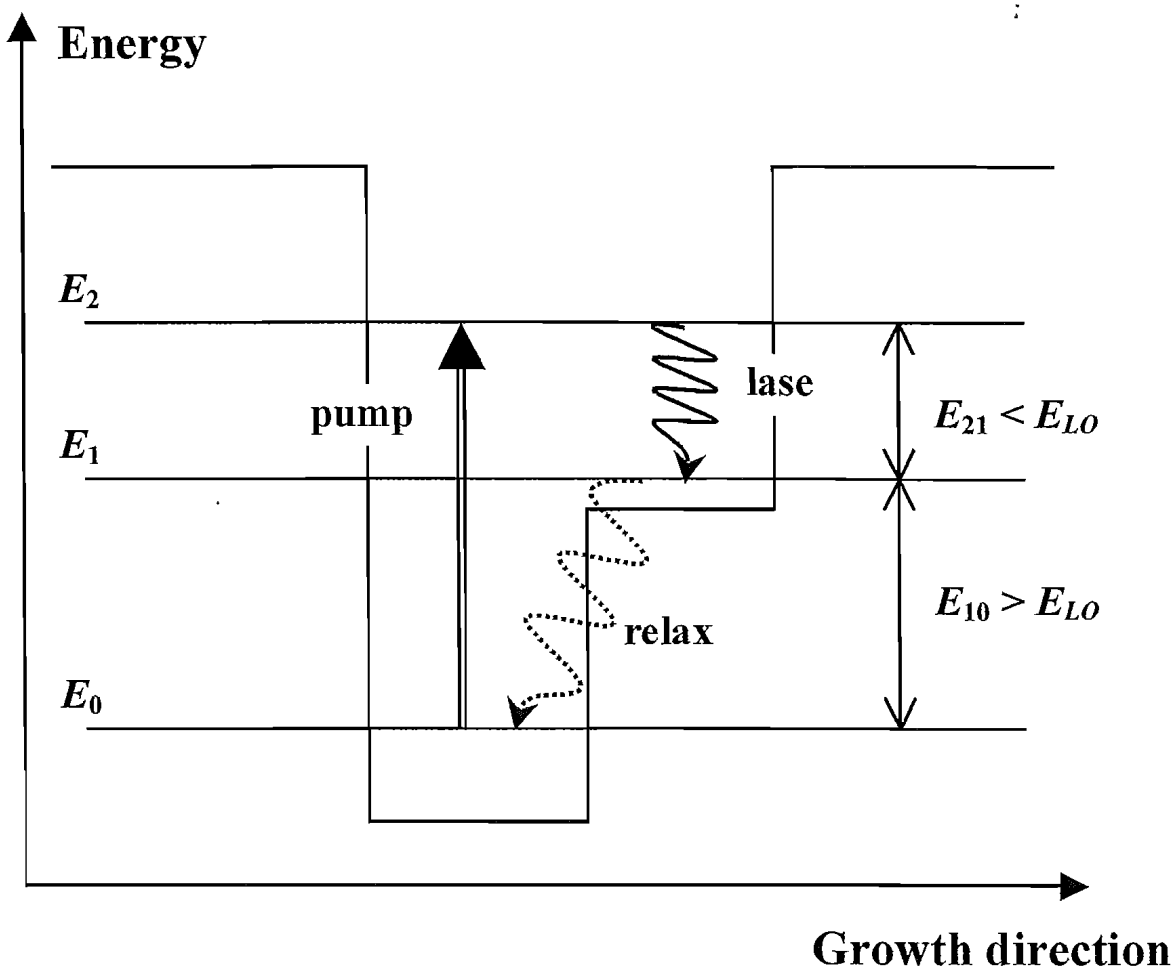

Figure 2.3. Intersubband transitions involved in the stepped QW, 3-level FIR laser. The energy separation between subbands are chosen such that the lower laser level is depopulated faster than the upper laser level. The energy separations are chosen to be smaller (larger) than the LO phonon energy, such that the non-radiative rate is low (high).

Naturally, for a laser transition between E_2 and E_1, it is desirable that the energy separation E_{21} to be less than the LO phonon energy. Hence, the slower acoustic phonon assisted scattering will dominate the E_{21} transition. In addition, the fast removal of electrons from the lower laser level is very efficient if the energy separation favours the fast LO phonons scattering. Our design has thus ensured that E_{10} is greater than E_{LO} to facilitate the fast removal of electrons from the lower laser level, as shown in Figure 2.3. Note that E_{20} is also greater than E_{LO}, which may imply a fast scattering rate from the upper laser level back to the ground level. However, due to the larger wavefunctions overlap between E_2 and E_1 compared to the overlap between E_2 and E_0, the relaxation of electrons from E_2 is dominated by the E_2 to E_1 transition [30]. For our stepped QW design, the wave function for E_0 is mainly confined in the narrow lower

well, such that the pump (E_0 to E_2) and depopulation (E_1 to E_0) transition rates are high. In contrast, the nonradiative transition rate from E_2 to E_0 is low since the wave function for E_2 is mainly in the stepped well region.

2.1.4 Optically pumped lasers

Optically pumped intersubband lasers have been demonstrated in the mid-infrared, in particular the quantum fountain lasers [34, 35, 46], and the intersubband Raman laser [75]. Although less convenient than electrically injected pumping, optically pumped system still offers many advantages [25, 26, 28, 30, 31, 35, 45, 67, 76]. One of the reasons why optically pumped lasers are widely studied is the easy ability of the powerful and inexpensive pump source, especially the CO_2 laser.

In electrically pumped lasers, the injection of electrons from an upper subband and depopulation of electrons from a lower subband are accomplished by the electrons tunnelling across thin barriers. The resonant tunnelling must take place perfectly such that the depopulation from one subband at the lower well can be injected to the upper subband of the next well [9]. This tunnelling process relies on very accurate control of the epitaxial growth. On the other hand, optically pumped lasers based on asymmetric stepped QW do not involve tunnelling process. Electrons are supplied to the pump-relaxation process by ionisation of the dopants, which are selectively doped in the QW structure. The doping schemes will be further discussed in section 2.3.

In addition, injection layers are needed in electrically pumped QC lasers for the enhancement of the injection and depopulation of electrons from the subbands. This is not the case for optically pumped lasers as the ionised electrons are confined and excited from within the well. Electrical contacts are needed to facilitate the current flow across the structure in electrically pumped devices. This normally requires complicated design and device processing [9, 37, 39]. Conversely, as no current flow is required in optically pumped lasers, there is no electrical contact layer needed, resulting in further simplification in device processing. Hence, in general optically pumped lasers are structurally much less complicated and thus offer great simplification in device design and fabrication. In addition, optically pumped lasers have a lower pump threshold due to the low free carrier loss. This is especially advantageous in long wavelength lasers. For electrically pumped lasers, however the free carrier loss is unavoidable due to the required current flow.

In our optically pumped FIR laser, electrons are excited from the ground subband in the conduction band to the second excited subband [49]. The intersubband transitions of the laser are depicted in Figure 2.3, where the pump transition is chosen to resonant with a normal CO_2 laser line. For our case, a transversely excited atmospheric (TEA) pulsed CO_2 laser, model MTL-3 by Edinburgh Instruments [77], is used for the experiments. The laser is grating tuned to operate at laser lines between ~ 9 – 11 μm with a typical pulse width at full width half maximum (FWHM) of 55 ns, which delivers a maximum pulse energy at ~ 50 mJ/pulse. However, this pump source can alternatively be replaced by other mid-infrared semiconductor lasers, such as the QC lasers, to achieve an all solid state source. Under infrared intersubband absorption, the electrons are removed from the ground subband and E_2 is populated. For a monochromatic source, only E_2 is directly populated while E_1 is not filled by the pump. This is an additional advantage for an optically pumped system, where selective pumping of the subband levels is possible [67].

2.2 Calculation of the subband energy levels

In this section, we shall discuss the procedures to determine the subband energy levels confined in the QWs. For a MQW structure, where many periods of identical single QWs are repeated, the energy subbands need to be solved for a single QW only. This is true as long as the single QWs are each separated by a thick barrier in between, such that the wave functions of the electron subbands have effectively returned to zero in the barrier. We shall first discuss the solution of energy levels for a given potential energy profile. A model is built to solve for the subband energy levels, based on the discussion in section 2.2.1. This model has been modified and improvised from earlier feasibility studies of optically pumped FIR lasers [31, 32, 48]. Then, the contribution of electron distribution in the QW is introduced by using the Poisson equation in section 2.2.2, and making the additional modification to the energy subbands.

2.2.1 Schrödinger equation

The subband energy levels in a single quantum well can be determined by first solving the one dimensional time-independent Schrödinger equation [78-83], in Equation 2.5:

$$-\frac{\hbar^2}{2}\frac{\partial}{\partial z}\left(\frac{1}{m^*(z)}\frac{\partial}{\partial z}\psi_i(z)\right)+V(z)\psi_i(z)=E_i\psi_i(z) \tag{2.5}$$

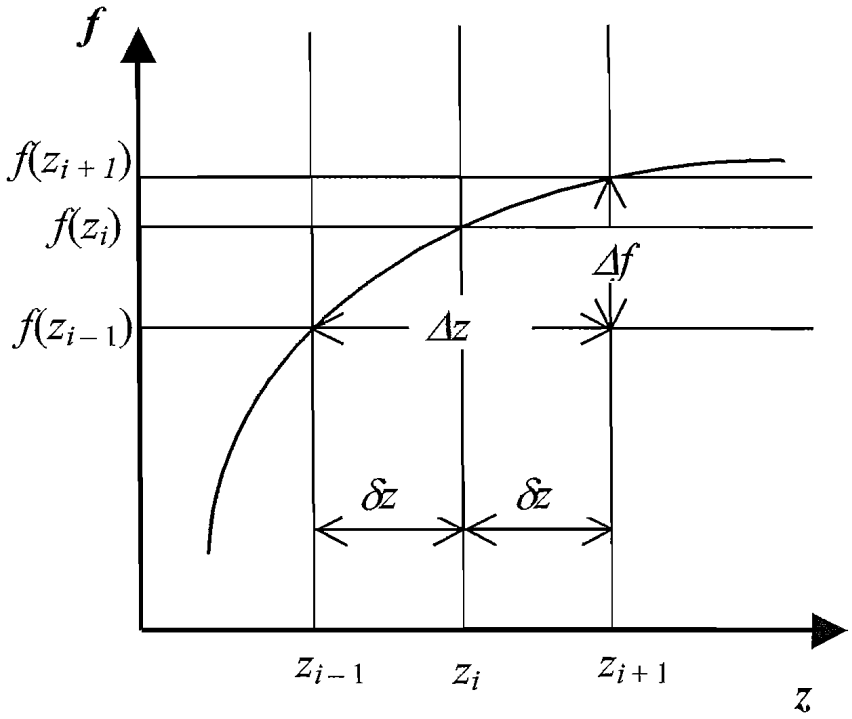

Figure 2.4. First derivative of a function $f(z)$ using the finite difference method is approximated by $\Delta f/\Delta z$. The distance between two successive mesh point is δz, and $\Delta z = 2\delta z$.

where $\hbar$ is the Planck's constant divided by 2π, $m^*(z)$ the electron effective mass, $V(z)$ the QW band energy profile along the growth direction z, $E_i(z)$ the i-th confined energy level, and $\psi_i(z)$ the corresponding wave function at the energy level. There are different numerical methods of solving the Schrödinger equation [78-83]. We have built a model based on a standard finite difference method, where Equation 2.5 can be modelled by dividing the QW layers into a small mesh size [79]. As illustrated in Figure 2.4, for any arbitrary function f, the first derivative can be approximated by:

$$\frac{df}{dz} \approx \frac{\Delta f}{\Delta z} = \frac{f(z+\delta z) - f(z-\delta z)}{2\delta z} \tag{2.6}$$

where $\Delta z = 2\,\delta z$.

Hence, by first taking the derivative of $\psi(z)$ and follows by a further differentiation with $m^*(z)$ included, Equation 2.5 is rewritten as

$$\frac{\hbar^2}{2(2\delta z)^2}\left[-\frac{\psi(z+2\delta z)}{m^*(z+\delta z)} - \frac{\psi(z-2\delta z)}{m^*(z-\delta z)} + \frac{\psi(z)}{m^*(z-\delta z)} + \frac{\psi(z)}{m^*(z+\delta z)}\right] + \psi(z)V(z) = \psi(z)E \tag{2.7}$$

Finally by transforming $2\delta z \rightarrow \delta z$, since δz only represents any small mesh size, Equation 2.7 can be written as:

$$\frac{\hbar^2}{2\delta z^2}\left[-\frac{\psi(z+\delta z)}{m^*(z+\frac{\delta z}{2})}-\frac{\psi(z-\delta z)}{m^*(z-\frac{\delta z}{2})}+\frac{\psi(z)}{m^*(z-\frac{\delta z}{2})}+\frac{\psi(z)}{m^*(z+\frac{\delta z}{2})}\right]+\psi(z)V(z)=\psi(z)E \tag{2.8}$$

Further, the position at the i^{th} mesh point can be written as z_i. Then, by using a matrix eigenvalues method, Equation 2.5 can be rewritten as the eigenvalue-eigenvector relation:

$$A\psi(z_i)=E_i\psi(z_i) \tag{2.9}$$

where the symmetric matrix A is a tridiagonal matrix, as all its nonzero entries are on the main diagonal and in the positions immediately adjacent to the main diagonal [84]. Elements of A can be deduced from Equation 2.8, which are given as:

$$\begin{aligned}
A_{i,i} &= V(z_i)+\frac{\hbar^2}{2\delta z^2}\left(\frac{1}{m^*\left(z_{i+1/2}\right)}+\frac{1}{m^*\left(z_{i-1/2}\right)}\right)\\
A_{i,i+1} &= -\frac{\hbar^2}{2\delta z^2}\left(\frac{1}{m^*\left(z_{i+1/2}\right)}\right)\\
A_{i,i-1} &= -\frac{\hbar^2}{2\delta z^2}\left(\frac{1}{m^*\left(z_{i-1/2}\right)}\right)
\end{aligned} \tag{2.10}$$

where the effective mass at $z_{i\pm1/2}$ is taken as the average value between the two consecutive z points:

$$m^*\left(z_{i\pm1/2}\right)=\frac{m^*\left(z_{i\pm1}\right)+m^*\left(z_i\right)}{2} \tag{2.11}$$

Consequently, by using a numerical method to solve for the eigenvalues in Equation 2.9, the corresponding confined subband energy levels can be deduced. Similarly, the associated electron wave function for the subband energy level is given by the eigenvector, ψ.

Later in this chapter, there will be discussion on a variety of ways of doping the QW structure in order to provide the electrons in the pump-relaxation of laser transitions. The high electron concentration in the QW will change the effective mass values in the materials. As the electrons can now be away from the conduction band edge at higher energy subbands, non-parabolicity effects need to be included. This is to account for the difference in energy relative to the bulk conduction band minima. In order to take into account these changes, an expression for doping concentration dependent effective mass by Raymond et al [85] is included into our model:

$$\frac{1}{m^*} = \frac{1}{m_0^*}\left(1 - \frac{2\Delta_E}{E_G}\right) \tag{2.12}$$

where

$$\Delta_E = \left(3\pi^2 n\right)^{\frac{2}{3}} \frac{\hbar^2}{2m_0^*}\left(1 - \frac{m_0^*}{m_0}\right)^2 \left(\frac{1 + x_\alpha + \frac{1}{4}x_\alpha^{\,2}}{1 + \frac{4}{3}x_\alpha + \frac{4}{9}x_\alpha^{\,2}}\right) \tag{2.13}$$

and

$$x_\alpha = \frac{\Delta_{so}}{E_G} \tag{2.14}$$

The spin-orbit split-off valence band energy for GaAs is $\Delta_{so} = 0.341$ eV [56, 85], and m_0^* is the conduction band edge effective electron mass while m_0 is the free electron mass. After taking into account the occupations of electrons in the higher subbands, the electron sheet density distribution n as a function of z can be obtained. E_G is the temperature dependent band gap energy in eV [51, 56, 57]:

$$E_G(T) = E_G(0) - \frac{5.405 \times 10^{-4} T^2}{T + 204} \tag{2.15}$$

where $E_G(0)$ at $T = 0$ is 1.519 eV for GaAs and T is the absolute temperature in units of Kelvin.

The value of m_0^* for $Al_xGa_{1-x}As$ is related to the Al composition x, for $x < 0.45$ where the material remains a direct band gap semiconductor [58], which is given by:

$$m_0^*(x) = m_0^*\big|_{GaAs} + (0.083x)m_0 \tag{2.16}$$

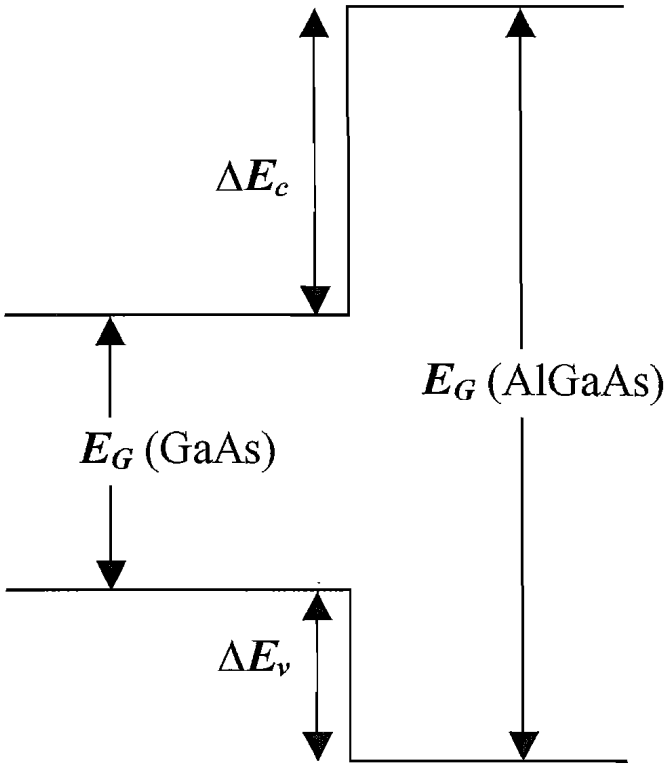

Figure 2.5. The band gap differences in the conduction band ΔE_c and valence band ΔE_v in a quantum well. The two values are not equal, but rather the larger offset value is found in the conduction band.

As the composition of the alloy changes, the energy band structure for AlGaAs varies and transforms from a direct- to an indirect-band gap material. The energy gap for AlGaAs ($x < 0.45$) can be specified as [51, 58]:

$$E_G(x) = E_G|_{GaAs} + (1.247x)q \tag{2.17}$$

The bottom of the conduction band edge for GaAs QW is taken as the zero point for the energy in the calculation. Therefore, the conduction band gap offset of the AlGaAs relative to GaAs is taken as the barrier or the stepped well energy. In addition, the empirical value of the conduction band offset factor between GaAs and AlGaAs, as shown in Figure 2.5 is defined as

$$\begin{aligned} \Delta_{offset} &= \frac{\Delta E_c}{E_G(AlGaAs) - E_G(GaAs)} \\ &= \frac{\Delta E_c}{(\Delta E_c + \Delta E_v)} \end{aligned} \tag{2.18}$$

This offset factor is important, which is generally taken between 0.6 – 0.7 for GaAs based structures, as it has been observed that the energy band gap does not distribute

equally between the conduction band and valence band [51]. Rather, a larger part of the band gap discontinuity is in the conduction band. In our model, a value of 0.67 is used for this offset factor [79].

2.2.2 Poisson equation

The Schrödinger model on its own is not adequate to accurately predict the subband energy levels, as the model has not included the effects of the large number of carriers present in the conduction band. A significant potential can be present due to these additional carriers, which modifies the conduction band profile of the QW structure. In turn, this affects the energy levels in the subbands. This additional electrostatic potential can be described by the one dimensional Poisson equation [78, 80-83, 86]:

$$\begin{aligned}\frac{\partial}{\partial z}\left(\varepsilon_r(z)\frac{\partial}{\partial z}\right)\phi(z) &= -\frac{\rho}{\varepsilon_0} \\ &= -\frac{q[N_d(z)-n(z)]}{\varepsilon_0}\end{aligned} \tag{2.19}$$

where ε_r is the dielectric constant of the material, ϕ is the additional electrostatic potential, ρ is the space charge distribution, q is the free electron charge, N_d is the ionised donor concentration, and n is the electron density distribution. This electron density distribution has taken into account the occupation of the subbands.

Hence, if the conduction band edge profile at zero doping is denoted as V_c, then the total potential term for the Schrödinger equation in Equation 2.5 is simply:

$$V(z) = -q\phi(z) + V_c(z) \tag{2.20}$$

A solver [78] developed by Snider et al is utilised to include the charge effects of the electrons, which iteratively computes the solutions for Equations 2.5 and 2.19 until both equations are simultaneously satisfied, the so-called self-consistent solutions. This solver utilises a matrix transform technique to enable a non-uniform mesh size being used. For non-uniform mesh size, the QW layers are discretised into different mesh spacing. For regions where the wave function is rapidly changing, smaller mesh size is used. On the other hand, larger mesh size is used for region where the wave functions only vary slowly. For instance, in the stepped QW, small mesh size is employed near the lower QW since the electrons concentration is highest and the wave functions are expected to vary rapidly in this region. Away from the lower QW, the electron concentrations at the barriers are low and the wave functions also only differ slightly

across the barrier. Hence, the mesh size can be increased in these regions to reduce the total number of mesh points. The real advantage of the non-uniform mesh size is that the computation time can be greatly reduced without sacrificing any significant accuracy.

2.2.3 Discussion on the computational procedures

As mentioned in the previous subsection, a one-dimensional solver developed elsewhere [78] is utilised to self-consistently solve the Poisson and Schrödinger equations. This solver utilises non-uniform mesh sizes to compute the solutions in short computational time, where the number of mesh sizes is limited to just 500 points. Note also that this solver uses different method to solve for the subband energy levels. In particular, this solver does not include the effects of electron concentration on the electron effective mass in the QW structure, as described by Equations 2.12 - 2.16. In contrast, the electron effective mass in an individual layer is assumed to be constant throughout the layer. Consequently, we have taken advantage of the fast computational time of this solver to obtain the conduction band energy profile $V(z)$ and the electron density distribution $n(z)$ for a single QW. After a self-consistent solution is achieved, the data for these two variables are recorded. These two set of values are then transformed into uniform mesh sizes, and calculated using our Schrödinger model that implements Equation 2.10. This model includes the modification to the effective mass as a result of the high electron concentration in the QW, as described in section 2.2.1. As this model uses uniform mesh sizes and considerably smaller mesh size than the self-consistent solver, a more accurate solution of the energy levels can be obtained. Nevertheless, the computational time for this model implemented in a Mathcad [87] environment is orders of magnitude larger than the non-uniform solver. The trade off in the accuracy of the solutions is acceptable as substantial valuable computational time can be saved.

Note that the effective mass term in Equation 2.5 is written inside the left hand derivative, to include the effects of varying $m^*(z)$ for different materials. This expression also satisfies the boundary conditions, where both $\psi(z)$ and

$$\frac{1}{m^*(z)}\frac{\partial\psi(z)}{\partial z} \tag{2.21}$$

are continuous.

In addition, note that the final approximation of the differential equation (Equation 2.8) does not contain the term $m^*(z)$. The disappearance of this term is attributed to the double application of the first order derivative (Equation 2.6). An alternative method exists where the product rule can be applied to the derivative of Equation 2.21 to yield

$$\frac{\partial}{\partial z}\left[\frac{1}{m^*(z)}\frac{\partial\psi(z)}{\partial z}\right] = -\frac{1}{m^*(z)^2}\frac{\partial m^*(z)}{\partial z}\frac{\partial\psi(z)}{\partial z} + \frac{1}{m^*(z)}\frac{\partial^2\psi(z)}{\partial z^2} \tag{2.22}$$

Hence, the second order derivative approximation can be used instead, as opposed to the approach described earlier in section 2.2.1. This method avoid the situation where the value of $m^*(z)$ is not present in the final equation. Nevertheless, this alternative method was not employed in our model, which used the method as described before in section 2.2.1 and in Ref. [79].

Moreover, we have found in our calculations that a mesh size of 1 Angstrom or less is needed to accurately compute the subband energy levels. As shown in Table 2.1, the computed values for the mesh sizes used have shown the desired convergence, where mesh sizes between 0.016 nm to 0.2 nm were compared. Listed in the tables are the first four subband energy levels, the relevant energy separations, and the corresponding transition wavelengths. Furthermore, in order to avoid loss in accuracy, the step size is chosen such that each individual layer can be divided into a whole number of mesh points. In our computational results, energy levels are normally computed to within 0.1 meV of consistency. In this example, the calculation is based on the parameters for sample A1580 (the details of this sample will be described later in the chapter).

Step size (nm)	E_0 (meV)	E_1 (meV)	E_2 (meV)	E_3 (meV)
0.200	62.110	171.052	186.636	216.815
0.100	62.094	171.309	186.883	216.992
0.050	62.151	171.242	186.808	216.939
0.025	62.126	171.186	186.754	216.895
0.020	62.163	171.211	186.785	216.939
0.016	62.170	171.217	186.790	216.941

E_{20} (meV)	E_{10} (meV)	E_{21} (meV)	λ_{20} (μm)	λ_{10} (μm)	λ_{21} (μm)
124.526	108.942	15.583	9.9578	11.3822	79.5719
124.789	109.214	15.575	9.9368	11.3538	79.6173
124.657	109.091	15.566	9.9473	11.3666	79.6623
124.627	109.059	15.568	9.9497	11.3700	79.6495
124.622	109.048	15.574	9.9501	11.3711	79.6183
124.620	109.047	15.573	9.9503	11.3712	79.6275

Table 2.1. Computational results as the step size of the Schrödinger model is varied. The first four subband energy levels, are shown. Also listed are the energy differences between E_{20}, E_{10}, and E_{21} and the corresponding wavelengths. These results show that the values have converged to a reasonably consistent final value. This calculation is based on a step QW sample (A1580).

2.3 Modulation doping in a stepped quantum well

Population inversion between a higher energy subband and a lower subband is one of the main criteria for a laser action. In order to achieve high electron population in a higher subband, electrons need to be excited from the ground subband to the higher subband. A high electron population is also needed in order to achieve a high gain from the stimulated emission to overcome the losses in a laser system. For a three level system, electrons excited to the second excited subband can partly relax to the first excited subband and partly to the ground subband. The electron relaxation from higher subbands involves both radiative and non-radiative transitions. Therefore, a two-dimension electron gas (2DEG) must first be confined in the ground subband to perform the pump-relaxation process. This is different from traditional interband lasers where electrons are excited from the valence band, across the band gap to the conduction band.

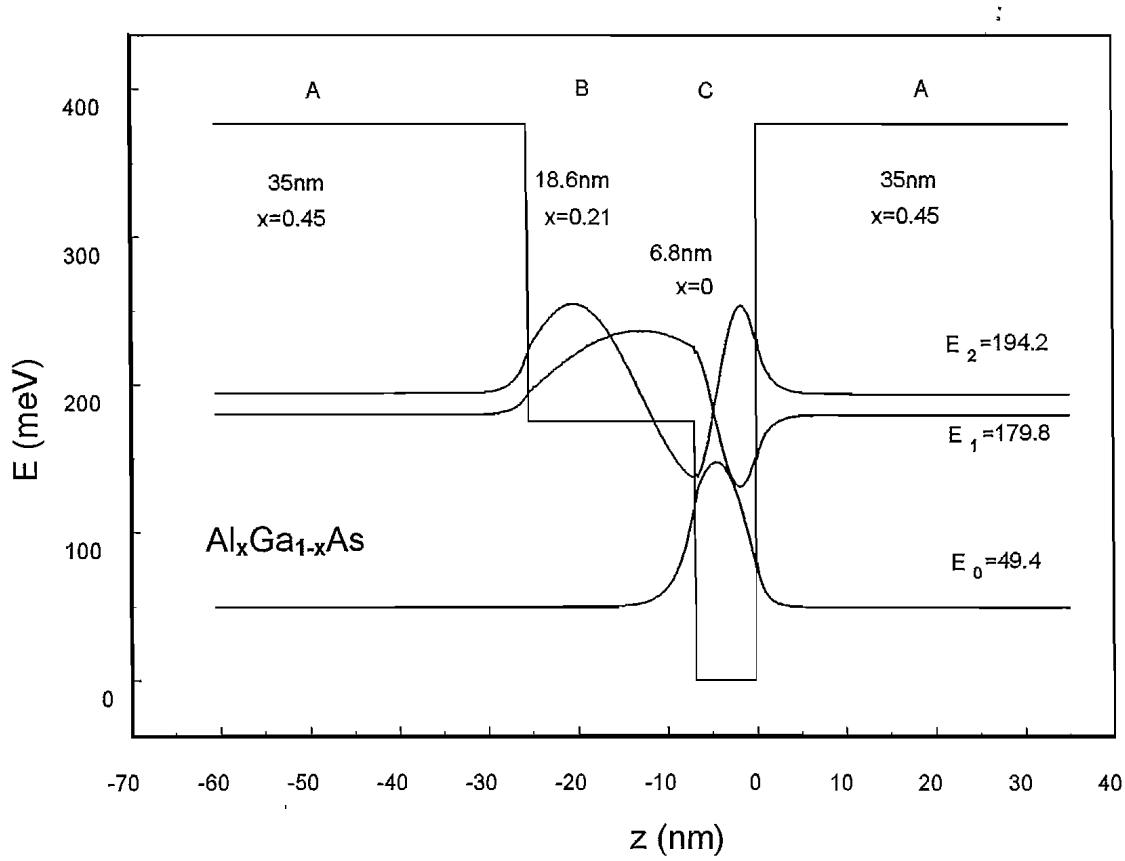

Figure 2.6. A QW band structure for no doping or doping in the lower well. There is minimal/no distortion to the QW profile. The thickness for the barrier, stepped well, and the lower well are 35 nm, 18.6 nm, and 6.8 nm respectively. The corresponding Al contents in the layers are x = 0.45, 0.21, and 0 respectively. The three lowest subband energies in meV, and the corresponding wavefunctions are also shown.

In order to form a 2DEG in a stepped QW intersubband laser structure, certain layers of the QW structure have to be doped, which is generally realised by modulation doping. Silicon is the chosen dopant for our GaAs based MQW structure. In a stepped QW, there are generally three available positions for doping as shown in Figure 2.6, namely at the barrier, stepped well, and the lower well (denoted as position A, B, and C respectively). The energy levels in Figure 2.6 are drawn assuming low doping levels and thus negligible distortion of the band structure by the dopant.

2.3.1 Doping at the barrier

Conventionally, dopants are located at the middle of barriers at position A, as shown in Figure 2.7, so called modulation doping [26, 79, 88, 89]. At room temperature and low doping levels (~ 10^{17} cm^{-3}), this ensures complete ionisation of dopants at the AlGaAs barrier. The electrons see lower energy levels at the GaAs well and thus transfer to the lower well by electron diffusion [51]. Formation of a 2DEG in the lower well is

therefore ensured. However this design also has the strongest impact on the potential bottom of the conduction band, as the space charge from the ionised dopants creates an electric field between the 2DEG and the dopants. This additional electric field is proportional to the sheet density of the space charge as described by the case of a parallel-plane capacitor. In other words, the space charge potential created is proportional to the effective distance between the doping region and the 2DEG. Consequently, the added potential subsequently distorts the profile of the conduction band bottom and subsequently changes the subband levels. If the doping concentration is increased, potential valleys can be created in the step well and the barrier, whilst a 2DEG can be confined there. These parasitic wells at the barrier or stepped well region can alter the wave functions of the confined energies and thus affecting the performance of the QW design. If excited electrons are trapped in these parasitic wells, the number of electrons available for population inversion can be reduced, which in turn reduce the gain of the laser.

In practice the distortion of the band profile leads to a strong coupling between the energy levels and the degree of doping. This is highly undesirable from a process control point of view, since the subband energy levels can be highly dependent of the actual doping concentration. Figure 2.7 shows the band structure after doping in the middle of 35 nm wide barriers with a moderate concentration of 1×10^{18} cm^{-3} (other structure parameters are as shown in Figure 2.6) in the SQW. The doping width is 6.8 nm, which yields a resulting sheet density that is close to those used in optically pumped intersubband lasers [45, 76, 90]. The optical gain in optically pumped intersubband lasers is proportional to the carrier sheet density where a high value is clearly desirable. As can be seen in Figure 2.7, the energy levels are already severely perturbed at this doping level, and (depending on the operating temperature) the potential valleys at A and B may also trap electrons. This is highly undesirable as the electrons available for the laser system will be reduced and free carrier loss may be increased due to the trapped electrons. In addition, coupling between adjacent QWs may occur and the individual QWs are not independent of each other due to the severely distorted barrier energies at high doping concentration.

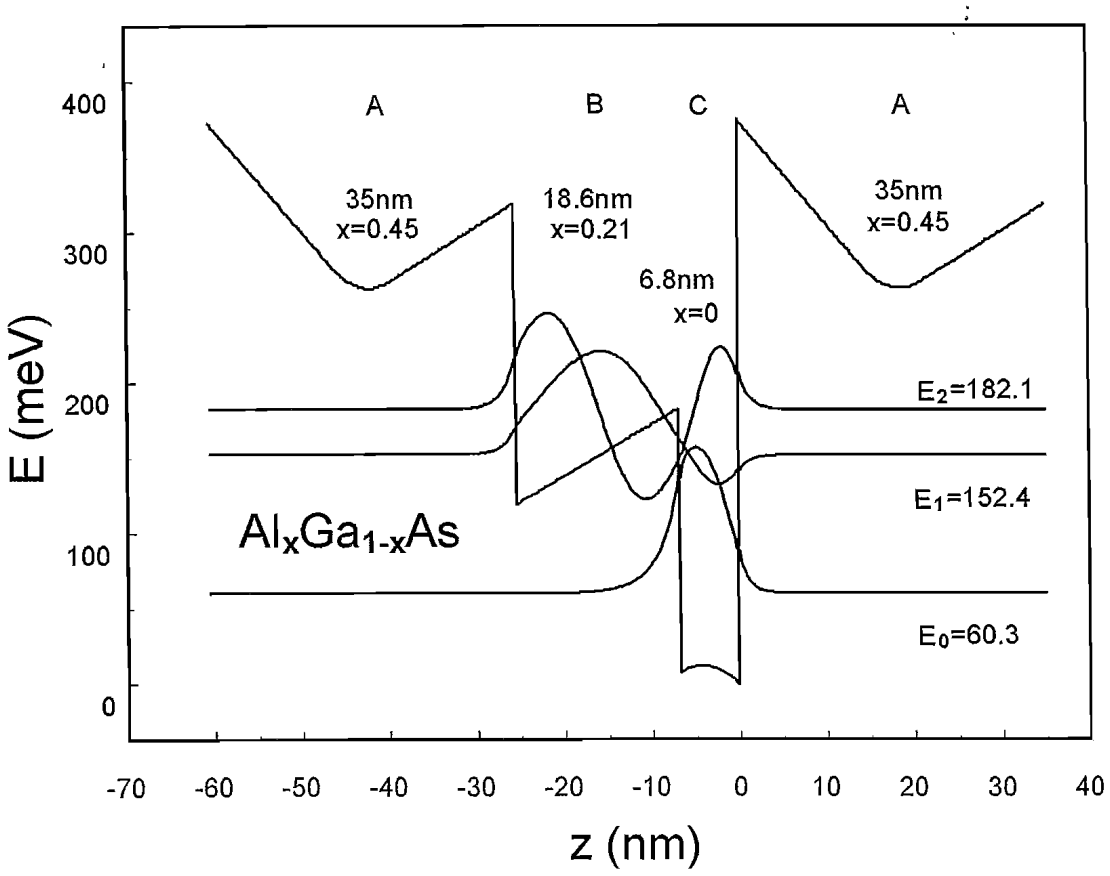

Figure 2.7. A self-consistent calculation of band structure for GaAs/AlGaAs multiple QWs with doping in the middle of barriers at a moderate concentration of 1.0×10^{18} cm^{-3}, which is equivalent to a sheet density of 6.8×10^{11} cm^{-2}. Other parameters are the same as Figure 2.6. Also shown are the three lowest subband energies and the corresponding wavefunctions.

2.3.2 Doping at the lower well

It is also possible to dope the lower well at position C [91]. In this case the ionised electrons have the least effect on the conduction band, as the ionised carriers are localized at their doping position. Figure 2.6 gives the band structure for this case. Nevertheless, the rate of ionisation will be crucially dependent on temperature since the energy level of the dopants is below the ground subband energy. Si has a donor energy of 2 meV below the conduction band of GaAs [92]. Hence, high temperature operation is needed to achieve high level of donor ionisation. This doping scheme is not attractive if a wide temperature range operation is desired. Additional complication on the operation is also introduced with the temperature dependence, which is highly undesirable for a practical laser. Figure 2.8 self-consistently calculates the temperature

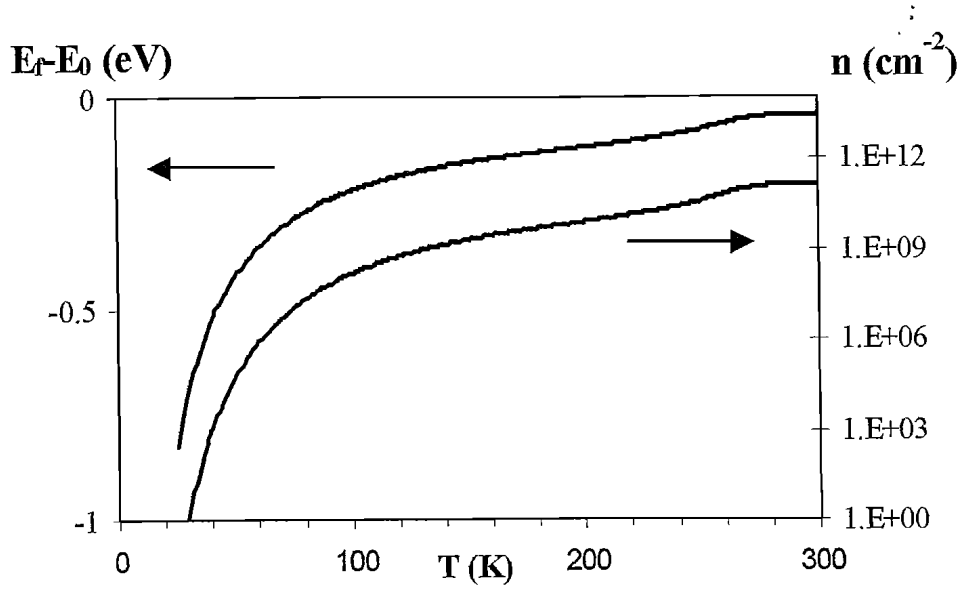

Figure 2.8. For doping at C (the lower well), the electron sheet density (right) realised in the ground subband and the Fermi level relative to the ground subband (left) as a function of temperature. The electron sheet density depends greatly on the temperature, and operation near room temperature is necessary for maximum ionisation of the dopants. Doping length is 6.8 nm (the well width) at a concentration of 10^{18} cm^{-3}.

dependence of electron sheet density and the Fermi level with reference to the ground subband. The data used in the calculation is as listed in Figure 2.6, where the lower well (6.8 nm) is doped at a doping concentration of 10^{18} cm^{-3}.

2.3.3 Doping at the stepped well edge

Alternatively, dopants can be placed at position B, which is at the edge of the stepped well close to the lower well. At this position, the dopant energy level is well above the Fermi energy level even for heavy doping, complete ionisation of the dopants is thus guaranteed. Furthermore, as the donor is located close to the lower well, this design has a much smaller space charge potential imposed on the conduction band bottom of the QW structure. Hence this doping scheme has smaller conduction band distortion and so

	Doping at B		**Doping at A**	
	ΔE_{21} **(meV)**	ΔE_{20} **(meV)**	ΔE_{21} **(meV)**	ΔE_{20} **(meV)**
N_d **+ 10%**	+0.3	-1.5	+1.0	-1.9
N_d **- 10%**	-0.3	+1.5	-1.1	+1.8

Table 2.2. Intersubband energy tolerance to a doping concentration fluctuation of ±10% at doping positions A and B. E_{20} and E_{21} correspond to the pump and laser transitions respectively.

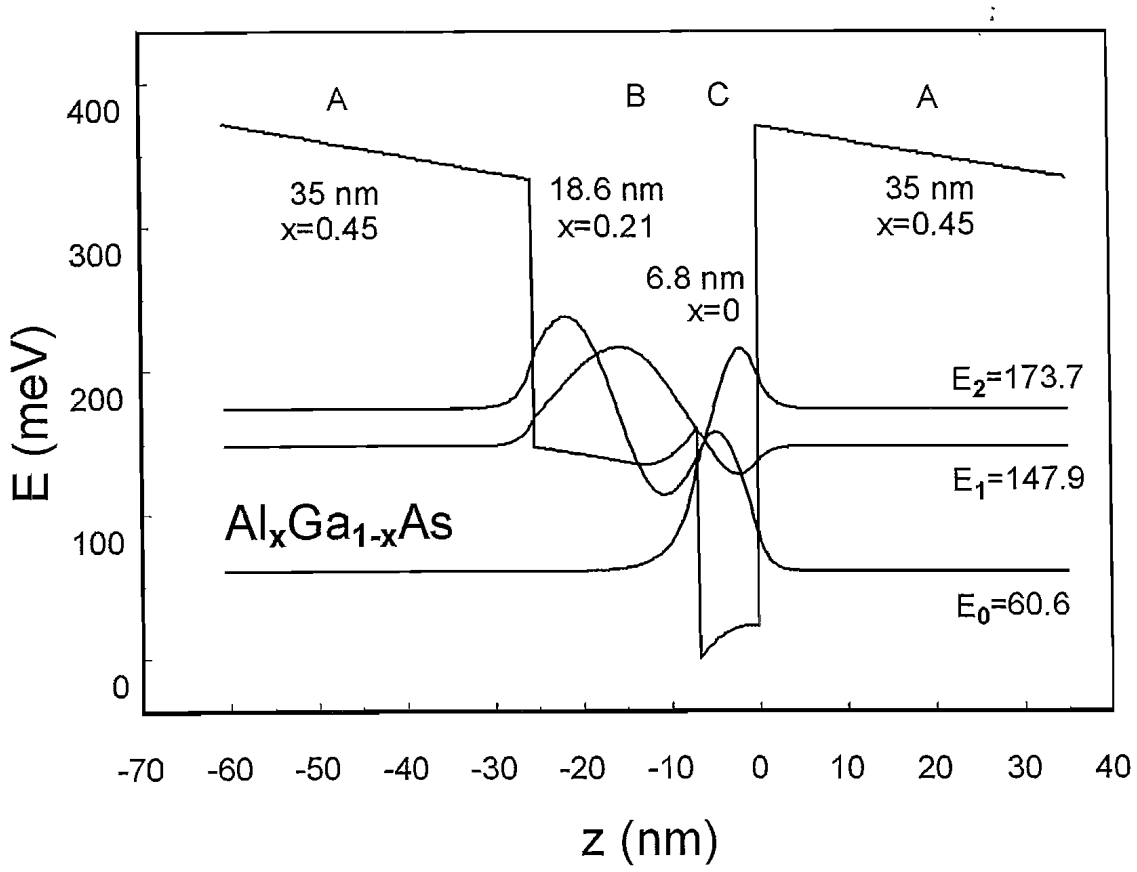

Figure 2.9. Band structure of a QW with a doping concentration of 1.0×10^{18} cm^{-3} at the edge of the step well, close to the lower well for a width of 6.8 nm. Calculated energy levels (meV) and the corresponding wave functions are shown.

it is technically more controllable when the structure is grown. Figure 2.9 simulates this case. All the parameters used in Figure 2.9 are the same as those in Figure 2.7 aside from the dopant position. No "parasitic" well is produced in the barriers, and that induced in the step is both shallow and has a very thin barrier.

Table 2.2 compares the changes of subband energy gaps ΔE_{21} and ΔE_{20} caused by dopant concentration fluctuation of ±10% in the two cases described in Figure 2.7 and Figure 2.9. It is evident that for a small variation of doping concentration, the energy gap changes are much greater for doping at A than for doping at B. In other words, the tolerance to doping fluctuation for doping at B is much higher than that for doping at A.

Overall, the sensitivity of the terahertz laser transition energy E_{21} to dopant level fluctuations is substantially reduced by a factor of 3.3, whilst the pump transition sensitivity is marginally reduced by a factor of 1.3. The unconventional placement of dopant at the stepped well edge thus brings two significant advantages: elimination of parasitic wells, and reduced sensitivity to errors in dopant concentration level. This

improved controllability is especially significant for the laser transition, whilst full dopant ionisation at low temperatures is retained.

2.4 Transmission spectra measurement

The intersubband absorption of a MQW structure can be determined by taking the transmission spectrum of the structure. A Perkin-Elmer Spectrum 2000 Fourier Transform Infrared Spectrometer (FTIR) [93] is utilised to measure the transmission spectra. The basic principle of the spectrometer is that when an infrared beam is passed through a sample, the beam is absorbed at different wavelengths, as illustrated in Figure 2.10. The radiation beam is split into two beams by the beamsplitter, which are reflected by the two mirrors before being recombined into a same beam. This beam is then directed at the sample, and the transmitted radiation is detected. When the movable mirror is scanned across some distance, an interference pattern is detected due to the different optical paths of the beams. This interference pattern encodes the spectrum of the source and can be Fourier transformed to retrieve the transmission spectrum. The FTIR instrument is capable of measuring transmission spectra from the

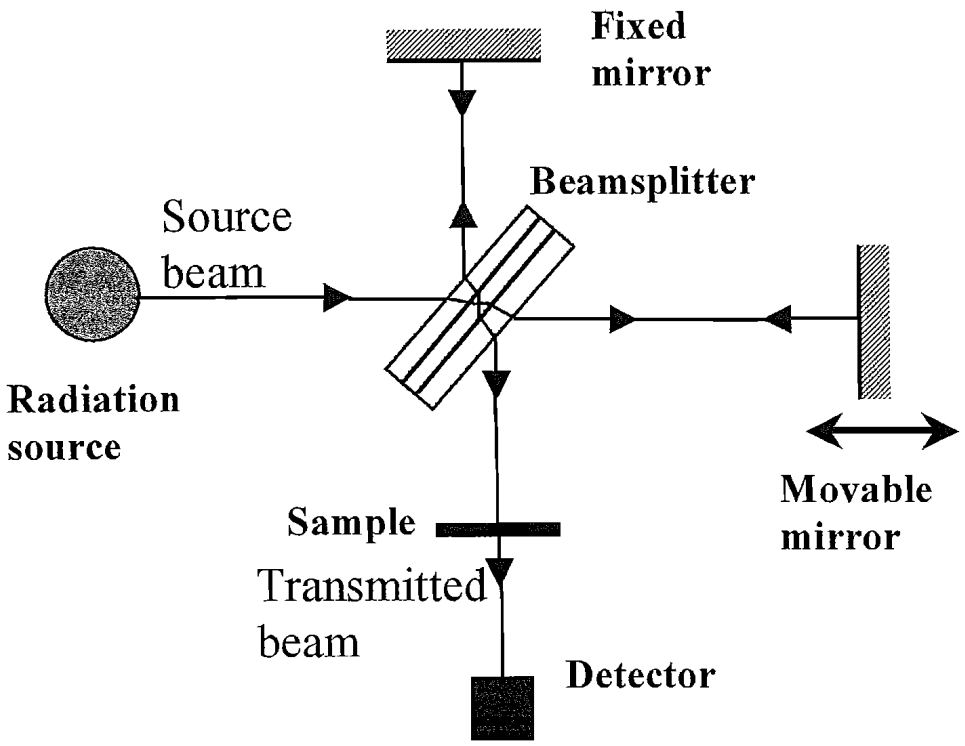

Figure 2.10. FTIR measurement is based on the absorption of infrared beam at different wavelength of a sample. The radiation from the source is split and delayed before being recombined and directed at the sample. The transmitted signal is then recorded by a detector and Fourier transformed to obtain the transmission spectrum.

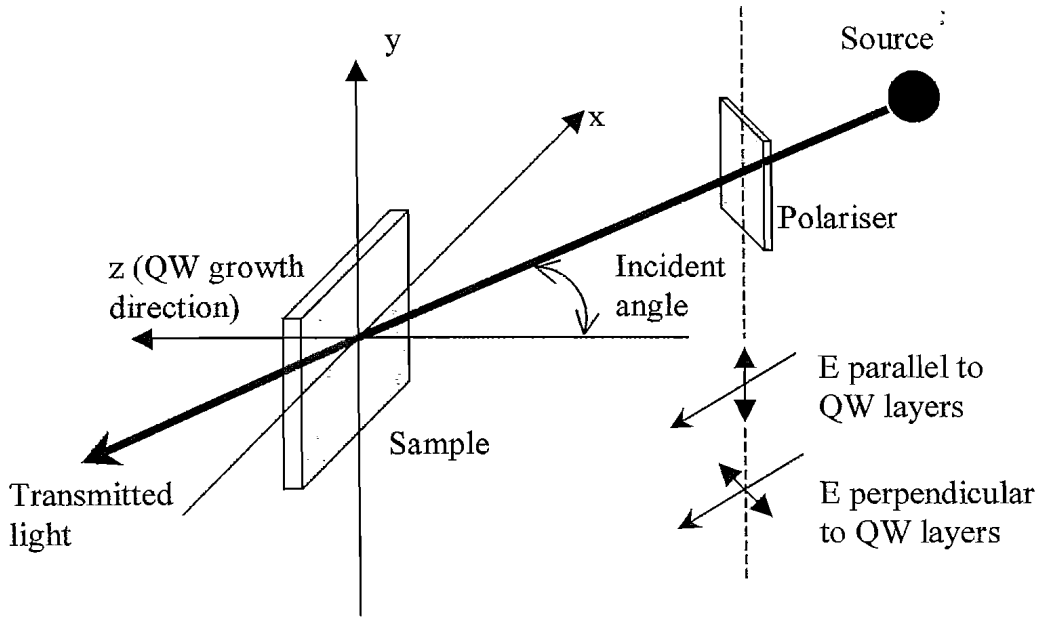

Figure 2.11. Experimental arrangement for measurement of the transmission spectrum of a MQW sample. The radiation from the source is incident at an angle to the MQW sample after passing through a polariser. The polarisation angle is varied such that the radiation light is polarised from parallel to the QW layers to normal to the QW layers.

near infrared to far infrared. This is achieved by using suitable combinations of optical windows, beam splitters, radiation sources as well as the detectors. Very high quality and reproducible spectra are obtainable using this spectrometer [94].

For our MQW structures, the spectra should show two absorption bands correspond to the E_{01} and E_{02} intersubband transitions. The sample is mounted with the beam directed at an incident angle at the Brewster angle for GaAs (~73 °). At Brewster angle, the radiation beam polarised in the plane normal to the QW layers suffers no reflection losses at the surface [49, 95]. The experimental arrangement for measuring the transmission spectra is illustrated in Figure 2.11. Only the light perpendicular to the QW layers is absorbed by intersubband transitions. Hence by use of a polariser between the source and the sample, the transmission change due to the intersubband energy absorption can be distinguished by polarising the incident beam at different angles. As shown in Figure 2.12, the absorption band is observed at a light polarisation angle normal to the QW plane. This absorption band becomes weaker as the light polarisation is changed, and eventually disappears when the polarisation is parallel with the QW plane. For features that are not related to the intersubband transitions, changing the polarisation angle has not altered the transmission patterns. In the inset of Figure 2.12, the same spectra have been shifted vertically for clarity.

The overall transmission is reduced as the angle of polarisation is changed from perpendicular to parallel with the QW plane. This is due to the increase in reflected light as compared to the transmitted light, as the polarisation of the source light is changed. Moreover, apart from the absorption band due to the intersubband transitions, some parasitic features may also be observed. These features have magnitude that is comparable to the intersubband absorption bands, which are only of the order of a few percent of the total transmission. One of the origins for these features is due to the reflection from the MQW substrate, especially when the light polarisation is not perpendicular to the QW layers, which appears as fringes in the spectrum. Therefore, the transmission spectra of the MQW samples may not show the absorption bands clearly. In order to distinguish the intersubband absorption features from the fringes, other analysis techniques may be needed. For example, the angle of incidence to the sample can be varied, such that the fringes are moved to different wavelengths while the intersubband absorption wavelengths are unaffected. Modulation techniques can also be used by applying voltage to the sample, which changes the surface electron density and resulting in a better background noise level [96]. Furthermore, the measured spectra of doped MQW samples can be compared or ratioed against undoped samples or un-growth, GaAs substrate to exclude any intrinsic features.

Transmission spectra measurements for the MQW samples are taken at room temperature and at low temperature (6 K) using a cryostat. Figure 2.13 shows the transmittance spectra at 6 K (a) and at room temperature (b) for sample RMB1564, This sample has 50 periods of QWs, which is modulation doped at the middle of the barrier for 5 nm with a doping concentration of 2×10^{18} cm^{-3}. The transmission when light is polarised parallel to the MQW plane is subtracted from the transmission with perpendicularly polarised light. This will minimise the instrumental, substrate, and free carrier absorption contributions [71]. Nevertheless, some parasitic features can still be observed, especially at the longer wavelength part of the absorption band. The absorption bands are fitted with a combination of Lorentzian curves, taking into account the two absorption transitions, E_{01} and E_{02} [32, 66].

$$Absorption = \frac{K}{1+\left[2\pi c T_2\left(\frac{1}{\lambda}-\frac{1}{\lambda_0}\right)\right]^2} \tag{2.23}$$

Equation 2.23 describes the Lorentzian lineshape used for fitting the homogeneously broadened linewidth of the intersubband absorption [71], where c is speed of light, $T_2 = 2/\Delta\omega$ is the dephasing time of spontaneous emission, $\Delta\omega$ is the full width at half maximum (FWHM) of the spontaneous emission (linewidth broadening), λ_0 is the resonant wavelength of the intersubband transition, and K is a fitting constant. The dephasing time T_2 is in general shorter than the intersubband lifetime due to the scattering of electrons while remaining in the same subband [32, 71]. The same value of T_2 is used for the transitions E_{01} and E_{02} but different values are used for the room temperature and 6 K measurements, which are 80 fs and 82 fs respectively. These values correspond to FWHM linewidth broadening energy $\hbar\Delta\omega$ of 16.5 meV at room temperature, which is broader than the 16.1 meV linewidth at 6 K. These values are close to the values reported for a stepped QW (17-18 meV) in Ref. [89]. Moreover, the linewidth broadening due to temperature increase has been observed before [26, 71, 97]. This increased broadening has been attributed to the increased scattering and the redistribution of electron population at high temperature. There are also slight shifts in the absorption band at different temperatures, particularly the E_{01} absorption. For the measurement at room temperature, wavelengths of $\lambda_{02} = 9.18 \pm 0.05$ μm and $\lambda_{01} = 9.95 \pm 0.05$ μm are deduced for a reasonably good fit. Similarly, the spectrum at 6 K is fitted with values of $\lambda_{02} = 9.19 \pm 0.05$ μm and $\lambda_{01} = 9.85 \pm 0.05$ μm. These spectra reveal two absorption bands that are significantly overlapped, which is understandable due to the small energy separation of E_{21}. The pump efficiency can be reduced due to this overlap, as some of the excited electrons are likely to populate E_1 instead of E_2, the upper laser level. Hence, it is desirable that the pump transition is detuned slightly to the higher energy wing (shorter wavelength) of the absorption band to reduce the possibility of the population of E_1. Determining the absorption bands in a MQW intersubband laser structure is thus important as the pump laser wavelength can be tuned to resonant with the observed absorption bands.

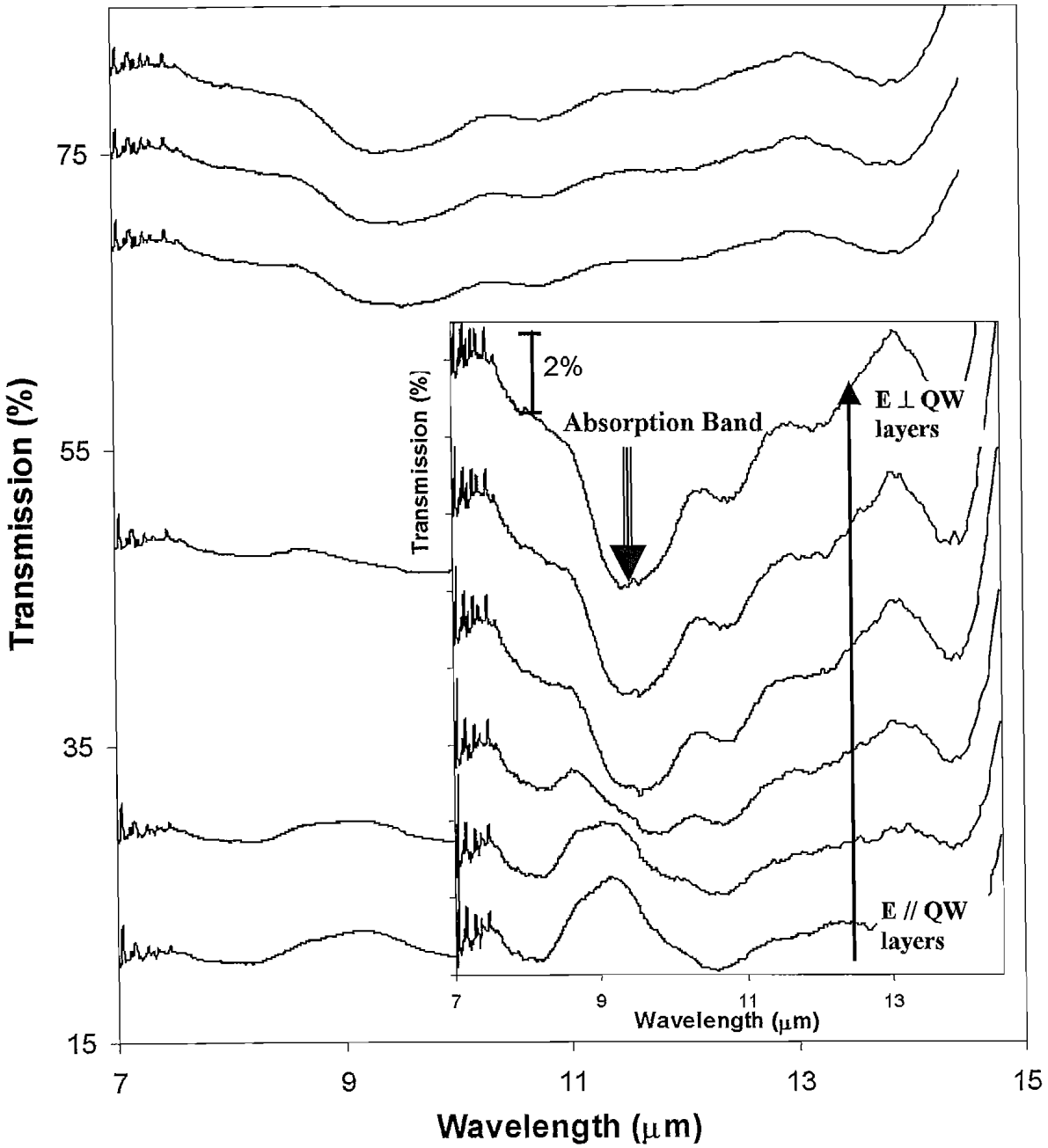

Figure 2.12. Transmission spectra for a MQW sample (RMB1564) at different polarization angle for the source beam. The upper most spectrum is where the beam is polarized at an angle normal to the QW plane, whereas at the lowest spectra, the angle of polarization becomes parallel to the QW plane. The inset shows the same spectra that have been vertically shifted for clarity. The intersubband absorption band can be observed, as pointed by the arrow.

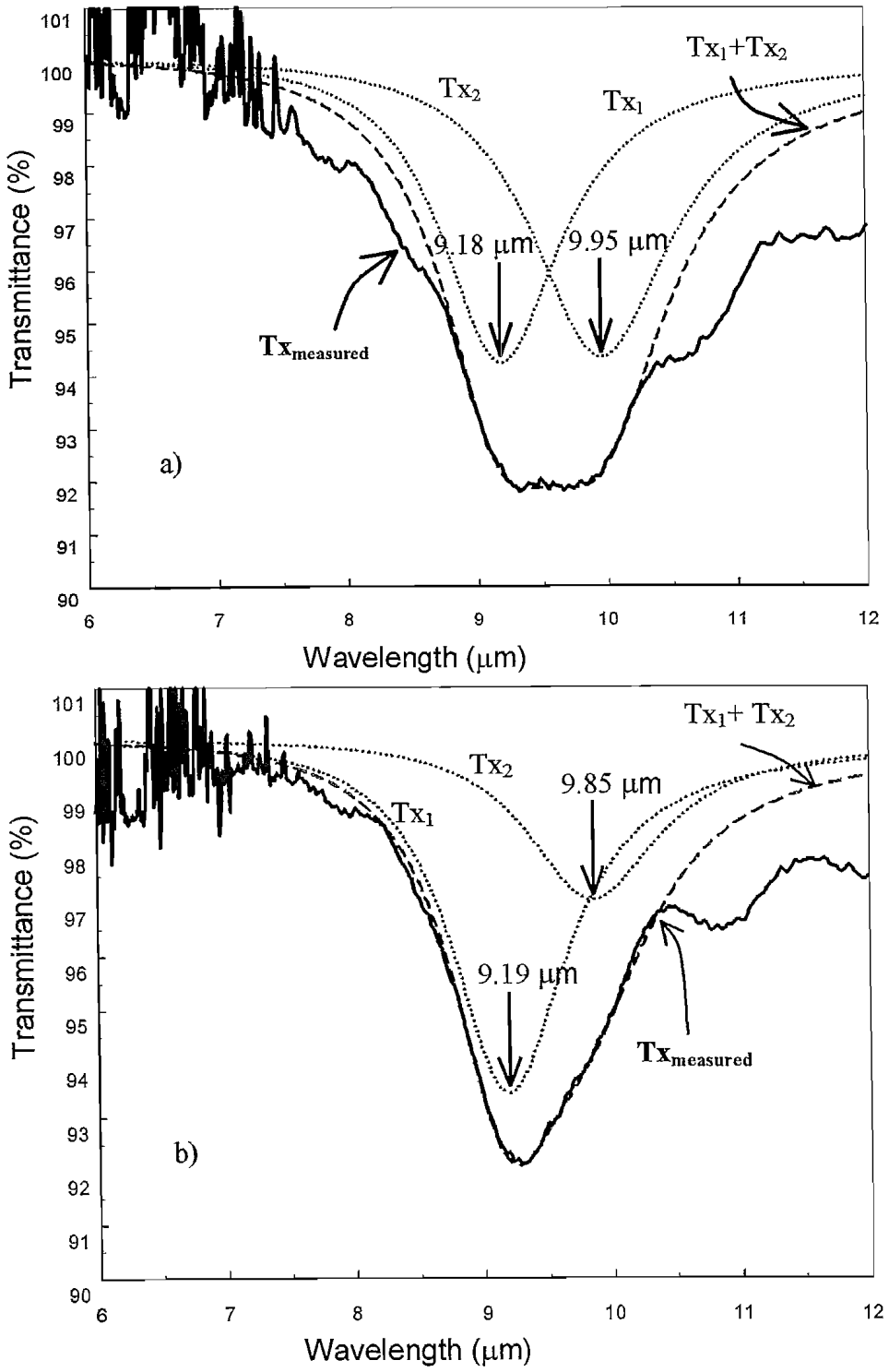

Figure 2.13. The spectral transmittance of the sample (RMB1564) at room temperature (a) and 6 K (b) with the source TM polarised and the beam incidents at the Brewster angle (solid lines). A combination of two absorption lines are used (Tx_1 + Tx_2, dashed lines) to fit the spectra. The uncertainties in the absorption wavelengths are ± 0.05 μm for a reasonably good fit. Absorptions due to the subband transitions (Tx_1 and Tx_2) are indicated by the dotted line. The FWHM linewidths for the fitted plots correspond to 16.5 meV and 16.1 meV for (a) and (b) respectively.

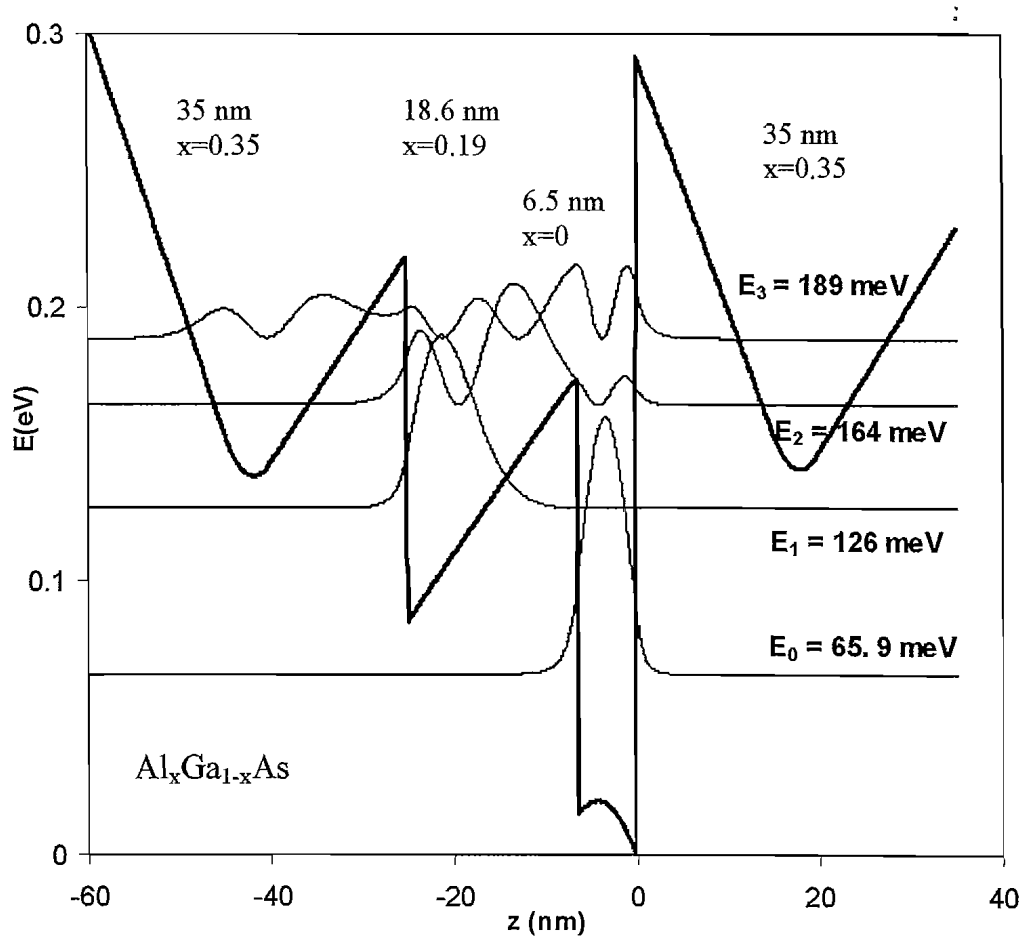

Figure 2.14. Energy profile of the MQW sample RMB1564. This sample is modulation doped at the middle of the barrier for 5 nm at a concentration of 2×10^{18} cm^{-3}. The separation of the donor at the barrier and the ionised electrons at the stepped and lower wells causes the deformation of the conduction band profile. Also shown in the figure are the confined energy subband levels and the square of their corresponding wave functions. The deformed conduction band has resulted in deep parasitic wells at the stepped well and the barrier, which may confine electrons and reduce the electrons available for the excitation-relaxation process of the laser system.

2.5 Discussion

At the early stage of this work, the distortion to the QW energy profile was not taken into consideration when designing the MQW samples. Rather a constant potential was assumed for each of the layer. Conventional modulation doping at the middle of the barrier was adopted. Sample RMB1564 was one of these early designed samples. As depicted in Figure 2.14, the QW band profile for this sample was self-consistently solved. The calculated energy separations were E_{30} = 122.7 meV, E_{20} = 98.2 meV, and E_{10} =60.5 meV, which corresponded to λ_{30} = 10.1 μm, λ_{20} = 12.6 μm, and λ_{10} = 20.5

μm. Since electrons are aimed to be excited from E_0 to E_2 by a CO_2 laser, it was clear that wavelength λ_{20} was beyond the operation range of this pump laser. Hence, the grown sample had significantly different energy levels from those required for a FIR laser.

Comparison between the measured transmission spectra and the modelled result revealed that shorter wavelength transitions, or larger energy separations were observed. Note that E_1 in Figure 2.14 appeared to be a confined energy level due to the parasitic stepped well and the corresponding wave function had very little overlap with the wave function for the ground subband. Hence, it was expected that the absorption E_{01} was weak, compared to other stronger transitions such as E_{02}. This energy subband was localised at the stepped well and electrons could be trapped. There was no observable absorption band that related to the E_{01} transition. In addition, the deformed barriers had formed parasitic wells, which could confine energy subbands (not shown in the figure) at energy close to E_2 and E_3 in Figure 2.14. For the subsequent discussions in the following chapters, the first two excited subbands shall be regarded as E_2 and E_3 for sample RMB1564. In this case, the absorption bands in the transmission spectra for sample RMB1564 in Figure 2.13 corresponded to the E_{02} and E_{03} transitions. In Chapter 3, the observation of electrons trapping in the parasitic wells in the barrier of this sample will be discussed.

In view of the distortion of the doped-barrier MQW samples, the doped-stepped well design was implemented, where the energy profile and transmission spectrum for sample A1580 are shown in Figure 2.15 and Figure 2.16, respectively. The self-consistently calculated subband energy levels for sample A1580 showed that $E_{20} = 125$ meV, $E_{10} = 109$ meV, and $E_{21} = 15.6$ meV, which corresponds to $\lambda_{20} = 9.95$ μm, $\lambda_{10} = 12.4$ μm, and $\lambda_{21} = 79.6$ μm. If compared with the FTIR transmission spectrum in Figure 2.16, the fitted values for the intersubband absorption were 137 ± 1 meV and 125 ± 1 meV for E_{20} and E_{10}, which were higher than the modelled values by about 12 meV and 16 meV, respectively. Moreover, the resulting laser transition energy E_{21} from the transmission spectra revealed a lower value of 12 ± 2 meV, resulting in an increase of laser wavelength ~20 μm. The reasons for these shifts in intersubband transition energies have yet to be determined. One possible explanation to the subband energy shifts is the error in the quantum well layers during the MQW growth process. The typical errors that may occur in the grown sample include a slight variation from the

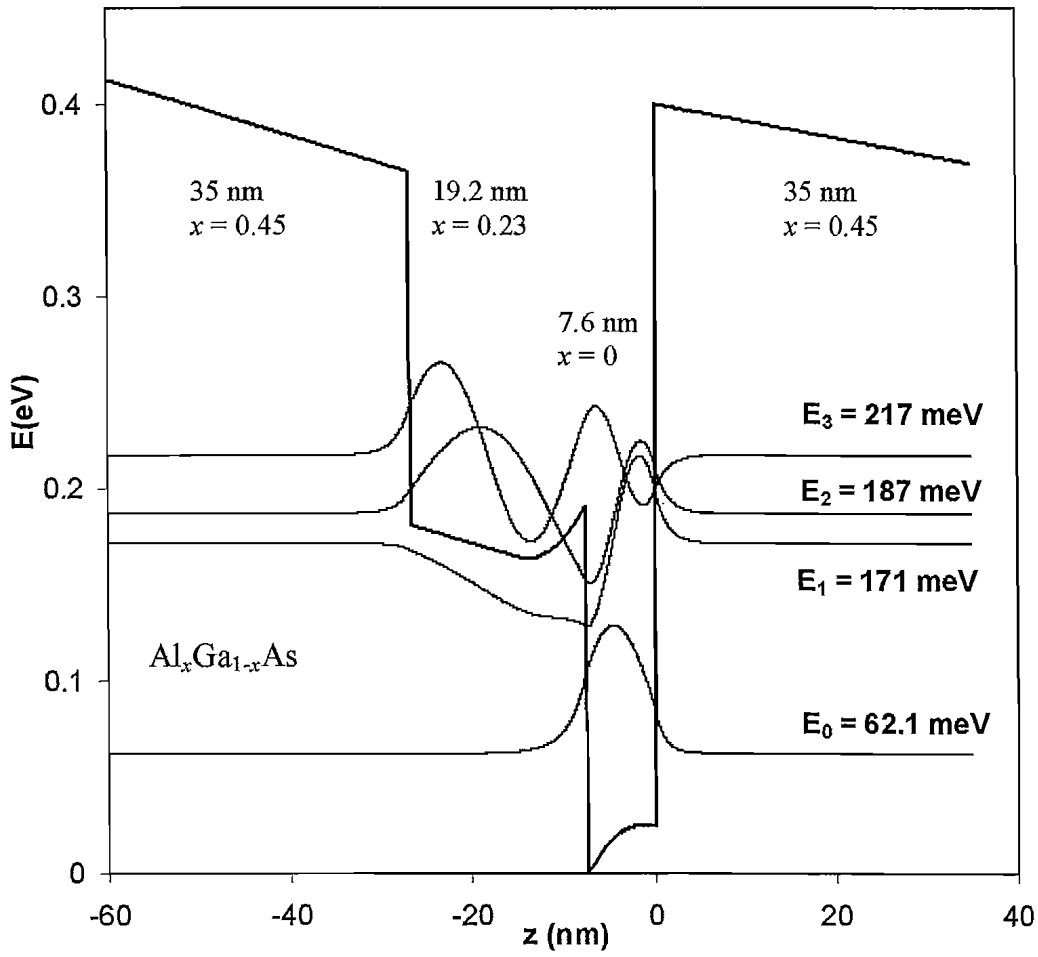

Figure 2.15. QW energy profile for sample A1580 calculated using a self-consistent model. The four lowest confined subband energy subband energy levels and the corresponding wavefunctions are presented. This sample is doped at the stepped well edge for 7.1 nm at a concentration of 10^{18} cm^{-3}.

designed values in the layers thickness, Al content, and the dopants concentration or distribution. There errors have been found to cause subband energy shifts [32].

As shown in Table 2.3, although these errors are small, they can cause significant changes to the energy subband levels and consequently the transition wavelengths. The simulation results assumed that the errors occurred systematically for each of the individual QWs, which may not be the case in practice. In fact, the observed wavelength shifts in the transmission spectrum are larger than the simulated errors listed in Table 2.3. In particular, note that the effects on the laser energy are almost always of positive energy shifts. On the other hand, the changes in E_{10} and E_{20} have similar energy shifts pattern to the different errors, albeit at different magnitude. The

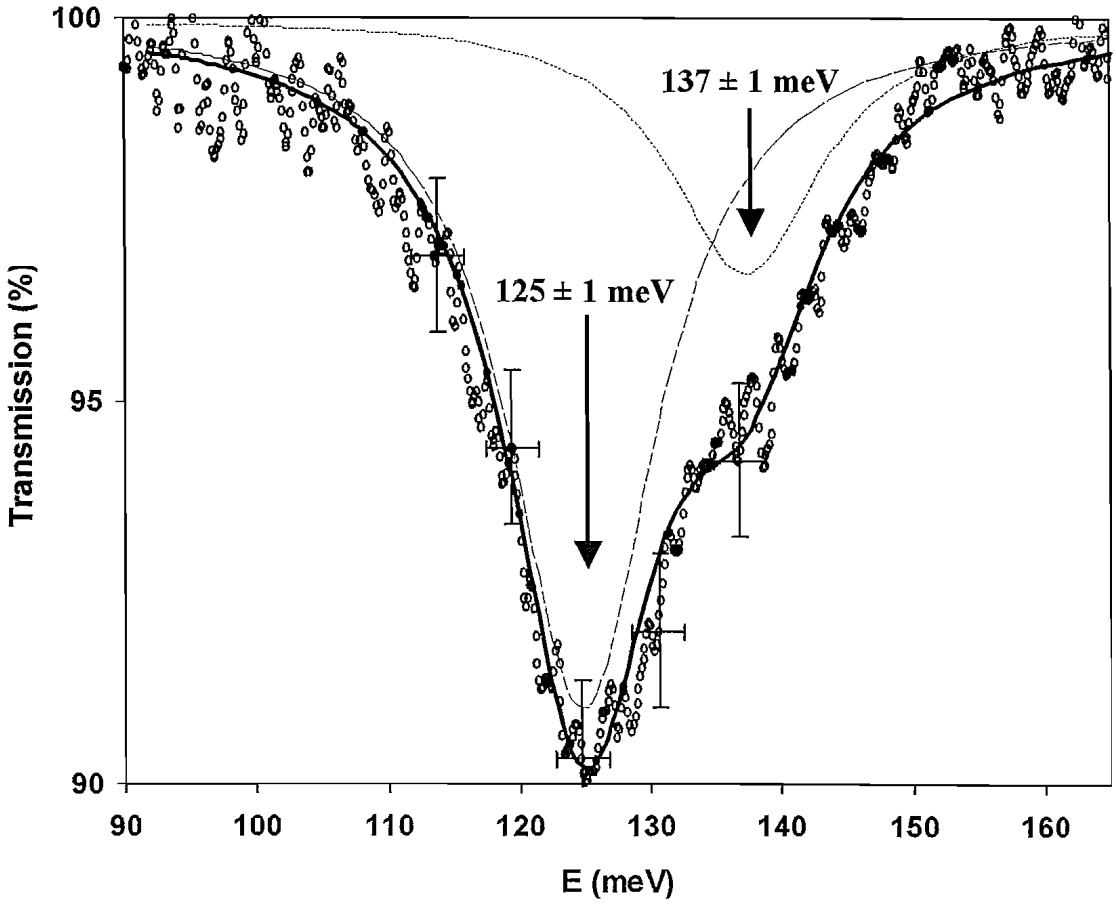

Figure 2.16. FTIR transmission spectrum for the doped stepped well structure (A1580) as a function of photon energy. The circles are the measured transmission data while the solid line is the Lorentzian fitted absorption band. This fit reveals two absorption bands at 137 ± 1 meV(dashed line) and 125 ± 1 meV(long dashed line), with the latter has a stronger absorption.

table shows that the relative changes in E_{10} and E_{20} generally cause positive shifts in E_{21}, or resulting in shorter laser wavelengths. Conversely, our observations show an increase in the laser wavelength. Thus the growth errors discussed here alone may not explain the apparent energy disagreement from the modelled values. The level of growth errors, although not usual in well controlled MBE facilities, can of course be greater than those listed in Table 2.3.

Moreover, a combination of errors during the epitaxial growth of the MQW samples is possible, and may contribute to the energy shifts. Hence, further investigations are required to resolve this issue since the changes due to the discussed growth errors can not fully explain the energy shifts. For example, the MQW structures may be examined using secondary ion mass spectrometer (SIMS) and X-ray diffractometer (XRD) to obtain the material contents and structure thickness of the QWs [98, 99]. This will provide us with the structural information and help to determine the degree of the growth errors.

Table 2.4 lists the values of the oscillator strength calculated for Sample A1580. The presence of large oscillator strengths for transitions E_{21} and E_{20} points to the possibility of a strong radiative transition for E_{21}, while pumping from E_0 to E_2. As shown in Table 2.4, $F_{1\rightarrow2}$ is greater than $F_{0\rightarrow2}$ due to the larger overlap integral of the wave functions

Error in Al content in the stepped well (Δx)		**Pump energy change, ΔE_{20} (meV)**	**E_{10} change, ΔE_{10} (meV)**	**Laser energy change, ΔE_{21} (meV)**
- 0.01	- 4.35 %	- 4.8	- 5.7	+ 0.9
+ 0.01	+ 4.35 %	+ 5.4	+ 4.9	+ 0.5
Error in the doping length in the stepped well (ΔL_d)				
- 5 Å	- 7.04 %	+ 3.0	+ 2.5	+ 0.5
+ 5 Å	+ 7.04 %	- 2.9	- 3.0	+ 0.1
Error in the doping density in the stepped well (ΔN_d)				
- 10^{17} cm^{-3}	- 10 %	+ 3.1	+ 2.3	+ 0.8
+ 10^{17} cm^{-3}	+ 10 %	- 2.9	- 2.6	- 0.3
Error in the lower well width (ΔL_w)				
- 3 Å	- 3.95%	+ 1.8	+ 0.5	+ 1.2
+ 3 Å	+ 3.95 %	- 1.1	- 1.7	+ 0.6

Table 2.3. Simulated changes to the pump transition energy (E_{20}), energy difference of ground to first excited subband (E_{10}), and the FIR laser transition energy (E_{21}) due to a selection of epitaxial growth errors in a MQW sample (A1580). Assuming the errors are equal for each individual QW, the errors considered are the Al content, the doping length and doping density in the stepped well, and the lower well width. The size of the errors are with respect to the designed values for this sample, as described in Figure 2.15.

Transition	Energy (meV)	λ (μm)	$F_{i\to f}$
$E_0 \rightarrow E_1$	109	11.4	0.583
$E_0 \rightarrow E_2$	125	9.95	0.265
$E_0 \rightarrow E_3$	155	8.01	0.054
$E_1 \rightarrow E_2$	15.6	79.6	0.829
$E_1 \rightarrow E_3$	45.7	27.1	0.062

Table 2.4. Calculated oscillator strengths for Sample A1580 for the different transitions involved. The energy differences and the corresponding wavelengths are also presented.

between E_2 and E_1. This ensures that the excited electrons in the upper laser level (E_2) favour the transition to the lower laser level (E_1) instead of direct relaxation back to the ground level (E_0) [30]. Note also that a transition from a higher energy to a lower energy has a negative oscillator strength value but of the same magnitude as the opposite transition.

The transmission spectra were also taken for other MQW samples that were grown for this work, but were not included in the discussion so far. These spectra together with the designed QW parameters are included as Appendix 3. The absorption wavelengths correspond to the intersubband transitions energy are also estimated, following the same procedures as discussed before in the previous section.

2.6 Gain analysis

In the following discussion, the achievable optical gain of the FIR laser and the required pump threshold are estimated, based primarily on the analysis and discussion in Refs. [66] and [31]. In our 3-level laser system, the optical gain is directly proportional to the population inversion sheet density, Δn_{21} (in units of inverse area) achieved between the second and first excited subbands. The optical gain per unit length, $g(\lambda)$ as a function of wavelength in a QW involving radiative transition between two subbands can be written as [31, 66]:

$$g(\lambda)=\frac{\Delta n_{21}\lambda^2 T_2}{4\pi d n_r^2 \tau_{spon}}\left(1+4\pi^2 c^2 T_2^2\left(\frac{1}{\lambda}-\frac{1}{\lambda_0}\right)^2\right)^{-1} \qquad (2.24)$$

where Δn_{21} is the population difference between E_2 and E_1, d is the MQW layer thickness, n_r is the refractive index of the MQW material (the value of GaAs is

assumed here for simplicity), T_2 is the electron dephasing time (0.21 ps [71]), c is the speed of light, λ_0 is the resonant wavelength, and τ_{spon} is the spontaneous radiative time between the subbands. The spontaneous radiative time is inversely proportional to the oscillator strength of the laser transition, $F_{1\to2}$ [66]:

$$\tau_{spon} = \frac{1}{F_{1\to2}} \frac{m^* \varepsilon_0 \lambda^2 c}{2\pi n_r q^2} \qquad (2.25)$$

where m^* is the effective electron mass, ε_0 is the permittivity of free space, and q is the electron charge.

Laser action occurs when the optical gain equals to all the losses of the laser system. These losses include the absorption loss of the sample, α_{abs} and the reflective loss at the cleaved surface. Hence, we can estimate the gain threshold, g_{th} required for lasing as:

$$\Gamma_{act} g_{th} = \alpha_{abs} + \frac{1}{L} \ln\left(\frac{1}{R}\right) \qquad (2.26)$$

where Γ_{act} is the mode confinement factor (i.e. the confined mode overlap with the active MQW layers), L is the laser cavity length, and R is the reflectivity of the cleaved surface.

By utilising a transition rate model developed in Ref. [31], the population inversion per unit area can be related to the pump rate, N_p by:

$$\frac{\Delta n_{21}}{N_p} = \frac{W_{10} - W_{21}}{W_{10}(W_{21} + W_{20})} \qquad (2.27)$$

where W_{20} and W_{10} are the non-radiative transition rates due to LO phonon scattering for transitions E_{20} and E_{10}, respectively. In contrast, W_{21}, the scattering rate for the transition E_{21} is dominated by acoustic phonon scattering, since the transition energy difference is smaller than the LO phonon energy. Previous lifetime measurements give W_{21} in the order of 10^{10} s^{-1}. Since $W_{21} < W_{10}$, population inversion can be expected between E_2 and E_1.

Consequently, the threshold pump intensity, I_{th} required to achieve the population inversion can then be estimated as [31]:

$$I_{th} = \frac{N_p \hbar \omega}{\eta \Gamma} \qquad (2.28)$$

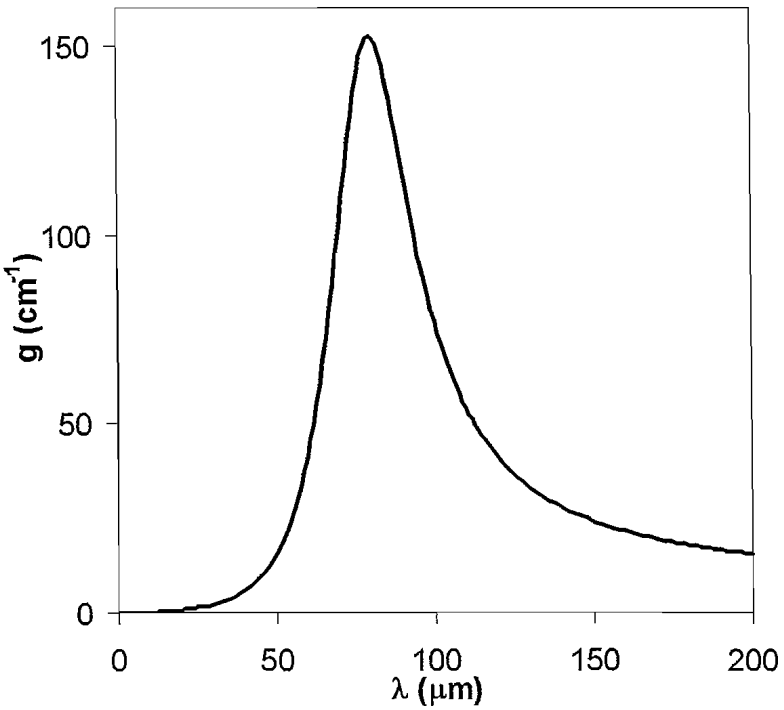

Figure 2.17. Gain spectrum of simulated intersubband emission of a MQW laser, with a peak gain of 153 cm^{-1} at a resonant wavelength of 80 μm.

where η is the overall quantum yield of the pump light (0.15 [31]), Γ is the product of the overlap ratios Γ_p and Γ_l of the pump and laser modes with the MQW layers, respectively.

A list of the parameters used in the gain analysis for the FIR laser is listed as Table 2.5. At λ_0 corresponds to the lasing wavelength for sample A1580, values for n_r and R of GaAs are assumed [100]. The thickness of the active layers is for typically 50 periods of QWs at 60 nm each. Similarly, the oscillator strength is calculated based on sample A1580, together with the transition rates, which we obtain $W_{20} = 8.9 \times 10^{11}$ s^{-1} and $W_{10} = 1.7 \times 10^{12}$ s^{-1}. On the other hand, $W_{21} = 10^{10}$ s^{-1} is assumed, which is consistent with the experimental values for acoustic phonon dominated scattering [29, 69-73].

Assuming $\Gamma_{act} = 25$ % and $\alpha_{abs} = 26$ cm^{-1} (achievable values using for example, the surface plasmon guided structures described later in Chapter 4), then applying Equation 2.26 gives $g_{th} = 153$ cm^{-1}. Then, by applying Equations 2.24 and 2.25, the required population inversion to reach the optical gain threshold is obtained, which yields $\Delta n_{21} = 1.2 \times 10^{12}$ cm^{-2}. Finally, the threshold pump intensity is calculated using Equation 2.28, where we make $\Gamma_l = \Gamma_{act}$, and the value of $\Gamma_p = 0.8$ is reasonable as the pump mode is mostly confined in the active layer for a surface plasmon guided structure. Assuming a

Parameter	Value	Parameter	Value
n_r	3.7	m^*	0.067 m_0
d	3 μm	η	0.15
T_2	0.21 ps	Γ_p	0.8
λ_0	80 μm	Γ_l	0.25
L	1 mm	$F_{1\to 2}$	0.83
R	0.33		

Table 2.5. List of parameters used in the gain analysis for the optically pump FIR lasers

pump wavelength of 10.6 μm, the threshold pump intensity is found to be ~700 kW/cm^2.

This pump intensity is easily achievable using the high power mid infrared pump sources, such as the CO_2 gas lasers or even the free electron lasers. On the other hand, current optical power from mid infrared solid-state lasers in the order of watts can be achieved (e.g. 3.5 W at $\lambda \sim 9$ μm [101]). With suitable focusing of the pump light to a spot size of the order of the pump and laser wavelengths, the threshold intensity required is in the limit of the pump source. For example, a pump power of 10 W focussed into a spot size of 20 × 200 μm^2 yields a pump intensity of 250 kW/cm^2. With further advances in the mid-infrared quantum cascade lasers, the required pump intensity is realisable. Moreover, the threshold pump intensity can be further reduced by improving the reflection loss of the cleaved facets, or further enhancement of the laser mode waveguide.

2.7 Conclusion

The intersubband design for the optically pumped FIR lasers based on MQW structures was described. Unlike conventional interband semiconductor lasers used widely in the visible to mid-infrared wavelength, intersubband lasers rely only on transitions of electrons for the radiative emission where no recombination of electron hole pairs is involved. Due to the quantum confinement of the thin QW layers, energy subband levels are confined when materials of different energy band gaps are epitaxially grown into layered structures. By changing the material parameters of the grown structures, the resulting subband energy levels can be selectively determined. These subband levels are selected to favour radiative emission, achieve strong gain and ensure population inversion between the upper and lower laser levels. A solver is first used to find the solutions to the one-dimensional Schrödinger equation and Poisson equation

self-consistently. From the computed results, the subband energy levels and their associated wavefunctions are obtained in another fine mesh size model that includes the effects of the high electron concentration in the QWs.

Our MQW structures were based on the 3-level stepped QW design, which was previously found to offer a lower threshold than the 4-level coupled wells design. In such laser, electrons need to be first confined in the QW to enable the pump-relaxation process. We have discussed the merits of doping at the stepped well for this necessary supply of electron gas in the QW, with comparison to other doping positions. The conventional modulation doping at the middle of the barrier was found to have high electron density dependence for the energy subbands. At high doping concentration, the additional potential difference due to the separated dopants and the ionised electrons becomes significant. This potential can cause deformation to the energy profiles of the QW structure, thereby changing the subband energy levels. Moreover, the deformed conduction band, especially the parasitic well at the barrier, can trap excited electrons and thus reducing the gain of the laser. In order to minimise the effect of the deformation in the conduction band due to the high electron concentration in the QW, the structure was alternatively doped at the edge of the stepped well. This doping scheme has reduced parasitic effects on the QW energy profile. The deformation in the conduction band profile is greatly reduced compared to the modulation doping at the barrier. In particular, parasitic wells at the barrier are eliminated. The subband energy levels also have smaller dependence on the changes in the electron concentration, which improves the control on the laser performance.

In addition, the measurement to determine the transmission spectra of the QW samples using a FTIR spectrometer was introduced. These spectra were valuable in determining the absorption bands of the fabricated QW structure, in comparison with the design parameters. By knowing the absorption band, the pump laser can be tuned to be in resonant with the corresponding intersubband transition. A general discussion on samples RMB1564 and A1580 were presented. The doped-barrier sample clearly showed severe distortion to the QW band profile due to the presence of ionised electrons at a high concentration in the QW structure. On the other hand, the doped-stepped well sample has shown promising improvements compared to the previous sample. Nevertheless, observed absorption bands for A1580 showed that the ground to the first and second excited subbands transition energies are shorter than the predicted

values. This shift in transition energies could be due to the uncertainties in the growth process of the sample, which would alter the QW parameters. Further investigations are needed to resolve the issue of disagreement in the intersubband transitions.

Finally, the gain threshold for the optically pump MQW laser was estimated. Assuming the design values from sample A1580, and waveguide loss based on the surface plasmon guided structures, the estimated value was achievable using the CO_2 laser. The level of pump threshold may also be possible using mid-infrared QC lasers to achieve an all solid-state system.

3 Intersubband electron lifetime measurement

In an optically pumped, 3-level intersubband far infrared laser, the laser relies on population inversion between the second excited subband and the first excited subband. Population inversion in intersubband lasers depends crucially on the non-radiative electron lifetimes of the excited subbands [28, 29]. The knowledge of these lifetimes is very valuable in understanding the performance of our MQW structures. It is now generally agreed that the intersubband relaxation lifetime is dominated by the LO phonon scattering if the subband energy difference is larger than the LO phonon energy in the host material. Lifetimes on the scale of sub-ps to a few ps have been reported [69-71]. On the other hand, for subband energy difference that is smaller than the LO phonon energy, the non-radiative scattering is dominated by acoustic phonons. Various measurements revealed that the lifetime then is of the order of 10 ps to 1 ns [29, 72, 73]. At the expected threshold pump power for our MQW FIR laser, in the region of 100 kW/cm^2 [31], the electrons in the excited subbands can be well away from equilibrium lattice temperature and become hot electrons. The hot electrons that may result from high pump intensity can significantly increase the non-radiative emission, through LO phonon emission. This will consequently reduce the electron lifetime in the second excited subband.

The intersubband electron lifetimes of our MQW samples have been measured using a three-beam pump and probe technique at the Free Electron Laser for Infrared Experiments (FELIX) in Nieuwegein, the Netherlands [17]. The experimental measurement has been carried out in collaboration with the FELIX researchers, which provided the main experimental setup. The author was responsible for the measurement and collection of data, as well as the analysis of the results. This time–resolved technique of obtaining intersubband relaxation lifetimes by using a free electron laser (FEL) is now well established [72, 102, 103]. Briefly, an excitation beam (pump), tuned to the energy transition required, excites electrons from the ground energy level to a higher energy level and causes a change in the transmission of the sample. This transmission change is monitored with a time-delayed beam (probe) using a suitable detector. The decay time of the excited electrons can then be determined by this change in the transmission as a function of the time difference between the pump and probe beams.

This chapter is divided into six main sections. The first section briefly describes the properties of free electron lasers, with particular reference to the FELIX free electron laser. Then, the experimental setup for the pump-probe measurements to obtain the sample lifetimes is discussed in the following section. The results collected from the measurements on several MQW samples are then analysed and discussed. In addition to the lifetime measurement, photoluminescence signals have also been observed from one of the samples, which will be included in section 3.4. Section 3.5 then describes a three-level rate equation model, which is utilised in analysing the result from the pump-probe measurements. Finally, a general conclusion is drawn for the chapter.

3.1 Free electron lasers

The FEL is a highly tunable source with high power and ultrashort pulses. An electron gun or particle accelerator generates a stream of electrons travelling at a speed close to that of light. This electron beam can give up some of the energy to a beam of photons travelling in the same direction, by passing through a set of alternating polarisation magnets, the so-called wiggler or undulator. The electrons oscillate due to the periodic magnetic field generated by the wiggler and a monochromatic radiation is emitted. The wavelength of the emission is determined by the electron beam energy, the magnet spacing and the magnetic field strength [13]. A wide spectral range of emission can be achieved by varying these parameters. Hence, the high tunability of the FEL offers an ideal tool for studying the kinetic characteristics of our MQW structures.

The FELIX free electron laser is a user facility for the European research community, but researchers from the United Kingdom are allocated at least 20 % of the available beam shifts under the agreement between the Foundation for Fundamental Research on Matter (FOM) [104] of the Netherlands and the Engineering and Physical Sciences Research Council (EPSRC) [105]. The FELIX infrared beam consists of a train of short micropulses, which have duration adjustable between 1-10 ps and are separated by intervals of 1 or 40 ns. This FEL can operate in the wavelength range of 4.5-250 μm with peak micropulse power at up to mega Watts. The micropulses in turn form a train or the so-called macropulse. These macropulses are repeated at up to a rate of 10 Hz with duration up to 15 μs, as illustrated in Figure 3.1. The FELIX micropulse was reported to be near Fourier transform limited, where the micropulse duration and the spectral width are directly related. By changing the cavity length of the FEL, the micropulse duration and the spectral width can be controlled. As the micropulse width

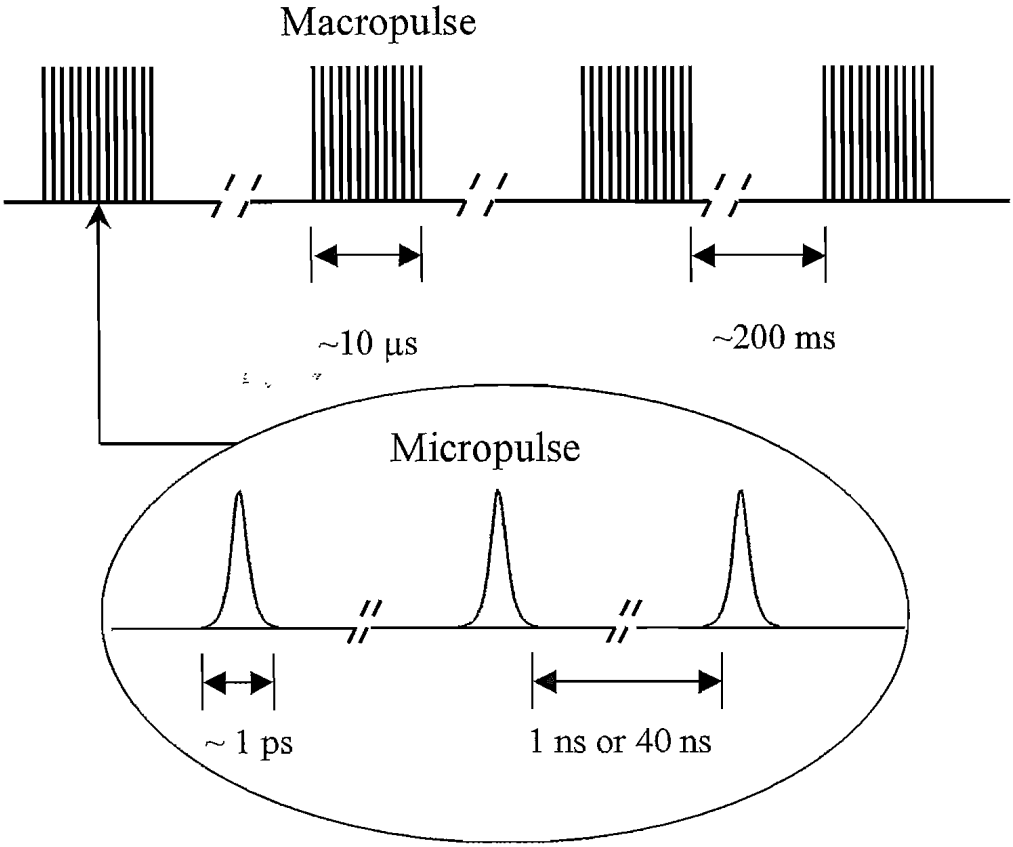

Figure 3.1. A train of FELIX micropulses separated by 1 ns or 40 ns form the macropulse, with a typical duration of 10 μs. The macropulse is repeated at 5 Hz to have a low average power.

is decreased, the micropulse energy increases, which results in higher peak power and wider spectrum. Past measurements showed that the FELIX micropulse shape is not Gaussian but closer to a *sech* pulse, with a minimum time-bandwidth product (TBP) of 0.3 [106]. The TBP is normally defined as the product of the full width at half maximum (FWHM) of the pulse duration and spectral width.

3.2 Experimental setup in FELIX

The technique employed to measure the intersubband lifetime is commonly known as a pump-probe experiment. This technique generally involved a pump beam to excite the electrons to higher energy levels and a probe beam, which was time delayed and monitored. However, a modified three beams setup was used in our experiments [107]. The pump-probe experimental setup for our lifetime measurement is depicted in Figure 3.2. By using a zinc selenide (ZnSe) beam splitter, the picosecond FELIX beam was first split off at a ratio of 95 % : 5 %. The stronger beam became the pump beam

whereas the weaker beam was further split with equal intensity, to obtain a probe beam and a reference beam. This reference beam was optically delayed by 20 ns and back reflected onto the same optical path as the probe beam, using a –1 telescope. These three beams were then focussed onto the sample at the same position but with different incident angles. A liquid nitrogen (N_2) cooled mercury-cadmium-telluride (MCT) detector, whose bias was modulated and synchronised with the FELIX beam, was utilised to detect the transmitted probe and reference beams. With the MCT detector bias modulated at 25 MHz, the probe pulse was thus positively modulated while the reference pulse was negatively modulated, since the pulses were 20 ns apart. Optical alignment was done with a Helium-Neon (HeNe) laser, which was well aligned with the FELIX output.

This pump-probe setup was to compensate for the fluctuation between successive micropulses of the FELIX pump beam. When no pump beam was applied, the integrating electronics showed an output of zero magnitude from the detector. This was the case since the system was in balance due to the opposite signs of the reference and probe pulses, as illustrated in Figure 3.3. However, when the pump beam was applied,

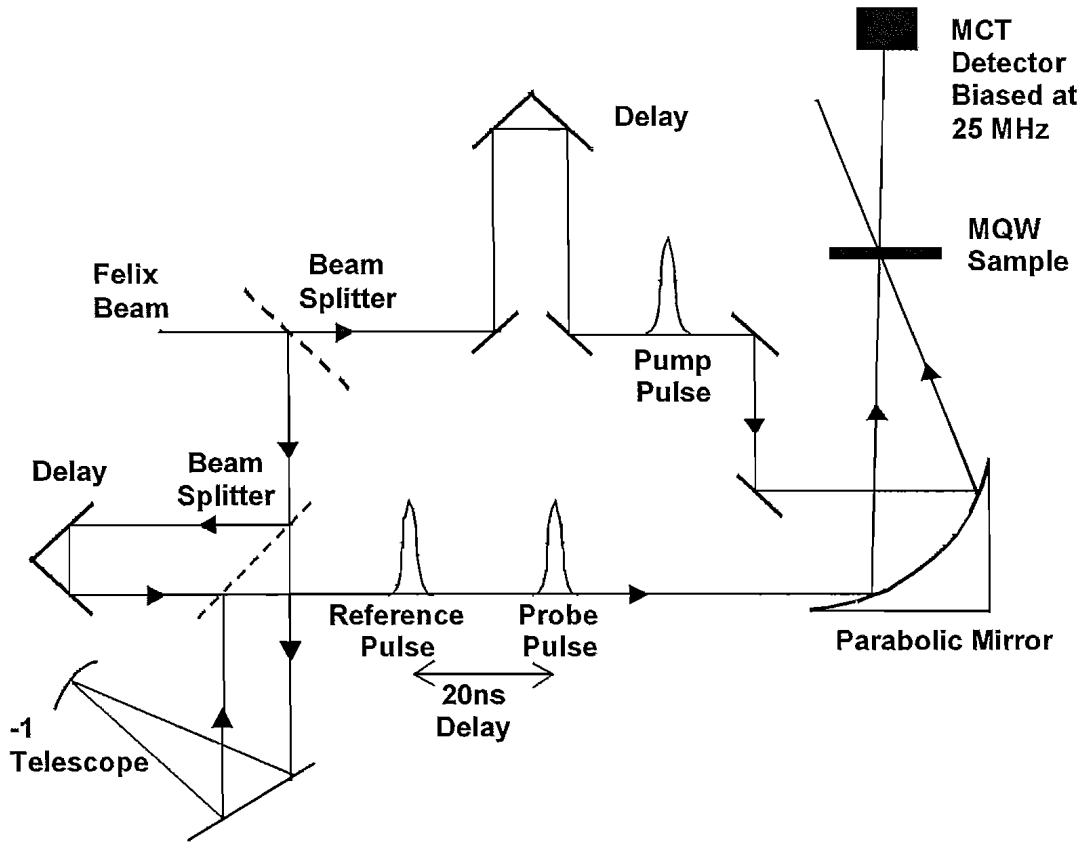

Figure 3.2. Pump-probe experiment setup in FELIX for measuring the intersubband electron lifetimes. Adapted from FINDLAY et al., *Phys. Rev. B*, 58 pp. 12908, 1998.

changes in the transmission of the sample occurred and the signal strength of the probe pulse was altered while the reference pulse was unaffected. Hence, the integrator output changed according to the variation in the transmitted signal [107]. In our experiment a micropulse separation of 40 ns was chosen, which was much longer than the characteristic electron lifetime in our structure (in the order of ps). This ensured that the micropulses could be safely considered as independent of each other. On the other hand, the macropulse was repeated at 5 Hz to ensure low average power. Consequently, sample heating due to the FELIX pulses should be minimised.

By using a boxcar integrator, relative transmittance of the sample was obtained from the integrated signal. The relative transmittance of the probe beam was collected as a function of the time delay between the pump and probe beams. A movable retro-reflector was used as the optical delay line. Note that either the pump beam or the probe beam can be delayed since only the relative delay between the two beams that matter. A few scans were taken and the average was then recorded, which reduced the random noise due to each individual scan. The time delay corresponded to the distance moved was then calculated as

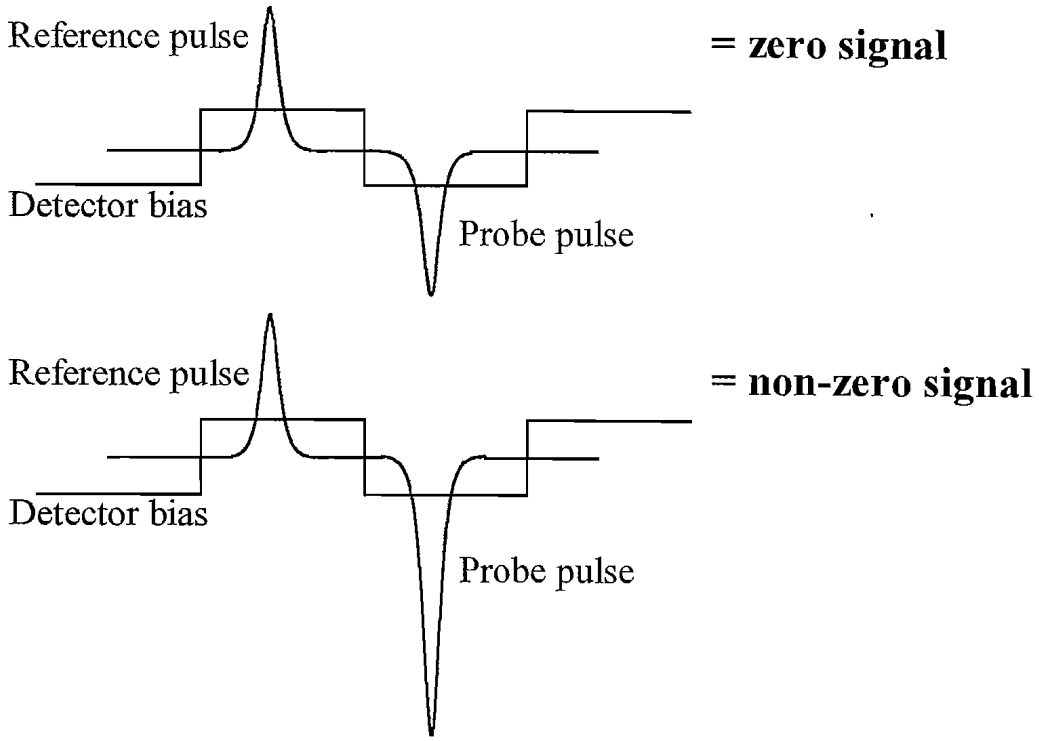

Figure 3.3. The MCT detector were modulated such that the reference pulse and probe pulse were opposite in sign. The integrated signal showed a zero output signal when the reference and probe beams were equal whereas a non-zero output signal was obtained when the beams were different in magnitude.

$$\text{Time delay} = \frac{2L_{Delay}}{c} \tag{3.1}$$

where c is the speed of light and L_{Delay} was the distance that the retro-reflector was moved.

In order to carry out the experiment at various sample temperatures, the sample was mounted to the cold finger in a liquid Helium flow cryostat. This cryostat covered a temperature range of 4-300 K, which was easily controlled with a temperature controller and a heater. The experiment was then performed at various sample temperatures down to ~4 K and experimental wavelength was tuned to resonant with the intersubband gaps between the ground level and the first or second excited level.

3.3 Result and discussion

Measurements were carried out on some of the MQW samples over several visits to the FELIX facility. In the following subsections, the measured results from these samples, which were significantly different in design parameters will be discussed.

3.3.1 Sample doped in the barrier

Measurements were first conducted on a sample that was modulation doped in the barrier in the conventional manner. The spectral measurement showed that the resonant wavelength for this sample (RMB1564) from ground to second and first excited subbands were $\lambda_{02} = 9.19$ μm and $\lambda_{01} = 9.85$ μm respectively at 6 K. The pump wavelength was slightly longer than the resonant wavelength between the ground subband and the second excited subband. However, it was at the peak absorption of the sample, as can be seen in Figure 2.13. Figure 3.4 shows the differential transmission signal of the probe pulse as a function of time delay relative to the pump pulse. This was taken at a pump wavelength of 9.35 μm and the sample cooled to 4.2 K. A 2.5 ± 0.2 ps lifetime was measured for the transition from the second excited subband to the ground subband. This value was in general agreement with the reported lifetimes for energy separation larger than the LO phonon energy, although it was several times longer than some reported lifetimes for rectangular QWs [71, 108]. This longer lifetime may be attributed to the smaller overlap of the wavefunctions in a stepped QW compared to that in rectangular QWs [29].

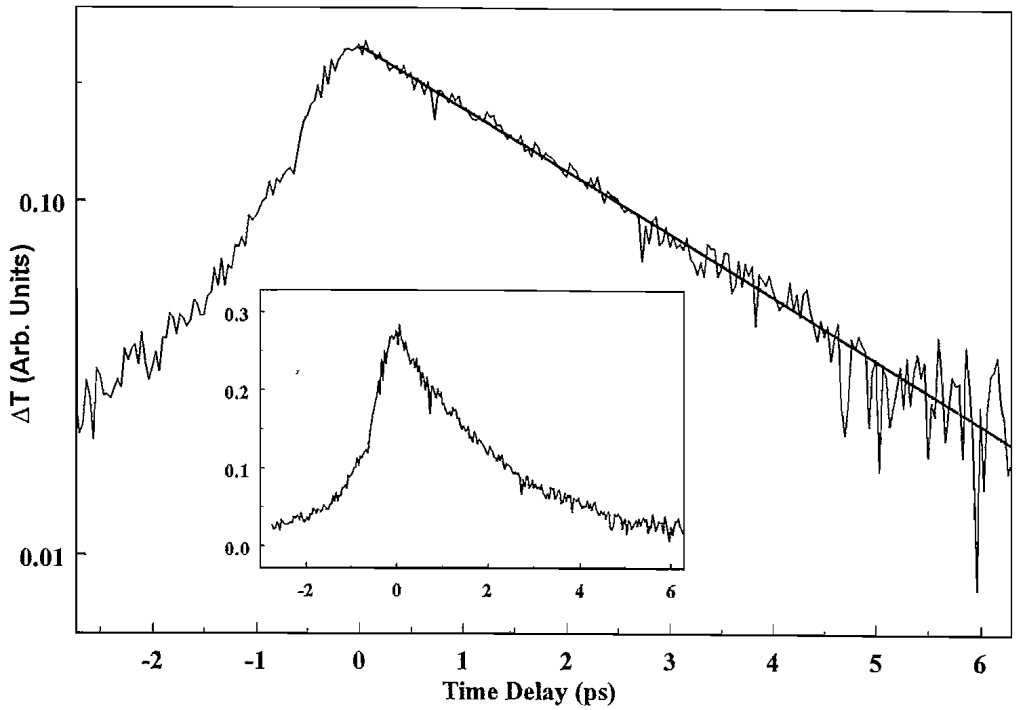

Figure 3.4. Pump-probe transmittance signal with 9.35μm pump wavelength on a logarithmic scale. The inset shows the same signal on a linear scale. The solid straight line is fitted with an exponential curve with lifetime of 2.5 ps. This structure (RMB1564) is doped at the middle of the barrier.

3.3.2 Sub-nanosecond absorptive signal

The intersubband lifetime signal in the previous section was only attained after a −10 dB attenuator was applied to the FELIX output to reduce the pump intensity. At pump intensities without the attenuation, a strong absorptive signal followed immediately after the short decay lifetime, but with a much longer decay lifetime. The slow decay lifetime was two orders of magnitude longer as compared to a normal electron intersubband lifetime of a few picoseconds at most. As shown by Figure 3.5, this absorptive signal caused a large reduction in the transmission of the sample before it decayed on a sub-nanosecond time scale. Also, the absorption showed a strong dependence on the pump pulse intensities.

As attenuation was applied to the pump pulse, the magnitude of this strong absorption was greatly reduced. When the FELIX output beam was attenuated by 10 dB, the strong absorptive signal and the slow decay were no longer visible. Note that these plots had been shifted vertically for clarity. This phenomenon was clearly observable for all the temperatures in our experiment. In addition, no slow decay from the absorptive signal appeared for long pump wavelength. This was evidenced by Figure

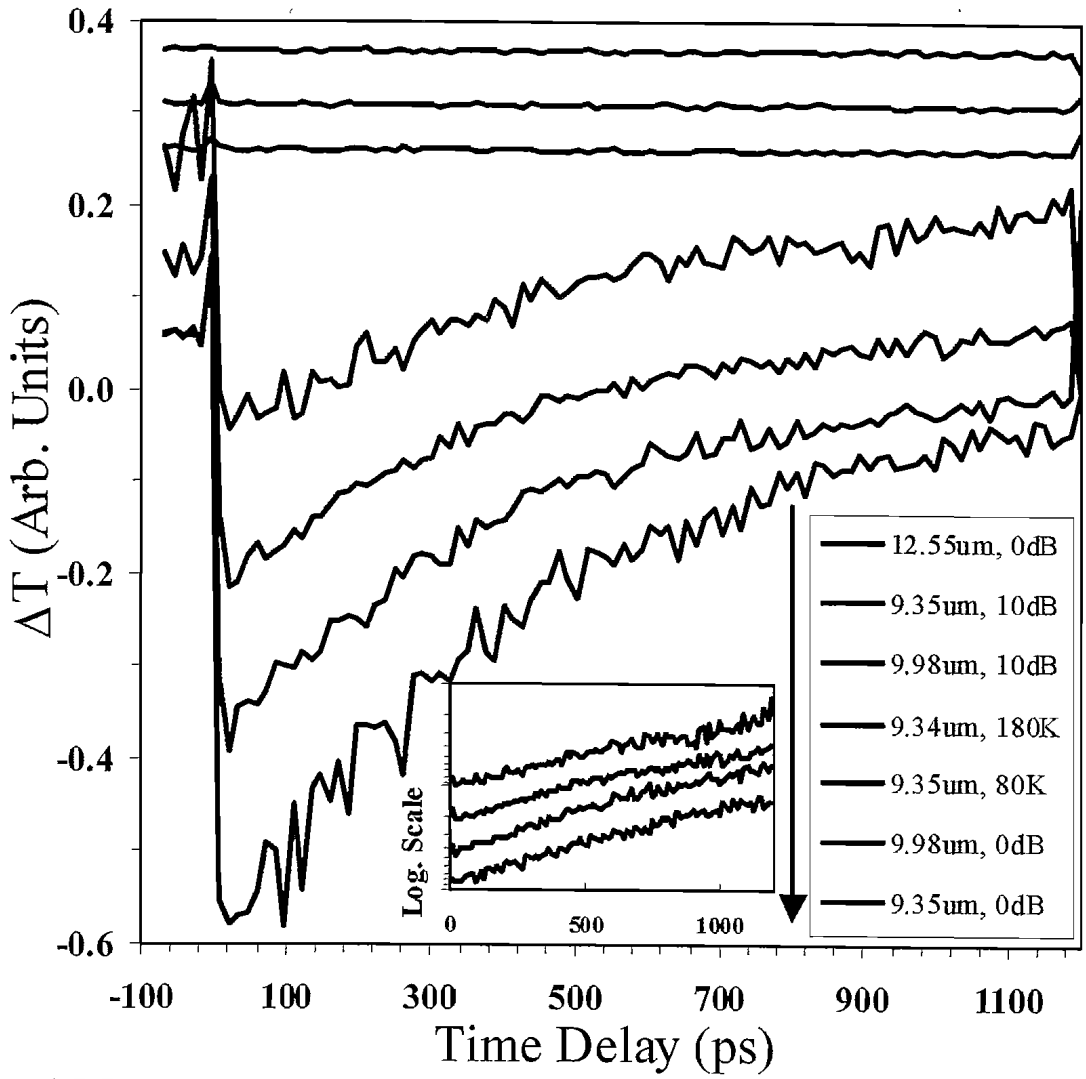

Figure 3.5. Pump-probe signals at different pumping intensities, wavelengths and temperatures for sample RMB1564. They were taken at 4 K unless specified otherwise. The inset shows a logarithmic magnitude plot of the slow decay lifetime part of the bottom four plots in the main figure.

3.5, where for a pump wavelength of 12.55 μm, no absorptive signal was observed. Disappearance of the absorptive signal was expected because the long wavelength pump beam was out of the resonant absorption range for this MQW sample, as shown before in Figure 2.13.

3.3.3 Multi-photon absorption

The strong intensity dependence and disappearance of the long decay signal at low intensities suggest that an incoherent two-photon or multi-photon absorption process may be involved in the pump probe experiment at high pump intensities. At high pump intensity, the first transition subband of the sample could be significantly populated, as in the case for a laser. This was observed through the positive transmissive signal. A

considerable number of electrons could be further excited from this excited subband to the continuum or quasi continuum conduction band. Hence, electrons were first excited to the intermediate level (the excited subbands) before further excited to the continuum conduction band in this two-photon absorption process. The free electrons at the continuum band were able to perform 3-D absorption, which was much stronger than the absorption taking place in the 2-D environment in the QWs. Hence, the free carrier absorption would overwhelm the absorption change due to ground subband electron depopulation. Intersubband two-photon transitions from the ground subband to the continuum states [109] and electromagnetically induced two photon resonant between subbands [110] have been demonstrated previously in symmetric QWs.

As depicted in Figure 3.6, the high concentration of ionised dopants in the barrier layers resulted in severe deformation to the conduction band. This deformation is due to the extra potential energy introduced to the conduction band as a result of the separation between the ionised dopants and electrons. The two-photon excited electrons were held by the deformed conduction band in the barrier. A much longer time was needed for these electrons to relax back to the quantum well. The very long lifetime of

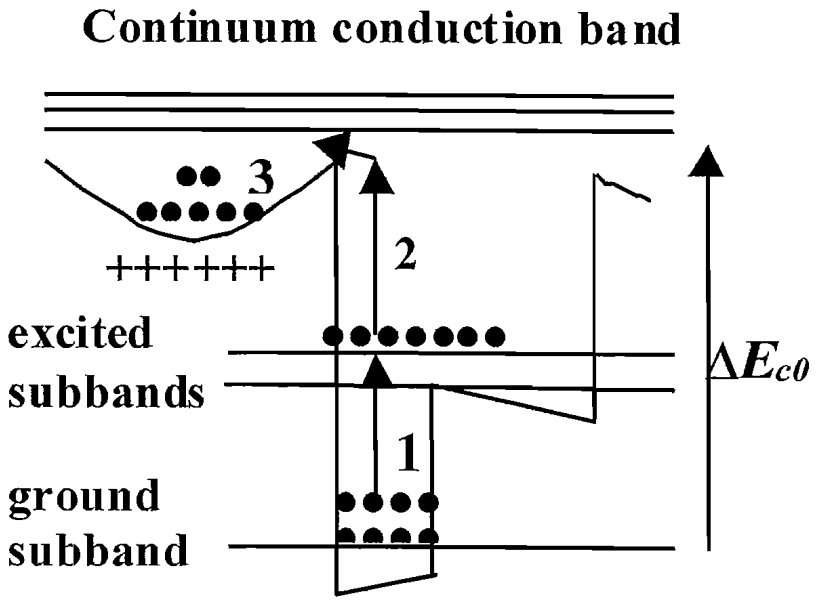

Figure 3.6. A schematic illustration of the two-photon process in a stepped QW with modulation doping. (1) Electrons were optically pumped from the ground subband to populate the excited subbands. (2) At saturated pump intensities, these electrons can be further excited to the continuum conduction band, (3) which subsequently diffuse and drift to the doping region. ΔE_{c0} indicates the energy gap between the ground subband and the bottom of the continuum conduction band.

the slow decay suggests that the electrons were removed from the immediate vicinity of the well into the barrier regions. Rapid recapture of the electrons by the ionised donors would be expected, before they were reionised and returned to the well in a sub-nanosecond scale.

As a test to the explanation in the previous paragraph, the sample position was rearranged so that the incident angle of the probe beam was at 0° (i.e. normal to the sample) and the incident angle of the pump beam remained nonzero (we used 25°). The probe beam will now have no response to any variation of the electron population in the subband, but will strongly dependent on the population of 3-D free electrons in the continuum conduction band. As shown in Figure 3.7, only the slow absorptive signal was detected in this geometry, which is in consistent with our argument. Moreover, since the electric vector of the pump and probe beams has a large component in the QW plane, any effect on the intersubband lifetime measurement due to intrasubband (i.e. within the same subband) absorption [111] should be detectable. However, there

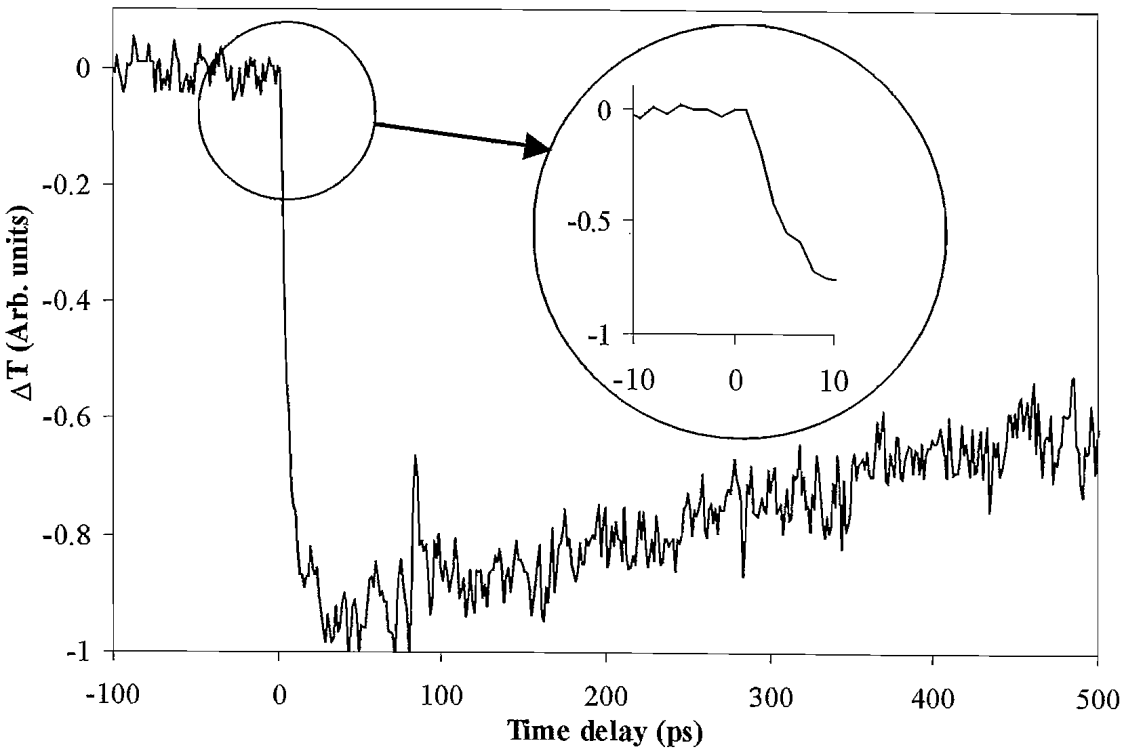

Figure 3.7: Pump-probe signals at 4 K for sample RMB1564 when the probe beam is directed at a normal angle to the MQW sample. The inset shows clearly that the positive transmission signal is not detected by the probe pulse, as the probe pulse is polarised parallel to the QW layers. Hence intersubband electron transitions are not detected, but the free carrier absorption effect can still be observed.

was no perceivable positive signal in this case, which suggests that any contribution from intrasubband effects were negligible in this measurement.

3.3.4 MQW structure with higher barrier

In order to confirm that two-photon absorption (TPA) was responsible for the long decay, a second structure with higher barrier was grown. This structure (M2193), shown in Figure 3.8 was similar to the previous structure, except that a higher Al composition was used for the barrier (x = 0.45 as compared to x = 0.35). Consequently, the higher barrier energy was greater than the two-photon energy for the ground to excited subband, for pump wavelength > 8 μm. This modified structure was expected to eliminate the two-photon effect. The same pump-probe measurement was repeated for this structure. The slow decay was not observable for most cases (with similar pump intensities as sample RMB1564) of the experiment with this improved sample.

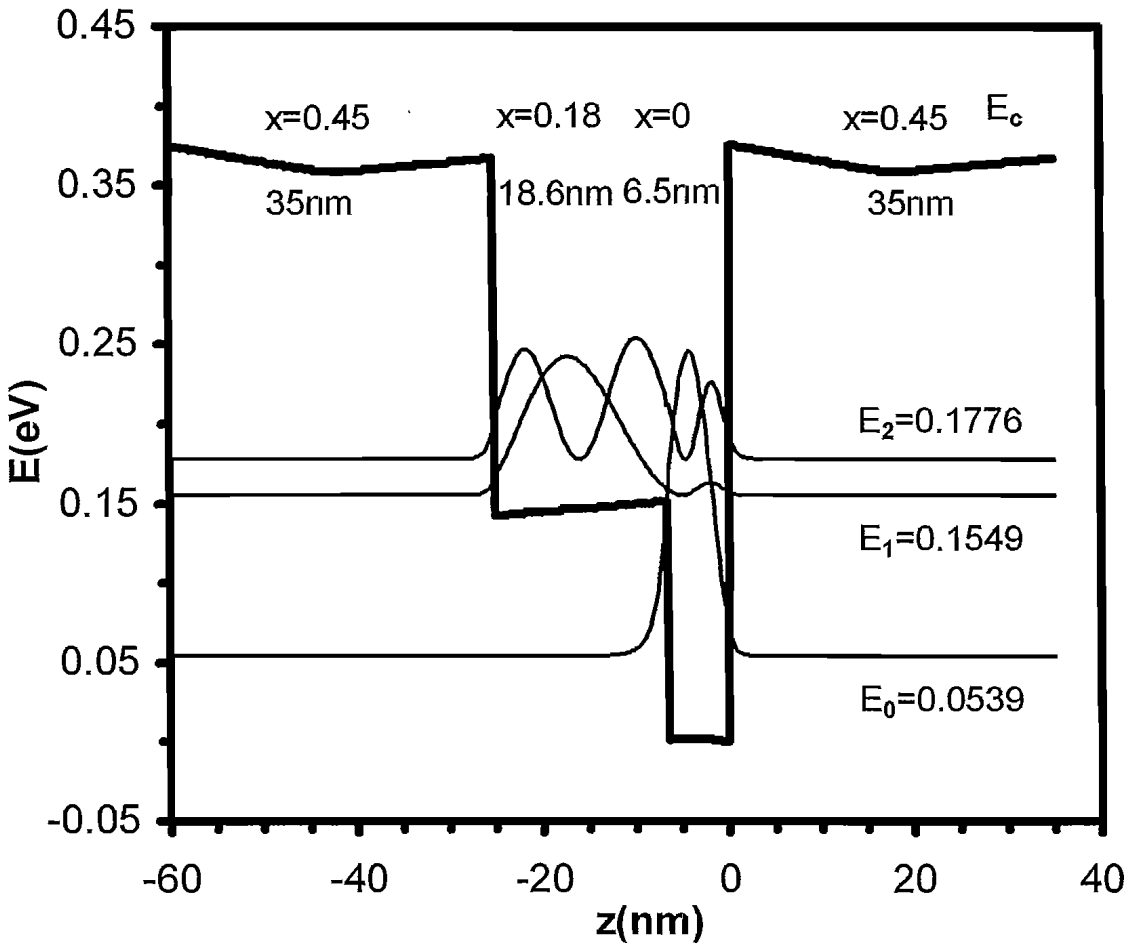

Figure 3.8: Energy structure and wavefunctions of a stepped GaAs/AlGaAs QW, sample M2193. This structure is modulation doped at the barrier. The Al concentration for the barrier is raised to $x = 0.45$.

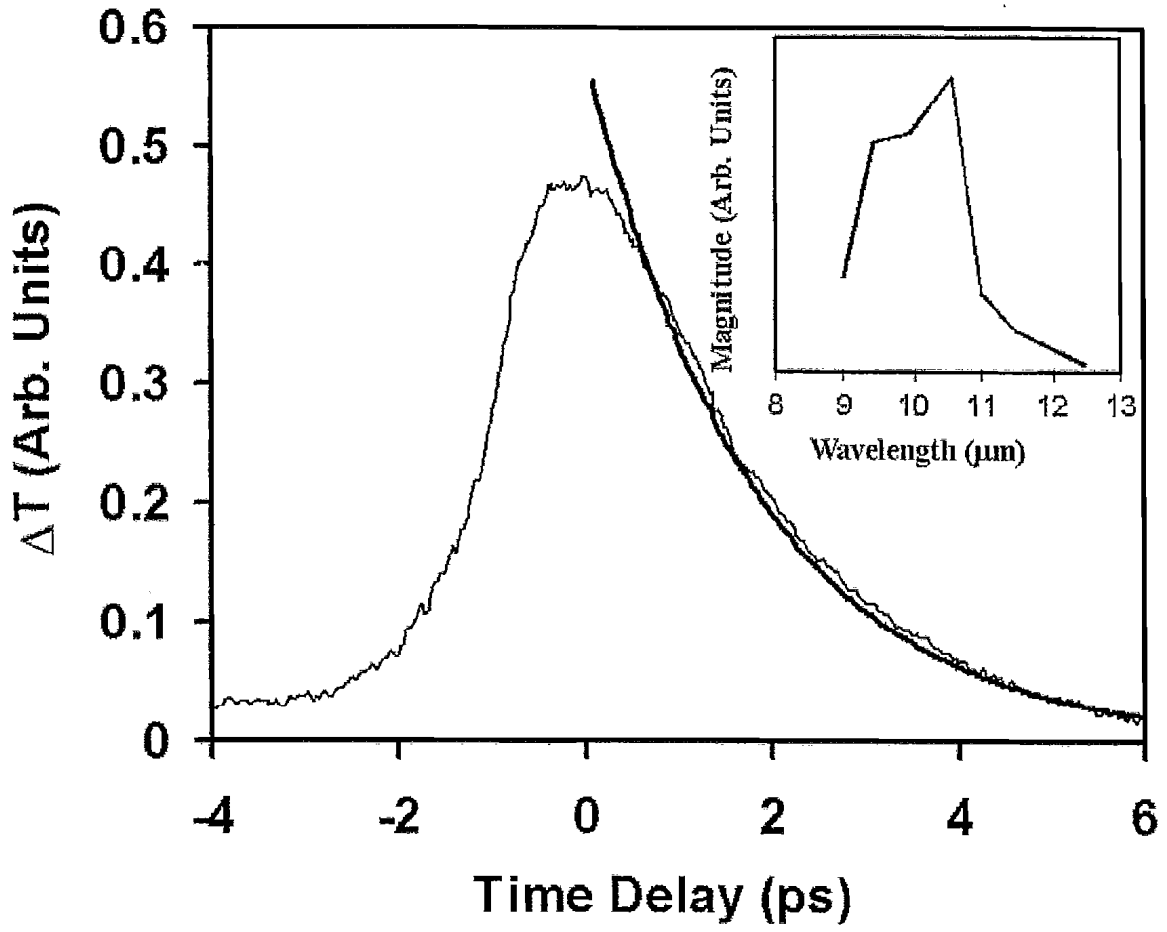

Figure 3.9. Differential transmission signal (M2193) of the probe pulse with respect of time delay resulting from the electron depopulation in the ground subband. The bolder line was fitted with a decay lifetime of 1.8 ps. The inset shows the change of the peak signal of ΔT against the wavelength.

Nevertheless, weak residual signals were observed in cases where very high pump intensity was used, which were most probably due to higher order of absorption, three-photon absorption for example. The measured signal is shown in Figure 3.9, with a fitted lifetime of 1.8 ± 0.2 ps. The inset shows the peak of the detected signal as the wavelength of the pump beam was varied.

3.3.5 Sample doped in the stepped well edge

As a result of the intersubband lifetime measurements, which highlighted the potential disadvantage of the QW design with the doping at the barrier between consecutive QWs, a new structure (A1580) doped at stepped well was grown. Similar experiment to determine the lifetime was carried out on this structure. The design of this structure was discussed previously in Section 2.3.

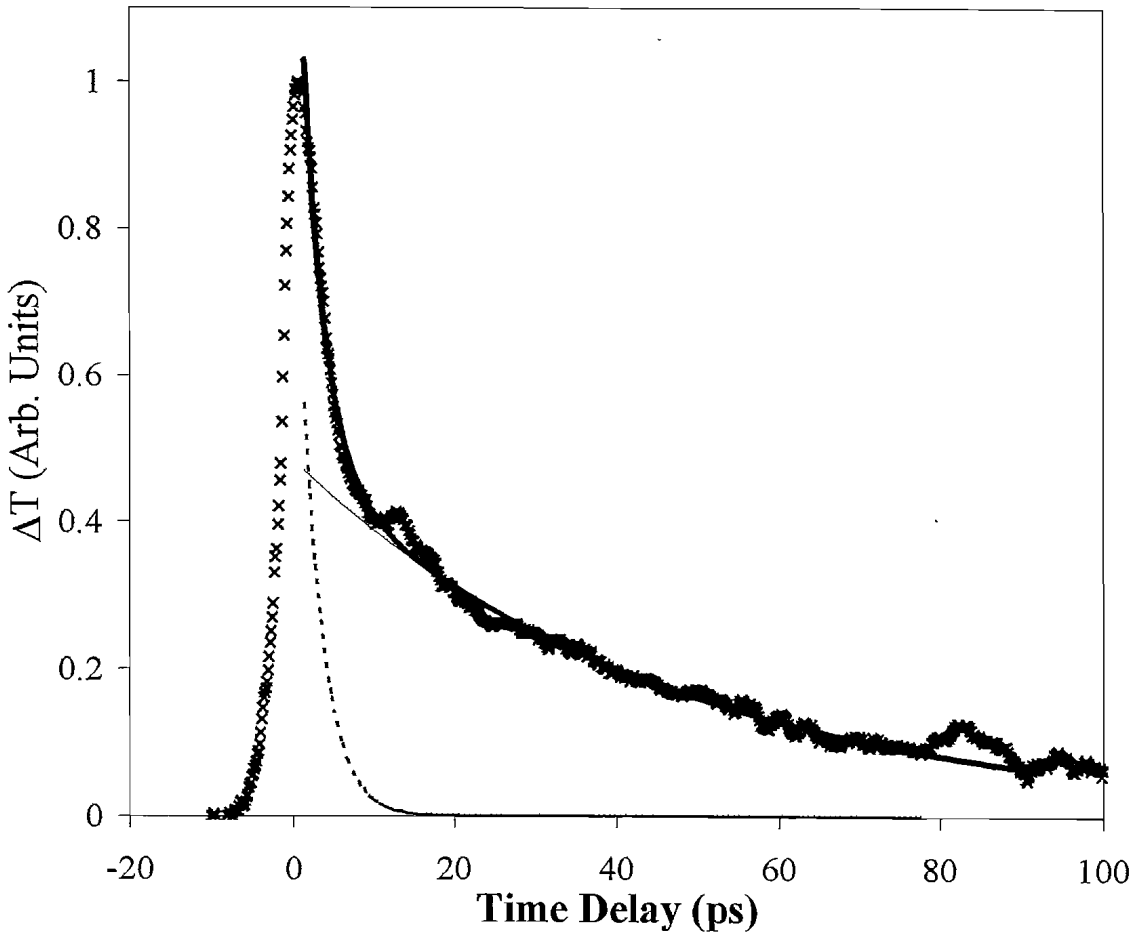

Figure 3.10. Pump-probe measurement at 3 K of the doped stepped well structure (A1580). The crosses are experimental data while the bold solid line is the exponential fit with a combination of two lifetimes. The two components are the 2.7 ± 0.2 ps intersubband lifetime (dashed line) and the slower carrier recombination lifetime from the deformed stepped well of 45 ± 5 ps (thin solid line).

The FTIR transmission spectrum measurement revealed that two absorption bands at 9.03 ± 0.06 μm and 9.93 ± 0.08 μm for the ground to first and ground to second excited levels respectively, as shown in Figure 2.16. The Lorentzian fit on the spectrum also suggests that the absorption strength for the ground to first excited subband is stronger, which is not ideal for the laser structure. With the FELIX laser beam tuned to narrow spectrum, the intersubband lifetime shows two-time constant features. The first, faster lifetime is attributed to the normal relaxation lifetime from the excited level back to the ground level. The second lifetime, which is much longer, is most probably due to the relaxation of electrons being pumped to the deformed stepped well and eventually returned to the ground subband in the well. The fitted result is illustrated in Figure 3.10.

3.3.6 Temperature dependence in the lifetime measurements

One of the features of the strong absorptive signal was that the relaxation lifetime was not strongly dependent on temperature. As shown in the inset of Figure 3.5, where the long decay parts were normalised and the magnitude plotted on a logarithmic scale, the temperature dependence of the lifetime was very weak. At low sample temperature, electrons excited to the continuum subband could recombine with the ionised donors at the centre of the barrier. Unless the thermal excitation energy was greater than the ionisation energy of the donors, these electrons were frozen at the barrier. This electrons recombination and freezing process should be a function of temperature, which in turn should be reflected by the change in the lifetime for the long decay signal. Nonetheless, our experimental data at different temperatures did not show a noticeable temperature dependent. This could be attributed to the large field of view (FOV) (refer to Figure 3.11.a) of the sample, which meant radiation from outside of the cryostat could easily reach the sample. The half-angle FOV values were estimated as 56 ° and 76 ° for the front and back surface of the sample respectively. Consequently, the background thermal radiation might be the excitation source for the bound electrons in the deformed conduction band at very low temperatures. This excitation energy would only depend on the background temperature for low sample temperatures. As the temperature of the MQW sample in the cryostat was varied, the background condition

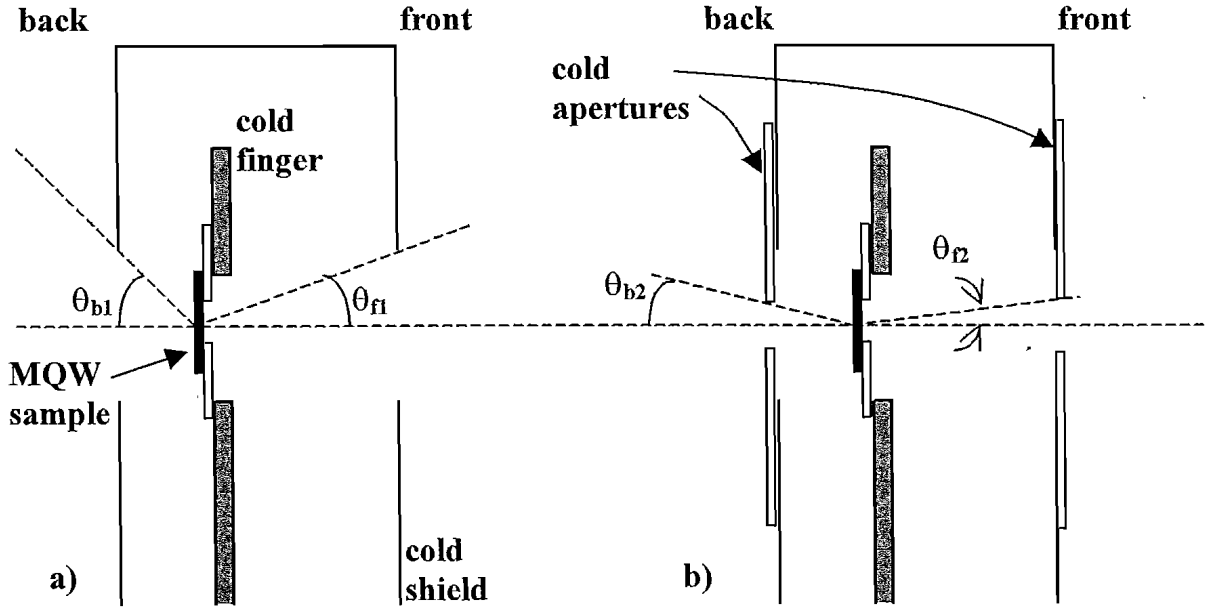

Figure 3.11. (a) Half-angle field of view (θ_{f1}) and (θ_{b1}) of the sample mounted on the cold finger are limited by the original cold shield of the cryostat. (b) The field of view (θ_{f2} and θ_{b2}) angles are reduced when additional cold apertures are placed on top of the cold shield.

seen by the sample remained the same with the same excitation energy.

Subsequently, an experiment was carried out to investigate this assumption. Additional cold apertures (at a temperature comparable to the sample temperature of 4 K) were attached to the original cold shield of the cryostat, near the cold finger, to limit the background radiation received by the cooled MQW sample, as shown in Figure 3.11.b. As the cryostat used in the experiment had two optical windows at opposite side of the sample, two different apertures were used. The FOVs were reduced to 20 ° and 37 ° for the front and back surfaces respectively. If these apertures sufficiently limited the thermal radiation seen by the sample, a substantial change to the decay lifetime of the absorptive signal would be expected. However, no substantial change in the long decay lifetime has been observed. As a result, the background photon flux that could be seen by the MQW sample was estimated. This estimation is included in section A.2.2 of Appendix 2. The estimated result revealed that the flux was indeed too small to reionise the electrons trapped in the barrier. Consequently, it is believed that the background radiation only contributed weakly to the observed results.

Another explanation to the lack of temperature dependence in the results could be due to heating of the sample by the pump and probe pulses. If the sample was sufficiently heated during the pump-probe measurement, then electrons that were trapped in the barrier would have enough thermal energy to reionise and return to the well. This may be the case due to the focused FELIX beams were incident at the sample at intense energy.

3.3.7 Discussion

The lifetime of the electrons out of the wells can be prolonged by the distortion of the conduction band in the barrier layers due to high modulation doping concentration, as shown in Figure 3.6. The electrons pumped to the top of the QWs therefore can quickly diffuse and drift to the dopants region under the forces induced by chemical and electrical potentials. This spatial separation of the excited photoelectrons from the QWs can significantly delay their recombination time to the empty states in the QWs, which is normally in the region of a picosecond [91]. This is why τ_3 in Figure 3.12(sample M2193) is shorter than that in Figure 3.5(sample RMB1564) as the latter had a much higher doping concentration. Furthermore, the energy gap between the ground subband and the bottom of the continuum conduction band (ΔE_{c0} in Figure 3.6) for sample

RMB1564 is far closer to the two-photon resonant energy than that in sample M2193. Consequently, even though the pumping intensity for sample M2193 was much stronger than that for sample RMB1564, the latter still needed a larger attenuation to totally suppress the negative signal. Due to overlap of the absorption spectra of ΔE_{01} and ΔE_{02}, the pump transition of the electrons may not only occur between the ground and second excited subbands. However the analysis here and the above are still applicable, as the electrons are pumped to the higher subbands before being further excited to the continuum conduction band.

It has been considered that the second order nonlinear effect [112, 113] could be involved in the experiment due to the asymmetric quantum well structure in addition to very high pump intensity. In particular this nonlinear effect can be enhanced due to the fact that the energy difference of the ground subband to the bottom of the continuum

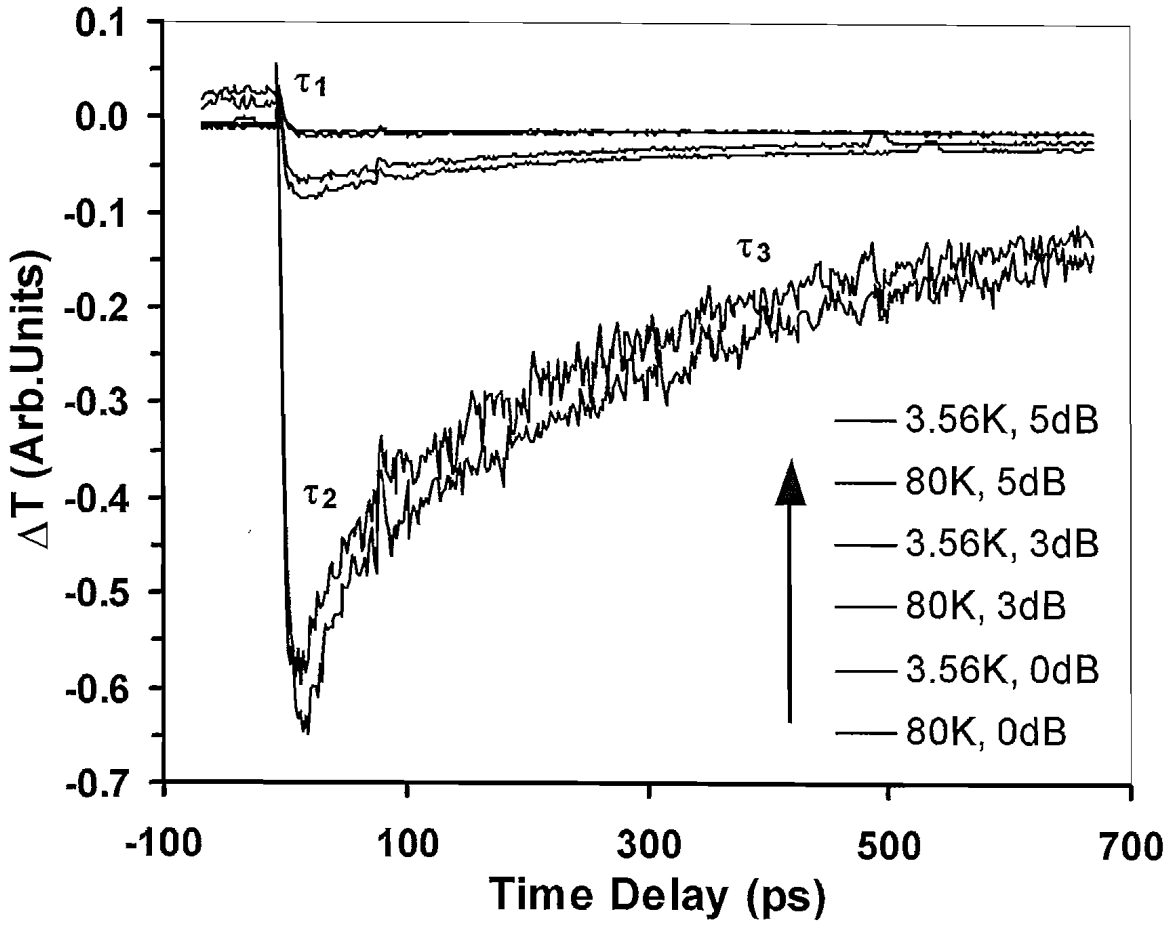

Figure 3.12. Differential transmission signal of the probe pulse with respect of time delay at different temperature and pump intensities for the sample with higher barrier energy. The pump wavelength was at 10.6 μm.

conduction band in the barrier layers that is close to the resonant energy of the second harmonic generation. A short wave pass filter (CaF_2) added in front of the detector showed that no evidence of appreciable second harmonic generation was observed, although care must be taken with significant levels of odd harmonic radiation in the FEL pump beam. These FEL harmonic signals can readily be confused with genuine second harmonic signals.

The measured intersubband lifetimes for the MQW samples are comparable and consistent with the reported value in the mid-infrared quantum fountain laser [34] and previously calculated value for a similar FIR stepped QW structure [31]. These lifetimes are longer than the reported fast LO phonon assisted subband lifetimes. The first excited subband is thus expected to have a shorter lifetime than the second excited subband. Hence, it appears feasible that population inversion can be achieved in the stepped QW structures due to the lifetime difference of the two excited subbands.

3.4 Photoluminescence measurement

Photoluminescence in a MQW intersubband laser can occur when electrons are excited from the ground subband to higher subband levels. Excited electrons can spontaneously emit radiations during the relaxation process to lower energy subband levels. This is the radiation from which a laser will build up. The emitted luminescence signal has the wavelength that corresponds to the energy separation between the energy levels of the radiation transition. Laser emission is not possible from a MQW structure unless sufficient population inversion between the excited subbands has been achieved in the pumping process. However, the FELIX pump beam is only of the order of 1 ps, which is small compared to the measured intersubband lifetime in our structures. In addition, the sample needs to be cleaved into a small laser bar to form a laser resonator, where the radiation could be reflected within the resonator to allow for the feedback and build-up of radiation. However, the pump pulse period was also too short for the radiation to complete a round trip propagation, for the structure that was used. There was no additional waveguide implemented for this structure to improve the laser mode confinement. Hence, there is not enough build-up of the emission to achieve laser oscillation. Furthermore, the loss from the structure was high and would prevent any laser action. The mode confinement issues will be discussed in Chapter 4.

Nevertheless, observing photoluminescence signals can be regarded as a major step forward before achieving laser emission from the MQW structures. An experiment was

carried out utilising the FELIX laser beam to pump the MQW structure to observe the FIR photoluminescence signal. The MQW structure was mounted to the cold finger of the liquid He cooled cryostat to conduct the experiment at low temperature. A Ge:Ga photoconductor, which was also liquid He cooled, was used to detect the FIR signal. A description of this type of photoconductor can be found later in Chapter 5. The wavelength of the FELIX laser was varied around the ground to second excited subband energy gap. In this experiment, the FELIX beam was tuned for two different settings of wide and narrow spectral width. As mentioned before in Section 3.1, the FELIX micropulse duration and spectral width are directly related. Therefore, a spectrally wide FELIX output beam corresponds to an intense and short duration micropulse. However, electrons may be excited to different subbands that are very close in energies. On the other hand, a spectrally narrower pump beam is lower in peak intensity and has longer micropulse duration. Electrons can thus be excited to a chosen subband for a longer period of time.

The FELIX beam was directed at the MQW sample through a ZnSe window at the cryostat and the photoluminescence signal collected from the opposite side of the cryostat. A polyethylene window was used to allow FIR signals to exit the cryostat. Similarly, a polyethylene window was used as the input window for the cryostat containing the Ge:Ga detector. In order to determine the wavelength range of the detected emission, various optical filters were placed in between the optical path of the sample and detector. Firstly, a long-wavelength-pass (LWP) filter that blocked the transmission of wavelength range of the pump pulses was placed in front of the output window for the sample. Then a variety of filters were placed in front of this LWP filter, where the transmission range of these filters are shown in Figure 3.13. When a fused silica or KRS5 filter was placed after the LWP filter, no emission signal was observed by the detector. However, when a 2 mm ZnSe filter was used, about 3 % of the total signal was observed. Lastly, 67 % of the emission signal was transmitted when a polyethylene filter was placed after the LWP filter. The polyethylene filter has ~80 % transmission in the 100 μm region [114].

After analysing the attenuation of the signal by the different filters, the detected signal was most probably in the FIR region of ~ 90-120 μm. Note that the upper limit is due to the cut-off point of the Ge:Ga response. (Refer to Section 5.1.1) This was consistent with the expected FIR emission wavelength of the MQW sample. According to the

measured absorption bands of the sample in Figure 2.16, the FIR emission for the E_{21} transition (12 ± 2 meV) was estimated as λ_{21} ~ 103 μm (λ_{21} ~ 89 – 124 μm considering the uncertainty of E_{21}).

With the combination of filters we used, scattered light from the pump beam was ruled out. This was particularly evidenced by the large attenuation of the signal by the ZnSe and KRS-5 filters, since these filters were largely transparent in the pump wavelength.

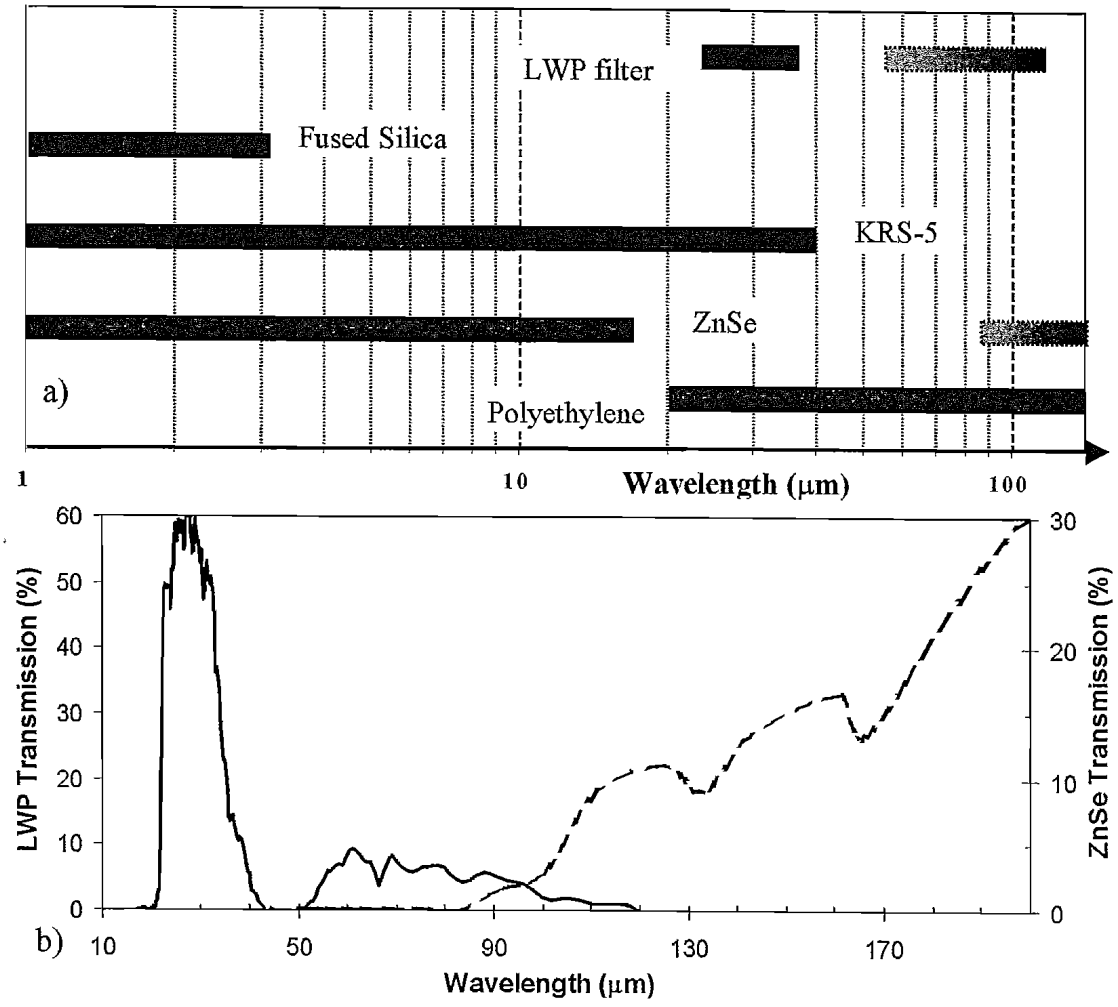

Figure 3.13. a) Wavelength range for the transmission of optical filters used in the FIR photoluminescence experiment. The dark colour bars indicate the wavelength range where the filters are largely transparent. The LWP filter has a transmission of a few percent in the longer wavelength range represented by the grey colour bar. A 2 mm ZnSe is transparent at the shorter wavelengths up to ~ 16 μm. At longer wavelengths, there is increasing transmission from ~ 90 μm with a few percent transmission at 100 μm. b) Measured transmission spectrum for the LWP filter (solid line, left-hand axis) and estimated 2 mm ZnSe transmission (dashed line, right-hand axis) from the absorption coefficient data from Ref. [115].

Pump attenuation (dB)	Detected signal (mV)
0	200
3	100
5	58
8	29

Table 3.1. Detector signal strength as the FELIX beam was attenuated. The signal is linearly dependent on the pump power.

In addition, the detected signal strength was approximately linearly related to the pump intensity (Table 3.1), where the FELIX pump beam was attenuated using different values of attenuators. Figure 3.14 shows the observed photoluminescence signals with varied wavelengths under two FELIX pump beam setup. The strong wavelength variation of the detected signal also reconfirmed that the detected signal was not the scattered pump light.

Although the above observation suggested that intersubband FIR emission may be the origin of the detected signal, caution needs to be taken to exclude other possible origins

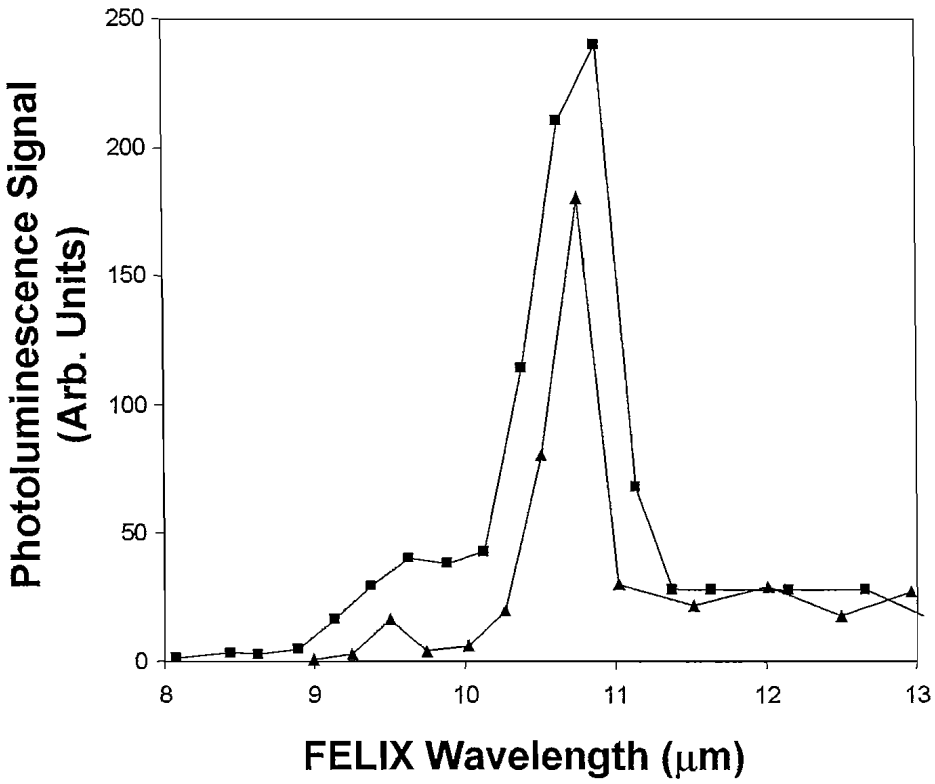

Figure 3.14. Photoluminescence signal for sample A1580 taken at liquid He temperature with a Ge:Ga detector. The FELIX pump beam was tuned at wide spectrum (squares) and narrow spectrum (triangles) respectively.

of the emission signal. To confirm that the emission signal was due to intersubband transitions, the emitted light must have polarisation normal to the QW layers. However, we have not carried out this test during the measurement. Hence, the polarisation of the emitted light was not determined. A possible emission source in the 100 μm region is the thermal emission (T ~30 K) from the sample due to resonant heating of the 2DEG. Nonetheless, the emitted light scaled linearly with the pump power, which suggested that thermal emission was not responsible. As the temperature rises, the peak power of the thermal emission would move across the wavelength range of ~100 μm, which should scale non-linearly to the pump intensity. Furthermore, no additional cold shields were added to limit the room temperature background thermal emission, which was more than two orders of magnitude stronger than the T = 30 K thermal emission at the 100 μm region. Therefore, any detected thermal emission should be dominated by the room temperature thermal emission, rather than the lower temperature thermal emission.

Note that due to the opaqueness of the LWP filter in the wavelengths range of ~40 – 50 μm, there is a possibility that some emission exists in this wavelength range. This may be the case, since the LWP filter was always used in conjunction with the other filters. Moreover, further analysis needs to be carried out to determine the spectrum of the emitted signal, for example using a FTIR spectrometer. Nevertheless, this was our first MQW sample that had possibly shown the FIR emission experimentally, using a sensitive detector. Observation of the photoluminescence signal could also support the improvements of the doped stepped well design, as opposed to other doping schemes presented previously.

3.5 Three-level rate equation modelling

In the process of analysing the data obtained from the FELIX measurements, a 3-level rate equation model is established to simulate the two-photon absorption process. This model is intended to provide an insight to the data obtained from the pump-probe experiment. Figure 3.15 schematically illustrates the conduction band energy level diagram for our rate equation model. The strong absorptive signal is believed to be due to a two-photon absorption process. Here, the continuum conduction band, denoted as E_c, is the top energy level. The middle energy level of our model, E_i represents the excited subbands of our MQW laser system. Finally, the bottom or ground energy level E_0, is the ground subband in the conduction band. Note that E_i generally includes both

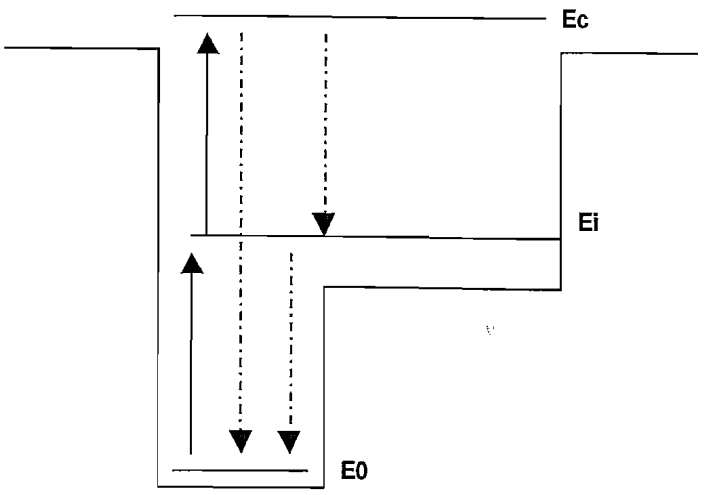

Figure 3.15. Three-level system for the rate equation model. E_c is the continuum conduction band, E_i is the excited subband and E_0 is the ground subband.

the first and second excited subbands in our structures. The simplified assumption of the model is very plausible as both the intersubband lifetime and the two-photon absorption process are of interests.

The electron dephasing time in a semiconductor QW is generally shorter than the intersubband lifetime [71, 116]. Hence, the incoherent two-photon effects largely dominate the absorption process. Therefore, the coherent two-photon absorption is not considered in this model. The justification is further provided by the experiment described before in Section 3.3.3.

3.5.1 Descriptions of the model

The model is represented by two rate equations and an equation for the total electron population (Equations 3.2-3.4). In these equations, N_0, N_i and N_c represent the populations at energy levels for the ground subband, the excited subbands and the continuum conduction band respectively. The total electron population is given by N, which is the sum of the populations in each energy level, taken to be the sheet density of the Si doping concentration. We have assumed that before the pump pulse is applied, all the electron population is at the ground level, i.e. $N_0 = N$, while the energy levels E_i and E_c are empty of any electron. This assumption is well justified at 4 K as most donors are ionised and the electrons are in the lower well.

$$\frac{dN_0(t)}{dt} = -\frac{\sigma_0}{\hbar\omega} I(t) N_0(t) + \frac{N_i(t)}{\tau_{i0}} + \frac{\sigma_0}{\hbar\omega} I(t) N_i(t) + \frac{N_c(t)}{\tau_{c0}} \tag{3.2}$$

$$\frac{dN_i(t)}{dt} = \frac{\sigma_0}{\hbar\omega} I(t)N_0(t) - \frac{\sigma_0}{\hbar\omega} I(t)N_i(t) - \frac{\sigma_i}{\hbar\omega} I(t)N_i(t) + \frac{\sigma_i}{\hbar\omega} I(t)N_c(t) - \frac{N_i(t)}{\tau_{i0}} + \frac{N_c(t)}{\tau_{ci}} \tag{3.3}$$

$$N_0(t) + N_i(t) + N_c(t) = N \tag{3.4}$$

The electron relaxation lifetime between energy levels is given as τ_{yx}, where subscripts x and y refer to the energy levels they represent, respectively. σ_0 and σ_i are the absorption cross sections (with the same dimension as area), from E_0 to E_i and E_i to E_c, respectively. The absorption cross section in the continuum conduction band is denoted as σ_c, which is two orders of magnitude greater than σ_0 and σ_i due to the stronger 3-dimensional absorption. The angular frequency of the pump pulse is given by ω where $\hbar\omega$ is the energy per photon of the pump pulse. The pump signal, $I(t)$ with respect to time (Equation 3.5), which models the FELIX pump beam is best described by a *sech* function with a peak intensity of I_0. FWHM of the pump pulse is denoted as τ_ω, with a value of 0.7 ps in our model [17].

$$I(t) = I_0 \sec h(\frac{t}{0.38\tau_\omega}) \tag{3.5}$$

The rate of change of the electron population in each energy level can be determined by considering both stimulated and spontaneous transitions. The spontaneous emission radiation from a higher to lower energy levels is represented as

$$N_y(t)/\ \tau_{yx} \tag{3.6}$$

which is proportional to the population in the higher y-th energy level. On the other hand, the stimulated transition is represented by

$$\frac{\sigma_x}{\hbar\omega} I(t)N_x(t) \tag{3.7}$$

for absorption from the x-th energy level, and

$$\frac{\sigma_x}{\hbar\omega} I(t)N_y(t) \tag{3.8}$$

for emission from the y-th energy level to the x-th energy level.

Note that the last term in the right hand side of Equation 3.3, which involves the electron recombination rate from E_c to E_i can be omitted. This simplification is justified as electrons that relaxed to the excited subbands before further relaxing to the ground subbands are indistinguishable from those electrons that relaxed directly from the continuum band to the ground subband. This is due to the large difference in the lifetimes between τ_{c0} and τ_{i0}. As a result, the actual occupation time of electrons in the continuum band may be a composite of τ_{ci} and τ_{c0}. In addition, further simplification can be achieved by omitting the stimulated term from the continuum band to the excited subbands (fourth term in Equation 3.3). This omission can be made since the free electrons in the continuum conduction band were captured in the barrier and optical transition back to the excited subbands should be minimum due to the spatial separation of the electron states. Our simulation further shows that there is no significant difference in omitting this term.

By solving the three rate equations simultaneously, we obtain the populations at each energy subband. An example of solution to the rate equations is depicted in Figure 3.16. As clearly shown in the figure, the electron population in the ground level is decreased while the electrons are pumped to the excited subbands. Portions of the electrons are further excited to the continuum band. The population at E_c clearly has a longer relaxation time as compared to those of populations at E_0 and E_c.

Equation 3.9 models the transmission change of the probe signal as a function of time delay between the pump and the probe signal, where K is an arbitrary constant.

$$S(t_d) = \int_{-\infty}^{+\infty} K \cdot I(t_d - t) \cdot \exp\left[-\left\{\sigma_0\left(N_0(t) - N_i(t)\right) + \sigma_i\left(N_i(t) - N_c(t)\right) + \sigma_c\left(N_c(t)\right)\right\}\right] dt \tag{3.9}$$

The pump and probe pulses in our pump-probe experiment are of the same origin albeit different intensity. The absolute value of the intensity is not relevant since only the change in transmission relative to the time delay is of interest. Hence, the probe pulse after a time delay of t_d with respect to time t of the pump pulse will have the same wavelength, pulse duration, and pulse shape as the pump pulse.

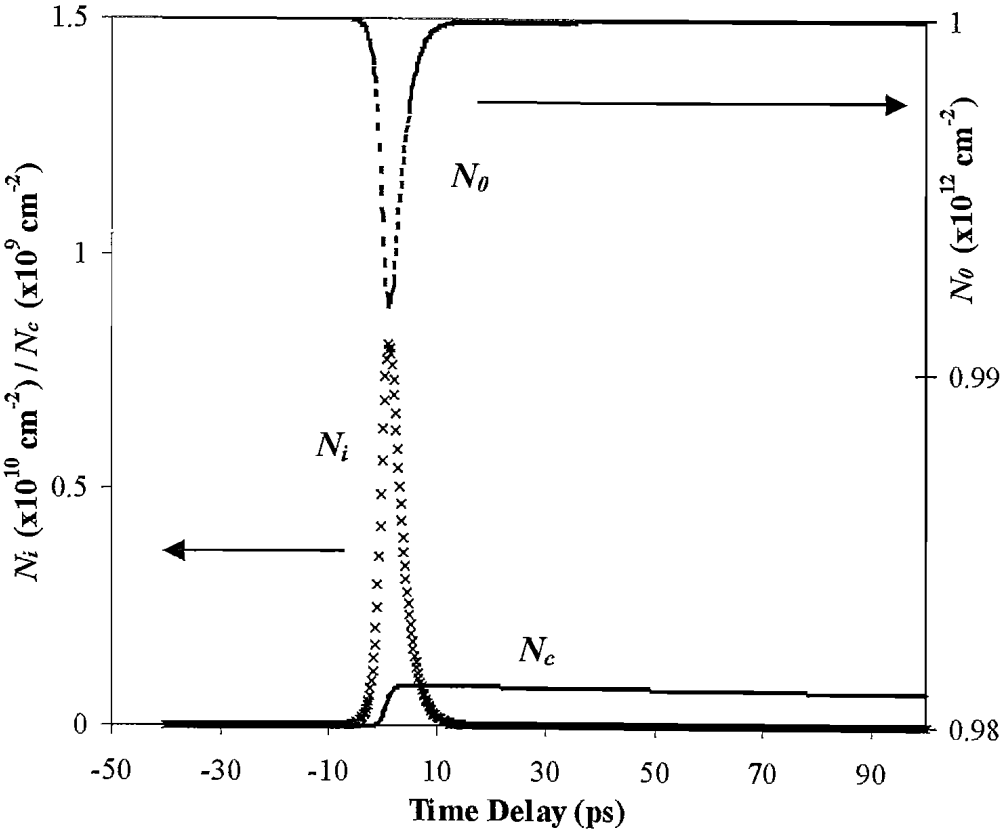

Figure 3.16. Modelled electrons populations in ground energy level N_0 (dashed line, right axis), excited subbands energy level N_i (crosses, left axis), and continuum conduction band energy level N_c (solid line, left axis), as a function of time delay between the pump and probe pulses. Note that the values are plotted on different scales.

3.5.2 Modelled result

With the parameters listed in Table 3.2, the experimental result for both samples M2193 and RMB1564 were fitted using this model, as shown in Figure 3.17. The total population of the electrons per unit area was taken as equal to the dopant concentration of the samples. For the intersubband absorption cross-section of the ground to excited subband (σ_0), a value of 2.6×10^{15} cm^2 was estimated:

$$\sigma_0 = \frac{-\ln(0.95)}{d_{eff} N_d} \tag{3.10}$$

where 5 % of absorption strength was assumed, $N_d = 2 \times 10^{17}$ cm^{-3} is the electron doping density, and d_{eff} is the effective MQW thickness. For a 50 period MQW structure, d_{eff} is taken as 3 μm divided by the refractive index (~3.1). On the other hand, the ratios of the cross-sections with respect to the ground subband for the excited

Parameters	Symbols	Sample M2193 values	Sample RMB1564 values
Total population	N_0	1 x 10^{11} cm^{-2}	1 x 10^{12} cm^{-2}
Cross section in E_0 to E_i absorption	σ_0	2.6 x 10^{-15} cm^2	2.6 x 10^{-15} cm^2
Cross section in E_i to E_c absorption	σ_i	0.8 x 2.6 x 10^{-15} cm^2	0.8 x 2.6 x 10^{-15} cm^2
Cross section in E_c absorption	σ_c	150 x 2.6 x 10^{-15} cm^2	150 x 2.6 x 10^{-15} cm^2
Intersubband electron lifetime	τ_{i0}	1.8 ps	2.5 ps
Continuum band to ground subband lifetime	τ_{c0}	550 ps	700 ps
Pump wavelength	λ_ω	10.6 μm	9.35 μm
Pump pulse width	τ_ω	0.7 ps	0.7 ps

Table 3.2. Parameters and corresponding values used in the rate equation model for fitting the pump-probe measurement data for sample M2193 and RMB1564. N_0 is taken as the dopants sheet density of the samples. σ_0 is estimated assuming 5% absorption strength. Note that the fit is only sensitive to the relative values of σ_i/σ_0 and σ_c/σ_0. The two lifetimes (τ_{i0} and τ_{c0}) of the experimental data are fitted using the model. Pump wavelength and pump pulse width are those used in the pump-probe experiment.

subband (σ_i/σ_0) and the continuum conduction band (σ_c/σ_0) were taken as 0.8 and 150, respectively. Since the absorption process in the continuum band is not confined to the two-dimensional process as in the subbands, the two orders of magnitude difference in the cross-section can be justified. Lastly, the experimental pump wavelengths and the FELIX pulse widths used in the respective measurements are also listed in Table 3.2.

The fitted result for both samples agrees reasonably well with the experimental data, except in the initial 100 ps region of the long decays (Figure 3.17.b and Figure 3.17.d). For sample M2193, the intersubband lifetime was fitted with a value of 1.8 ± 0.2 ps (Figure 3.17.a), wheareas the long decay lifetime was 550 ± 100 ps (Figure 3.17.b). Fitting of data from sample RMB1564 gave a 2.5 ± 0.2 ps intersubband lifetime (Figure 3.17.c) and a 700 ± 100 ps slow decay lifetime (Figure 3.17.d). It is noticeable that in all cases, the strong and long lifetime negative signal is always preceded by a short lifetime, positive signal. The unique feature of a short positive lifetime signal followed by a strong, negative long decay is clearly reproduced in the model. The model also shows that reducing the pump intensity will reduce, and eventually eliminate the long decay lifetime signal, as shown in Figure 3.18, which is in consistent with the

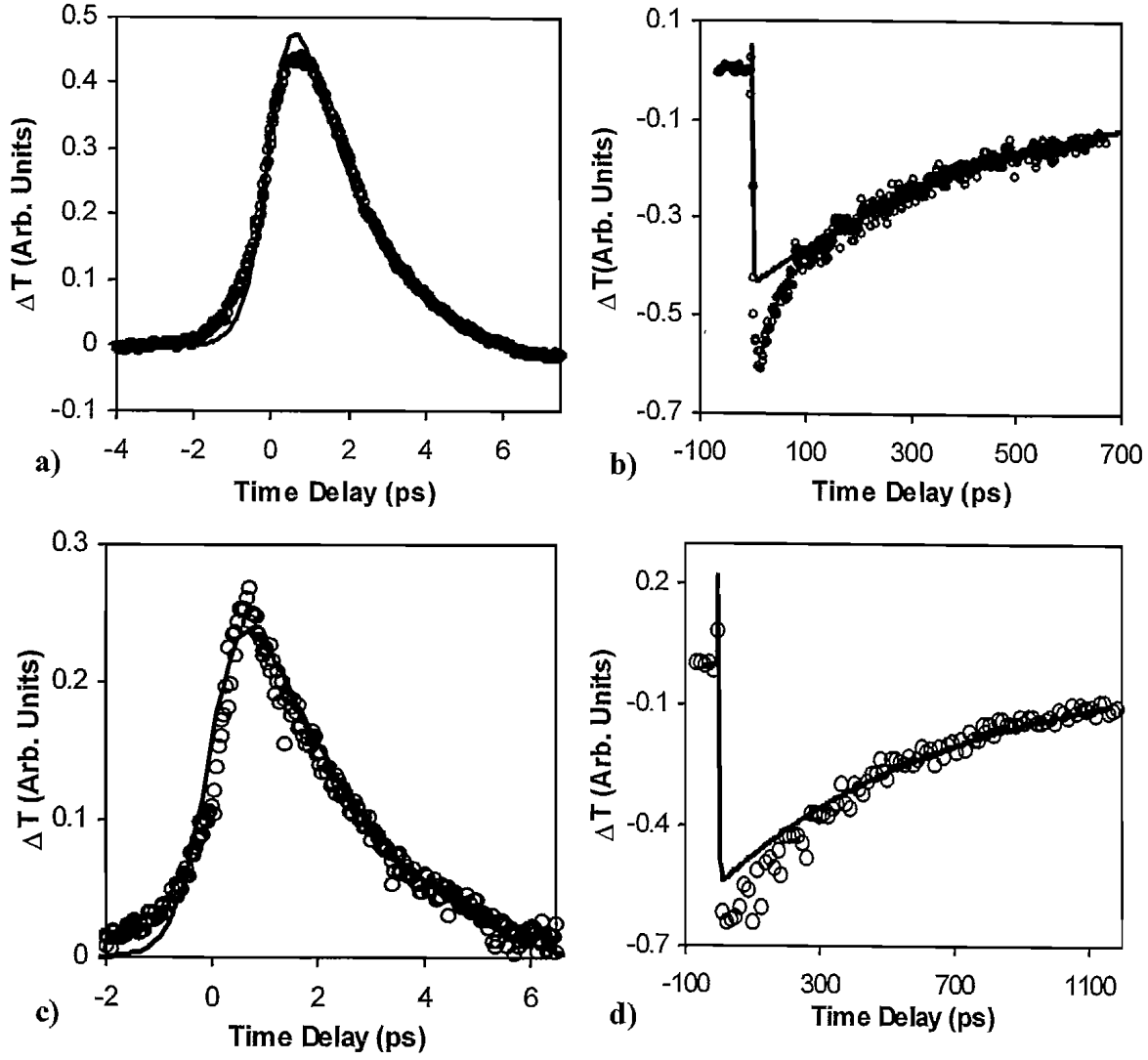

Figure 3.17. The pump-probe intersubband lifetime measurement (circles) for sample M2193 with the solid lines fitted using the rate equation model with intersubband lifetime of 1.8 ps (a) and the slow decay fitted with a lifetime of 550 ps (b). The corresponding intersubband lifetime for sample RMB1564 is 2.5 ps (c) with a 700 ps (d) slow decay lifetime.

experimental data. The direction of the arrow indicates increasing pump intensity. Hence, the model is consistent with our argument that a TPA process is involved, which in turn requires a high pumping intensity.

Although in multi-parameter fits of this type caution must be employed, the parameters τ_{c0} and τ_{i0} are sensitive in the fit and can be reliably determined in the model. In contrast, the model is insensitive to σ_c, σ_i, and σ_0, but the ratios between them are more reliably determined. In some cases (e.g. Figure 3.17.b and Figure 3.17.d), there is evidence of a two-component decay (τ_2 and τ_3 in Figure 3.12) to the absorption signal whose detailed origin is unknown. This observation however is not apparent for other

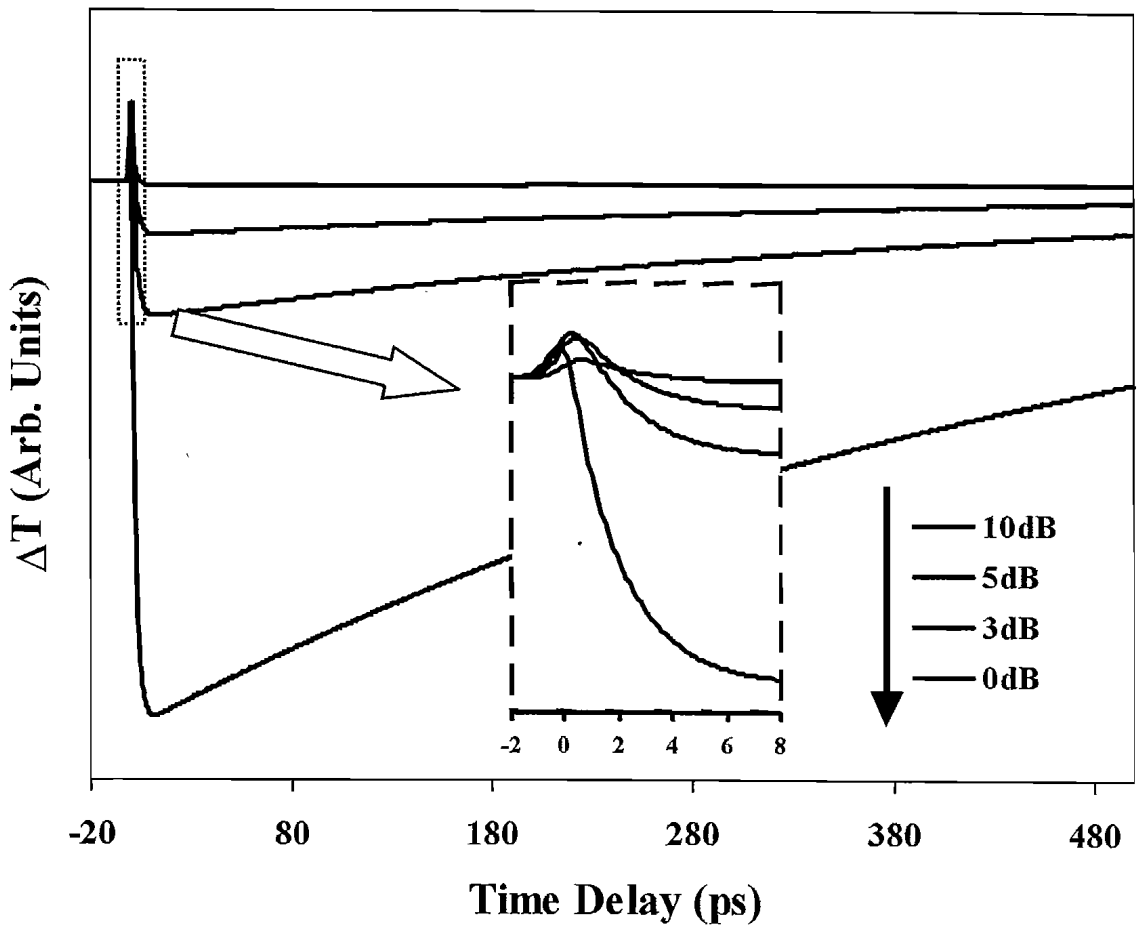

Figure 3.18. Simulated pump-probe signals with varying pump intensities using the 3-level rate equation model. The direction of the arrow indicates increasing pump intensity for the plotted lines. When large attenuation is introduced, the strong negative signal disappears. The inset shows the positive signals near zero time delay.

cases, e.g. those in Figure 3.5. The two-time-constant decay is most strongly observed for strong, on-resonance pumping.It is thus probably associated with the dynamics of the electrons in the disturbed barrier potential (Figure 3.6) when a significant fraction of the population is transferred (i.e. saturation is approached).

3.6 Conclusion

In this chapter, measurements of the lifetime of our MQW samples were described. We have conducted the pump-probe measurement with the FELIX free electron laser. The measured intersubband lifetime of our stepped well structures, of the order of a few picoseconds were in general slightly longer than the reported values for subband separation greater than the LO phonon energy. This is understandable due to the smaller wavefunction overlap of the second excited subband and the ground subband

compared to the overlap between the second and first excited subbands. Consequently, the excited electrons in the second excited subband would favour the slower transition to the first excited subband. These measured lifetimes also suggested that population inversion is possible between the second and first excited subbands. Hence, the measured lifetime is in general agreement for the FIR laser. Provided that other optical and free carrier losses are kept low, then the laser build up is possible with the pulsed CO_2 laser as a pump source.

In addition, due to the deformed conduction band for structures with modulation doping at the barrier, long decay absorptive signals have been observed in some of the samples at high excitation intensities. Two-photon absorption process (or higher order multi-photon absorption in some cases) is believed to have caused this long decay signal, in samples that were modulation doped at the barriers. At high pump intensities, the excited electrons at the higher subband energy levels were further pumped to the continuum subband. The donor in the barriers recaptured some of these electrons before they were ionised and returned to the QW. A rate equation model was constructed based on the two-photon absorption process. Modelled results agreed well with the experimental data. In the lifetime fitting in section 3.5, only the relative change of transmission is of concerned. Any other temperature dependent factors, e.g. electron mobility, are of secondary importance.

Multi-photon absorption is highly undesirable and may contribute to higher pump threshold of the FIR laser system. The experimental result has improved our understanding of the FIR MQW structure. As a direct contribution from the pump-probe experiment, the doping method in the structure was changed, from doping at the central barrier to the edge of the stepped well. It was found that the modulation doping at the barrier could cause serious deformation to the QW energy profile, especially at high doping density. This is highly undesirable, as the electron sheet density required in FIR lasers is substantially high ($\sim 10^{12}$ cm^{-2}). Electrons trapping in the parasitic wells in the barrier of deformed conduction band can further reduce the gain of the laser structure. High free carrier loss may also result from these electrons.

On the other hand the design with doping at the stepped well edge has shown an improved performance. The arguments of this design have been discussed in Chapter 2. Further measurements with the new structure have shown that the two-photon absorption process due to the trap carriers in the barrier has been eliminated. However,

the pump-probe measurement showed an additional lifetime component that may be due to the relaxation of electrons trapped in the step well.

Moreover, an experiment to observe FIR photoluminescence signals from the doped stepped well structure shows encouraging results. We are unable to definitely confirm the observed signal as intersubband emissions due to the lack of polarisation data from the emitted signals. Simple analysis of the emitted signal using a combination of filters reveals that the wavelength of the luminescence signal is consistent with the subband energy difference of the structure. This observation can be seen as an important step towards realising a laser.

4 Mode overlap with the QW layers

Achieving a good optical mode overlap with the active area has been a fundamental problem in optically pumped QW terahertz lasers [31, 51]. Firstly, there is a huge difference between the pump and laser wavelengths. The former is normally a CO_2 laser at 10.6 μm, while the latter can operate anywhere between 30 and 300 μm. This makes it very difficult to obtain good overlaps between both the pump and laser modes with the active layer of the laser when they operate in a single mode as is desirable. Secondly, due to considerations of morphology and uniformity [32, 48] and the cost of wafer growth, QW structures grown by the MBE technique are normally limited to an epitaxial thickness of ~10 μm as compared to a typically 350 – 500 μm thick substrate. Hence the overlaps of the modes at both wavelengths with the active layer will inevitably be very low unless some method of confinement is used. Thirdly, the grown epi-layers are of course always on the surface. This makes the mode overlap even poorer since the peak intensity of the mode is not near the active area. Although thinning the substrate can mitigate the second and third difficulties, the mechanical strength of the laser device will deteriorate and handling becomes difficult. Generally, a key issue for a single slab device is its poor mode overlap due to a thin and superficial QW layer grown on a substrate.

In addition, the refractive index of the GaAs substrate is higher than the average value of the MQW active layers. This presents a further complication as compared to the dielectric waveguide used in conventional semiconductor lasers at shorter wavelengths. Traditionally, the mode confinement for these lasers relies on the small difference in the refractive indices in the active layers and the surrounding cladding layers, or the substrate. The confined mode dimension is roughly proportional to the effective wavelength, which is the free space wavelength divided by the refractive index of the structure. Consequently, this will result in the growth of very thick core of active and cladding layers for FIR devices, in the order of 10 μm. This thickness is at the growth limit of most present growth facilities for a good quality wafer. It is thus clear that the usual methods used successfully for the mode confinement in shorter wavelengths are not applicable for the FIR region. As mentioned previously, the free carrier loss, which is proportional to λ^2, is much higher for long wavelength lasers. Therefore it is crucial that the FIR laser mode is confined effectively while keeping the modal loss low. This

chapter will discuss further the methods that may improve the mode overlap and confinement in the FIR lasers.

4.1 Stacked double QW slabs

A novel design is proposed, which mechanically overlays a laser slab on another identical slab such that the QW sides of the two laser slabs are facing each other. The layout is illustrated schematically in Figure 4.1, showing the pump excitation and the lasing emission directions. A CO_2 laser is used to excite the shorter side of the stacked samples. THz emission is perpendicular to the pump beam, but concentrated at the front edge of the MQW samples near the pump side, as the gain is the highest there. Such a mechanical juxtaposition is only feasible because no electrical currents are required to flow across the mechanical boundary, and any gaps caused by irregularities on the

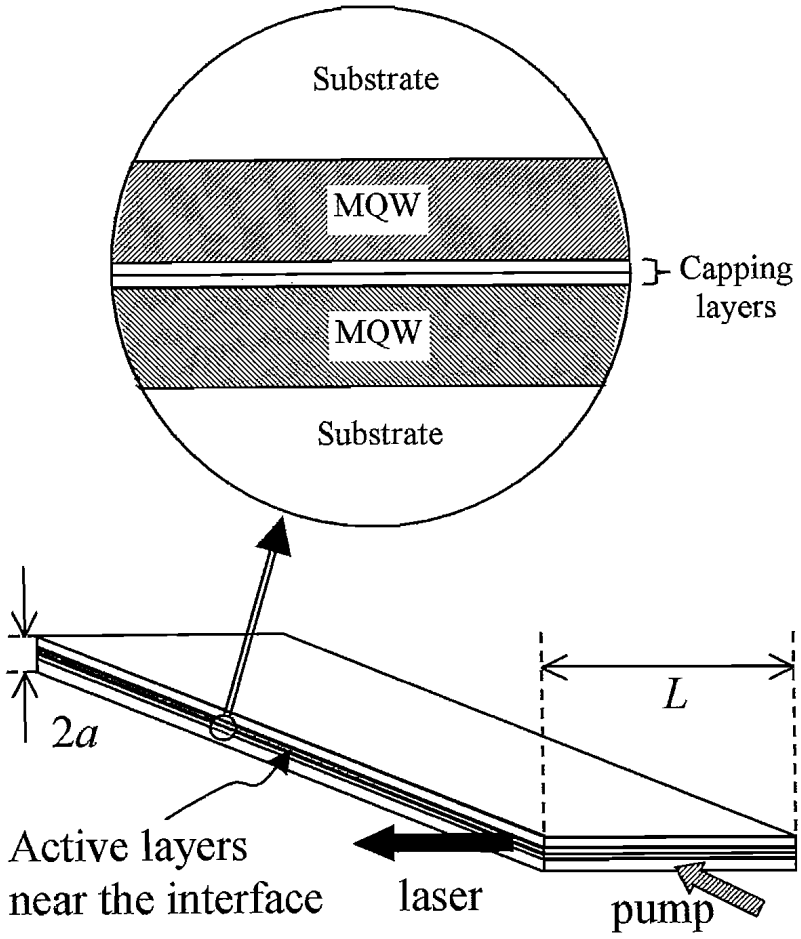

Figure 4.1. Double, stacked MQW slabs pumping scheme, showing the direction of the optical pumping excitation and resulted laser emission directions. As shown in the diagram, the laser cavity has a length *L*, which is the width of the MQW slab. Each of the MQW slab has a thickness *a*. The inset shows a closed up view of the cross sections.

	Design factors	Single slab (thinned)	Stacked (not doped)	Stacked (doped)	Stacked (not doped but thinned)
i	**Laser TE_0 mode overlap**	9.8 %	1.9 %	68.2 %	28.8 %
ii	**Free carrier loss (dB/cm)**	- 34	- 35	- 903	- 26
iii	**Transmission product of (i) and (ii)** [a]	0.02	0.004	$\sim 10^{-9}$	0.09
iv	**Misalignment tolerance**	N/A	~ 4 μm	~ 1 μm	[b]
v	**Durability**	Poor	Good	Good	Poor
vi	**Fabrication complexity**	High	Low	Low	Very high

Table 4.1. Several design factors for a single slab with substrate thinned, two stacked slabs with doped layers, two stacked slabs without doped layers, as well as two stacked slabs with substrate thinned to a thickness of 15.75 μm. In these calculations, the thickness of the MQW layers is assumed to be 3 μm thick. The overlap value of single slab with thinned substrate is obtained using the same criteria as the two stacked slabs case. The total thickness of the slab is assumed to be 300 μm for the un-thinned cases.

[a] This is calculated as the product of mode overlap and the roundtrip transmission ratio, $\exp(-2\alpha L)$ where the chosen cavity length, L = 1 mm and α is the absorption coefficient for the sample. A higher value indicates a lower threshold for laser action.

[b] The thinned slabs are only 15.75 μm thick for each slab, which is comparable with the laser wavelength. Hence, the diffraction loss cannot be calculated here with the diffraction integral method. The misalignment tolerance is estimated to be between 1 - 4 μm based on the mode confinement ratio as compared to the other cases.

surfaces will be far smaller than the CO_2 laser and far infrared wavelengths involved, and thus optically negligible. Consequently the QW layers are situated near the centre of the stacked slabs and the thickness of the active layer is doubled. This overcomes the previous drawbacks with a single slab. These two slabs can be held together either mechanically or, for example by direct wafer bonding [117, 118]. The overlap between the QW active layers and laser mode is however very poor, estimated in the order of a few percent. Clearly this overlap ratio is not very attractive and further improvements can be made. However, this scheme does have an advantage that the free carrier loss is small, calculated to be - 35.4 dB/cm for a structure described in Table 4.1.

Alternatively, as mentioned earlier in this chapter, thinning the substrate of the MQW slabs can improve the laser mode overlap with the active layer. As shown in Table 4.1,

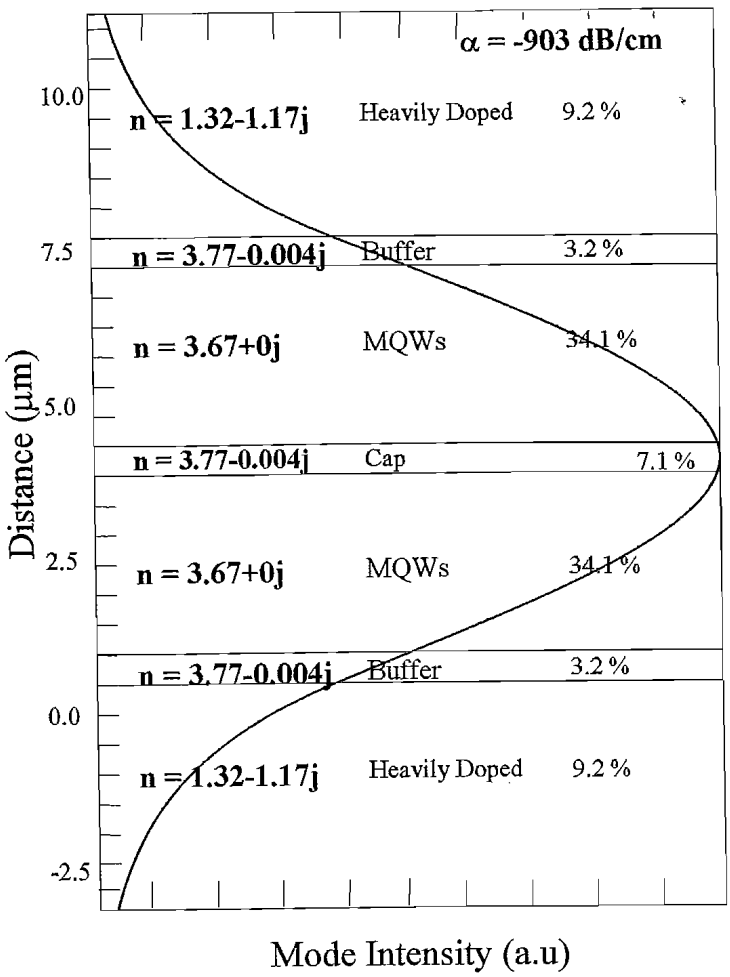

Figure 4.2. Laser mode intensity profile for a double, stacked MQW slabs pumping scheme at 60 μm, with plasmon enhanced heavily doped GaAs layers. The large overlap of the mode with the lossy doped layers result in a high value of modal loss.

an improvement of three times in the ratio of laser mode overlap for the terahertz TE_0 mode by stacking the thinned slabs is achieved.

The waveguide confinement can be enhanced by growing a doped layer on top of the substrate, just before the buffer and MQW layers. In this case, the plasmon enhanced mode overlap can be greatly improved as can be seen in Figure 4.2. The refractive index for the MQW layers is taken as the average value [100, 119] since at the wavelengths involved, the thickness of each individual QW layer is much less than the pump or laser wavelength.

This confinement method utilises the changes in the refractive index of the doped layer near the corresponding plasma frequency at the doping concentration. Refractive index values in the doped layers are calculated by use of the standard plasmon and phonon oscillator model [66], which will be discussed further in the following sections. The

doping concentration for the layer acting as enhanced plasmon confinement is at 3×10^{17} cm^{-3} for this example. Although the confinement factor is very good, the modal loss is too high due to a large mode overlap with the doped layers. If heavier doping is used, then the structure will suffer an even stronger loss although greater overlap can be gained. This loss mainly results from free carrier absorption at the heavily doped layer. With such value of mode loss, it is thus impractical to use this doped layer for the waveguide.

4.2 Surface plasmon waveguide

Sirtori et al [120] first suggested the use of surface plasmon in the waveguide for their mid-infrared QCL structures. Metals were used as the guiding layers, owing to their negative real part of the dielectric constant. For a heavily doped semiconductor, the real part of the complex dielectric constant becomes negative, rather similar to a metal at infrared wavelengths. We shall first discuss the formulation of the complex refractive index in semiconductors. Then, the proposed design based on surface plasmon guided structures will be introduced.

4.2.1 Complex refractive index of a doped layer

The refractive index of a doped semiconductor is altered when the carrier concentration is modified due to the changes to the material carrier effective mass, mobility and the associated plasma resonance. Hence, it is essential to be able to have a good estimate of the refractive index of the doped semiconductor before the associated changes are utilised for guiding the laser emission. A model is built for refractive index calculation for doped GaAs, based on the following discussions.

The complex dielectric constant of n-type GaAs can be described by a classical Drude model [66]:

$$\begin{aligned}\varepsilon(\omega) &= \{n(\omega) - j\kappa(\omega)\}^2 \\ &= \varepsilon_\infty\left(1 + \frac{\omega_L^2 - \omega_T^2}{\omega_T^2 - \omega^2 + j\omega\gamma_{ph}} - \frac{\omega_p^2}{\omega(\omega - j\gamma_{pl})}\right)\end{aligned} \tag{4.1}$$

where ε_∞ is the high frequency dielectric constant, ω_L and ω_T are the angular frequency of the LO and transverse optical (TO) phonons respectively, γ_{ph} and γ_{pl} are the damping constants of the phonons and the plasmons respectively in units of angular frequency,

and ω is the angular frequency. The complex refractive index $\boldsymbol{n}(\omega)$, is simply the square root of Equation 4.1, where $n(\omega)$ and $-\kappa(\omega)$ are the real and imaginary parts of the refractive index. $\kappa(\omega)$ is also commonly referred to as the extinction coefficient as it represents an absorption (or attenuation) of the electromagnetic wave. This attenuation is best described by the attenuation coefficient α, which is related to the extinction coefficient by:

$$\alpha = \frac{4\pi\kappa}{\lambda} \tag{4.2}$$

The plasma frequency is expressed as

$$\omega_p^2 = \frac{N_d e^2}{m^* \varepsilon_\infty \varepsilon_0} \tag{4.3}$$

where N_d is the doping density of the doped layer in inverse volume, e is the electron charge, and ε_0 is the permittivity of vacuum. The damping constant for the plasmon is obtained from

$$\gamma_{pl} = \frac{e}{\mu m^*} \tag{4.4}$$

where μ is the electron drift mobility, and m^* is the effective electron mass. The parameters [100] used in our calculations are listed in Table 4.2.

Parameters	Values
ω_L	292.1 cm^{-1}
ω_T	268.7 cm^{-1}
γ_{ph}	2.4 cm^{-1}

Table 4.2. Parameters used in the Drude model to calculate the complex refractive index of doped GaAs layers.

The electron mobility and effective electron mass are both dependent on temperature and doping density [85, 92, 121, 122]. The electron mobility values have been extracted from the literature. The same calculation for the carrier concentration dependent effective mass as described in Chapter 2 is utilised here. Table 4.3. lists the complex

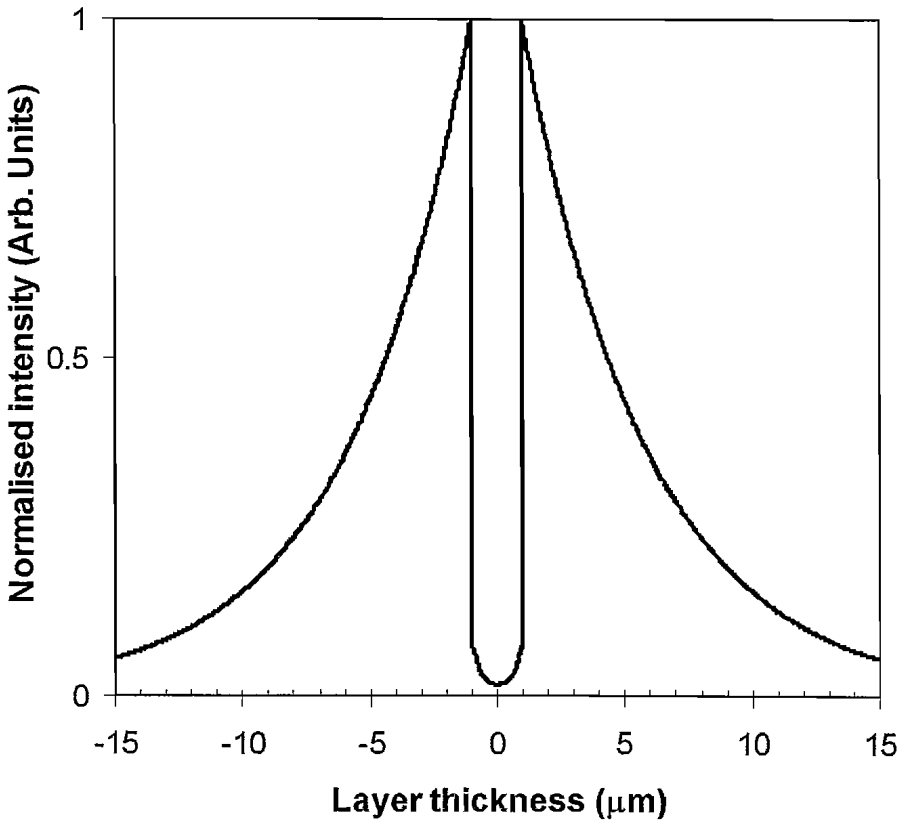

Figure 4.3. Normalised optical mode profile at $\lambda = 60$ μm for a surface plasmon guided mode. A 2 μm heavily doped GaAs layer ($N_d = 5 \times 10^{18}$ cm^{-3}) in the middle is sandwiched between undoped GaAs layers. The mode intensity decays rapidly away from the semiconductor and heavily-doped interface in the heavily doped layer. Conversely, the decay is at a much slower rate in the semiconductor layers.

refractive index at 60 μm of the doped layers at selected temperatures and doping concentrations.

At heavy doping levels, the imaginary part of the complex refractive index of the semiconductor becomes large as compared to the real part, i.e. $k \gg n$. By combining a heavily doped layer with the active layers, which have opposite sign in the dielectric constants, the surface plasmon at the interface can guide the FIR laser emission. The surface plasmon modes are TM polarised, and decay exponentially away from the interface between the two layers [123, 124]. The mode decays more rapidly in the heavily doped layer than in the semiconductor layer, as shown in Figure 4.3. This ensures that the resulting mode loss is small even though the extinction coefficient in this layer is very large. In other words, the penetration of the mode into the heavily doped layer is rather small as compared to that into the dielectric semiconductor layers.

	T = 77 K	T = 300 K
m_0^*/m_0	0.0665	0.0635
E_G	1.51 eV	1.42 eV
ε_∞	10.70	10.98
μ		
($N_d = 3 \times 10^{17}$ cm^{-3})	3600 cm^2/Vs	3800 cm^2/Vs
($N_d = 2 \times 10^{18}$ cm^{-3})	2400 cm^2/Vs	2400 cm^2/Vs
($N_d = 5 \times 10^{18}$ cm^{-3})	2100 cm^2/Vs	2000 cm^2/Vs
$n - j\kappa$ ($\lambda = 60$ μm)		
($N_d = 3 \times 10^{17}$ cm^{-3})	1.323-1.171j	1.293-1.238j
($N_d = 2 \times 10^{18}$ cm^{-3})	1.537-8.270j	1.611-8.397j
($N_d = 5 \times 10^{18}$ cm^{-3})	2.285-13.120j	2.458-13.187j

Table 4.3. Complex refractive index of doped GaAs layers, for the corresponding temperature and doping concentration, together with the values for m_0^*/m_0, E_G, and μ. Values for μ at T = 77 K are extracted from Sanborn B A, 1995, *Phys. Rev. B*, 51 (20) pp. 14256-14264, and at T = 300 K from Sze S M, 1969: '*Physics of Semiconductor Devices*' (John Wiley & Sons, New York), pp. 40.

To date, surface plasmon and double surface plasmon waveguides have been demonstrated for devices emitting in the FIR region [39, 125]. These devices have shown low modal loss while keeping a reasonable confinement or overlap factor. A transfer matrix model is constructed to compute the confined TM mode in surface plasmon guided structures. This model will be described later in this chapter in section 4.3.

4.2.2 Surface plasmon mode for the double-stacked slabs

Following the idea of overlaying two slabs for our FIR system, a heavily doped layer is included between the substrate and the active layers to achieve a surface plasmon guided structure. Figure 4.4 shows the mode intensity profile of such a double-stacked slab FIR laser system at 60 μm. Note that the mode intensity always decay away from the interface between the semiconductor and doped layers, in consistent with the mode profile in Figure 4.4. The surface plasmons existing at the two doped layers interfaces merge into a single mode, resulting in the apparent minimum in the centre of the mode.

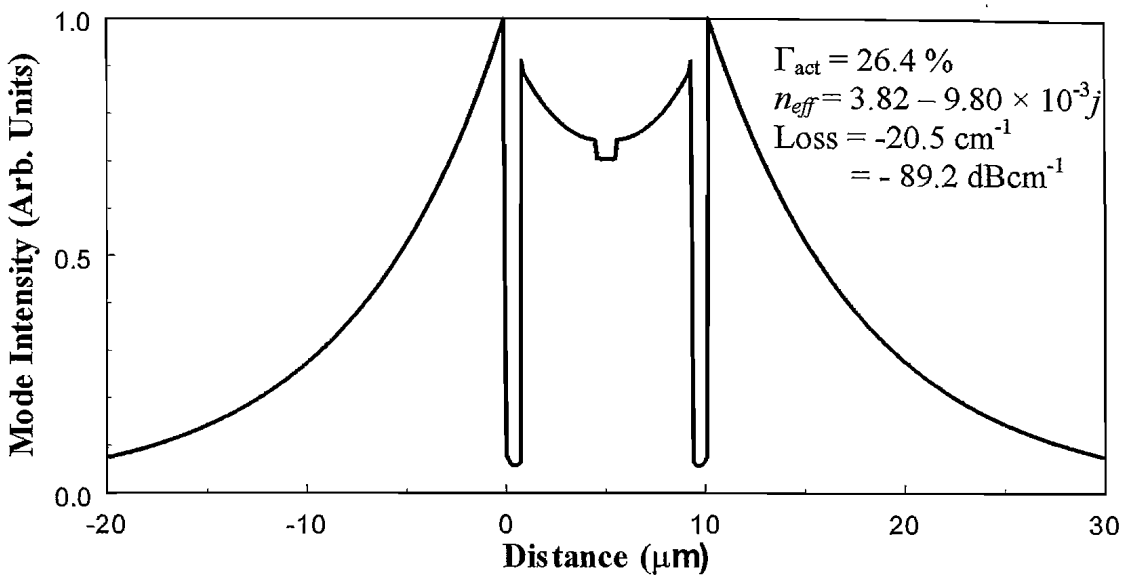

Figure 4.4. Normalised mode intensity profile for a surface plasmon guided, double-stacked slabs FIR laser system at $\lambda = 60$ μm. The abscissa origin is at the interface of the substrate and the buffer layer of the bottom slab. The resulting modal loss and confinement factor Γ_{act} are –89.2 dBcm^{-1} and 26.4 % respectively. Note that we have taken the active area as the two MQW layers, i.e. layer 3 and layer 5, in this case.

This structure assumes that there are 60 QW periods in each slab, which are doubled when the two slabs are stacked. As described earlier in this chapter, the slabs are identical in design. Table 4.4 lists the corresponding parameters and resulting overlap factors of the individual layer for this structure. The confinement of this mode is provided by the 750 nm thick heavily doped, $N_d = 5 \times 10^{18}$ cm^{-3}, GaAs layers on each of the slabs. The refractive index at this doping level is calculated using the Drude model described previously.

The level of doping concentration and layer thickness are chosen such that a reasonably good confinement factor (> 20 %) is achieved while keeping the modal loss at a sufficiently realistic figure. In general, the confinement factor and modal loss both increase with the doping concentration. On the other hand, the thickness of the doped layer is also found to affect the overall mode confinement. If the doped layers thickness is increased, then confinement is improved. However the corresponding modal loss is also dramatically increased. A modal loss of – 89.2 dBcm^{-1} and a confinement factor of 26.4 % are computed in this case. These figures are very favourable values for a FIR system, and comparable to the reported values elsewhere [39, 125, 126].

i	Waveguide Layer	Layer thickness, d_i (μm)	Refractive index, n_i	Overlap factor, Γ_i (%)
0	GaAs substrate (bottom slab)	-	$3.77 - 4.0\times 10^{-3} j$	34.6
1	GaAs heavily doped layer, $N_d = 5 \times 10^{18}$ cm-3	0.75	$2.29 - 13.12 j$	0.2
2	AlGaAs buffer layer	0.10	$3.64 - 4.0 \times 10^{-2} j$	0.4
3	MQW active layers	3.71	3.67	13.2
4	GaAs top capping layers for both slabs	1.00	$3.77 - 4.0 \times 10^{-3} j$	3.2
5	MQW active layers	3.71	3.67	13.2
6	AlGaAs buffer layer	0.10	$3.64 - 4.0 \times 10^{-2} j$	0.4
7	GaAs heavily doped layer, $N_d = 5 \times 10^{18}$ cm-3	0.75	$2.29 - 13.12 j$	0.2
8	GaAs substrate (top slab)	-	$3.77 - 4.0 \times 10^{-3} j$	34.6

Table 4.4. Refractive indices, thickness and their corresponding overlap factors for the waveguide structure where the modal profile is shown in Figure 4.4.

4.2.3 Surface plasmon waveguide for a metal-dielectric-doped-layer

A metal layer coated on top of the surface of semiconductor epitaxial layers has been utilised successfully for surface plasmon guided mid-infrared QC lasers [120, 127, 128]. Nevertheless, a single sided surface plasmon waveguide does not provide a very effective confinement for FIR emission. A way to improve the waveguide is by embedding an additional doped layer between the active layer and the substrate. Hence, a layer of gold can be coated on top of the surface of the structure used in the previous section to realise this scheme. The refractive index of gold and certain metals FIR wavelength have been measured previously [129, 130]. A comparable waveguide performance can be obtained, as shown in Figure 4.5. The mode is well confined in the active layer, together with a decaying mode profile in the substrate. Again, a similar argument on modal loss versus the confinement factor is applicable as to the choices of doping concentration and thickness of the doped layer. The figure of merit $\Gamma_{act} \times e^{-2\alpha L}$ is 1.25×10^{-3} for this case, as compared to the double-stacked slabs of 4.38×10^{-3}. Similar structures with comparable performance have been demonstrated in THz QC lasers recently [39, 125].

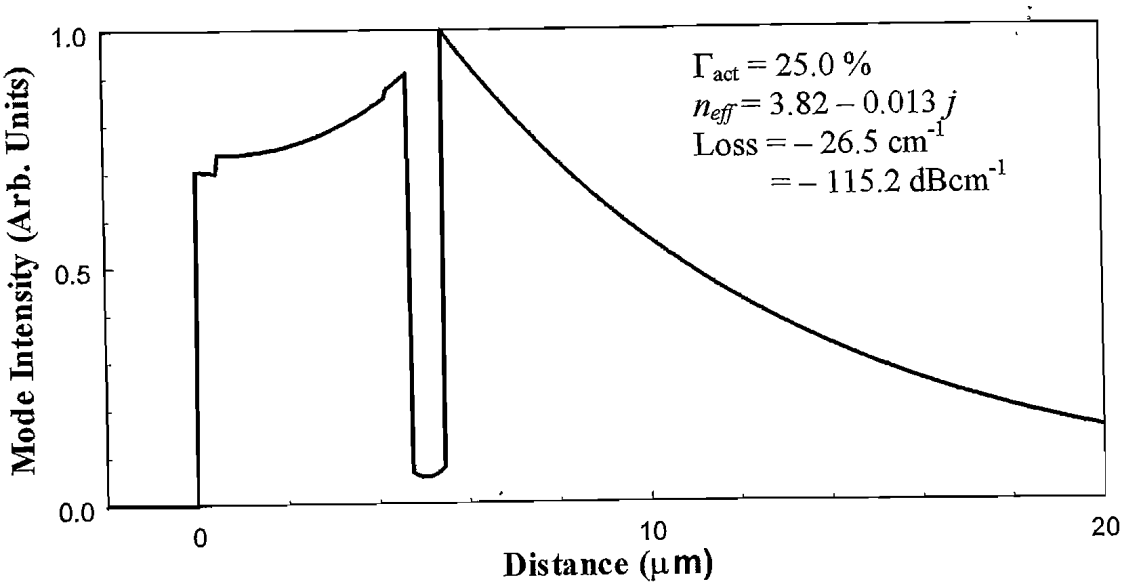

Figure 4.5. Mode intensity profile for a gold-MQW-doped layer-substrate surface plasmon waveguide laser structure. The abscissa origin is at the interface of the gold-semiconductor layer. Comparable performance to the double-stacked scheme can be achieved.

Both of the surface plasmon guided designs offer device performance that is more attractive compared with the cases shown previously in Table 4.1, after considering the other design issues. These issues include the complexity of the device fabrication and durability of the device. Nevertheless, the surface plasmon guided double stacked slabs scheme with heavily doped layers have twice the number of active MQW layers compared to the single slab (metal-dielectric-doped-layer) surface plasmon scheme. This effectively doubles the gain achievable from the laser device, which is very advantageous. All things considered, the surface plasmon guided double stacked slabs scheme with heavily doped layers is believed to offer the best design compromise.

4.3 Transfer matrix model for a planar waveguide

A 2 × 2 transfer matrix model is built and utilised to numerically evaluate the optical TM mode of the general multilayer MQW waveguide structures, including the surface plasmon guided mode. This transfer matrix technique is a very convenient method to solve for the mode solutions in multilayer semiconductor planar waveguide system [123, 131]. For any multilayer waveguide structure, the system transfer matrix M_T, can be formulated by the product of each of the individual layer transfer matrices, M_i. These transfer matrices describes the properties associated with the individual layers. Hence, this method allows us to specify the form of electromagnetic fields in each

medium of the waveguide, and consequently the mode profile of the waveguide. The model that was used to compute the confined mode in the previous section will be described.

4.3.1 Formulation of the transfer matrix

For a MQW structure, it can be considered as a planar, non-magnetic, and is made up of layers of different media. If the individual medium is assumed to have a constant refractive index, then the electromagnetic fields propagating along the z-direction for a TM mode can be taken as [123, 132]:

$$\begin{aligned} \boldsymbol{E} &= \boldsymbol{E}_0 e^{j(\omega t-\beta z)} \\ \boldsymbol{H} &= \boldsymbol{H}_0 e^{j(\omega t-\beta z)} \end{aligned} \tag{4.5}$$

where $\boldsymbol{E}_0 = (E_x, 0, E_z)$ and $\boldsymbol{H}_0 = (0, H_y, 0)$.

For the discussion that follows, the exponential phase dependence will be ignored and only the magnitude is considered. This model is based on a P-layer and P + 2 media multilayer system, where the transverse direction of the layers are along x-direction, as shown in Figure 4.6.

For $x \leq 0$, the first medium of the multilayer structure, the corresponding refractive index is denoted as n_0. The general solutions for $H_y(x)$ and $E_z(x)$ of the TM mode in this layer are

$$H_y(x) = C_0 \exp(K_0 x) + D_0 \exp(-K_0 x) \tag{4.6}$$

and

$$E_z(x) = \frac{jK_0}{\omega \varepsilon_0 n_0^2}\left(C_0 \exp(K_0 x) - D_0 \exp(-K_0 x)\right) \tag{4.7}$$

where K_0 is the transverse wavenumber in the medium. In which

$$K_0 = \sqrt{\beta^2 - n_0^2 k_0^2} \tag{4.8}$$

where β and k_0 are the mode propagation constant and the wavenumber for free space respectively.

For the following P layers, each layer has a thickness d_i and refractive index n_i, where the subscript i refer to the i^{th} layer in the structure. In other words, for $i = 1 \rightarrow P$ and Σ_i $d_{i-1} \leq x \leq \Sigma_i$ d_i, the modal fields of the i^{th} layer can be written as:

$$H_y(x)_i = C_i \sin(K_i x) + D_i \cos(K_i x) \tag{4.9}$$

and

$$E_z(x)_i = \frac{jK_i}{\omega \varepsilon_0 n_i^2}\left(C_i \cos(K_i x) - D_i \sin(K_i x)\right) \tag{4.10}$$

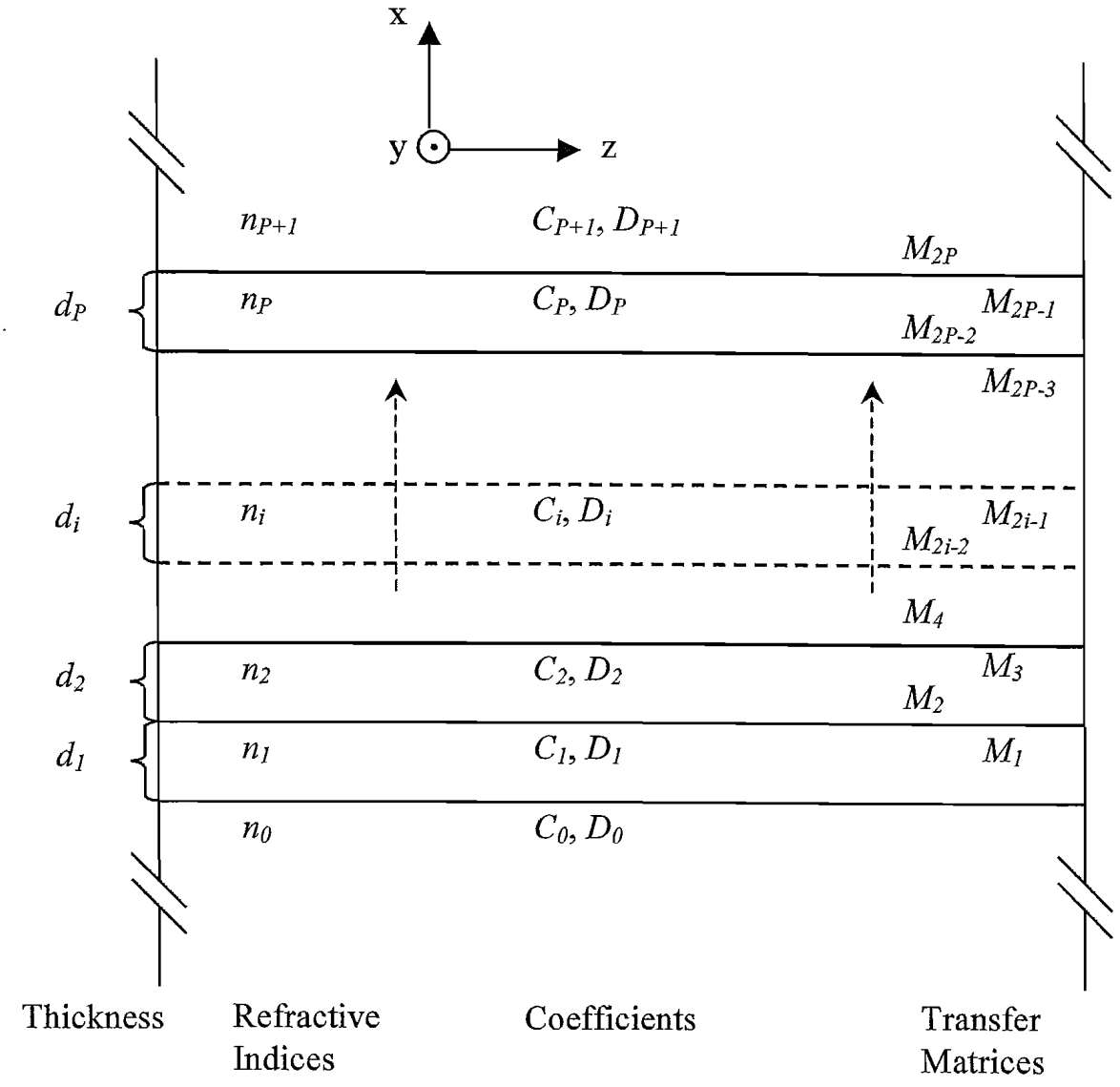

Figure 4.6. The P-layer, P + 2 media planar waveguide system with a transfer matrix approach, showing the associated refractive indices, the field coefficients, transfer matrices and the thickness of the layers.

where

$$K_i = \sqrt{n_i^2 k_0^2 - \beta^2} \tag{4.11}$$

and $d_0 = 0$. Note that the thickness of the first and last media need not be determined as they are considered to be indefinitely thick. Finally, the fields for the remaining medium with n_{P+1}, i.e. $x \geq \Sigma_{i=1\rightarrow P}\, d_i$ are

$$H_y(x)_{P+1} = C_{P+1}\exp(K_{P+1}x) + D_{P+1}\exp(-K_{P+1}x) \tag{4.12}$$

and

$$E_z(x)_{P+1} = \frac{jK_{P+1}}{\omega\varepsilon_0 n_{P+1}^2}\left(C_{P+1}\exp(K_{P+1}x) - D_{P+1}\exp(-K_{P+1}x)\right) \tag{4.13}$$

where

$$K_{P+1} = \sqrt{\beta^2 - n_{P+1}^2 k_0^2} \tag{4.14}$$

Now, the transfer matrices for each layer can be defined by matching the fields at the interface. As the fields must decay exponentially for a confined mode far away from the mode centre, D_0 can be set equal to zero. Furthermore, the value of C_0 can be arbitrary set to unity, as the absolute values of the field magnitudes are not important. Thus, substituting the value of C_0 will yield $D_1 = 1$ and $C_1 = K_0 n_1^2 / K_1 n_0^2$ by matching the field solutions at the first interface, i.e. at $x = 0$. It can be shown that, except for the first ($x = 0$) and final ($x = \Sigma_{i=1\rightarrow P}\, d_i$) layer interfaces, the corresponding transfer matrices for the interface between the i^{th} and $(i+1)^{th}$ layer are given by:

$$\begin{aligned} M_{2i} &= \begin{pmatrix} \sin(K_{i+1}x) & \cos(K_{i+1}x) \\ \dfrac{K_{i+1}}{n_{i+1}^2}\cos(K_{i+1}x) & -\dfrac{K_{i+1}}{n_{i+1}^2}\sin(K_{i+1}x) \end{pmatrix}, x = \sum_i d_i \\ M_{2i-1} &= \begin{pmatrix} \sin(K_i x) & \cos(K_i x) \\ \dfrac{K_i}{n_i^2}\cos(K_i x) & -\dfrac{K_i}{n_i^2}\sin(K_i x) \end{pmatrix}, x = \sum_i d_i \end{aligned} \tag{4.15}$$

As for the final layer interface, M_{2P-1} is simply the same as Equation 4.15 with $i = P$, but M_{2P} is given by

$$M_{2P} = \begin{pmatrix} \exp(K_{P+1}x) & \exp(-K_{P+1}x) \\ \dfrac{K_{P+1}}{n_{P+1}^2}\exp(K_{P+1}x) & -\dfrac{K_{P+1}}{n_{P+1}^2}\exp(-K_{P+1}x) \end{pmatrix}, x = \sum_{i=1\rightarrow P} d_i \tag{4.16}$$

With all the definitions of the transfer matrices in place, and after some simple manipulations the following relation is derived,

$$\begin{pmatrix} C_{P+1} \\ D_{P+1} \end{pmatrix} = M_T \begin{pmatrix} C_1 \\ D_1 \end{pmatrix} \tag{4.17}$$

where the transfer matrix for the whole system is simply the product of the matrices and inverse matrices given by:

$$M_T = \prod_{i=1}^{P} M_{2i}^{-1} M_{2i-1} \tag{4.18}$$

Once again, there must not be an exponentially growing field for $x \to \infty$. This boundary condition leads us to set the coefficient C_{P+1} to zero. If the elements of M_T are defined as

$$M_T = \begin{pmatrix} m_{11} & m_{12} \\ m_{21} & m_{22} \end{pmatrix} \tag{4.19}$$

then an eigenvalue equation emerges as:

$$m_{11} C_1 + m_{12} = 0 \tag{4.20}$$

Hence, this model solve for the root of Equation 4.20, which corresponds to the mode propagation constant β. It is this value that will lead to the solutions of all the individual field components of each layer. The modal profiles and loss can then be deduced, which is described in the next subsection.

4.3.2 Modal loss and overlap factor

It is often very convenient to express the confined mode of a waveguide in terms of the effective refractive index n_{eff}, which is defined as the ratio of the mode propagation constant over the free space wavenumber β/k_0. Moreover, the modal loss is related to the extinction coefficient of n_{eff}, as defined in Equation 4.2.

The level of confinement depends on the overlap factor of the mode intensity profile with the active or core area. The total power carried by a TM mode is given by,

$$P_{Total} = \frac{\beta}{2\omega} \int_{-\infty}^{+\infty} \left| \frac{H_y^2(x)}{\varepsilon(x)} \right| dx \tag{4.21}$$

The overlap of the mode for a certain layer is simply the ratio of the power confined in that layer to the total power. Hence, for the i^{th} layer, the overlap factor Γ_i is given as,

$$\Gamma_i = \frac{P_i}{P_{Total}} = \frac{\int_{d_{i-1}}^{d_i} \left| \frac{H_y^2(x)}{\varepsilon(x)} \right| dx}{\int_{-\infty}^{+\infty} \left| \frac{H_y^2(x)}{\varepsilon(x)} \right| dx} \tag{4.22}$$

Therefore, the confinement factor of a waveguide mode of a laser system is generally taken as the total overlap factor for all the active layers, the so-called waveguide core.

4.4 Cavity loss modelling

In practice, an epitaxially grown wafer is first cleaved into strips and then into small size slabs. Then, two slabs from the same strip will be stacked on top of each other to make a device. Hence, the two slabs used in the laser device for the stacked design are of the same width. However it is possible to misalign the two slabs axially when they are mounted for optical experiments. If this mismatch happens at the two facets acting as cavity mirrors transverse to the pump direction, it will naturally result in phase shift from the two misaligned reflecting facets. Consequently this will have an adverse effect on the mode diffraction loss. On the other hand, the misalignment in the pump direction, which is normal to the lasing direction, is unimportant, as the pump beam is absorbed and not resonated. In this section the tolerance to this cavity misalignment is estimated. This form of cavity, laterally split into two parts of equal length but displaced with respect to each other, has not previously been analysed to our knowledge. The loss sensitivity to the axial displacement is a critical issue with regard to the practicality of using such a stacking method.

The size of the misalignment however will very much depend on the technique used in aligning and placing the two slabs. As additional diffraction loss due to imperfectness in aligning the two MQW slabs may be a crucial factor in the laser gain threshold, it is thus vital that this loss is estimated. The model described here is based on the diffraction integral method first used by Fox and Li [133] to prove the existence of transverse modes in Fabry-Perot interferometers. In the following analysis, it is assumed that a GaAs/AlGaAs MQW slab with dimensions of $2.5 \times 1.0 \times 0.3$ mm^3 for

the length, width and the thickness respectively is used. Only the stacked design without the doped layers can be analysed with this model.

4.4.1 Diffraction integral model

Briefly, the method is analogous to propagating an electromagnetic wave back and forth within a resonator with two end mirrors. An arbitrary wave, a plane wave for example, is chosen and launched from one side of the cavity. According to diffraction theory, the resulting field in the other end of the mirror is related by an integral to that at the originating end. After many transits, a fundamental mode of the cavity can be obtained. On the contrary, all other higher order modes suffer a larger diffraction loss and quickly disappear. Once this fundamental mode is achieved, the propagating field will return to its original value after one round trip propagation, albeit differing by a complex multiplicative constant γ. Here, the main concern is the vertical misalignment at both ends of the slabs. As shown in Figure 4.7, the steps at both ends result in the difference of optical paths travelled by the propagating field along the cavity in the axial direction. This step at position $x = 0$ is in effect represented as a phase jump in the integral in Equation 4.23. Hence, a one-dimensional calculation is sufficient to calculate the axial diffraction loss of the cavity. This saving in numerical calculation is advantageous as the other transverse plane is effectively infinite for the dimensions involved and can be safely ignored.

The model assumes that the distance between the two end mirrors of the cavity far exceeds the transverse dimensions of interest, i.e. the mirror dimensions. Consequently, the complex amplitude of the wave at some point on the second mirror U_{q+1}, which is related to that of the wave at the first mirror U_q, can be expressed as the following integral:

$$U_{q+1}(x_2) = \frac{\exp\left(j\left[\frac{\pi}{4} - \frac{kL}{2}\right]\right)}{\sqrt{\frac{\lambda L}{n}}} \cdot \int_{-a}^{+a} U_q(x_1) \exp\left(-\frac{jk[x_1 - x_2]^2}{2L}\right) dx_1 \qquad (4.23)$$

where subscript q refers to the number of transits associated with the wave propagation within the laser cavity. The thickness of the MQW slab is taken to be identical for both slabs and denoted as a while L is the cavity length i.e. the width of the slabs, as shown in Figure 4.1. Note that L should not be confused with the slab length since the laser cavity is along the shorter side of the slab. As mentioned earlier, the process of

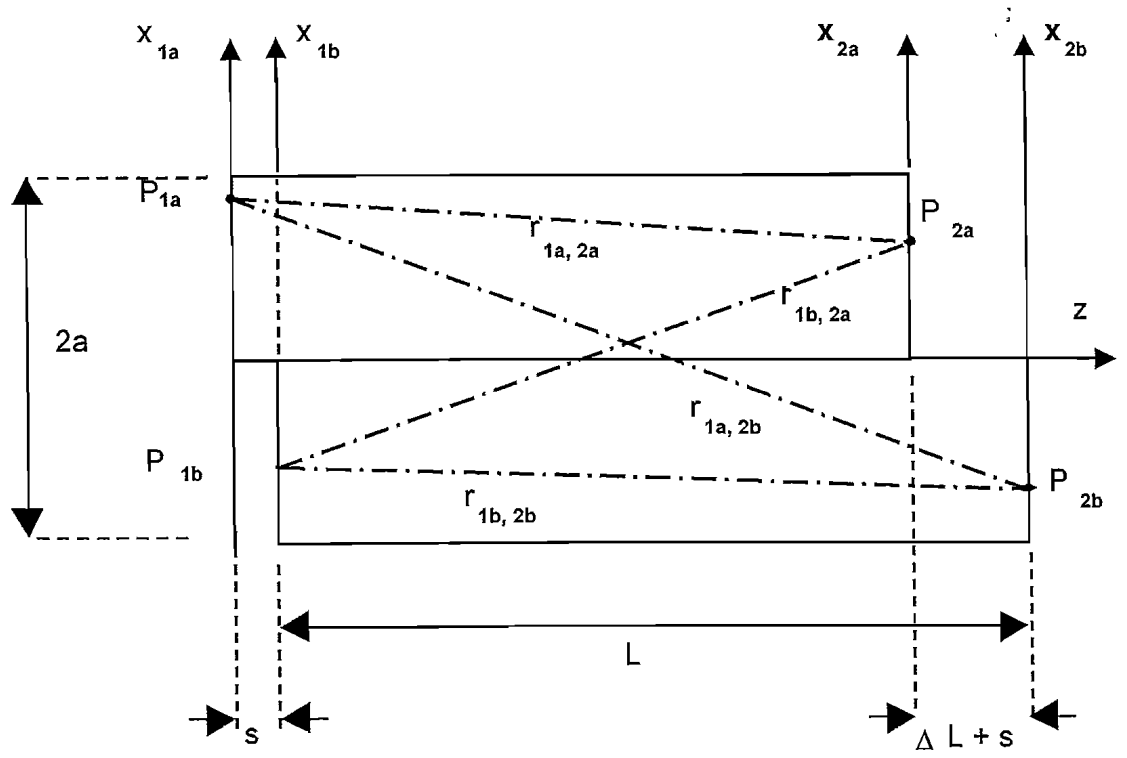

Figure 4.7. Schematic diagram showing the shorter side of two MQW slabs stacked together to form the terahertz laser cavity. The lower slab has a cavity length of L, whereas the upper slab is shorter by ΔL, and the misalignment between the two slabs is s. Note that ΔL can be zero for sample slabs from the same cleaved bar of sample. The relative optical path lengths ($r_{1a,2a}$, $r_{1a,2b}$, $r_{1b,2a}$, and $r_{1b,2b}$) between two corresponding points (P_{1a}, P_{2a}, P_{1b}, and P_{2b}) at the opposite end of the cavity are indicated by the dot-dashed lines.

preparing the slabs ensures that the difference in the slabs width is minimised. The wave propagating constant k is equal to $2n\pi/\lambda$ where n is the refractive index of the medium and λ the electromagnetic wavelength. The n value is taken to be the average value of the substrate and the epitaxial layers since each individual layer is small compared with the long wavelength involved. A field at point x_2 at the second mirror thus results from the integration of each point x_1 at the first mirror. The integral is limited to the thickness of the slabs thus assuming that the field outside of this limit is negligible.

Assumptions and simplifications from the diffraction theory that leads to Equation 4.23 are valid if the transverse mirror dimension is smaller than the length of the cavity while larger than the wavelength involved, summarised by the following definition of the Fresnel number N_0.

$$N_0 = a^2 n/L\lambda << (L/a)^2 \tag{4.24}$$

If condition 4.24 is satisfied, the actual dimensions of L and a become unimportant whereas the parameter that is significant is the Fresnel number. Generally, the larger the N_0 value, the smaller the power loss as a result of the smaller intensity of the diffracted wave at the edge of the mirror. Any misalignment or a difference in the two slabs that make up the resonator cavity can be included easily by considering the optical path length r between two points at the opposite end mirrors. As shown in Figure 4.7, there are four different scenarios that r may take, each depends on the positions of the two corresponding points at the upper or lower half of the end mirror. In addition, the integral has to take into account the corrections separately for the forward and backward propagations since they follow different optical paths. The difference in the cavity length and the misalignment size are denoted as ΔL and s respectively. If the bottom slab is wider than the top slab, i.e. a longer distance between two end mirrors of the lower laser cavity, then ΔL will be positive and vice versa. Note that since the pair of the laser slabs can be taken from the same cleaved bar, the theoretical value for ΔL is zero for perfectly cleaved slabs.

After defining the model parameters, Equation 4.23 can be expanded to include ΔL and s. Two different integrals are needed to accommodate the different scenarios of propagation. Imagine an arbitrary electromagnetic field U_q is launched at the left end of the laser cavity. The first resulting field U_{q+1} at the surface of the right mirror due to the forward propagation of the initially launched field, from the left of the cavity to the right, can be represented as integral Equation 4.25.

$$\begin{aligned} U_{q+1}(x_2) = {} & \frac{\exp(j\pi/4)}{\sqrt{\lambda/n}} C_1 \int_{-a}^{0} U_q(x_1) \exp\left(-jkC_2[x_1 - x_2]^2\right) dx_1 \\ & + \frac{\exp(j\pi/4)}{\sqrt{\lambda/n}} C_3 \int_{0}^{+a} U_q(x_1) \exp\left(-jkC_4[x_1 - x_2]^2\right) dx_1 \end{aligned} \tag{4.25}$$

This newly computed field distribution is then propagated backward from right to left of the cavity. The field U_{q+2} seen at the left mirror, after one round trip propagation is represented by Equation 4.26. The corresponding factors C_1 to C_8 in the two integrals are summarised in Table 4.5. These factors incorporate the adjusted optical path due to

	$-a < x < 0$	$0 < x < +a$
C_1	$\sqrt{\frac{\exp(-jkL)}{L}}$	$\sqrt{\frac{\exp(-jk[L-\Delta L-s])}{L-\Delta L-s}}$
C_2	$1/2L$	$1/2(L\text{-}\Delta L\text{-}s)$
C_3	$\sqrt{\frac{\exp(-jk[L+s])}{L+s}}$	$\sqrt{\frac{\exp(-jk[L-\Delta L])}{L-\Delta L}}$
C_4	$1/2(L+s)$	$1/2(L\text{-}\Delta L)$
C_5	$\sqrt{\frac{\exp(-jkL)}{L}}$	$\sqrt{\frac{\exp(-jk[L+s])}{L+s}}$
C_6	$1/2L$	$1/2(L+s)$
C_7	$\sqrt{\frac{\exp(-jk[L-\Delta L-s])}{L-\Delta L-s}}$	$\sqrt{\frac{\exp(-jk[L-\Delta L])}{L-\Delta L}}$
C_8	$1/2(L\text{-}\Delta L\text{-}s)$	$1/2(L\text{-}\Delta L)$

Table 4.5. Corresponding values for the adjustments to the integrals, taking into account the optical paths of the propagation, where $x = x_2$ and $x = x_1$ for equations (4.25) and (4.26) respectively.

the misalignments. Note that the actual positions of the two points concerned in the equations are unimportant, as only the relative optical path lengths are of interest.

$$U_{q+2}(x_1) = \frac{\exp(j\pi/4)}{\sqrt{\lambda/n}} C_5 \int_{-a}^{0} U_{q+1}(x_2)\exp\left(-jkC_6[x_2 - x_1]^2\right) dx_2 + \frac{\exp(j\pi/4)}{\sqrt{\lambda/n}} C_7 \int_{0}^{+a} U_{q+1}(x_2)\exp\left(-jkC_8[x_2 - x_1]^2\right) dx_2 \quad (4.26)$$

By iteratively computing these two integrals, the field distributions at both end mirrors of the cavity are obtained. Taking the normalised magnitude of each field function computed, the fundamental mode is obtained when the iteration has converged to within a small fraction of the steady state value. The test of convergence is clearly illustrated by plotting the diffraction loss of the cavity mode as a function of the number of iteration or round trip propagation. Once convergence is satisfied, subsequent iteration will yield negligible changes to the field function, except for a

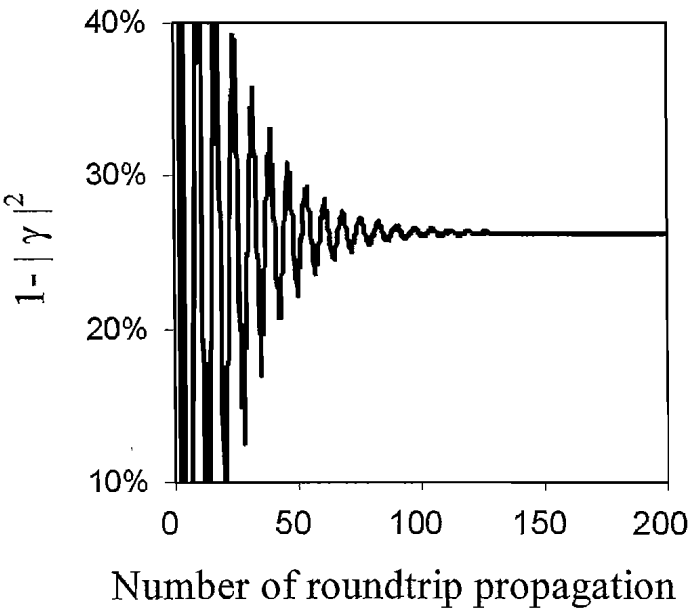

Figure 4.8. The factor of 1 - $|\gamma|^2$ in percent as a function of roundtrip propagations for the case of $N_0 = 1.45$, $s = 2$ μm and $\Delta L = 2$ μm, for $\lambda = 60$ μm and $n = 3.77$. This factor can be equated to the diffraction power loss once convergence to a final value has been achieved.

factor γ. This factor is simply the ratio of the returning field over the originating field, i.e.

$$\gamma = U_{q+2}(x) / U_q(x) \tag{4.27}$$

for any arbitrarily chosen point within the mirror, e.g. at the centre of the top slab $x = 0.5a$.

The diffraction power loss, P_d of the resulting mode can be deduced from γ when the iteration has achieved a reasonable convergence. This relation is given by Equation 4.28 where $|\gamma|$ is the magnitude of the multiplicative constant.

$$P_d = 1 - |\gamma|^2 \tag{4.28}$$

Figure 4.8 depicts the iteration process where P_d is plotted as a function of the number of roundtrip propagation for an arbitrarily chosen case of $N_0 = 1.45$, $s = 2$ μm and $\Delta L = 2$ μm. As shown on the figure, the loss value has converged to a final value at the 130th propagation where further iteration will cause negligible change to this value. In general, our calculation has converged at less than 200 roundtrip propagations,

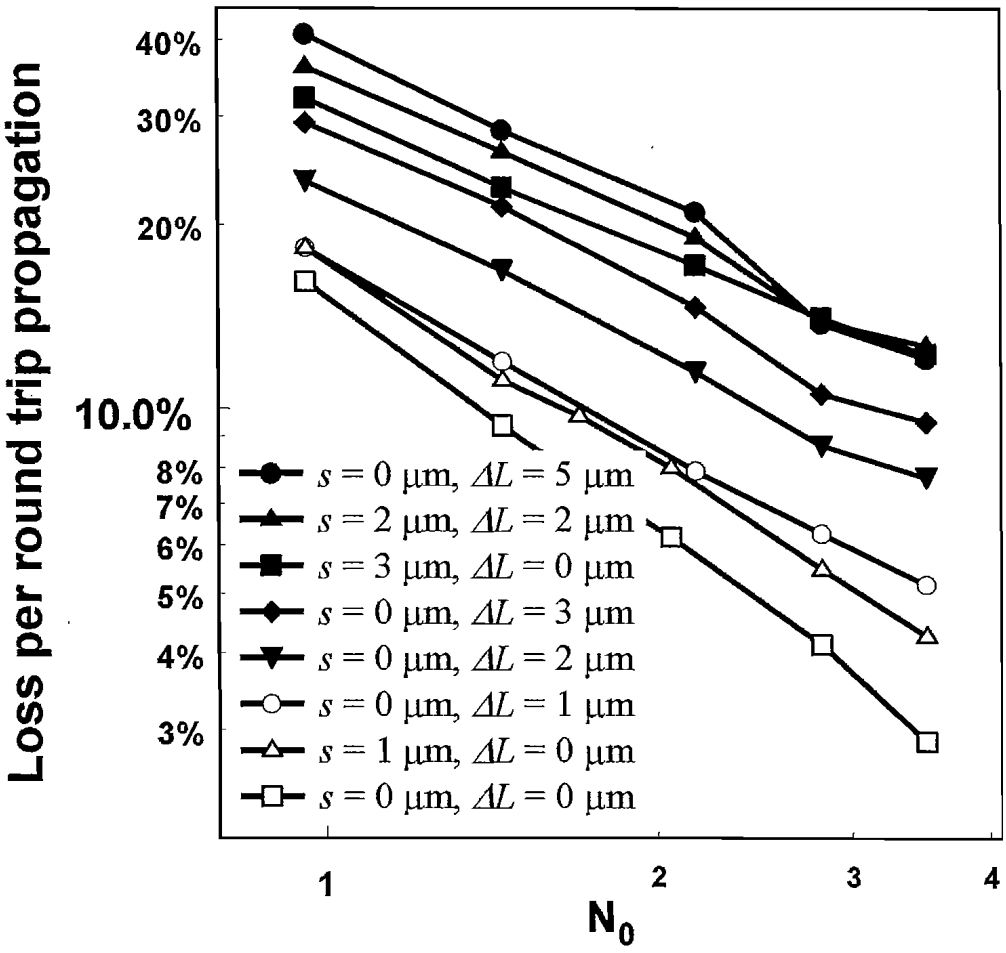

Figure 4.9. One dimensional diffraction power loss per roundtrip propagation for various combination of misalignment size and difference in cavity length, plotted against the Fresnel number in log-log scale.

although in certain cases more iterations are needed especially when larger misalignment sizes are introduced in the model. The large value (or negative value) oscillation of P_d in the graph at the early stage of the propagation is due to the varying intensity distribution before the steady state is reached.

Figure 4.9 shows the diffraction loss per round trip as a function of Fresnel number for a number of combinations of misalignment and cavity length difference. Note that the irregularities of the loss values for the top two lines at high Fresnel number are probably due to the condition in Equation 4.24 has not been well satisfied. For comparison, the Fresnel reflectivity of the uncoated GaAs if used as a mirror is 33.7% at laser wavelength of 60 μm [100], so that losses substantially less than 66% are expected to have a small effect on the device threshold.

4.4.2 Discussion

Figure 4.10 shows, for $N_0 = 2.82$ when $\lambda = 60$ μm, the mode power distribution across the normalised cavity mirror thickness for the different cases of misalignment steps or variation in cavity length. The result shows that the resulting mode concentrates in the slab with a longer cavity. This will seriously reduce the mode overlap ratio with the active layers near the centre, $x = 0$. On the other hand, if the two slabs are misaligned, the effect on the mode distribution is less obvious. For $x/a > 1$, i.e. outside of the slabs, the mode intensity is small and thus justifying the model assumption to limit the

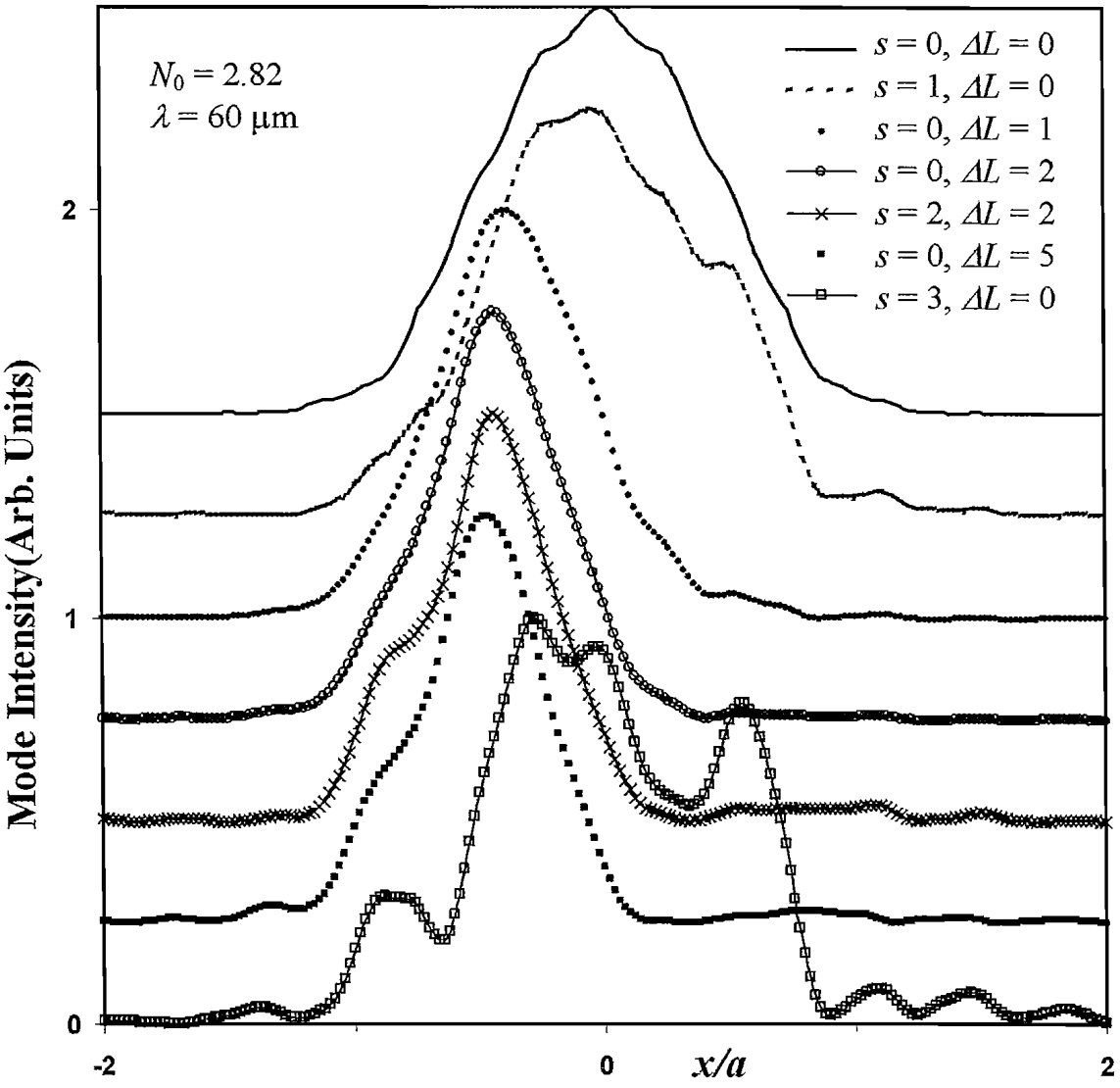

Figure 4.10. The calculated mode intensity using the diffraction integral model for the case of $N_0 = 2.82$ at $\lambda = 60$ μm for different scenarios of misalignments. The graphs are plotted (normalised and vertically shifted for clarity) against the normalised slab thickness x/a. Both s and ΔL are specified in μm.

integral to within $\pm a$.

The log-log scale plot of the diffraction power loss against the Fresnel number in Figure 4.9 shows decreasing loss for increasing N_0, consistent with previous results on square mirrors [133]. The calculated result suggests that a high increase in the mode diffraction loss results if the misalignment step and length variation is more than a few micrometers in size. This alignment precision of a few micrometers is achievable in practice, with careful processing and handling of the slabs.

In addition, the model has some numerical issues that prevented useful calculation when certain choices of Fresnel numbers are used. An amplitude mismatch in the integrals resulting from Equations 4.25 and 4.26 at the interface ($x = 0$) may occur, which is physically prohibited. The issues can be avoided by choosing another value of N_0, which is close to the original choice if the integral iteration does not converge. This is particularly apparent when the size of s and ΔL are increased. For the dimensions chosen in our analysis, the corresponding N_0 is 5.66, which incidentally does not satisfy condition (4.24) very effectively. However, based on the result calculated in Figure 4.9, there is sufficient evidence that the diffraction loss is expected to be low if compared to other type of losses, such as the free carrier loss and reflection loss, provided that the misalignment size is kept low, at a few micrometers (< 4 μm).

As for the case of the stacked slabs with doped layers, the diffraction loss can be estimated by considering the higher order modes loss of a reflected wave from a plane mirror with a phase step in the centre. With a phase step introduced, the reflected wave consists of the fundamental mode plus the sum of all the higher order modes. Considering a symmetric mode wave function, as in our case, the electromagnetic field ratio of the fundamental modes in the reflected wave over the incident wave is given by $\cos(2n\pi s/\lambda)$. This expression is obtained assuming that the laser mode is fully confined between the doped layers of the MQW slabs. Hence, the power loss per transit due to the higher order modes is simply $1- \cos^2(2n\pi s/\lambda)$. The symbols have the same meaning as in previous paragraphs. For example, a misalignment length, s of 1 μm results in a diffraction loss per transit of 14.1 %, using the average refractive index value of 3.67 for the MQW layer at $\lambda = 60$ μm. The diffraction loss greatly increases to 48.3 % for $s = 2$ μm, suggesting an increase in sensitivity to the axial misalignment compared to the stacked slabs without heavily doped layers. Similarly, for the surface plasmon guided

structures, an increase in the accuracy of aligning the slabs will be expected due to the larger confined mode in the interface region.

This approach of stacking two slabs is also unlikely to be practical for shorter wavelength in the mid-infrared region, due to the higher accuracies needed for the alignment. Moreover, poor electrical contact between the stacked slabs is not an issue for optically pumped lasers, since no electrical current flows across the interface. In contrast, this method is not suitable for electrically pumped lasers.

4.5 Conclusion

In this chapter, we have discussed the fundamental issues of achieving a good confinement of FIR mode, while maintaining the free carrier loss at low and manageable values. Several possible design schemes have been explored, with the advantages and disadvantages being compared to achieve an optimum mode confinement system. Although high confinement factor and reasonable loss may be achieved by thinning of substrates, the extra complexity of the device processing and the fragility of the laser device make the thinning scheme rather impractical. Stacking two unthinned laser slabs appear to have reasonable loss, but the confinement factor is very poor. If moderately doped layers are sandwiched in between the active layer and the substrate, the confinement factor is greatly increased. However, this scheme is highly impractical due to the extremely large free carrier loss, as shown in Table 4.1. On the other hand, by utilising the effects of surface plasmon at the interfaces between two media of opposite polarity in the real part of the dielectric constants, a waveguide can be achieved. For our FIR laser structures, the surface plasmon guided mode can be achieved in two different ways. The first scheme is by growing a heavily doped layer on top of the substrate before the active MQW layers are grown. Then, two slabs are stacked to form a double-plasmon guided waveguide structure. Alternatively, the second scheme utilises only a single slab. A layer of metal is deposited on top the epilayer of the MQW slab to act as the top guiding layer, whilst the bottom guiding layer is provided by the heavily doped layer. Mode modelling results suggest that these two schemes have fairly similar performance in terms of the free carrier loss and mode confinement factor. However, given that the first scheme having twice the number of MQW layers, it is expected that a higher laser gain can be achieved compared to the single slab case. Taken into account the complexity of the device fabrication and the durability issues, the surface plasmon guided double-stacked slabs with doped layers

scheme thus looks more attractive than the other schemes described before. It is therefore our opinion that this scheme offers the best compromise of device performance.

In addition, the considerations and procedures taken into account for arriving at the surface plasmon guided design are discussed. These include the methods to estimate the refractive indices at a certain donor concentration and modelling the resulting mode profile. A transfer matrix technique is used in order to model the surface plasmon waveguide system. This technique enables us to identify the resulting mode intensity profile, effective refractive index, as well as the modal loss.

A critical issue with the stacked slabs pumping scheme is to minimise the axial misalignment between the two slabs. A model based on diffraction theory is utilised to estimate the additional diffraction loss that may be contributed by the misalignment. Results from the model suggest that small misalignment in the order of less than 4 μm, or about 7 % of the wavelength, can be tolerated. In view of this, the stacked scheme is unsuitable for shorter wavelengths in the mid and near infrared regions. Despite being unable to obtain the expected diffraction loss value for the case of interest $N_0 = 5.66$ directly using this model, the results from smaller N_0 sufficiently supports the argument that the scheme is practical and realisable.

5 FIR optical signal

Unlike the previous chapters, in which we discuss the design and the characterisation of the MQW samples, the attentions will be turned towards the experimental arrangements for working with FIR signals. In general, optical signals in the FIR region have been studied using techniques that are very similar to those used for the visible and near- or mid-infrared. However, some of the optical properties of FIR signals require different techniques or instruments. In this chapter, the optical expects of the study of FIR will be discuss, most importantly the detectors and optical materials used for the FIR experiments.

Unlike the easy availability of detectors in other regions, there is almost no commercially available FIR detector that is both sensitive and has fast response time. The photon energy in FIR is small, for example, $E = 12.4$ meV at $\lambda = 100$ μm, compared to the thermal energy $kT = 12.9$ meV at $T = 150$K, where k is the Boltzmann constant. Therefore, thermal noise in the detection of FIR signals needs to be kept small compared to the FIR energies. Consequently, most detectors in the FIR are cryogenically cooled for very low temperature operation (liquid He temperature), and can achieve very high sensitivity. The experimental work that has been carried out in order to achieve the detection of the FIR signals will be discussed. In particular, the principle of a gallium-doped germanium (Ge:Ga) photoconductor that is used for the FIR detection in our work is described. This Ge:Ga detector is carefully tested to ensure that satisfactory detection of the FIR signals can be achieved and the detector can be confidently utilised in the FIR measurement for our FIR laser signals. Time and responsivity measurements on this detector using a variety of FIR sources will be examined.

On the other hand, optical transmission in the FIR often utilises different materials that are not common in the other wavelength regions. A review is included for some of the materials that are useful and important in the optical system for this work. In particular, emphasis is placed on the optical properties of these materials in the FIR and the mid-infrared, i.e. the pump laser wavelength region. Apart from the cryogenically cooled detector, room temperature pyroelectric detectors are widely used in this work and thus will be discussed. An optically pumped FIR gas laser is also designed as an experimental tool for this work. The details of the gas laser design are described,

including the gas medium, laser cavity and FIR emission analysis. Finally, a method of increasing the FIR optical signal from the MQW structures by coating a layer of metal at the cleaved surface is introduced before concluding the chapter.

5.1 Detectors in the far infrared

Unlike other region in the electromagnetic spectrum, detectors for the FIR are quite well developed but comparatively less commonly used. Commercially marketed FIR detectors are almost nonexistent. Hence, many FIR detectors are confined to applications in research laboratories. In general, detectors for FIR radiation can be divided into two categories: thermal detectors and quantum detectors [95, 114]. Thermal detectors operate by sensing the change in temperature due to the increase in radiant energy. On the other hand, quantum detectors or photoconductors sense the absorption of the photon energy due to the promotion of carriers (usually electrons) into higher energy levels.

Thermal detectors are broadband devices, and are widely used throughout the infrared region. Incident radiation is absorbed by the bulk material, or by a blackened surface that in turn heats up the detector material by conduction. Hence, the change in the detector temperature due to the radiation energy causes some physical changes that can be measured. One of these detectors is the thermopile that has long been used in the infrared region, with their main advantage of being inexpensive and reliable. Although still being used nowadays, it is insensitive and has a slow response time. Bolometers, on the other hand need to operate at cryogenic temperature, although they can be very sensitive and have short response time. Germanium bolometers are one of the widely used detectors in FIR. Two thermal detectors that can operate at room temperature are the Golay cell and the pyroelectric detectors. Both of these detectors have good sensitivity, where the former has slow response time whereas the latter have very short response time. The pyroelectric detectors will be further discussed later in this chapter.

Quantum detectors for FIR normally involve the ionisation of dopants in a doped semiconductor, which is cooled to very low temperature, where the majority dopants are frozen out. Then the signal current due to the free carrier drift motion under an externally applied electric field can be detected. These detectors are the extrinsic semiconductor photoconductors such as the doped Germanium and doped Silicon detectors [114, 134]. These photoconductors have great advantages that they are highly sensitive and have good time response.

In intrinsic materials, incident radiation generates electron-hole pairs by promoting electrons from the valence band to conduction band. Both electrons and holes contribute to the photocurrent generated. As such, no intrinsic material is used for FIR detection due to the small band gap required. In contrast, for extrinsic semiconductor detectors like Ge:Ga, photoconductivity is solely produced by the majority carriers from photoionisation of the dopants. The lightly doped semiconductor can produce either donor levels close to the conduction band, or acceptor levels close to the valence band. At low temperature, the number of thermally excited electron is small compared to the number excited by radiation. A low energy photon can then excite an electron or a hole. The incident radiation changes the electron concentration that in turn changes the conductivity of the detectors. As photons of higher energy than the ionisation energy are required for the change in electron distribution, these detectors are wavelength dependent with a sharp detectivity fall off at the long wavelength limit. A Ge:Ga photoconductor is used for the FIR detection for our MQW laser system, which will be described next.

5.1.1 Ge:Ga photoconductor

An extrinsic germanium doped with gallium crystal is a widely used photoconductive detector in the FIR region. The use of Ge:Ga detector for FIR detection was first reported by Moore and Shenker [135] in 1965. Since then, the Ge:Ga detector has found wide use in various applications such as astronomical and atmospheric observations, particularly in the wavelength range from ~40 μm to 120μm [114, 134, 136-138]. However, the research and development of Ge:Ga detectors has been mostly from a small number of universities research group or national laboratories, due to the lack of commercial interest in such detectors. Considerable efforts have also been made in development of Ge:Ga array in the past decade [134]. With the increased research activities and new applications in the FIR region, especially from the successful invention of FIR semiconductor lasers [39, 125], this detector may well see further development in the near future. Apart from gallium, other dopants added to germanium are also used as detectors with different cut-off wavelength and performance. Dopants that have been used include zinc (Zn), copper (Cu), indium (In), gold (Au), antimony (Sb), and cadmium (Cd) [139, 140].

The Ge:Ga semiconductor has an acceptor impurity level of 10.4 meV, which corresponds to a cut-off wavelength of 120μm [114]. This low impurity level thus

requires that the detector to be cooled to near liquid helium temperature (4.2 K) in order for it to work as a photoconductive detector. At high temperature, lattice vibrations easily excite the charge carriers, thereby making them no longer available for photon excitations. This photoconductor has a fast response time of the order of ns. The cooling machine used in our laboratory is a closed cycle cryostat, which achieves lowest temperature of 6 K. Although slightly higher than liquid He temperature, our measurements (which will be discussed later in this chapter) have shown that the detector has worked very well at this temperature.

5.1.2 Operation of the Ge:Ga detector

The Ge:Ga crystal used for this work, which has a dimension of a cube of $(4\ mm)^3$, has a bandwidth of greater than 10 MHz and noise equivalent power (NEP) of better than 10^{-11} $W/Hz^{1/2}$ [141]. As such, detection of laser pulses as short as 30 ns is possible with this detector, which is ideal for our application since the pump laser (CO_2 laser) pulse width is ~ 55 ns. The Ge:Ga detector is indium-soldered to the oxygen-free-high-conductivity (OFHC) copper base to provide a good thermal and electrical contact, especially at low temperature. An electrical contact is then made from the upper side of the detector, where the detected signal will be taken. As for the other contacting point, the metal body of the cryostat is utilised to act as the ground connection for the electronic circuit.

A bias voltage is applied across the detector such that the change in current can be measured. The optimum signal to noise ratio is achieved when the bias voltage across the detector is close to 1 V [141]. At low bias field, the detector shows an ohmic feature, while at higher bias field carrier heating and breakdown may occur [138]. Since the detector is very sensitive, the high power CO_2 laser beam can be easily detected during pumping of the FIR system. Consequently, it is important that a combination of windows and filters are used in the optical path of our FIR system to eliminate the detection of the pump signal. The arrangement of the filters in our experiment is depicted in Figure 5.1. The transmission characteristics of various optical materials will be discussed later in this chapter, together with a selection of transmission spectra of these materials given in Appendix 1. In addition, an aluminium (Al) shielding box is added to cover the detector from any unwanted background radiation and avoid electromagnetic pick-up.

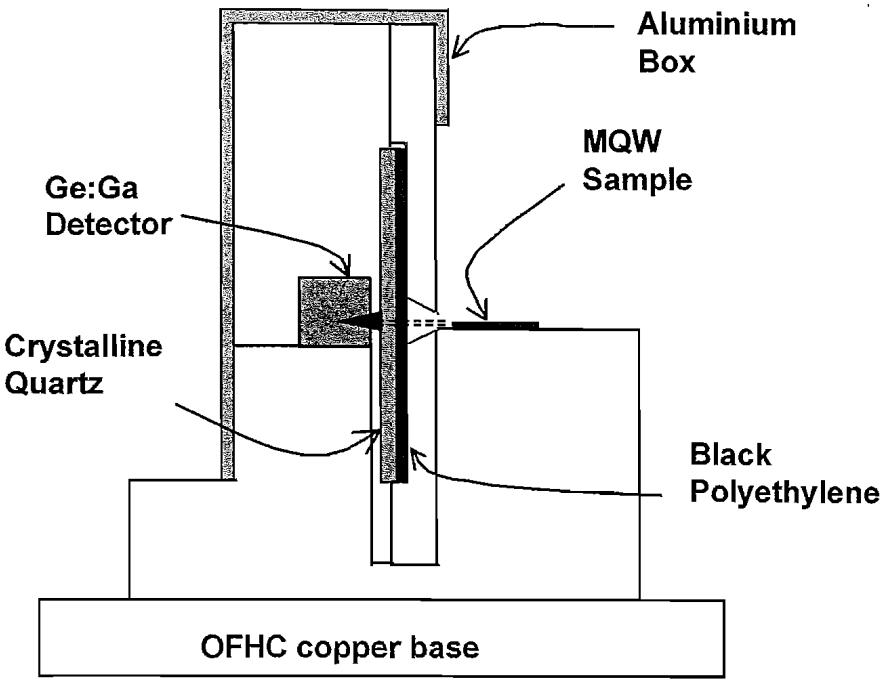

Figure 5.1. Detector and sample holder for the MQW FIR laser experiment. The Ge:Ga detector is soldered to the copper base, and further mounted to the cold-finger of a cryostat. Optical windows and shield are included to filter out the background radiation as well as the scattered pump laser light.

5.1.3 Transimpedance preamplifier for the FIR laser detection

The noise voltage from a low temperature Ge:Ga detector is very small, and can be a few nanovolts (nV) or less than 1 nV in a 1 Hz bandwidth. Amplifying signals that are comparable to such a low noise voltage without introducing extra noise presents a considerable challenge. A preamplifier is thus needed to amplify the signal to a higher level so that a commercially available amplifier can be utilised to further amplify this signal. A transimpedance amplifier was designed, utilising an Analog Devices AD9631AN wideband operational amplifier (Op Amp) [142], where the circuit diagram is shown in Figure 5.2. The transimpedance gain of the preamplifier is defined by the value of the feedback resistor, which is chosen to be 7.5 kΩ in our case to yield a 7 MHz bandwidth response for the preamplifier. In a transimpedance amplifier, the input current will be amplified by the same value of the feedback resistor to produce a low impedance output signal. The corresponding feedback capacitor is chosen to give a flat frequency response and to suppress oscillation. Table 5.1 lists the parameters of the transimpedance preamplifier constructed for the amplification of the detector signal. One of the greatest concerns in this preamplifier is the parasitic capacitance between the input pins of the Op Amp and the ground, which will have a very serious effect on

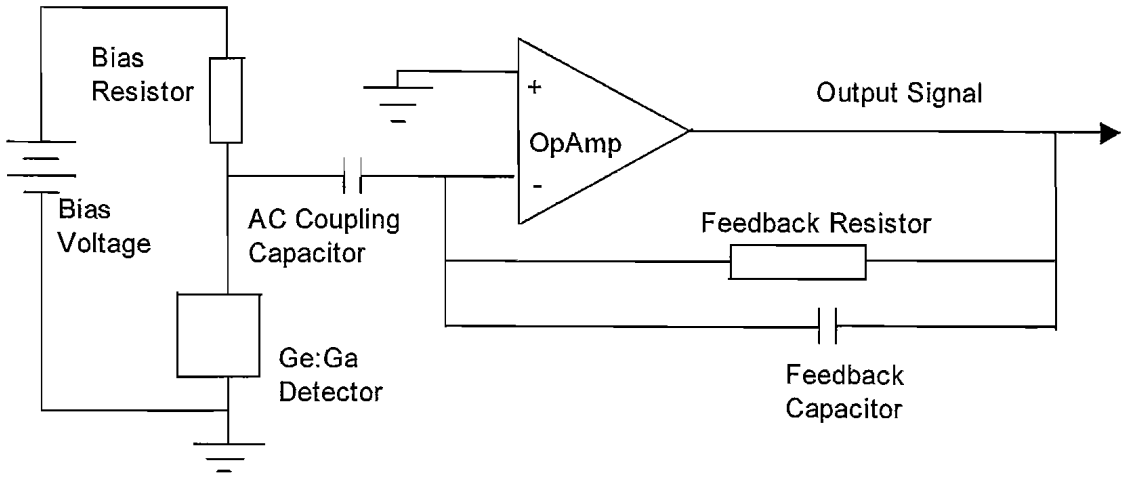

Figure 5.2. Schematic diagram of the preamplifier circuit for detection of the FIR signals using a Ge:Ga detector.

the performance of the preamplifier and thus should be minimised. For this reason, circuit components were soldered to a printed circuit board (PCB), where various precautions were taken on the board layout to minimise the parasitic capacitance.

High frequency decoupling capacitors were placed near the power supply pins of the operational amplifier, while metal-film resistors were used to provide good high frequency performance. In addition, the operational amplifier was soldered directly onto the board to avoid any parasitic capacitance introduced by using a socket [142-144].

Parameters	Values
Transimpedance gain	7500 V/A
Feedback resistor	7.5 kΩ
Feedback capacitor	5 pF
Decoupling capacitors	0.1 μF
Bias Voltage	9 V
Bias Resistor	390 kΩ
Preamplifier 3 dB bandwidth	~ 7 MHz
AD9631AN Gain-Bandwidth product	320 MHz
Ge:Ga resistance at $T = 6$ K	60 kΩ

Table 5.1. Parameters and the corresponding values for the transimpedance preamplifier design to amplify the signal of the Ge:Ga detector.

The preamplifier circuit board was placed near to the Ge:Ga detector so that any parasitic capacitance from the cable connecting the detector and the preamplifier was minimised. Nevertheless, due to the very low temperature of the cryostat (~6 K), it was not possible to put the preamplifier near the cold finger. At very low temperature, the electronic devices of the preamplifier circuit, especially the operational amplifier, would cease to work as intended. Hence, the preamplifier was placed inside the cryostat where the temperature was near the liquid Nitrogen temperature, i.e. 77 K. A temperature test on the preamplifier at 77 K was first carried out, which confirmed that the preamplifier functions normally at this temperature.

Furthermore, reducing the operating temperature of the preamplifier also had the advantage of reducing the thermal noise from the resistors and other circuit components. This was in addition to the advantage of minimising the length of the signal path from the Ge:Ga detector to the first amplifying stage, i.e. the transimpedance preamplifier, thereby reducing the parasitic capacitance.

The bias resistor for the detector was chosen such that the voltage across the detector is near the optimum value. This was done by first using a potentiometer as the bias resistor until the desired voltage across the detector has been achieved. A resistor with the value of the resistance measured then replaced the potentiometer. However, it was found that the detector resistance was very sensitive to temperature changes at low temperature. In the temperature range of 6.0 K to 6.7 K, the corresponding detector resistance varied between 60 kΩ to 20 kΩ. These high resistance values at low temperature were expected as most of the dopants were frozen out, as the ionisation energy was only a few meV. In addition, the base temperature at the cold head of the cryostat was found to fluctuate at a low frequency of 2 Hz. This had an undesired effect of resistance fluctuation as the temperature of cold head varies. Fortunately, this problem could be overcome by AC coupling the input to the preamplifier at a high frequency through a capacitor between the detector and the Op Amp. Since the fluctuation was at low frequency whereas the interested signal was in the order of MHz, the detector performance was not reduced.

5.1.4 Detector response to a blackbody source

As a test for the sensitivity of the Ge:Ga detector in the response range, a blackbody infrared source was used [145]. All thermal sources emit electromagnetic energy at all wavelengths. However, the spectral distribution of the energy emitted is related to the

temperature of the thermal source. A true blackbody source is a perfect emitter where the maximum number of photons is emitted per unit time, for a given surface area in a wavelength interval. The total optical power, W radiated from a hot object is given as [49]:

$$W(T) = \varepsilon \sigma A T^4 \tag{5.1}$$

where σ is the Stefan-Boltzmann constant, ε is the emissivity, A is the area, and T is the temperature of the hot body.

An ideal blackbody has an emissivity value of unity whereas other thermal sources have emissivity values of between zero to near unity. The blackbody will absorb any radiation falling upon it and this is where the name has arisen [49, 140]. Like all thermal sources, the blackbody source emits only a small amount of power in the FIR region compared with that emitted in shorter wavelength. Consequently, it is essential to filter out the short wavelength radiation with filters like polyethylene, crystalline quartz and TPX. Figure 5.3 shows the experimental arrangement for testing the detector with a blackbody source. A 3 mm TPX was used as the window for the cryostat. In addition, black polyethylene and quartz filters were placed in front of the detector. The blackbody source has an internal cavity, which is heated and temperature controlled by

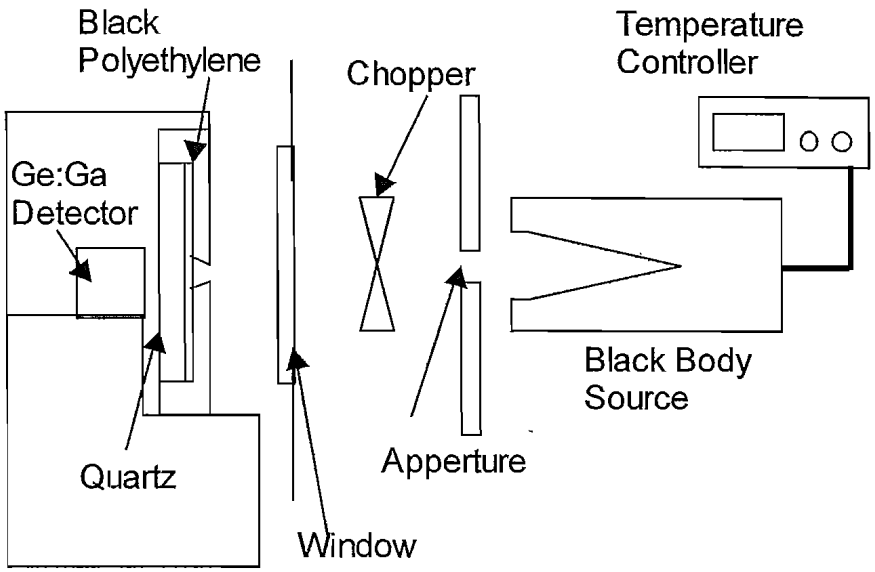

Figure 5.3. Experimental setup for testing the Ge:Ga detector with a blackbody source. Temperature of the blackbody source is controlled and the radiation is limited by the aperture as well as modulated using a mechanical chopper. The black polyethylene and quartz are used to filter lower wavelength radiation from the source, while the input window to the cryostat is TPX.

a temperature controller. An aperture in front of the blackbody opening determines the amount of radiation emitted by the blackbody cavity. The spectral radiant emittance of a blackbody source is described in Appendix 2. A chopper was used to modulate the emitted radiation from the blackbody source at frequencies up to 1.2 kHz. Measurements have been taken with various aperture sizes and chopping frequencies at temperature of 1177 °C, equivalent to 1450 K.

A responsivity value of 2.0 A/W was estimated for the Ge:Ga detector in the wavelength range of 40 μm to 120 μm, where the calculations were detailed in Appendix 2. This value did not include any transmission loss due to FIR absorption of water vapour in the atmosphere. Hence, the actual amount of infrared energy received by the detector was less than the value used in our calculation. Furthermore, the transmission factor of the optical path in Equation A.7 was dependent on the optical filters. As the transmission spectra for the filters involved in the measurements were dependent on the wavelength, the transmission factor chosen was only an estimated figure based on the average value. Hence, the detector response should have at least or close to the performance described here.

5.1.5 Detector response to a CO_2 pulsed laser

It is very valuable to ensure that a detector has a good time response to a short pulse signal. Hence, the Ge:Ga detector was then tested using the CO_2 pulse laser to study the pulse response of the detector. As the CO_2 laser intensity was very high (of the order of kW/cm^2) for a high sensitivity detector, the CO_2 beam was not directed towards the detector. Instead, only a small amount of the reflected CO_2 beam was enough to be detected by the Ge:Ga detector. In addition, attenuators were placed before the optical window (ZnSe was used in place of the TPX) of the cryostat to further reduce the incident pulse intensity at the detector. Moreover, the black polyethylene and quartz filters were not used in this measurement. Figure 5.4.a and Figure 5.4.b show the pulse response of the Ge:Ga detector to CO_2 laser pulses of different intensities. The signal of the former was a factor of ten greater in output voltage than the latter, which was linearly proportional to the attenuation used for the CO_2 laser signal. Although the CO_2 pulsed laser was tuned to a wavelength of 9.35 μm, which was away from the optimum detection range for the detector, the signal was easily detected. These results showed that the CO_2 pulses had a FWHM of 100 ns, which was somewhat wider than the value provided by the manufacturer (~55 ns for the laser line at 10.6 μm). The detected FIR

output signal was taken directly from the output of the transimpedance preamplifier, which has amplified the signal from the photoconductor, and observed with a 100 MHz oscilloscope. The absolute power or intensity in these measurements was not recorded since heavy attenuation was applied to the CO_2 beam in order to avoid saturating the detector. However, the time responses of the Ge:Ga detector can be easily measured.

These pulse responses were compared to those obtained with a pyroelectric detector (Figure 5.4c and Figure 5.4d), with a 50 Ω terminating resistor, albeit at much higher pulse intensities (more than five orders of magnitude). At this configuration, the pyroelectric detector is suitable of detecting the CO_2 laser pulses due to the high peak pulse intensity. A FWHM pulse width of 100 ns was recorded from the measurements with the pyroelectric detector. For a pyroelectric terminated with a 50 Ω resistor, the typical response time is only a few ns [146]. Hence, the pyroelectric should be capable

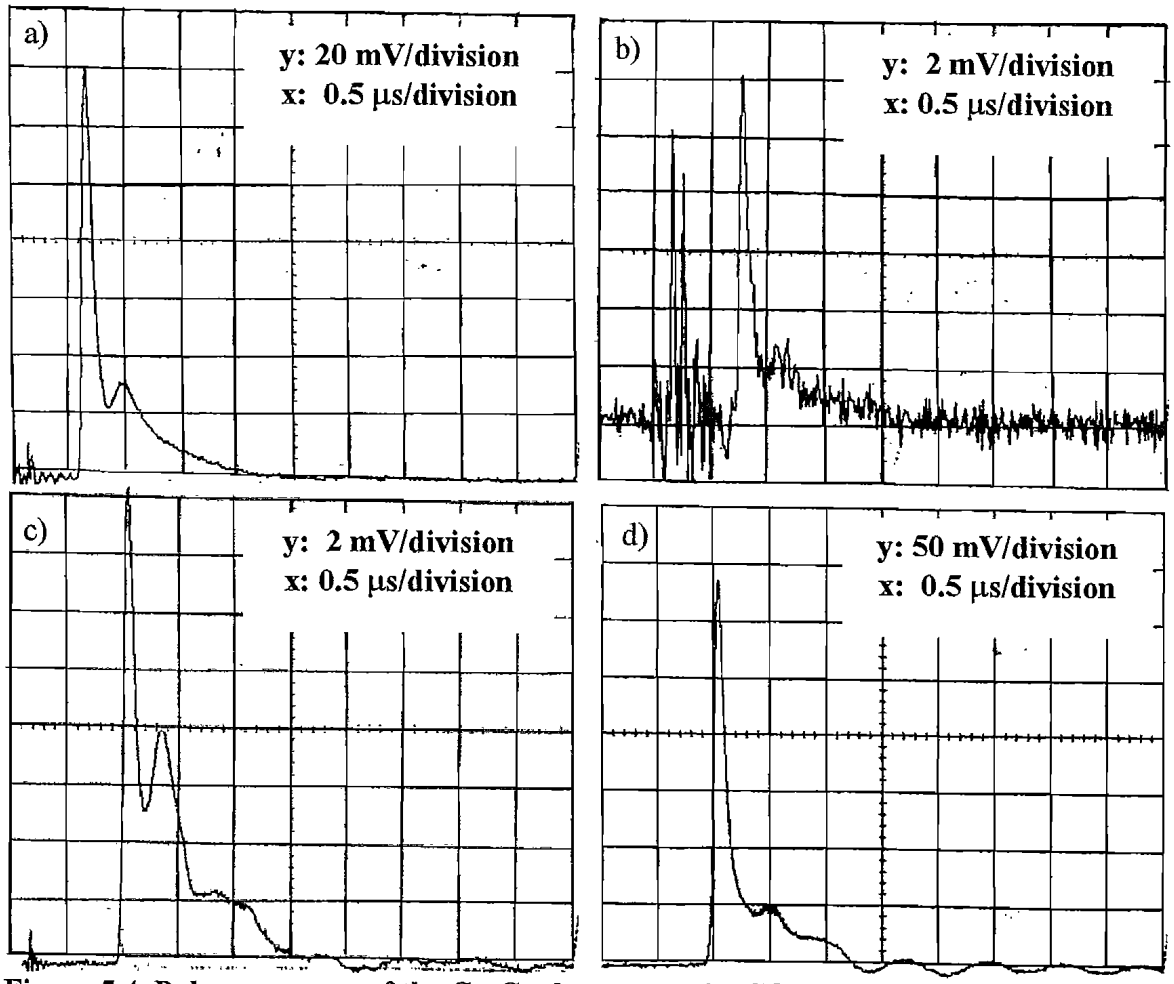

Figure 5.4. Pulse responses of the Ge:Ga detector to the CO_2 laser pulse, a) & b) at different intensities. The output signal of a) is an order of magnitude greater than the output signal of b). These are compared to those detected with a pyroelectric detector, c) & d) albeit at much higher pulse intensities. For all cases, the FWHM pulse width is measured as ~ 100 ns.

of resolving the pulse response of the CO_2 laser pulses. Comparing the pulse responses in Figure 5.4, the results show that the Ge:Ga detector is working well in resolving the pulse response from the CO_2 laser. This is a clear indication that the detector can be utilised for the detection of the FIR signal which is expected to have a pulse response that is of the same order as the pump source, which is the CO_2 laser in our case.

Interestingly, the Ge:Ga detector was found to respond to the CO_2 pulse response very strongly even though it was shielded with metal or other filters. When an optical window that blocked, i.e. opaque to the laser wavelength was used for the cryostat window, no signal was detected by the photoconductor. However, when the same filters that had large attenuation to the CO_2 beam were placed inside the cryostat, it was found that the CO_2 signal could always be observed by the photoconductor. A variety of filters were used, including thin aluminium foil, thin stainless steel sheet, crystalline quartz, black polyethylene, and lead sheet, which all are largely opaque in the laser wavelength. Moreover, there was no observable signal when the detector was unbiased. This suggested that the observed signal was unlikely to be an electrical pick-up signal from the preamplifier. As the MQW sample may be mounted at the same holder as the detector, the shielding of scattered CO_2 laser beam is naturally an important issue. Despite extensive investigations and testing of numerous hypotheses as to the origin of this signal, it remains unexplained. Since this signal limits the utility of the detector, further investigation is needed.

5.1.6 Detector response to a FIR laser

FIR laser emission from an optically pumped methanol gas laser has been observed using the Ge:Ga detector. This gas laser thus represents a coherent FIR source that is ideal for determining the effectiveness of the detector in observing short pulse FIR signal. This FIR gas laser is optically pumped by the pulsed CO_2 laser and will be described in more detail later in Section 5.4. Figure 5.5 shows a typical pulse signal for the FIR methanol laser, as measured by the Ge:Ga detector. The laser wavelengths of the emission were determined using a cavity scanning technique that will be described in Section 5.4.4. TPX window was used for the cryostat, with additional crystal quartz and black polyethylene filters placed inside the cryostat. This detected FIR signal was heavily attenuated (< 5 % of original signal was transmitted) when a 3 mm ZnSe filter was placed in between the optical path of the gas laser and the Ge:Ga detector. In contrast, when a TPX filter or a black polyethylene filter was used, little attenuation

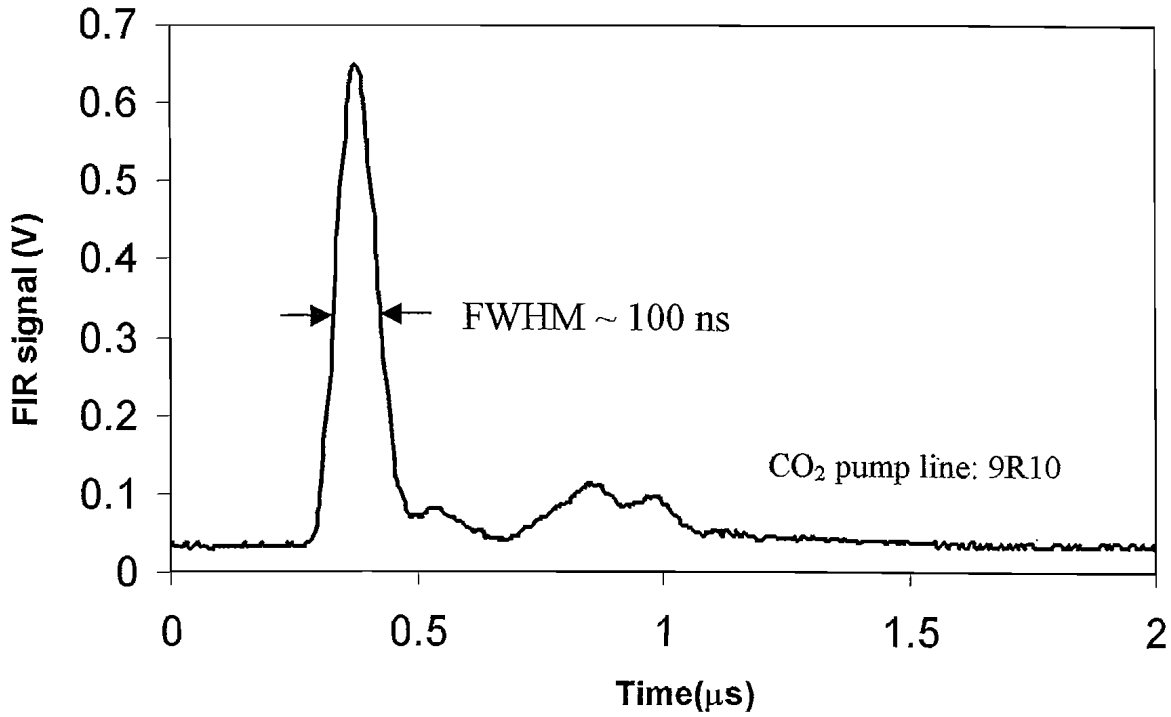

Figure 5.5. Detected FIR methanol gas laser signal by the Ge:Ga detector when pumped by 9R10 line of the CO_2 pulsed laser. Cavity scan of the emission suggests that laser emissions occur at both wavelengths of 70 μm and 136 μm (refer to Figure 5.8). The FWHM of the pulse is measured to be ~ 100 ns.

was observed (> 80 % of the original signal was transmitted). The different attenuation levels of the signal to these filters thus indicated that the scattered pump light was not the detected signal and ensuring the signal was indeed in the FIR. Measured transmission spectra for these filters can be found in Appendix 1. Although the upper optimum detection range of the detector is 120 μm, emission of wavelength longer than this optimum range can still be detected, albeit at a reduced sensitivity. Furthermore, the FWHM pulse width for the FIR gas laser was measured as 100 ns, which is similar to the CO_2 laser pulse width. This further evidenced that the Ge:Ga detector has a good response for the FIR detection, especially near the target emission region of the MQW FIR laser.

5.2 Optical materials

Optical materials that have been used successfully in the visible and near-infrared region ($\lambda < 10$ μm) are generally not suitable for use in the FIR. Some of the materials used for the optical components, which may be physically less strong than their visible counterparts, are quite unique to the FIR. Crystalline materials that have a high

reflectivity region in the infrared can be used as band stop filters. At this wavelength region, termed the reststrahlen region, the crystal materials have very high absorption coefficients due to the ion vibrations in the crystal lattice [114]. These vibrations interact directly with the infrared light and result in high absorption and reflection losses. We shall discuss the different materials utilised in our work both for the pump CO_2 laser as well as the FIR laser. The transmission spectra of these materials are given as Appendix 1. The spectra were measured using the FTIR spectrometer at room temperature.

5.2.1 FIR transmission and CO_2 rejection

Optical windows and filters used in the experiments and measurement of the optically pumped FIR lasers have to consider the pump wavelength rejection issue. Materials chosen must be able to transmit most of the FIR wavelength while at the same time attenuate substantially the pump wavelength, in our case the CO_2 laser beam. Some of the optical materials used throughout this work are reviewed in the following sections.

5.2.1.1 Zinc Selenide (ZnSe)

Zinc selenide is a useful material in the infrared regions, but it is very absorptive in the ultraviolet region [115, 147]. The low absorption loss of ZnSe in the mid-infrared makes it a popular window material in this region. It is transparent throughout the emission wavelengths of the CO_2 laser (9-11 μm). ZnSe is also used as beamsplitters to the CO_2 laser beam in this work. Depending on the thickness of the material, ZnSe is highly absorptive and opaque in the wavelength region ~ 20 – 90 μm. Beyond ~ 100 μm, the absorption loss drops and ZnSe transmits again in the longer wavelengths of FIR.

5.2.1.2 Germanium (Ge)

Germanium is a widely used infrared window material, which is insoluble in water and fairly inactive chemically. Although opaque in the visible, Ge transmits FIR radiation although it suffers high lattice and free carrier absorption at room temperature [114]. Due to the high refractive index ($n = 4$ at $\lambda = 10$ μm) values, antireflection coating is normally needed in some applications to reduce the reflection loss. Ge windows are also mounted at the Brewster angle to the plane polarised light as another way of reducing the reflection loss, although this angle is rather impractical (76° normal to the plane of the window).

5.2.1.3 Crystalline quartz (SiO_2)

A 1 mm thick crystalline quartz is opaque between 4-40 μm [114] and thus it is a good filter to remove the CO_2 emission at 9-11 um. Quartz is a hard crystal and transparent at visible wavelengths. Due to the high transmission in FIR, crystalline quartz has long been used as the window material. It can be cooled to near liquid Helium temperature, when it has a sharp cut on at 40 μm.

5.2.1.4 TPX (polymethylpentene)

TPX is optically transparent in the visible and FIR, thus it is a very useful material as an FIR window [114]. This allows optical systems to be set up or aligned using visible light. Moreover, TPX has high melting point (>200 °C), and offers high chemical resistance and electrical insulation. The refractive index of TPX is 1.46, which is largely independent of wavelength in the visible to infrared. The transmission spectrum of TPX shows a lossy region in mid-infrared, but transmission gradually increases from 30 μm, and becomes transparent beyond 100 μm.

5.2.1.5 Polyethylene

Polyethylene is a widely used window material in the FIR [114]. Black polyethylene, where the carbon contained is used to filter out short wavelengths, is opaque in the visible range but transparent in the far infrared. This material is very cheap and chemically resistant to most solvents. However, as the amount of carbon varies in the types of polyethylene, the transmission also varies. The melting point of polyethylene is rather low at 120 °C, such that operation much higher than room temperature is not possible. A good cold filter can be obtained, where background radiation up to 40 μm can be effectively removed by combining black polyethylene and crystal quartz windows.

5.2.1.6 Potassium chloride (KCl)

Potassium chloride is a soft crystal, which is water soluble. Therefore, care needs to be taken against using it in a humid environment. 'Fogging' will form on the window once it is exposed to moisture for a certain period. KCl is highly transparent at visible to mid-infrared region, but it is opaque at FIR. Hence, KCl can be used as a filter in FIR, with its reststrahlen reflection peak at 64 μm, or window in the mid-infrared [114].

5.2.1.7 Potassium bromide (KBr)

Potassium bromide has a very similar characteristics and transmission range as KCl. However, the transmission spectrum for KBr has a slightly longer cut-off wavelength at mid-infrared compared with KCl. KBr is transparent in the visible to mid-infrared but opaque in the FIR region. The reststrahlen peak for KBr is at 80 μm [114].

5.3 Pyroelectric detectors

Pyroelectric detectors are popular in the whole infrared region, due to their largely wavelength independent response as well as room temperature operation. At low frequency operation, pyroelectric detectors can have high responsivity. On the other hand, they can have a fast response time when used in high optical power detection. They are widely used in mid- and far infrared detection, as alternate detection systems can be orders of magnitude in costs. Furthermore, no cryogenic cooling is required for the operation of pyroelectric detectors. These detectors are now also commercially used, such as detectors in intrusion alarm systems in average households.

Pyroelectric detectors are made of ferroelectric materials that develop surface charge when cut in an appropriate way to a unique axis where a permanent dipole moment exists [95, 140]. These surface charges are highly sensitive to changes in temperature and consequently the current flow can be measured. Some of the most widely used materials for pyroelectric detectors include Triglycine sulphate (TGS), lithium tantalate ($LiTaO_3$), strontium barium niobate, ceramic materials based on lead zirconate titanate (PZT), and some polymer films [140]. As pyroelectric detectors only respond to the change in temperature, thus they must be used in AC mode. If used with continuous wave (CW) sources, the light beam must be chopped or modulated using a frequency controlled chopper in order for the detection with a pyroelectric detector.

Since pyroelectric detectors are responsive to light of all wavelengths, it is thus essential to incorporate filters that allow transmission in the wavelength range required while blocking unwanted light in other regions. For example, a pyroelectric detector (model 420 from ELTEC) with a germanium window is used as the detector for the reference signal to the CO_2 laser beam. In this application, the detector has no integrated electronics associated with it but simply terminated with a 50 Ω resistor, and the signal observed with an oscilloscope. As shown in Figure 5.4, fast pulse response can be obtained in this configuration. This is possible since the incident power from the laser is high enough for the signal to be detected. For lower power detection, additional

electronic components such as a field effect transistor (FET) circuit can be included with the sensing element within the same package. Normally, a source follower circuit with a high resistance load resistor and a FET is used, which offers low output impedance. The load resistor will determine the frequency response of the overall detector output. For a wideband flat frequency response, a lower resistance value is chosen, but at the expense of lower responsivity. With a source follower, the gain of the detector is about unity and determined by choosing an external source resistor.

5.4 Optically pumped methanol gas FIR laser

Optically pumped FIR gas lasers have played a major part in exploring the FIR electromagnetic region [148]. An optically pumped FIR laser is constructed as a tool for testing the Ge:Ga detector, as well as an alternative FIR source in the development of our solid state FIR laser. This FIR laser utilises methanol vapour as its gain medium, due to its easy availability, low cost, and the many laser lines that optically pumped methanol lasers are known to have achieved. By using the CO_2 pulsed laser, the methanol molecule is excited to a higher vibrational-rotational energy state. The molecule then relaxes to a lower energy state by emitting a photon, which has an energy that corresponds to the FIR wavelength.

5.4.1 Methanol as a laser medium

Of the different types of gases used as the source for FIR gas lasers, methanol (CH_3OH) is the most widely used and easily available. Hundreds of CO_2 laser pumped lines have been reported for methanol [22, 149]. Only several strong laser lines have thus been chosen from the literature, which are suitable to be pumped by our pulsed TEA CO_2 laser. The primary interest for this laser is the laser emission wavelengths between ~60 – 120 μm, which correspond with the detection range of the Ge:Ga photoconductor used for the FIR detection. Nevertheless, the Ge:Ga can easily detect strong FIR emission over this wavelength range, as long as 200 μm [114], due to the high sensitivity of the detector. Moreover, this range is also inline with our aim for the MQW FIR laser emission of ~60 μm to 100 μm. Table 5.2 displays some of the possible laser pump lines and the reported FIR laser lines for methanol. It is nevertheless possible to operate the gas laser at other laser wavelengths, by using suitable gases and pump line. Furthermore, different laser lines can be obtained if the isotopic forms of methanol are used. They have been studied extensively, where known

methanol isotopes that emit FIR include $C^{13}H_3OH$, $CH_3O^{18}H$, CD_3OH, CD_3OD, and CH_3OD [23, 149, 150].

Medium: Methanol (CH_3OH)

Pump Line	Pump wavelength λ_P (μm)	Laser wavelength λ_L (μm)
9R22	9.24	84.908
9R18	9.27	82.8
9R14	9.30	100.806
9P14	9.50	74.10
		80.843
		117.960
9P16	9.52	87.70
		109.90
		113.45
		118.38
		118.57
		118.80
9P18	9.53	103.2
9P22	9.54	117.64
9P24	9.58	92.544
10R18	10.25	92.8
10R16	10.27	77.905
10P16	10.55	84.913
		88.819
		99.861
10P18	10.57	75.932
		100.010

Table 5.2. A selection of strong CO_2 laser line, and their corresponding wavelengths. Wavelengths for the reported FIR laser lines are given. Note that more than one FIR laser lines have been observed from the same pump line.

5.4.2 Gas laser cavity

The FIR gas laser cavity is constructed using a 1 m long and 150 mm inner diameter QVF borosilicate glass tube. This glass tube is sealed by attaching two stainless steel plates at both ends of the glass tube to form the gas cavity, as shown in Figure 5.6.

Optical windows and vacuum outlets are built into the end plates to facilitate the vacuum evacuation as well as allowing the radiation in and out of the cavity. The gas cavity is first vacuum evacuated, before being filled with methanol vapour at a pressure in the region of about 1 torr. At too low vapour pressure, the available methanol molecules are not sufficient to sustain the laser gain excitation against losses. On the other hand, if the methanol is filled to a much higher pressure, the rate of collision between excited molecules increases. If the rate of collisions in which the excited molecules can be de-excited is higher than or comparable to the rate of populating the upper laser state, then the laser oscillation is greatly reduced [151]. At this pressure, the mean time between collisions of the molecules are expected to be greater than the pump pulse width.

A Fabry-Perot resonant cavity is formed with a pair of gold-coated copper mirrors. In order to have a large mode overlap between the laser and pump radiation, a semiconfocal resonator is chosen, where the input mirror is plane and the output mirror is spherical. The entrance and exit of the input excitation beam and output laser emission from the laser resonator cavity are via small through holes at the centre of the mirrors. In addition, the laser cavity length is designed to be slightly adjustable (a maximum movement of 2.5 mm in the axial axis). This is to ensure that the length of the resonator can be tuned to resonant with the axial mode of the resonator, where at certain cavity lengths, no laser output can be obtained. The variation in the cavity length is also useful in the analysis of the FIR laser emission. When the resonator length is adjusted, a phase shift is introduced after one round trip. Hence, the output power from the laser can be maximised with appropriate tuning of the resonator length. This feature can also be used in determining the emission wavelength of the laser, as will be describe in the coming section. The resonator movement is provided by attaching the output end-mirror to a micrometer controlled movable stage, which is further coupled out of the gas cavity through a rotational turning knob. A potassium chloride (KCl) window, which transmits very well in the CO_2 emission region (refer to Figure A. 3), is chosen as the input window for the gas cavity. At the output end of the cavity, a TPX window is used to allow for the transmission of FIR emission while at the same time blocking the CO_2 laser beam.

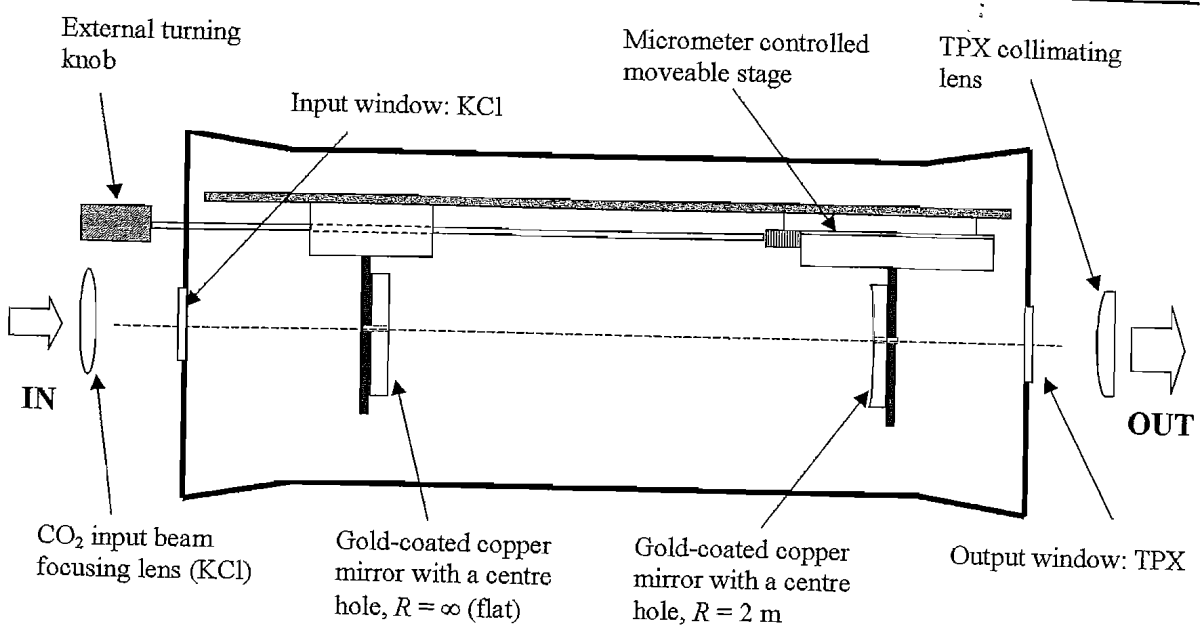

Figure 5.6. Schematic diagram of the optically pumped FIR gas laser. The gas cavity for the laser is formed by sealing a glass tube with two flat metal plates tightly secured at both end of the cylinder tube. Optical windows and other outlets are incorporated into the end-plates. The cavity is first vacuum pumped to low pressure before being filled with methanol vapour to a pressure of ~ 1 torr.

5.4.3 Optical resonator cavity

The TEA CO_2 laser beam typically has a waist diameter of 6 mm, which is focused into the laser cavity by a KCl lens with a focal length of 30 cm. The focussed beam waist is located at the input end-mirror (M_1), with the beam then diverging before being reflected by the output end-mirror (M_2). By careful choice of cavity length and mirror diameter, the overlap of the pump beam and laser mode can be maximised. With a laser cavity length of 0.75 m, i.e. the distance between the two mirror-fronts, the field spot size of the FIR laser mode is as depicted in Figure 5.7, which shows a mode waist at the flat mirror front. M_2 has a radius of curvature of 2 m, such that the divergence of the pump beam inside the cavity is reduced when reflected at this mirror. In order to allow for the pump beam to reflect at least twice within the cavity, as shown in Figure 5.7, the diameter of the mirrors used must be sufficiently greater than the first two reflected pump beam diameters. Mirrors with 38 mm diameter are used for both mirrors, which satisfy the requirements mentioned above. The pump beam enters the cavity through a 1.2 mm diameter hole in the centre of M_1. The laser emission is coupled out of the cavity by a 1.5 mm diameter hole in the centre of M_2. By using such holes coupling, the power losses of the FIR laser mode at the input and output ends

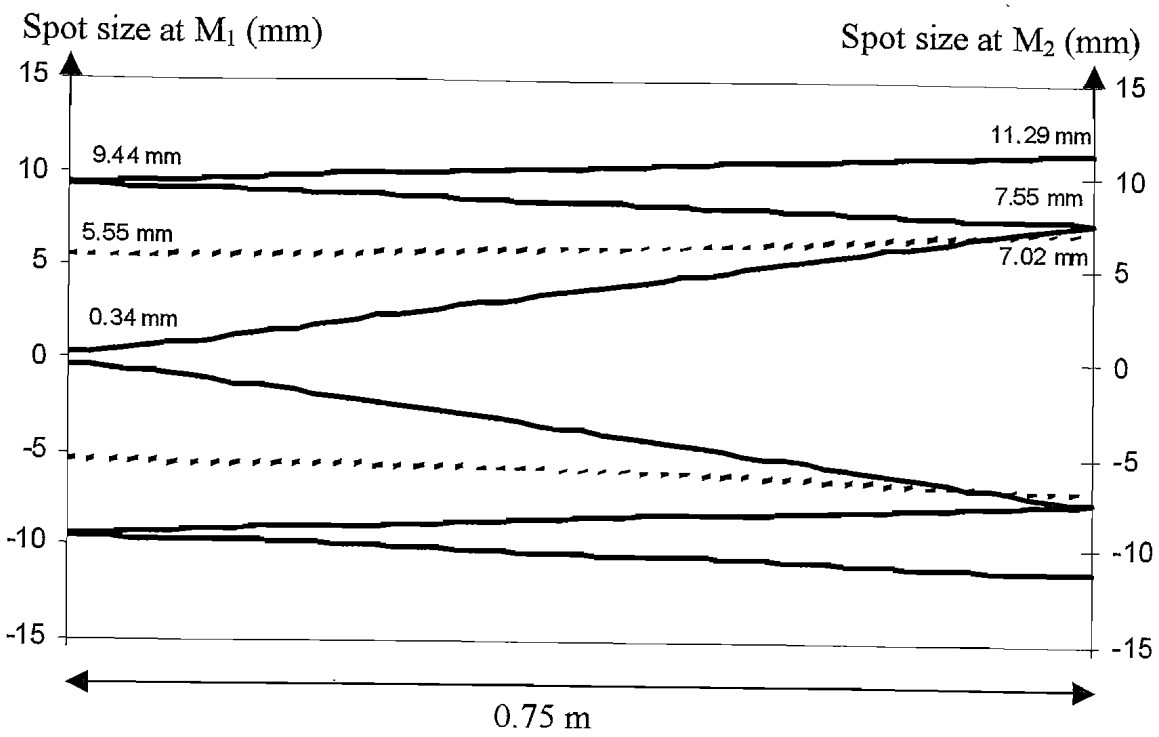

Figure 5.7. The field spot size of the focused CO_2 pump pulse (solid line) and the FIR laser mode (dashed line) for the gas laser. They are calculated based on the pumped and FIR laser lines of 10.6 μm and 100 μm respectively. The cavity length is taken to be 0.75 m between the two end mirrors, M_1 and M_2.

need to be kept low to have low laser threshold. The main interest in this gas laser is to test the Ge:Ga detector and hence high output power from this laser is not essential. Higher optical power can be achieved if a larger output coupled hole is used, at the expense of higher laser loss and threshold.

The power loss for a Gaussian mode with a central coupled hole is estimated as [68]:

$$P_{loss}(a) = \frac{2}{\pi w^2}\int_0^a 2\pi r \exp\left(-2\frac{r^2}{w^2}\right)dr = 1-\exp\left(-2\frac{a^2}{w^2}\right) \tag{5.2}$$

where a is the radius of the hole and w is the FIR mode radius at the mirror. By substituting the coupling holes radii into Equation 5.2, the power loss at the input and output mirrors are calculated to be 2.31 % and 2.26 % respectively, assuming a wavelength of 100 μm. Hence, the total power loss from the cavity due to the coupling holes is reasonably low. As the Fresnel number N_0 for the circular mirrors laser cavity is reasonably high ($N_0 \sim 5$, assuming $\lambda = 100$ μm), diffraction loss is estimated to be

low (~ 5% per round-trip propagation) [152]. In addition, the reflection loss is expected to be low as the gold-coated mirrors have very high reflectance in the FIR region. Therefore, this gas laser is aimed to easily emit FIR laser signals for use as an alternative FIR source, rather than to achieve very high output power.

As the FIR laser emission out of the cavity is diverging, it is necessary to collimate the FIR beam. A TPX plano-convex lens is employed to collimate the emitted FIR beam at the output. With a focal length of 15 cm, the collimated beam size is expected to be ~13 mm assuming the emission is at λ = 100 μm. Gold-coated copper mirrors are then needed to reflect the FIR beam in the optical path for detection and analysis.

5.4.4 Cavity scan

In order to allow for tuning in the cavity length, M_1 is mounted fixed but M_2 is mounted in a micrometer-controlled moveable stage, as shown in Figure 5.6. This mounting arrangement enables the tuning of the cavity length whilst preserving the optical alignment of the mirrors. When the cavity length is varied, distinctive and well-defined peak output power can be observed. These successive peaks when the cavity length is changed can indeed be used to calculate the wavelength of the laser emission. This is often referred to as cavity scan [148], which is widely used in optically pumped gas laser to determine the emission wavelengths. To a great accuracy, the successive peaks occur at a scanning distance corresponds to a half of the emission wavelength [148]. To improve the accuracy of the wavelength measurements, the cavity length is scanned for a distance such that many peaks can be observed. The mechanical scanning can be easily provided by using a DC motor, coupled to the external turning knob (refer to Figure 5.6) via a flexible rubber belt.

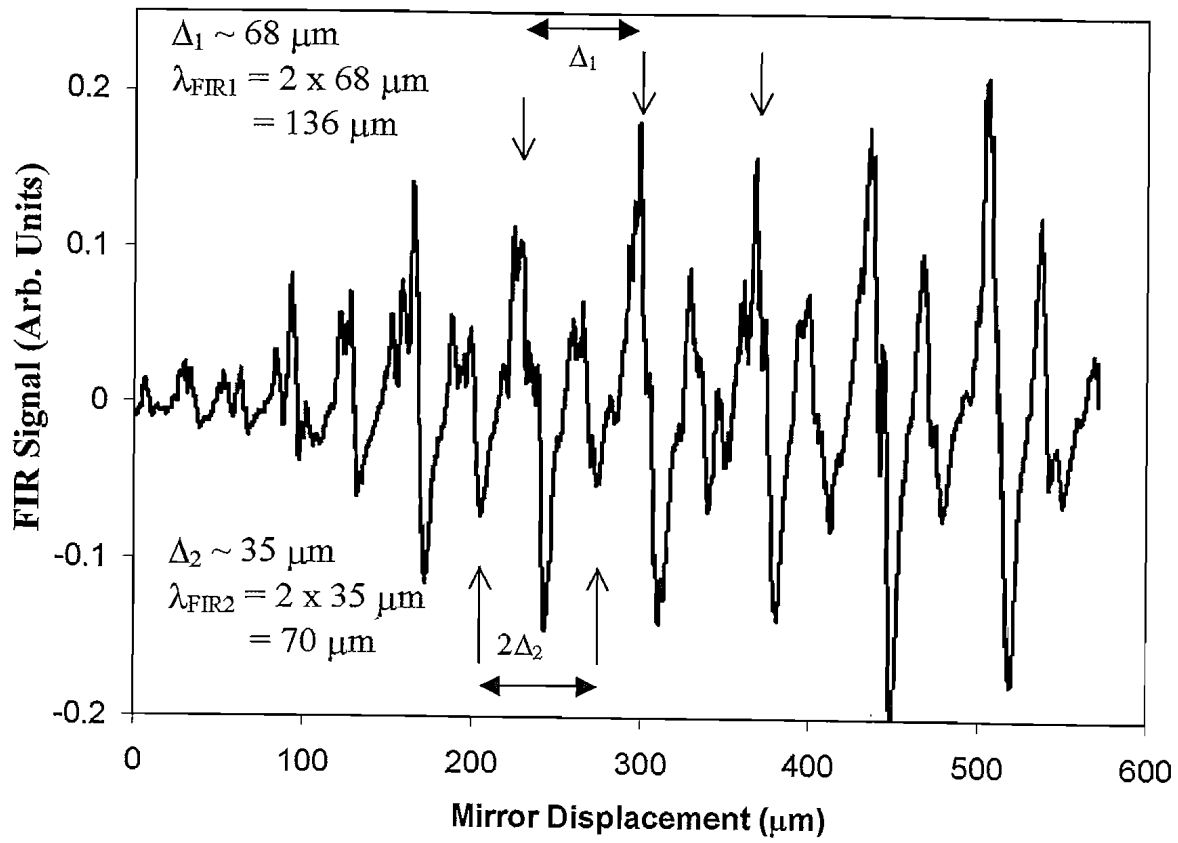

Figure 5.8. The integrated FIR signal as a function of the mirror displacement, when the CO_2 pump line is at 9R10. The distance between two successive peaks in the signal is related to a half of the FIR wavelength. This graph reveals two wavelength components at 136 μm and 70 μm, which are not uncommon in methanol gas lasers.

An example of the typically obtained integrated signal when the mirror was displaced at a small distance (< 1 mm) is shown in Figure 5.8. By using a boxcar integrator, the detected FIR signal was first averaged and then integrated. This integrated signal was then recorded as the resonator length was slowly changed, typically at the order of 10 μm/s. More than a single FIR laser emission wavelength can be present at any CO_2 pump line. Hence, the recorded cavity scan signals often showed a combination pattern of two or more peaks, such as that shown in Figure 5.8. The estimated wavelengths in this case were obtained taking only the clear maxima of the signal, since other wavelength components were not easily extracted due to the fluctuation of the emitted signal. This complex pattern is most possibly caused by multiple FIR transverse modes, which have different axial resonance.

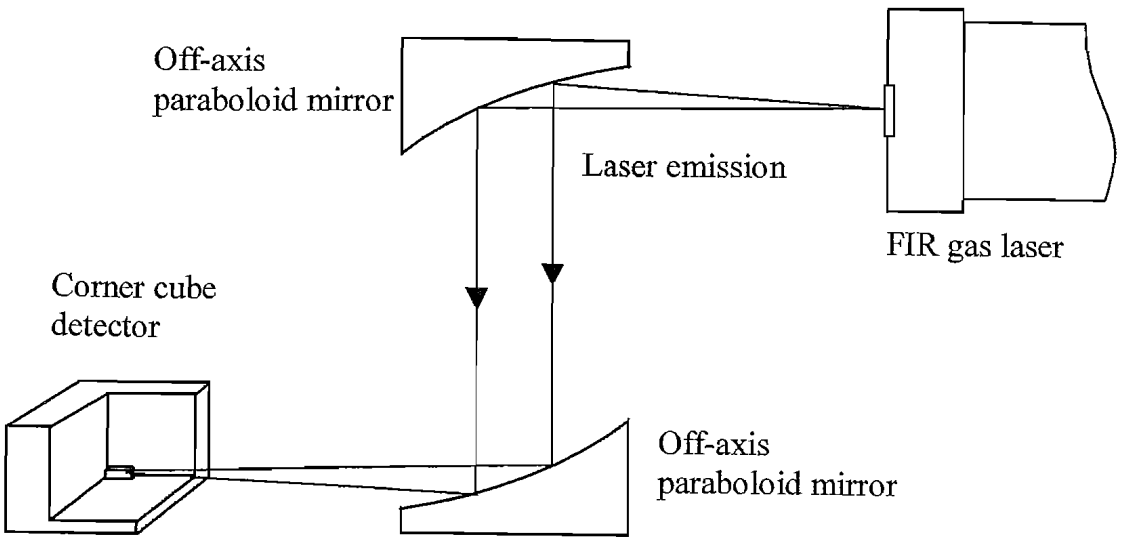

Figure 5.9. A pair of off-axis paraboloid mirrors are utilised to focus the FIR signals into the corner cube reflector. The mirrors are gold-coated and off-axis at right angles.

5.4.5 Detection of FIR emission

A corner cube detector from Farran Technology capable of resolving the pulse response of the FIR emission is utilised to detect the FIR laser emission. The detector is essentially a long wire antenna connecting with a low-capacitance Schottky diode that is combined with a corner cube reflector. This detector is useful for detection range of 100 – 150 μm, with a typical responsivity of 15 V/W and NEP of 10^{-8} W/Hz^{½}. A pair of off-axis parabolic mirrors are utilised to focus the detected radiation into the corner cube reflector, as shown in Figure 5.9. The output signal from the detector is then enlarged by a 40 dB preamplifier and monitored in a digital oscilloscope. After first using the corner cube detector to observe the emission from the methanol laser, the Ge:Ga detector is utilised once the FIR emissions have been obtained from the gas laser. Although this detector is less sensitive than the Ge:Ga detector (by three orders of magnitude), it is convenient to use and operating at room temperature. Optical output from the gas laser is sufficiently large to be detected using this detector.

5.4.6 Discussion

It will be very interesting to study the FIR methanol laser in more detail, for example to record the possible strong laser emission from this laser when pumped by different CO_2 lines. However, due to the time constraint of the project, a more detail study of the methanol laser was not carried out. Instead, only a few CO_2 laser lines were chosen as the pumped line and the FIR emission observed with either the corner cube detector or

the Ge:Ga detector. Clearly, it will take considerate amount of time and effort to perform more detail studies of this laser, given the vast laser lines that have already been reported for methanol and its isotopes as the laser medium. Moreover, most of the reported lines are for CW pumped and relatively little pulsed laser lines are listed [22, 148, 149].

In addition, the laser signal was not very stable as the emission of the laser fluctuated. This caused particular difficulties to the cavity scan process as the recorded signal strength varied and the maxima may not be consistent. Improvements to the laser may be obtained by amplitude or frequency stabilisation [153], and more accurate wavelength measurements by external scanning, e.g. a Fabry-Perot interferometer [148]. However, the FIR gas laser is adequate for our test purpose, as described before in the pulse response of the Ge:Ga detector.

5.5 End mirror coating

In our optically pumped FIR lasers, the cleaved surfaces of a MQW slab can be utilised to form the resonator cavity. FIR emission in the active layers that propagates along the axial direction is reflected between the cleaved surfaces of the slabs. The reflection process along the resonator is essential to build up the stimulated emission until a substantial gain is achieved to overcome the various losses before laser action is possible. Ideally, the cleaved surfaces need to have high reflectivity in order to reduce transmission loss and increase the stimulated emission gain. However, the reflectivity from the cleaved surface of GaAs is fairly low, estimated to be 34 %, assuming n = 3.77 at λ = 60 μm. This will mean more than half of the initial emission is lost at each reflection at the cleaved surface, making the laser emission very hard to realise, if not impossible. Consequently, it is desirable that this reflection loss can be reduced. A very effective way of increasing the reflectivity of the cleaved surface is by applying a thin layer of metal. Metals such as Al and Au are good reflector in FIR region. A thin layer (~0.5 μm) of Al for example, can be coated at the long edge (cleaved side) of the MQW slab. This layer of metal can be easily coated using the vacuum evaporation technique. An Edward 306 coater can be utilised to evaporate the metal layer to the MQW slab. It is essential to avoid coating the shorter edge of the slab where the pump beam is focussed into (refer to Figure 4.1), in order to maximise the absorption of the pump energy by the MQW slab.

5.6 Conclusion

Detectors employed in our work of designing an optically pumped MQW FIR laser are described in this chapter. As there is hardly any commercially available detector for the FIR, a very low temperature extrinsic Ge:Ga photoconductor is chosen for the FIR detection system. This is a fast and sensitive detector, which has a wavelength response that is very suitable for our work. Working principles of this type of extrinsic detectors are first introduced. The output signal from this detector must first be amplified, preferably with the preamplifier located close to the detector element itself. As a result, a transimpedance amplifier was constructed for this purpose. A combination of filters and windows are necessary in working with the optically pumped laser system. The optical components are chosen based on their wavelength transmission properties. Several of these optical materials, which are utilised throughout this work, are listed and their properties detailed. In addition to the low temperature Ge:Ga detector, room temperature pyroelectric detectors are used extensively in our experimental work.

Optically pumped FIR gas lasers have played important roles in understanding the FIR region, even up until the present day where other sources have been discovered. An in-house FIR gas laser has been constructed, which is a useful experimental tool in the work for achieving the FIR emission from the MQW structures. In particular, this gas laser is valuable in characterising the Ge:Ga detectors. The design and working of this gas laser have been discussed, where the laser is based on methanol vapour as its gain medium. A simple cavity scan method is employed in determining the FIR emission from this gas laser. Several CO_2 laser lines are chosen to pump the methanol laser, where the emissions can be detected by using the Ge:Ga detector.

A blackbody source is used to check the responsivity of the Ge:Ga detector. The pulse response of the detector to the CO_2 laser pulse is compared to the response from a pyroelectric detector. A comparison of these pulse responses shows that the similar time response is achieved. Overall, the Ge:Ga detector has demonstrated expected responses to the FIR emissions from either the blackbody source or the methanol laser. Furthermore, the pulse responses of the detector to either the CO_2 laser or the methanol laser suggest that this detector is indeed capable of resolving the pulse response of the possible emission from the MQW laser. Hence, the Ge:Ga detector has proved to be working well and is functioning normally in the FIR measurements.

6 Conclusion and future work

6.1 Conclusion

This thesis describes the work to attempt an optically pumped FIR laser based on intersubband transitions with MQW structures. The working principles of the FIR lasers based on GaAs/AlGaAs MQW have been described in previous chapters. For an intersubband laser, the electron transitions between confined conduction subbands are responsible for the emission of photons in the FIR region. In contrast to most traditional semiconductor lasers, the transitions are not across the forbidden energy band gap between the conduction band and valence band. This is a major advantage for intersubband lasers, as wide band gap materials, such as the GaAs and AlGaAs compounds can be utilised to achieve the quantum confinement of the energy levels. These wide band gap materials are generally better studied and the epitaxial growth techniques are very advance. On the other hand, narrow gap materials are comparatively more difficult to grow into epitaxial layers.

As the photon energy is related to the energy separation between different energy subbands, the MQW structure has been designed to fulfil this requirement. The subband energy levels are in turn a function of several parameters of the individual layers. By choosing materials that have different energy band gaps, a QW is formed when these materials are grown into successive layers that are very thin, down to a few monolayers. In $Al_xGa_{1-x}As$, the energy band gap is determined by the content of Al in the compound material. In comparison, GaAs has smaller band gap energy. Therefore, a higher energy barrier is achieved when the amount of Al present is increased. A stepped QW is formed when a layer of GaAs and a layer of intermediate AlGaAs are grown in between two layers of higher Al content AlGaAs. This three-level stepped QW design is the basic of our structures for FIR lasers.

In this three-level laser system, the population inversion is realised between the second and first excited subbands. However, electrons can only make transitions across subband energy levels with odd quantum number difference in a symmetric QW. Therefore, asymmetric QW design is needed to break this restriction. The subband energy separation for the pump transition is designed for the use of a CO_2 laser as the pump source to the FIR laser. Moreover, the energy subband levels were designed to take advantage of the fast scattering of LO phonons for the removal of electrons from

the lower laser level. In contrast, the upper to lower laser levels transition is dominated by the acoustic phonon assisted scattering by ensuring the energy difference is lower than the LO phonon energy. Scatterings due to acoustic phonon are orders of magnitude slower than the LO phonon assisted scattering. Consequently, population inversion is possible due to the different scattering rate for the upper and lower laser levels.

A self-consistent solver was used to numerically compute the solution to the subband energy levels of the MQW laser structures. This solver solves for the Schrödinger equation and the Poisson equation simultaneously until the solutions satisfy both equations. Non-uniform mesh sizes are used in the solver to rapidly compute the energy levels and the electron concentration in the structure. Nevertheless, the solver has limited mesh number and does not include the non-parabolicity effects to the subband levels due to the high electron concentration. Therefore, a uniform mesh size model was built to include the changes to the electron effective mass as a result of the high electron concentration within the QWs. A much smaller mesh size is used in this model to solve for the final solution to the subband energy levels. For this reason, the computational time for this model is much higher than the first solver. Simulation results show that the model can successfully compute the subband energy levels for our MQW structures.

In order to provide electrons for the pump and relaxation cycle, intersubband lasers are selectively doped in certain layers. The possible ways of doping the stepped QW have been explored to achieve the best performance for the laser structures. As large number of electrons is needed in the QW to increase the gain of the laser system, the doping level is therefore necessary to be high. Traditionally, the donor position is located at the middle of the barrier, between two successive QWs. The ionised donor and electrons are separated and electric potential exists due to these charges. This method has served well in most laser structures. However, at the high doping concentration that is required in the FIR laser system, the resulting electric potential is very significant. This electric potential was found to have seriously distorted the energy band profile of the QW. Furthermore, the subband energy levels of the QW depend strongly on the doping concentration, as a result of the severely distorted energy profile. Electrons that are excited during the pumping process can be trapped in the resulting parasitic wells, especially in the barrier regions. This reduces the number of electrons that are available

for stimulated emission. Very high free carrier loss may also result from these electrons. As a result, an alternative way of doping the structure at the edge of the stepped well was proposed. Our modelled results suggest that improved control over the energy levels can be achieved. In addition, the issue of trapped electrons has been greatly improved, due to the elimination of the parasitic wells in the barriers. Nonetheless, a distorted parasitic well is formed in the stepped well region. Fortunately, this parasitic well is shallow and has a very thin barrier, hence electron tunnelling through the barrier is possible. Consequently, a sample based on this dopant placement in the stepped well was grown. Photoluminescence signal was observed for this sample when a FEL was used to excite electrons to the upper subband. Examinations of the signal showed that the FIR emission wavelength agreed with the transitions revealed in the measured intersubband absorption bands. Observing the photoluminescence signal from a laser structure is an encouraging progress in the effort towards realising a laser. Therefore, this observation has supported our arguments on the improvements of this design. Optical gain analysis of the laser was discussed where the threshold pump intensity required for population inversion was estimated.

Electron lifetimes at the subband energy levels play an important role in the operation of an intersubband laser. Thus, it is very valuable if these electron lifetimes, especially the upper laser level lifetime, can be measured. By using the FEL in the user facility at FELIX, three-beam pump-probe measurements have been conducted to study the electron lifetimes of the MQW structures. The measurements utilised the picosecond pulsed laser to excite electrons from the ground subband of the QW to higher subband energy levels. A change in the transmission of the structure occurred when these electrons were excited and then relaxed back to the ground subband. This change was monitored using a time delayed probe beam, which was also split from the same FEL beam. Consequently, the electron lifetime for the higher subband can be deduced from the transmission change as a function of the time delay between the pump and probe beams. Measurements have been successfully carried out for a few MQW structures, which are different in design. Electron lifetimes of the order of a few picoseconds were measured for these MQW structures, which are in consistent with other reported values.

In addition, long decay signals have been observed for some of the MQW samples, which were modulation doped in the barrier. These signals, which were on sub-nanosecond scale, could be attributed to the multi-photon absorption of the excited

electrons. At high pump intensities, electrons that were promoted to the higher subband could be further excited to the continuum subband. These electrons in the continuum conduction band can be recaptured by the donors at the barrier, before returning to the well when the donors are reionised. The strongest absorptive signal was observed with a MQW sample with the energy barrier close to the two-photon energy of the pump beam. As the pump intensities were reduced, the strength of the slow decay signal decreased, suggesting a strong intensity dependent. When the barrier energy was increased in another sample, only weak long decay signals were observed at high pump intensities. Although two-photon absorption was eliminated with this structure, higher order absorption was still possible. This agreed very well with our argument that multi-photon absorption was involved at high pump intensities. In the process of analysing the observation from the electron lifetime measurements, a rate equation model was derived. This 3-level equation model successfully reproduced the characteristic features shown by the electron transitions during the pump-probe experiments. All in all, the fitted result with the model agreed well with the experimental data.

Laser actions are not possible for the MQW samples unless the intersubband emissions are waveguided to allow for the laser gain to build up. This is necessary as the traditional method of confining laser emissions relies on the small difference in refractive index values of the core and cladding layers. However, the FIR wavelength is long compared to the active layers in a MQW laser structure. It is therefore impossible to grow a very thick structure using the same method. This problem has proved to be a major obstacle in realising a FIR laser. Various ways have been explored for potentially achieving the waveguide for our FIR laser. In particular, a novel idea of stacking two identical MQW slabs face to face has been proposed. One immediate advantage of such scheme is the doubled of gain area as the number of available QWs has been doubled. However, there is one possible disadvantage of this stacking scheme, which is the increased diffraction loss due to the error in aligning the slabs. Hence, a cavity model based on an open resonator approach was constructed. This model involves solving the Fresnel integrals, which assumes that an arbitrary wave is propagated to and forth two parallel mirrors. The simulated result shows that the diffraction loss is small compared to other losses, such as the reflection loss at the cleaved surfaces. This is true if the error is kept small (< 4 μm) but still achievable in practice.

Although the double-stacked slabs arrangement results in a low loss FIR mode, the mode overlap with the active layers is low. A plasmon-enhanced waveguide can be achieved with a medium doped layer embedded within the MQW structure. A much higher mode overlap value can indeed be obtained, albeit at a price of intolerably high modal loss. Consequently, designs based on surface plasmon guided structures with heavily doped layers are explored. A transfer matrix modal was first constructed to compute the TM mode for the structures. The refractive index of the heavily doped layer is computed using a Drude model. Modelled results suggested that low loss structures are possible with two approaches. By growing a heavily doped layer between the substrate and the MQW active layers, the surface plasmon exists at the interface of the doped layer and the undoped active layers. The mode overlap is further enhanced with a metal layer coated at the surface of the sample to achieve a double surface plasmon guided structure. Our modelled result shows that the laser mode is confined well within the active area, with a reasonable value of modal loss. Alternatively, the stacked slabs design can be applied using the samples with the heavily doped layers embedded. A favourable modal loss and confinement ratio are also predicted for this approach. As a whole, this design of stacked double slabs with heavily doped layers appears to offer the best design compromise and performance. This design has not been tested experimentally due to the time and financial constraint of this work.

The FIR optical system, although largely similar in principle to the visible and other infrared regions, requires the use of specific detectors and optical materials. Effective FIR detectors are hard to obtain commercially. Therefore, a Ge:Ga photoconductor has been utilised for the detection of FIR signals. The performance of the detector was analysed using the blackbody source and attenuated CO_2 laser beam to check for the responsivity and the pulse response. A preamplifier was first built to amplify the small signal from the detector before the signal was further amplified by other means, e.g. a commercially available amplifier. A FIR methanol gas laser was also constructed, which was useful in the analysis of the detector as well as providing an additional FIR source. The FIR emission from this laser was adequate to be effectively detected by the Ge:Ga detector. Overall, the detector has shown to be working effectively in the FIR measurements.

6.2 Future work

FIR or THz wave studies have now attracted increasing attention as the result of increasing research activities and inevitable breakthroughs being achieved in the field. Although real world applications for FIR lasers are scarce, possible uses are plenty. These potential uses range from medical or "T-ray" imaging, inter-satellite communication, planetary or astronomical objects sensing, plasma fusion diagnostics, and gas spectroscopy. Discussions on the terahertz technology can be found at a recent review by Siegel [154] and the references therein. New application in FIR or THz technologies may start to appear when the sources are more easily available. Ever since intersubband transitions have been reported, FIR or THz lasers based on intersubband lasers structure have received much attention. In particular, following the successful attempt of producing a QC THz laser, further development in the FIR field is anticipated. Nevertheless, many years are perhaps needed before the potential of the THz technologies can be fully exploited.

Although it has not been successful in this work to produce an optically pumped MQW FIR laser, the collected results throughout suggested that a laser emission is highly probable. Due to financial and time constraints, it has not been possible to produce a sample that would include the heavily doped layers for our surface plasmon guided device. The pumping arrangement of stacking two of these laser slabs has the potential to achieve a moderately low modal loss FIR laser system.

Appendix 1. Transmission spectra of the filters

Optical materials used in this work were selected mainly based on the light transmission properties of the materials at different wavelengths of interest. It is thus of interest to provide the transmission spectra of these materials as a reference. These spectra were measured at room temperature using the FTIR spectrometer at mid- and far infrared wavelengths. Materials used for Figure A. 1 to Figure A. 4 are listed in Table A 1. A Mylar film beam splitter was used for the measurement at FIR while a KBr beam splitter was utilised for mid-IR measurement. The detectors used were both TGS pyroelectric detectors.

Optical material	**Thickness (mm)**
Barium Fluoride (BaF_2)	3
Black polyethylene	0.1
Cesium Iodide (CsI)	4.5
Crystalline quartz (SiO_2)	1
Polymethylpentene (TPX)	3
Potassium bromide (KBr)	4
Potassium chloride (KCl)	4
Zinc selenide (ZnSe)	3

Table A 1. A list of materials and their thickness measured with the FTIR to obtain the transmission spectra at room temperature.

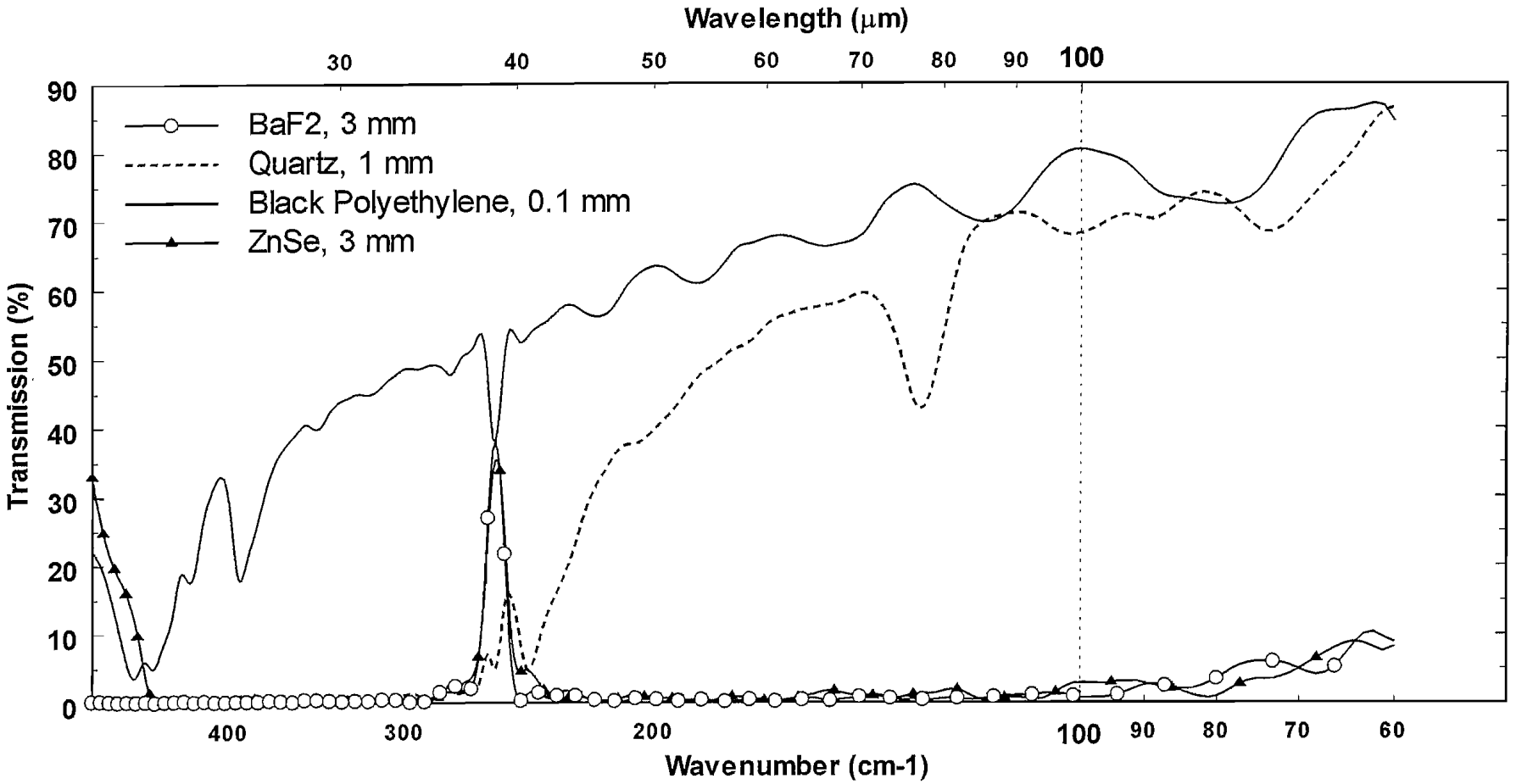

Figure A. 1. Transmission spectra of a 3 mm thick BaF_2, a 1 mm thick quartz, a thin (0.1 mm) black polyethylene, and a 3 mm thick ZnSe, as measured in a FTIR spectrometer at room temperature.

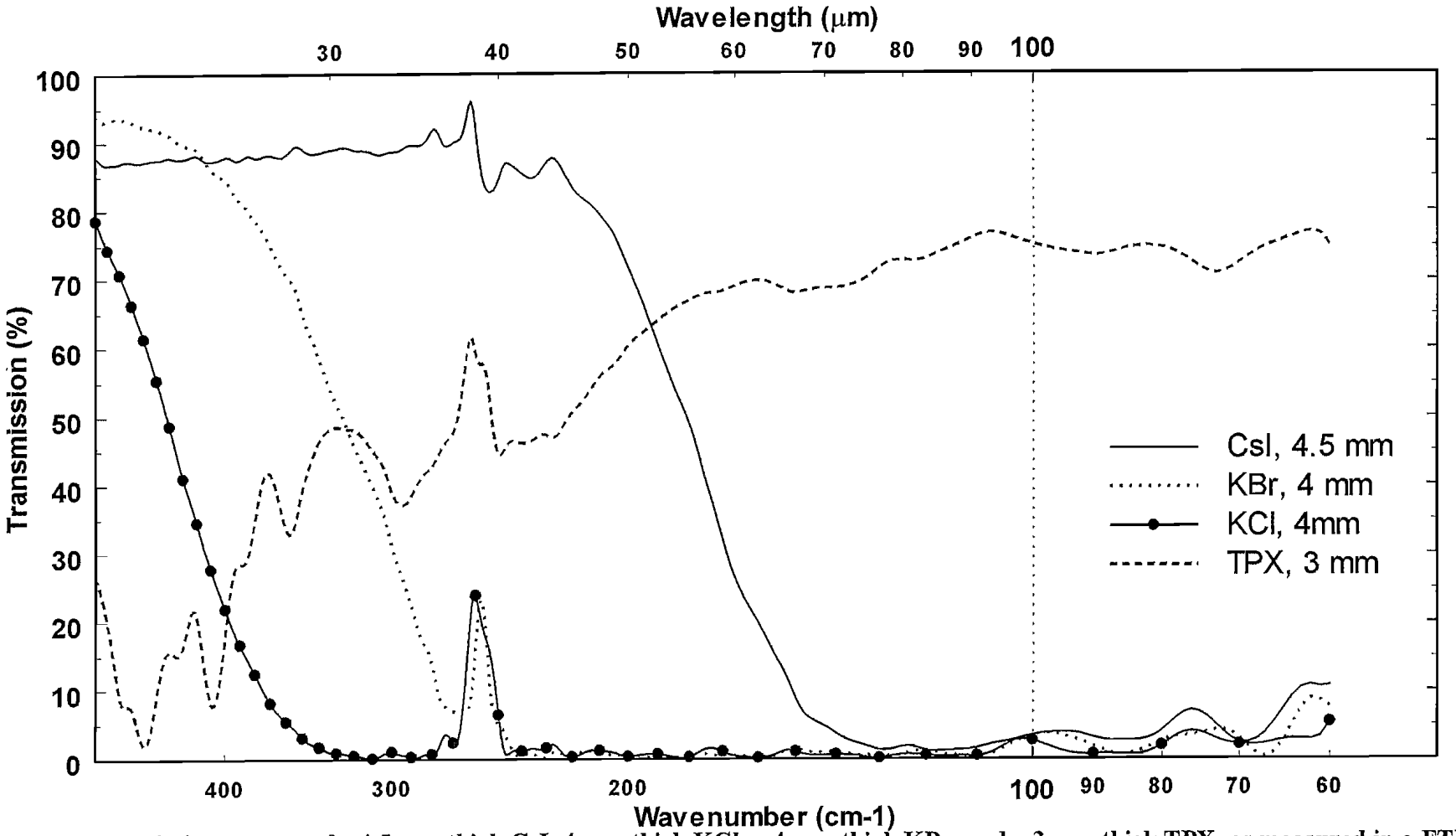

Figure A. 2. Transmission spectra of a 4.5 mm thick CsI, 4 mm thick KCl, a 4 mm thick KBr, and a 3 mm thick TPX, as measured in a FTIR spectrometer at room temperature.

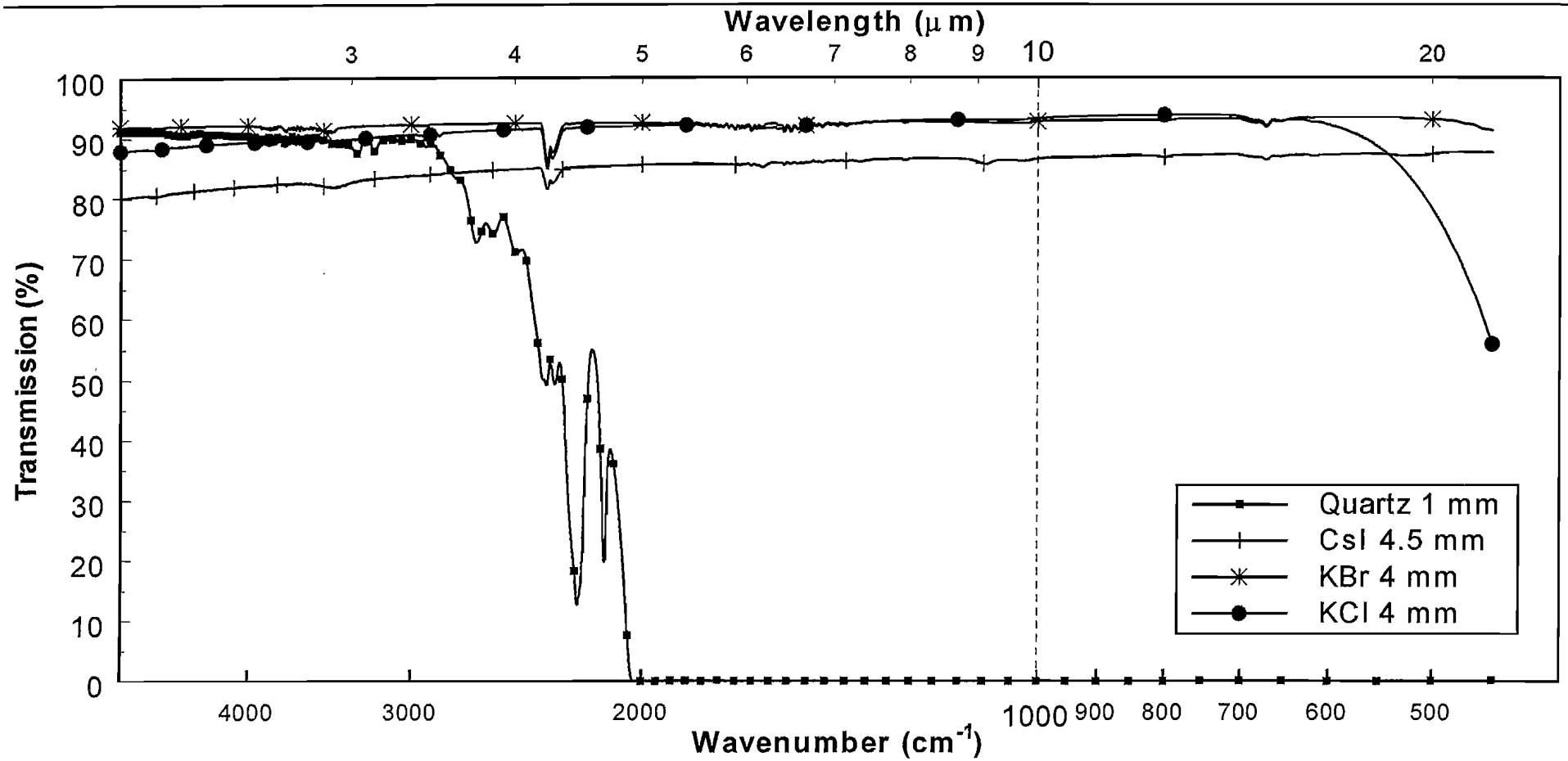

Figure A. 3. Transmission spectra of a 4 mm thick KCl, a 4 mm thick KBr, a 4.5 mm thick CsI, and a 1 mm thick crystalline quartz, as measured in a FTIR spectrometer at room temperature.

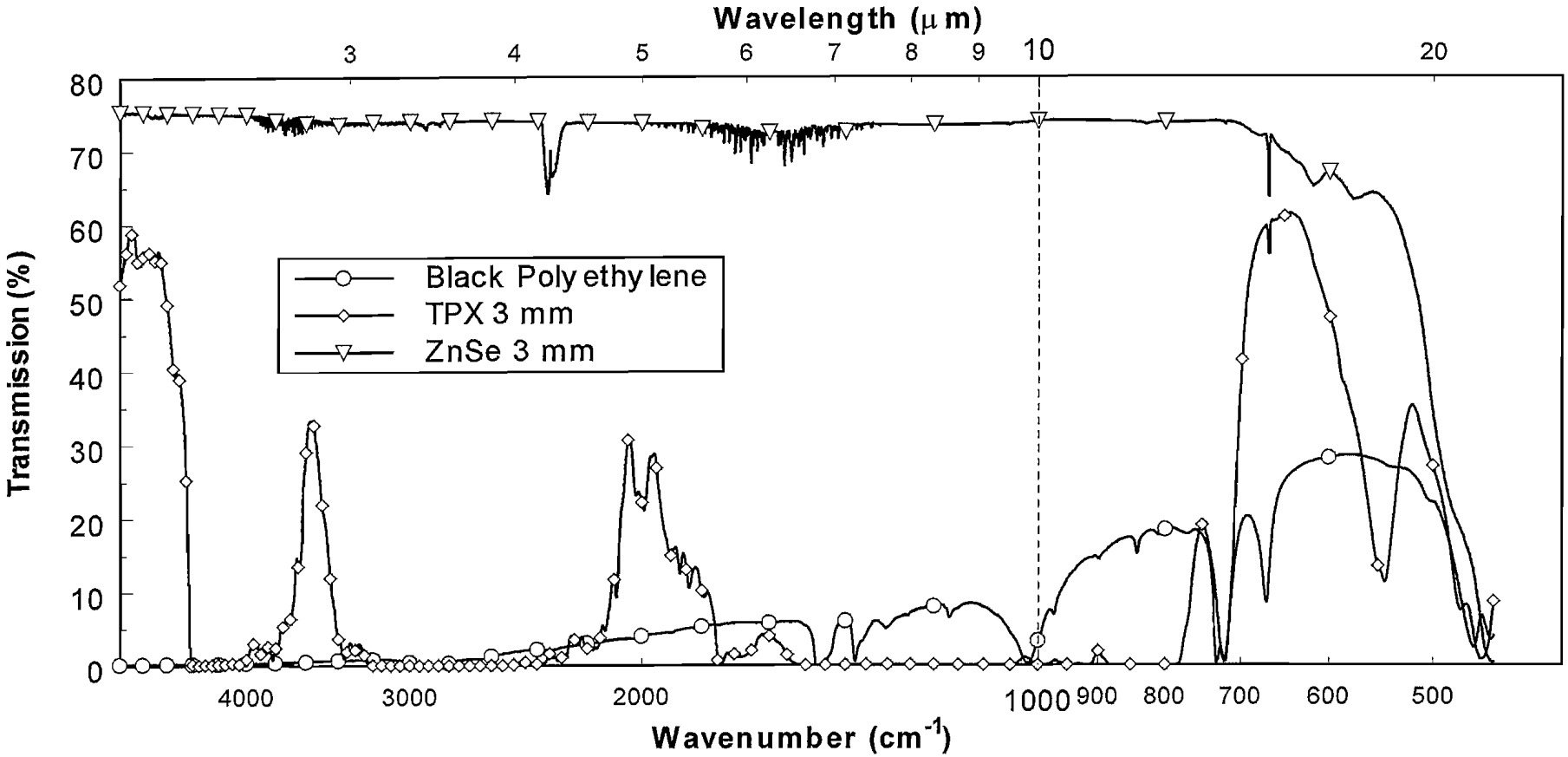

Figure A. 4. Transmission spectra of a 3 mm thick ZnSe, a 3 mm thick TPX, and a 0.1 mm thick sheet of black polyethylene, as measured in a FTIR spectrometer at room temperature.

Appendix 2. Blackbody emission

A.2.1 Spectral radiant emittance, W_λ

For a blackbody object at an absolute temperature T, the spectral emittance per unit area per unit wavelength is defined as [145]:

$$W_\lambda(T,\lambda) = \frac{C_1}{\lambda^5\left(e^{C_2/\lambda T}-1\right)} W/cm^2\,\mu m \qquad \text{(A.1)}$$

where $C_1 = 2\pi hc^2$ is the first radiant constant, $C_2 = hc/k$ is the second radiant constant, h is the Planck's constant, c is the velocity of light in free space, and k is the Boltzmann constant.

Figure A. 5. shows blackbody spectral emittance curves for various temperature calculated based on Equation A.1. The radiant emittance in terms of power for the wavelength range of λ_1 to λ_2 is given by Equation A.2:

$$W(T) = \int_{\lambda_1 \mu m}^{\lambda_2 \mu m} W_\lambda(T,\lambda)\,d\lambda \qquad \text{(A.2)}$$

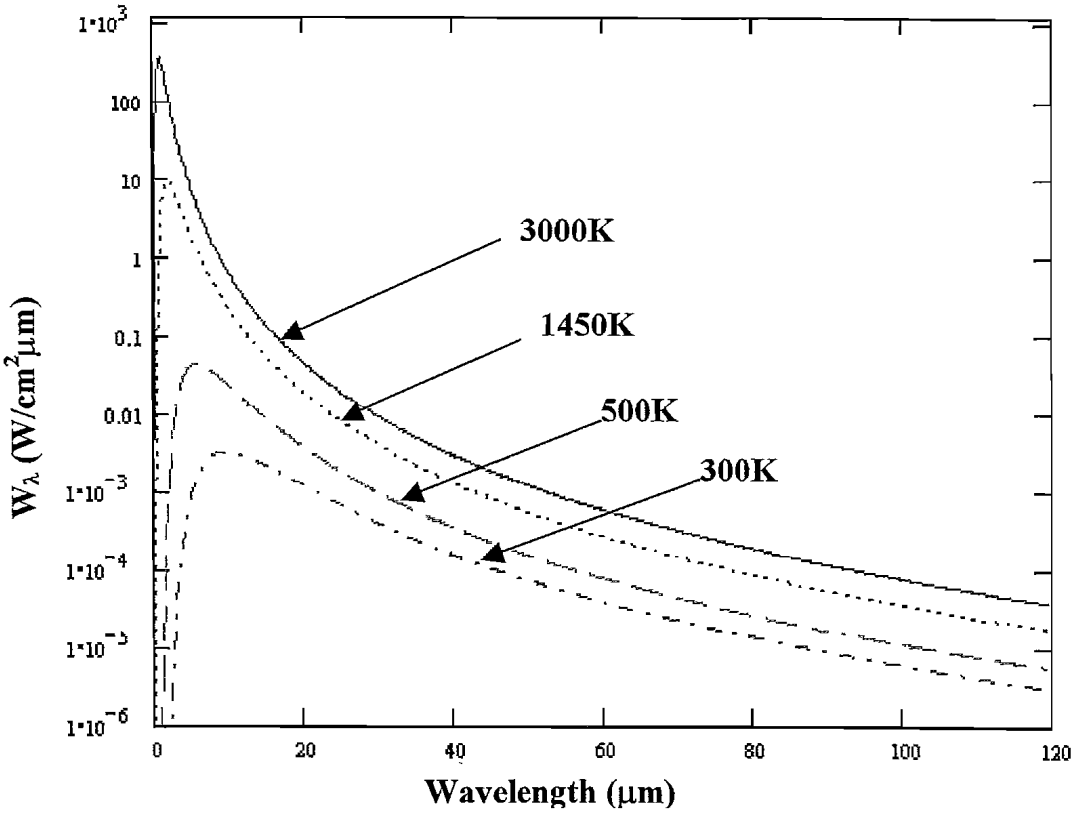

Figure A. 5. Blackbody spectral radiant emittance at various temperatures.

A.2.2 Background flux

In this section, the background radiation seen by the MQW sample inside a cooled cryostat is estimated for the pump-probe measurements as described in section 3.3.6. This background radiation can be regarded as emission from a blackbody source at room temperature. At a background temperature T, the flux per unit area or the irradiance is related to the half-angle FOV, θ [140]:

$$H_{photon}(T) = W_{photon}(T)\sin^2(\theta) \tag{A.3}$$

where the radiant emittance in terms of number of photon W_{photon} is used instead of the expression in Equations A.1 and A.2. This is given by:

$$W_{photon}(T) = \int_{\lambda_1}^{\lambda_2} \frac{2\pi c}{\lambda^4\left(e^{hc/kT\lambda} - 1\right)} d\lambda \tag{A.4}$$

Therefore, the total irradiance at the sample for the case where no additional cold apertures are added (as depicted by Figure 3.11.a) is given as:

$$H_{photon}(T = 293\text{K}) = \int_{0.6\mu m}^{18\mu m} \frac{2\pi c}{\lambda^4\left(e^{hc/kT\lambda} - 1\right)} d\lambda \times \left[\sin^2(55.5^\circ) + \sin^2(75.8^\circ)\right] \tag{A.5}$$

$$= 2.6\times10^{18}\ photons/cm^2 s$$

where the wavelength limits are determined by the transmission of the ZnSe windows used in the experiment. Similarly, the photon flux for the case with additional cold apertures (referred to Figure 3.11.b) is estimated to be about one third of the value in Equation A.5.

Consequently, the total number of photons per unit time that are detected by the sample is given by:

$$N_{photon} = \sigma H_{photon}(T = 293\text{K}) \tag{A.6}$$

where σ is the absorption cross sectional area of the electrons at the barrier of the QW. The value of σ is assumed to be that of free carriers absorption and is in the order of $\sim10^{-18}$ to 10^{-15} cm^2 for doping levels of the order of 10^{17} to 10^{18} cm^{-3}. N_{photon} will then be ~1 to 10^3 s^{-1}. Therefore, N_{photon} is too small to be the excitation source for reionisation of the electrons trapped in the barrier, where the electrons are then returned

to the well at a sub-ns rate. This is the case since the carrier sheet density is of the order of 10^{12} cm^{-2} and a significant number of electrons (~<1 %) may be excited to the barrier region at high pump intensities.

A.2.3 Responsivity of the Ge:Ga detector

The response of the Ge:Ga detector was measured by setting the blackbody source at a temperature of 1450 K, which will be described in this section. For a blackbody source, the amount of infrared energy incident on a detector's sensing area, the irradiance (H) in terms of power is calculated as [145]:

$$H(T) = W(T) F \frac{a^2}{4d^2} t \tag{A.7}$$

where F is the root-mean-square (RMS) conversion factor of the source, a is the limiting aperture diameter, d is the distance from the aperture plane to the sensing area plane, and t is the transmission of the optical path.

An aperture size of the blackbody source was selected at a diameter of 0.4" (~ 1.02 cm), and the distance from this aperture to the detector was 11 cm. The radiated signal from the blackbody was directed at the photoconductor, which was cooled to a temperature of 6.4 K. The detected signal was amplified by the transimpedance preamplifier, before being further amplified by a factor of 10 using a low noise preamplifier. The radiation was modulated using a mechanical chopper, with a frequency of 800 – 1000 Hz.

Using the transmission spectra of the filters used, namely TPX, crystalline quartz, and black polyethylene, the average values of the transmission factors are taken to be

$$\begin{aligned} t &= t(TPX) \cdot t(quartz) \cdot t(polyethylene) \\ &\approx (0.6)^3 \\ &= 0.216 \end{aligned} \tag{A.8}$$

With T = 1450 K, from Equations A.1 and A.2, we have

$$\begin{aligned} W(1450) &= \int_{40\,\mu m}^{120\,\mu m} \frac{C_1}{\lambda^5 \left(e^{C_2/1450\lambda} - 1 \right)} d\lambda \\ &= 0.017\ \mathrm{W/cm^2} \end{aligned} \tag{A.9}$$

This wavelength range is chosen due to the combination of the filters used (TPX, crystalline quartz and black polyethylene) and the cut-off frequency of the Ge:Ga detector. The incident radiation detected by the detector was limited by the small aperture of the holder, which has a dimension of 3×1.5 mm^2. A RMS factor of $1/\sqrt{2}$ for a sinusoidal signal was included since the blackbody source was chopped. Hence, by substituting the values into Equation A.7, the detected incident power is deduced as

$$\begin{aligned} P_{incident} &= H(T)Area \\ &= (0.017)\left(\frac{1}{\sqrt{2}}\right)\frac{1.02^2}{4(11)^2}(0.216)(0.3\times 0.15) \\ &= 2.512\times 10^{-7}\ \text{W} \end{aligned} \tag{A.10}$$

The photocurrent of the detector before amplification was calculated to be 0.5 μA. After dividing the current over the incident power, a responsivity value of 2.0 A/W is yielded.

Appendix 3. MQW samples

In this appendix, some additional MQW samples that have shown intersubband absorption when measured with the FTIR spectrometer are described. First, the samples parameters for samples A1407, A1573, and RM1784 are listed in Table A 2. This is followed by the transmission spectra for the samples, all taken at room temperature.

Figure A. 6 shows the transmission spectra for sample A1407, which is fitted with wavelengths of 9.85 ± 0.1 μm and 10.55 ± 0.1 μm. This sample was designed before I was involved in the project. The sample was doped in the centre of the barrier, at a very high doping density (2.5×10^{12} cm^{-2}). As a result, the QW energy profile was severely distorted and coupling between adjacent QWs may occur.

Figure A. 7 shows the transmission spectra for sample A1573, which is doped at the stepped well edge. The fitted result shows two absorption wavelengths at 9.75 ± 0.1 μm and 10.65 ± 0.1 μm. Similarly, the transmission spectrum for another doped stepped well sample (RM1784) is displayed in Figure A. 8. Intersubband absorption wavelengths of 9.02 ± 0.1 μm and 10.31 ± 0.1 μm were obtained. Note that these two samples have the same design parameters as sample A1580, except the number of QW periods.

QW period	Barrier		Stepped well		Lower well		Dopants		
	x_b	L_b(nm)	x_s	L_s (nm)	x_w	L_w (nm)	N_d (10^{18} cm^{-3})	L_d (nm)	position
50	0.35	35	0.19	18.2	0	6.5	5	5	barrier
Sample A1573									
80	0.45	35	0.23	19.2	0	7.6	1.0	7.1	stepped well
Sample RM1784									
100	0.45	35	0.23	19.2	0	7.6	1.0	7.1	stepped well

Table A 2. Sample parameters for three $Al_xGa_{1-x}As$ MQW samples (A1407, A1573, and RM1784). Listed are the number of QW periods, the Aluminium contents and the growth width in the barrier (x_b, L_b), stepped well (x_s, L_s), and lower well (x_w, L_w). The position of the dopants, the doping concentration (N_d) and the doping length (L_d) are also included.

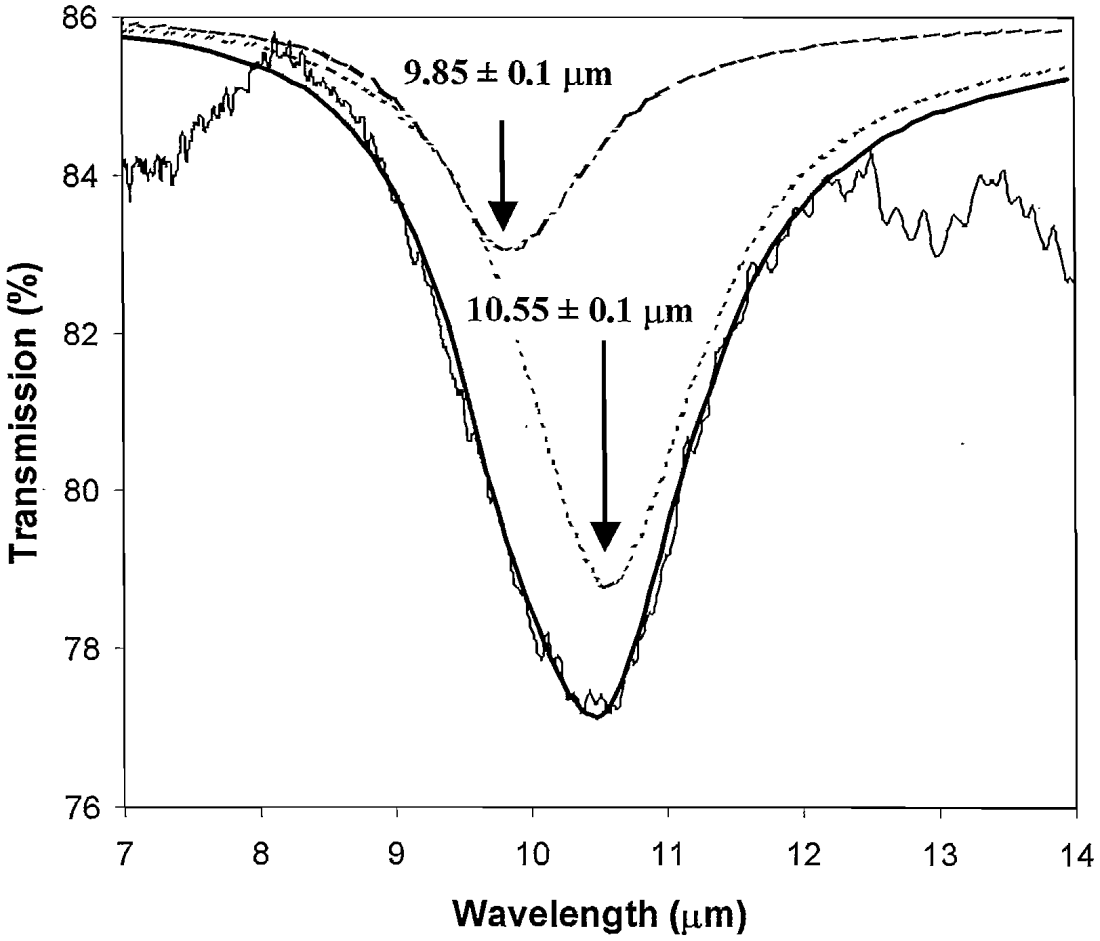

Figure A. 6. Transmission spectrum of sample A1407 taken at room temperature. The sample parameters are listed in Table A 2. Two intersubband absorption wavelengths were fitted at λ_{02} = 9.85 ± 0.1 μm (dash-dot line) and λ_{01} = 10.55 ± 0.1 μm (dashed line). The experimental data (thin solid line) was fitted with the combined absorption lines (thick solid line).

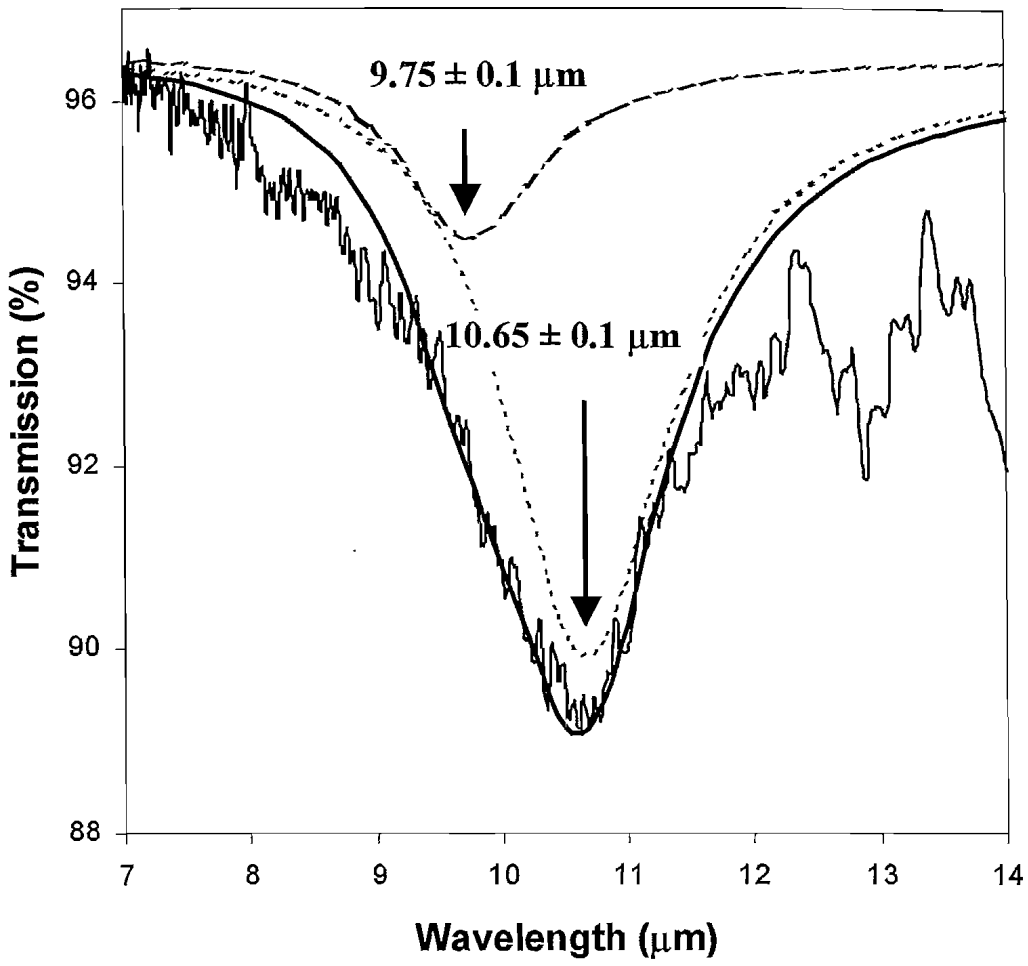

Figure A. 7. Transmission spectrum of sample A1573 taken at room temperature. The sample parameters are listed in Table A 2. Two intersubband absorption wavelengths were fitted at λ_{02} = 9.75 ± 0.1 μm (dash-dot line) and λ_{01} = 10.65 ± 0.1 μm (dashed line). The experimental data (thin solid line) was fitted with the combined absorption lines (thick solid line).

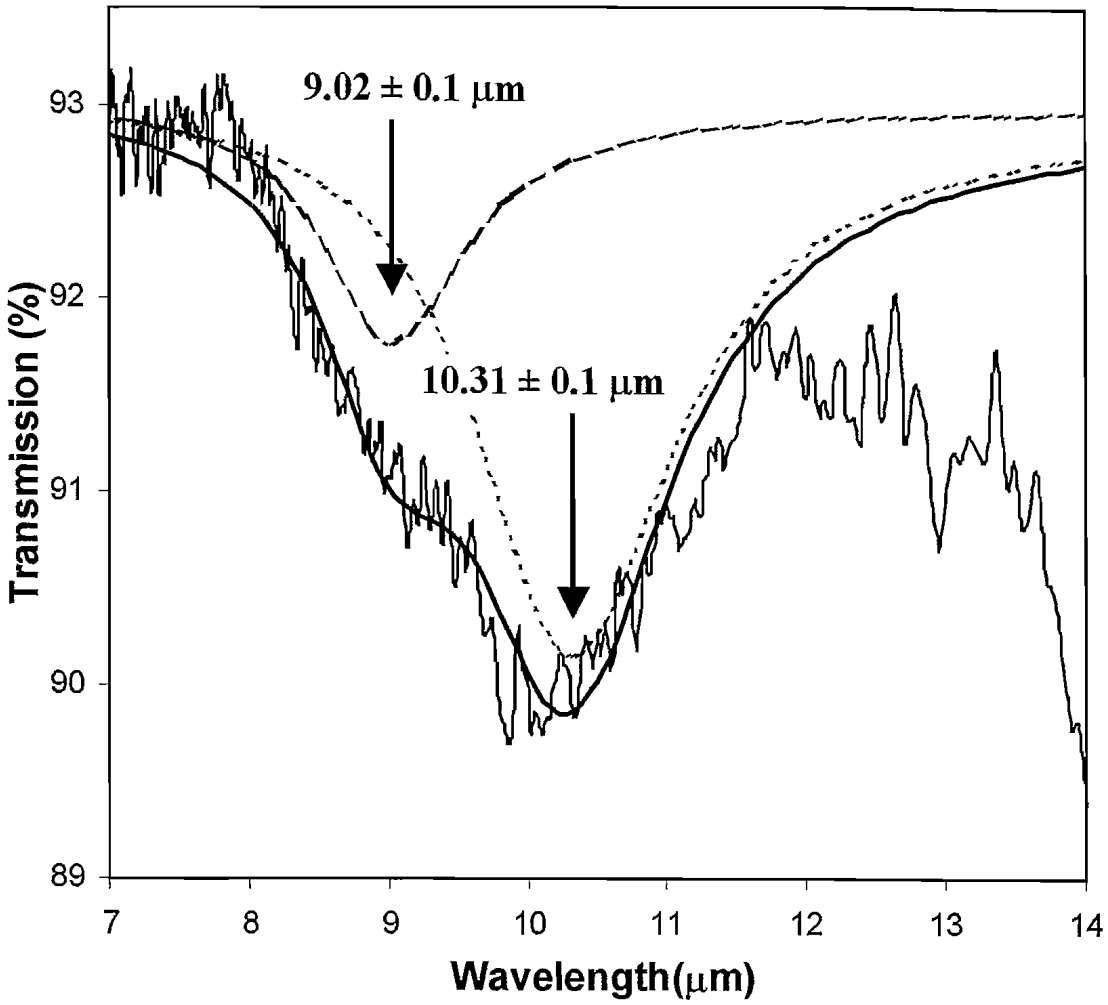

Figure A. 8. FTIR transmission spectrum of sample RM1784 taken at room temperature. The sample parameters are listed in Table A 2. Two intersubband absorption wavelengths were fitted at λ_{02} = 9.02 ± 0.1 μm (long dashed line) and λ_{01} = 10.31 ± 0.1 μm (dashed line). The experimental data (thin solid line) was fitted with the combined absorption lines (thick solid line).

References

[1] Chen P, Pearson J C, Pickett H M, Matsuura S and Blake G A, 2000: 'Submillimeter-wave measurements and analysis of the ground and v(2)=1 states of water', *Astrophysical Journal Supplement Series*, **128** (1) pp. 371-385

[2] Odashima H, Matsushima F, Kozato A, Tsunekawa S, Takagi K and Linnartz H, 1998: 'Tunable far-infrared spectroscopy of (KrD+)-Kr-82, (KrD+)-Kr- 84, (KrD+)-Kr-86, and (KrH+)-Kr-82', *J. Mol. Spectrosc.*, **190** (1) pp. 107-111

[3] Beard M C, Turner G M and Schmuttenmaer C A, 2002: 'Terahertz spectroscopy', *J. Phys. Chem. B*, **106** (29) pp. 7146-7159

[4] Genzel R and Cesarsky C J, 2000: 'Extragalactic results from the infrared space observatory', *Annu. Rev. Astron. Astrophys.*, **38** pp. 761

[5] Batchelor M, Adler D and Trogus W, 1996: 'New plans for first far infrared and sub-millimetre space astronomy mission for 2007', *Adv. Space Res.*, **18** (11) pp. 185-188

[6] Takeuchi T T, Hirashita H, Ohta K, Hattori T G, Ishii T T and Shibai H, 1999: 'The IRIS far-infrared galaxy survey: Expected number count, redshift, and perspective', *Publ. Astron. Soc. Pac.*, **111** (757) pp. 288-305

[7] Evenson K M, Jennings D A and Peterson F R, 1984: 'Tunable far-infrared spectroscopy', *Appl. Phys. Lett.*, **44** (6) pp. 576-578

[8] Tacke M, 2001: 'Lead-salt lasers', *Philos. Trans. R. Soc. Lond. Ser. A-Math. Phys. Eng. Sci.*, **359** (1780) pp. 547-566

[9] Faist J, Capasso F, Sivco D L, Sirtori C, Hutchinson A L and Cho A Y, 1994: 'Quantum Cascade Laser', *Science*, **264** (5158) pp. 553-556

[10] Mullins J, 2002: 'Using unusable frequencies - Solid-state terahertz laser opens door to applications previously closed', *IEEE Spectrum*, **39** (7) pp. 22-23

[11] Sirtori C, 2002: 'Bridge for the terahertz gap', *NATURE*, **417** (6885) pp. 132-133

[12] Gabriel F, Gippner P, Grosse E, Janssen D, Michel P, Prade H, Schamlott A, Seidel W, Wolf A and Wunsch R, 2000: 'The Rossendorf radiation source ELBE and its FEL projects', *Nucl. Instrum. Methods Phys. Res. Sect. B-Beam Interact. Mater. Atoms*, **161-163** pp. 1143-1147

[13] Oepts D, van der Meers A F G and van Amersfoort P W, 1995: 'The free-electron-laser user facility FELIX', *Infrared Phys. Techn.*, **36** (1) pp. 297-308

[14] Prazeres R, Glotin F, Rippon C and Ortega J M, 2002: 'Operation of the "CLIO" FEL at long wavelengths and study of partial guiding in the optical cavity', *Nucl. Instrum. Methods Phys. Res. Sect. A-Accel. Spectrom. Dect. Assoc. Equip.*, **483** (1-2) pp. 245-249

[15] Ramian G, Kaminski J and Allen S J, 1997: 'First lasing of the UCSB 30 mu m free-electron laser', *Nucl. Instrum. Methods Phys. Res. Sect. A-Accel. Spectrom. Dect. Assoc. Equip.*, **393** (1-3) pp. 220-224

[16] Schwettman H A, Smith T I and Swent R L, 1996: 'The Stanford picosecond FEL center', *Nucl. Instrum. Methods Phys. Res. Sect. A-Accel. Spectrom. Dect. Assoc. Equip.*, **375** (1-3) pp. 662-663

[17] 2002: 'The Infrared User Facilities FELIX, FOM-Institute for Plasma Physics 'Rijnhuizen', The Netherlands', Webpage: http://www.rijnh.nl/n4/n3/f1234.htm

[18] 2002: 'ELBE, Forschungszentrum Rossendorf (FZR), Dresden-Rossendorf, Germany', Webpage: http://www.fz-rossendorf.de/ELBE/

[19] 2002: 'Stanford Picosecond FEL Center, Stanford University, Stanford, California, USA', Webpage: http://www.stanford.edu/group/FEL/

[20] 2002: 'The CLIO Free Electron Laser, Centre Universitaire Paris-Sud, Orsay, France', Webpage: http://www.lure.u-psud.fr/CLIO/CLIO_ENG.HTM

[21] 2002: 'The UCSB Free-Electron Lasers, University of California at Santa Barbara (UCSB), Santa Barbara, California, USA', Webpage: http://sbfel3.ucsb.edu/homepage.html

[22] Morruzzi G and Strumia F, 1984: 'High resolution FIR and IR spectroscopy of CH_3OH', *Infrared Phys. Techn.*, **24** pp. 257-280

[23] Pereira D, Moraes J C S, Telles E M, Scalabrin A, Strumia F, Moretti A, Carelli G and Massa C A, 1994: 'A review of optically pumped far-infrared laser lines from methanol isotopes.' *Int. J. Infrared and Millimeter Waves*, **15** pp. 1-44

[24] Shastin V N, 1991: 'Hot Hole Intersubband Transition P-Ge Fir Laser', *Opt. Quantum Electron.*, **23** pp. S111-S131

[25] Julien F H, Saar A, Wang J and Leburton J P, 1995: 'Optically pumped intersub-band emission in quantum-wells', *Electron. Lett.*, **31** pp. 838-839

[26] Julien F H, Moussa Z, Boucaud P, Lavon Y, Sa'Ar A, Wang J, Leburton J-P, Berger V, Nagle J and Planel R, 1996: 'Intersubband mid-infrared emission in optically pumped quantum wells', *Superlattice Microst.*, **19** (1) pp. 69-79

[27] Lau K M and Xu W, 1992: 'Optically pumped submillimeter wave semiconductor lasers', *IEEE J. Quantum Electron.*, **28** (8) pp. 1773-1777

[28] Sun G and Khurgin J B, 1993: 'Optically pumped four-level infrared laser based on intersubband transitions in multiple quantum wells: feasibility study', *IEEE J. Quantum Electron.*, **29** (4) pp. 1104-1111

[29] Sung C Y, Norris T B, Afzali-Kushaa A and Haddad G I, 1996: 'Femtosecond intersubband relaxation and population and inversion in stepped quantum well', *Appl. Phys. Lett.*, **68** (4) pp. 435-437

[30] Afzali-Kushaa A, Haddad G I and Norris T B, 1995: 'Optically pumped intersubband lasers based on quantum wells', *IEEE J. Quantum Electron.*, **31** (1) pp. 135-143

[31] Xin Z-J and Rutt H N, 1997: 'Design of intersubband quantum well far-infrared lasers', *Semicond. Sci. Technol.*, **12** (9) pp. 1129-1134

[32] Xin Z-J and Rutt H N, 1998: 'Effect of inhomogeneity on quantum well far-infrared lasers', *J. Appl. Phys.*, **83** (3) pp. 1491-1495

[33] Tan H A, Xin Z-J, Rutt H N, Wells J-P R and Bradley I V, 2002: 'Intersubband lifetimes and free carrier effects in optically pumped far infrared quantum wells laser structures', *Semicond. Sci. Technol.*, **17** (7) pp. 645-650

[34] Gauthier-Lafaye O, Boucaud P, Julien F H, Sauvage S, Cabaret S, Lourtioz J M, Thierry-Mieg V and Planel R, 1997: 'Long-wavelength (~15.5 μm) unipolar semiconductor laser in GaAS quantum wells', *Appl. Phys. Lett.*, **71** (25) pp. 3619-3621

[35] Gauthier-Lafaye O, Julien F H, Cabaret S, Lourtioz J M, Strasser G, Gornik E, Helm M and Bois P, 1999: 'High-power GaAs/AlGaAs quantum fountain unipolar laser emitting at 14.5 mu m with 2.5% tunability', *Appl. Phys. Lett.*, **74** (11) pp. 1537-1539

[36] Helm M, Colas E, England P, DeRosa F and Allen S J, Jr., 1988: 'Observation of grating-induced intersubband emission from GaAs/AlGaAs superlattices', *Appl. Phys. Lett.*, **53** (1) pp. 1714-1716

[37] Colombelli R, Straub A, Capasso F, Gmachl C, Blakey M I, Sergent A M, Chu S N G, West K W and Pfeiffer L N, 2002: 'Terahertz electroluminescence from superlattice quantum cascade structures', *J. Appl. Phys.*, **91** (6) pp. 3526-3529

[38] Rochat M, Faist J, Beck M, Oesterle U and Ilegems M, 1998: 'Far-infrared (λ=88μm) electroluminescence in a quantum cascade structure', *Appl. Phys. Lett.*, **73** (25) pp. 3724-3726

[39] Köhler R, Tredicucci A, Beltram F, Beere H E, Linfield E H, Davies A G, Ritchie D A, Iotti R C and Rossi F, 2002: 'Terahertz semiconductor-heterostructure laser', *Nature*, **417** (6885) pp. 156-159

[40] Ajili L, Scalari G, Hofstetter D, Beck M, Faist J, Beere H, Davies G, Linfield E and Ritchie D, 2002: 'Continuous-wave operation of far-infrared quantum cascade lasers', *Electron. Lett.*, **38** (25) pp. 1675-1676

[41] Hubers H W, Pavlov S G, Greiner-Bar M, Rummeli M H, Kimmitt M F, Zhukavin R K, Riemann H and Shastin V N, 2002: 'Terahertz emission spectra of optically pumped silicon lasers', *Phys. Status Solidi B-Basic Res.*, **233** (2) pp. 191-196

[42] Pavlov S G, Hubers H W, Riemann H, Zhukavin R K, Orlova E E and Shastin V N, 2002: 'Terahertz optically pumped Si : Sb laser', *J. Appl. Phys.*, **92** (10) pp. 5632-5634

[43] Köhler R, Iotti R C, Tredicucci A and Rossi F, 2001: 'Design and simulation of terahertz quantum cascade lasers', *Appl. Phys. Lett.*, **79** (24) pp. 3920-3922

[44] Colombelli R, Capasso F, Gmachl C, Hutchinson A L, Sivco D L, Tredicucci A, Wanke M C, Sergent A M and Cho A Y, 2001: 'Far-infrared surface-plasmon quantum-cascade lasers at 21.5 μm and 24 μm wavelengths', *Appl. Phys. Lett.*, **78** (18) pp. 2620-2622

[45] Kinsler P, Harrison P and Kelsall R W, 1999: 'Intersubband terahertz lasers using four-level asymmetric quantum wells', *J. Appl. Phys.*, **85** (1) pp. 23-28

[46] Gauthier-Lafaye O, Seguin-Roa B, Julien F H, Collot P, Sirtori C, Duboz J Y and Strasser G, 2000: 'High-power tunable quantum fountain unipolar lasers', *Physica E*, **7** pp. 12-19

[47] Tomic S, Ikonic Z and Milanovic V, 2002: 'Interdiffusion-based optimal quantum-well profile shaping for unipolar quantum-fountain lasers', *J. Appl. Phys.*, **91** (8) pp. 4801-4805

[48] Xin Z-J and Rutt H N, 1999: 'Inhomogeneous broadening in quantum well lasers', *Infrared Phys. Techn.*, **40** (1) pp. 37-40

[49] Wilson J and Hawkes J, 1998: '*Optoelectronics: an introduction*', 3rd edn (Prentice Hall, London)

[50] Cho A Y and Arthur J R, 1975: 'Molecular beam epitaxy', *Prog. Solid-State Chem.*, **10** (3) pp. 157-191

[51] Singh J, 1995: '*Semiconductor Optoelectronics*' (McGraw-Hill Inc., London)

[52] 2002: 'MBE Research Group, Department of Electronics & Electrical Engineering, University of Glasgow, Glasgow, UK.' Webpage: http://www.elec.gla.ac.uk/groups/mbe/

[53] 2002: 'EPSRC National Centre for III-V Technologies, Department of Electronic and Electrical Engineering, University of Sheffield, Sheffield, UK.' Webpage: http://www.shef.ac.uk/eee/cf/main.html

[54] 2002: 'The University of Sheffield EPSRC III-V Semiconductor Facility Newsletter, Issue No. 14'

[55] Cho A Y, 1971: 'Film deposition by molecular-beam techniques', *J. Vac. Sci. Technol.*, **8** (5) pp. S31-S38

[56] Blakemore J S, 1982: 'Semiconducting and other major properties of gallium arsenide', *J. Appl. Phys.*, **53** (10) pp. R123-R181

[57] Vurgaftman I, Meyer J R and Ram-Mohan L R, 2001: 'Band parameters for III-V compound semiconductors and their alloys', *Journal of Applied Physics*, **89** (11) pp. 5815-5875

[58] Mitin V V, Kochelap V A and Stroscio M A, 1999: '*Quantum Heterostructures: Microelectronics and Optoelectronics*' (Cambridge University Press, Cambridge)

[59] Rutt H N, Xin Z-J and Tan H A, 2002: 'Design optimization of optically pumped terahertz lasers in stepped quantum wells', *J. Phys. D: Appl. Phys.*, **35** (16) pp. 1907-1913

[60] Lu P-Y, Wang C-H, Williams L M, Chu S N G and Stiles C M, 1986: 'Epitaxial $Hg_{1-x}Cd_xTe$ growth by low-temperature metalorganic chemical vapor deposition', *Appl. Phys. Lett.*, **49** (20) pp. 1372-1374

[61] Faurie J P and Million A, 1981: 'Molecular beam epitaxy of II-VI compounds: $Cd_xHg_{1-x}Te$', *J. Cryst. Growth*, **54** (3) pp. 582-585

[62] Schmit J L, 1987 'Development of HgCdTe for LWIR Images' in *Materials Research Society Symposia Proceedings: Materials for Infrared Detectors and*

Sources vol. **90** eds Farrow R F C, Schetzina J F and Cheung J T (Materials Research Society, Pittsburgh) p 27-37

[63] Partin D L, 1987 'Preparation and applications of lead chalcogenide diode lasers' in *Materials Research Society Symposia Proceedings: Materials for Infrared Detectors and Sources* vol. **90** eds Farrow R F C, Schetzina J F and Cheung J T (Materials Research Society, Pittsburgh) p 47-58

[64] Bachmann K J and Goslowsky H, 1987 'Issues in the growth of bulk crystal of infrared materials' in *Materials Research Society Symposia Proceedings: Materials for Infrared Detectors and Sources* vol. **90** eds Farrow R F C, Schetzina J F and Cheung J T (Materials Research Society, Pittsburgh) p 69-80

[65] Berding M A, Chen A-B and Sher A, 1987 'HgCdTe versus HgZnTe: Electronic properties and vacancy formation energies' in *Materials Research Society Symposia Proceedings: Materials for Infrared Detectors and Sources* vol. **90** eds Farrow R F C, Schetzina J F and Cheung J T (Materials Research Society, Pittsburgh) p 127-132

[66] Borenstain S I and Katz J, 1989: 'Evaluation of the feasibility of a far-infrared laser based on intersubband transitions in GaAs quantum wells', *Appl. Phys. Lett.*, **55** (7) pp. 654-656

[67] Berger V, 1994: 'Three-level laser based on intersubband transitions in asymmetric quantum wells: a theoretical study', *Semicond. Sci. Technol.*, **9** (8) pp. 1493-1499

[68] Siegman A E, 1971: '*An Introduction to Lasers and Masers*' (McGraw Hill, New York)

[69] Duboz J Y, Costard E, Rosencher E, Bois P, Nagle J, Berset J M, Jaroszynski D and Ortega J M, 1995: 'Electron relaxation time measurements in GaAs/AlGaAs quantum wells: Intersubband absorption saturation by a free-electron laser', *J. Appl. Phys.*, **77** (12) pp. 6492-6495

[70] Vodopyanov K L, Chazapis V and Phillips C C, 1996: 'Two-Color midinfrared saturation spectroscopy of intersubband transitions in multiquantum wells', *Appl. Phys. Lett.*, **69** (22) pp. 3405-3407

[71] Faist J, Capasso F, Sirtori C, Sivco D L, Hutchinson A L, Chu S N G and Cho A Y, 1993: 'Measurement of the intersubband scattering rate in semiconductor quantum wells by excited state differential absoprtion spectroscopy', *Appl. Phys. Lett.*, **63** (10) pp. 1354-1356

[72] Murdin B N, Heiss W, Langerak C J G M, Lee S-C, Galbraith I, Strasser G, Gornik E, Helm M and Pidgeon C R, 1997: 'Direct observation of the LO phonon bottleneck in wide GaAs/$Al_xGa_{1-x}As$ quantum wells', *Phys. Rev. B*, **55** (8) pp. 5171-5176

[73] Oberli D Y, Wake D R, Klein M V, Klem J, Henderson T and Morkoc H, 1987: 'Time-resolved raman scattering in GaAs quantum wells', *Phys. Rev. Lett.*, **59** (6) pp. 696-699

[74] Lavon Y, Sa'Ar A, Moussa Z, Julien F H and Planel R, 1996: 'Intersubband transitions from the second subband in acoupled quantum wells structure', *Superlattice Microst.*, **19** pp. 1-7

[75] Liu H C, Cheung I W, SpringThorpe A J, Dharma-wardana C, Wasilewski Z R, Lockwood D J and Aers G C, 2001: 'Intersubband Raman laser', *Appl. Phys. Lett.*, **78** (23) pp. 3580-3582

[76] Harrison P and Kelsall R W, 1997: 'Population inversion in optically pumped asymmetric quantum well terahertz lasers', *J. Appl. Phys.*, **81** (11) pp. 7135-7140

[77] 2002: 'Edinburgh Instruments Limited', Webpage: http://www.edinst.com/

[78] Tan I H, Snider G L, Chang L D and Hu E L, 1990: 'A self-consistent solution of Schrodinger-Poisson equations using a non-uniform mesh', *J. Appl. Phys.*, **68** (8) pp. 4071-4076

[79] Harrison P, 1999: '*Quantum wells, wires, and dots: theoretical and computational physics*' (John Wiley & Sons, Chichester)

[80] Moon C R, Choe B-D, Kwon S D and Lim H, 1997: 'Electron distribution and capacitance-voltage profiles of multiple quantum well structure from self-consistent simulations', *Appl. Phys. Lett.*, **70** pp. 2987-2989

[81] Abou-Elnour A and Schuenemann K, 1993: 'A comparison between different numerical methods used to solve Poisson's and Schroedinger's equations in semiconductor heterostructures', *J. Appl. Phys.*, **74** (5) pp. 3273-3276

[82] Abou-Elnour A and Schuenemann K, 1994: 'An efficient and accurate self-consistent calculation of electronic states in modulation doped heterostructures', *Solid State Electron.*, **37** (1) pp. 27-30

[83] Debaisieux G, Herve-Gruyer G, Filoche M, Bouchoule S and Palmier J F, 1997: 'Self-consistent 1-D solution of multiquantum-well laser equations', *Opt. Quant. Electron.*, **29** (6) pp. 651-660

[84] Kreyszig E, 1993 'Chapter 20 Numerical Methods for Differential Equations' in *Advanced Engineering Mathematics* 7 ed (John Wiley & Sons, New York) p 1061

[85] Raymond A, Robert J L and Bernard C, 1979: 'The electron effective mass in heavily doped GaAs', *J. Phys. C: Solid State Phys.*, **12** (12) pp. 2289-2293

[86] Cruz Serra A M and Abreu Santos H, 1991: 'A one-dimensional, self-consistent numerical solution of Schrodinger and Poisson equations', *J. Appl. Phys.*, **70** (5) pp. 2734-2738

[87] 2003: 'Mathcad', Webpage: http://www.mathcad.com/

[88] Liu H C, Costard E, Rosencher E and Nagle J, 1995: 'Sum frequency generation by intersubband transition in step quantum wells', *IEEE J. Quantum Electron.*, **31** (9) pp. 1659-1662

[89] Mii Y J, Wang K L, Karunasiri R P G and Yuh P F, 1990: 'Observation of Large Oscillator-Strengths for Both 1- 2 and 1- 3 Intersubband Transitions of Step Quantum-Wells', *Applied Physics Letters*, **56** (11) pp. 1046-1048

[90] Gauthier-Lafaye O, Sauvage S, Boucaud P, Julien F H, Glotin F, Prazeres R, Ortega J-M, Thierry-Mieg V and Planel R, 1998: 'Investigation of mid-infrared intersubband stimulated gain under optical pumping in GaAs/AlGaAs quantum wells', *J. Appl. Phys.*, **83** (6) pp. 2920-2926

[91] Levine B F, 1993: 'Quantum-well infrared photodetectors', *J. Appl. Phys.*, **74** (8) pp. R1-R81

[92] Sze S M, 1969: '*Physics of Semiconductor Devices*' (John Wiley & Sons, Inc., New York)

[93] 2002: 'PerkinElmer Instruments', Webpage: http://instruments.perkinelmer.com/index.asp

[94] Weisstein E W, 2002: 'Fourier Transform Spectrometer in Eric Weisstein's World of Physics', Webpage: http://scienceworld.wolfram.com/physics/FourierTransformSpectrometer.html

[95] Chantry G W, 1984: '*Long-wave Optics: Principles*',vol. 1 (Academic Press, London)

[96] Murdin B N, Langerak C, Helm M, Kruck P, Heiss W, Rosskopf V, Strasser G, Gornik E, Dur M, Goodnick S M, Lee S C, Galbraith I and Pidgeon C R, 1996: 'Time resolved studies of intersubband relaxation in GaAs/AlGaAs quantum

wells below the optical phonon energy using a free electron laser', *Superlattices Microstruct.*, **19** (1) pp. 17-24

[97] Xu Y, Almogy G, O'Brien J, Shakouri A, Xu W, Salvatore R A and Yariv A, 1997: 'Direct measurement of population-induced broadening of quantum well intersubband transitions', *Appl. Phys. Lett.*, **71** (6) pp. 838-840

[98] Pozina G, Ivanov I, Monemar B, Thordson J and Andersson T G, 1997: 'Optical characterization of MBE-grown GaNAs', *Mater. Sci. Eng. B-Solid State Mater. Adv. Technol.*, **50** (1-3) pp. 153-156

[99] Reisinger T, Lankes S, Kastner M J, Rosenauer A, Franzen F, Meier M and Gebhardt W, 1996: 'Growth, structural and optical characterization of MBE ZnCdSe/ZnSe quantum wells', *J. Cryst. Growth*, **159** (1-4) pp. 510-513

[100] Palik E D, 1985 'Gallium Arsenide (GaAs)' in *Handbook of Optical Constants of Solids* ed Palik E D (Academic Press, London) p 429-443

[101] Slivken S, Huang Z, Evans A and Razeghi M, 2002: 'High-power (~9 μm) quantum cascade lasers', *Appl. Phys. Lett.*, **80** (22) pp. 4091-4093

[102] Gauthier-Lafaye O, Sauvage S, Boucaud P, Julien F H, Prazeres R, Glotin F, Ortega J-M, Thierry-Mieg V, Planel R, Leburton J-P and Berger V, 1997: 'Intersubband stimulated emission in GaAs/AlGaAs quantum wells: Pump-probe experiments using a two-color free-electron laser', *Appl. Phys. Lett.*, **70** (24) pp. 3197-3199

[103] Murdin B N, Knippels G M H, van der Meer A F G, Pidgeon C R, Langerak C J G M, Helm M, Heiss W, Unterrainer K, Gornik E, Geerinck K K, Hovenier N J and Wenckebach W T, 1994: 'Excite-probe determination of the intersubband lifetime in wide GaAs/AlGaAs quantum wells using a far-infrared free-electron laser', *Semicond. Sci. Technol.*, **9** pp. 1554-1557

[104] 2002: 'The Foundation for Fundamental Research on Matter (FOM), the Netherlands', Webpage: http://www.fom.nl/

[105] 2002: 'The Engineering and Physical Sciences Research Council (EPSRC), UK', Webpage: http://www.epsrc.ac.uk/website/index.aspx

[106] van der Meer A F G, 1996: 'The international free electron laser user facility FELIX'. Nieuwegen: FOM Institute for Plasma Physics

[107] Findlay P C, Pidgeon C R, Kotitschke R, Hollingworth A, Murdin B N, Langerak C J G M, van der Meer A F G, Ciesla C M, Osward J, Homer A, Springholz G and Bauer G, 1998: 'Auger recombinatin dynamics of lead salts

under picosecond free-electron-laser excitation', *Phys. Rev. B*, **58** (19) pp. 12908-12915

[108] Schumacher K L, Collings D, Phillips R T, Ritchie D A, Weber G, Schulman J N and Ploog K, 1996: 'Inter- and intrasubband relaxation times in GaAs-Al0.35GaAs quantum wells measured by femtosecond time-resolved differential transmission', *Semicond. Sci. Technol.*, **11** pp. 1173-1177

[109] Dupont E, Corkum P, Liu H C, Wilson P H, Buchanan M and Wasilewski Z R, 1994: 'Two-photon intersubband transitions in quantum well infrared photoconductors', *Appl. Phys. Lett.*, **65** (12) pp. 1560-1562

[110] Serapiglia G B, Paspalakis E, Sirtori C, Vodopyanov K L and Phillips C C, 2000: 'Laser-induced quantum coherence in a semiconductor quantum well', *Phys. Rev. Lett.*, **84** (5) pp. 1019-1022

[111] Lutgen S, Kaindl R A, Woerner M, Elsaesser T, Hase A and Kunzel H, 1996: 'Nonlinear intersubband absorption of a hot quasi-two-dimensional electron plasma studied by femtosecond infrared spectroscopy', *Phys. Rev. B*, **54** pp. 17343-17346

[112] Khurgin J B, 1999 'Semiconductors and Semimetals' vol. **59** eds Garmire E and Kost A (Academic Press, London)

[113] Rosencher E and Bois P H, 1991: 'Model system for optical nonlinearities: asymmetric quantum wells', *Phys. Rev. B*, **44** pp. 11315-11327

[114] Kimmitt M F, 1970: '*Far-Infrared Techniques*' (Pion Limited, London)

[115] Deneuville A, Tanner D and Holloway P H, 1991: 'Optical-Constants of Znse in the Far Infrared', *Phys. Rev. B*, **43** (8) pp. 6544-6550

[116] Kaindl R A, Reimann K, Woerner M, Elsaesser T, Hey R and Ploog K H, 2001: 'Homogeneous broadening and excitation-induced dephasing of intersubband transitions in a quasi-two-dimensional electron gas', *Phys. Rev. B*, **63** (16) pp. 161308

[117] Okuno Y, Uomi K, Aoki M and Tsuchiya T, 1997: 'Direct wafer bonding of III-V compound semiconductors for free- material and free-orientation integration', *IEEE J. Quantum Electron.*, **33** (6) pp. 959-969

[118] Akatsu T, Plossl A, Scholz R, Stenzel H and Gosele U, 2001: 'Wafer bonding of different III-V compound semiconductors by atomic hydrogen surface cleaning', *J. Appl. Phys.*, **90** (8) pp. 3856-3862

[119] Glembocki O J and Takarabe K, 1991 'Aluminium Gallium Arsenide ($Al_xGa_{1-x}As$)' in *Handbook of Optical Constants of Solids II* ed Palik E D (Academic Press, London) p 513-553

[120] Sirtori C, Gmachl C, Capasso F, Faist J, Sivco D L, Hutchinson A L and Cho A Y, 1998: 'Long-wavelength ($\lambda \sim 8$-11.5 μm) semiconductor lasers with waveguides based on surface plasmons', *Opt. Lett.*, **23** (17) pp. 1366-1368

[121] Nakwaski W, 1995: 'Effective Masses of Electrons and Heavy Holes in GaAs, InAs, AlAs and Their Ternary Compounds', *Physica B*, **210** (1) pp. 1-25

[122] Sanborn B A, 1995: 'Electron-Electron Interactions, Coupled Plasmon-Phonon Modes, and Mobility in N-Type Gaas', *Phys. Rev. B*, **51** (20) pp. 14256-14264

[123] Yeh P, 1988: '*Optical waves in layered media*' (John Wiley & Sons, New York)

[124] Boardman A D, 1982 Electromagnetic Surface Modes (Chichester: John Wiley & Sons)

[125] Rochat M, Ajili L, Willenberg H, Faist J, Beere H, Davies G, Linfield E and Ritchie D, 2002: 'Low-threshold terahertz quantum-cascade lasers', *Appl. Phys. Lett.*, **81** (8) pp. 1381-1383

[126] Rochat M, Beck M, Faist J and Oesterle U, 2001: 'Measurement of far-infrared waveguide loss using a multisection single-pass technique', *Appl. Phys. Lett.*, **78** (14) pp. 1967-1969

[127] Tredicucci A, Gmachl C, Wanke M C, Capasso F, Hutchinson A L, Sivco D L, Chu S N G and Cho A Y, 2000: 'Surface plasmon quantum cascade lasers at $\lambda \sim 19$ μm', *Appl. Phys. Lett.*, **77** (15) pp. 2286-2288

[128] Unterrainer K, Colombelli R, Gmachl C, Capasso F, Hwang H Y, Sergent A M, Sivco D L and Cho A Y, 2002: 'Quantum cascade lasers with double metal-semiconductor waveguide resonators', *Appl. Phys. Lett.*, **80** (17) pp. 3060-3062

[129] Ordal M A, Bell R J, Alexander R W, Jr., Newquist L A and Querry M R, 1988: 'Optical properties of Al, Fe, Ti, Ta, W, and Mo at submillimeter wavelengths', *Appl. Opt.*, **27** (6) pp. 1203-1209

[130] Ordal M A, Bell R J, Alexander R W, Long L L and Querry M R, 1987: 'Optical-Properties of Au, Ni, and Pb at Submillimeter Wavelengths', *Appl. Opt.*, **26** (4) pp. 744-752

[131] Harris R D, 1996: 'Waveguide Surface Plasmon Resonance Biosensor', PhD Thesis, University of Southampton, Southampton.

[132] Yariv A and Yeh P, 1984: '*Optical waves in crystal: propagation and control of laser radiation*' (John Wiley & Sons, New York)

[133] Fox A G and Li T, 1961: 'Resonant modes in a maser interferometer', *Bell Sys. Tech. J.*, **40** pp. 453-488

[134] Haller E E, 1994: 'Advanced far-infrared detectors', *Infrared Phys. Techn.*, **35** (2/3) pp. 127-146

[135] Moore W J and Shenker H, 1965: 'A high-detectivity gallium-doped germanium detector for the 40-120μ region', *Infrared Phys.*, **5** pp. 99-106

[136] Jeffers W Q and Johnson C J, 1968: 'Spectral response of the Ge:Ga photoconductive detector', *Appl. Opt.*, **7** (9) pp. 1859-1860

[137] Hiromoto N and Fujiwara M, 1999: 'Slow transient response of Ge:Ga far-infrared photoconductors for space applications', *Infrared Phys. Techn.*, **40** pp. 387-393

[138] Hiromoto N, Saito M and Okuda H, 1990: 'Ge:Ga far-infrared photoconductor with low compensation', *Japanese J. Appl. Phys.*, **29** (9) pp. 1739-1744

[139] Kruse P W, McGlauchlin L D and McQuistan R B, 1963: '*Elements of Infrared Technology: Generation, Transmission, and Detection*' (John Wiley & Sons, New York)

[140] Dereniak E L and Boreman G D, 1996: '*Infrared Detectors and Systems*' (John Wiley & Sons, New York)

[141] Kimmitt M F, 1999, Personal Communication

[142] Wang T and Ehrman B, 1993: 'Compensate Transimpedance Amplifiers Intuitively', Burr-Brown Application Bulletion AB-050, USA.

[143] 1994: 'AD9631/AD9632 Product Data Sheet', Analog Devices, USA.

[144] Graeme J, 1995: 'Photodiode monitoring with Op Amps', Burr-Brown Application Bullettin AB075, USA.

[145] 1995: 'OL 480 Variable Temperature Blackbody Calibration Standard Manual', Optronic Laboratories, Inc., USA.

[146] '420 Pyroelectric Laser Detector for UV/Vis/IR', Product Datasheet, Eltec Instruments Inc., Daytona Beach, Florida, USA

[147] Adachi S and Taguchi T, 1991: 'Optical-Properties of Znse', *Phys. Rev. B*, **43** (12) pp. 9569-9577

[148] Douglas N G, 1989: '*Millimetre and Submillimetre Wavelength lasers: A Handbook of cw Measurement*' (Springer-Verlag, Berlin)

[149] Zerbetto S C and Vassconcellos E C C, 1994: 'Far infrared laser lines produced by methanol and its isotopic species: A review.' *Int. J. Infrared and Millimeter Waves*, **15** pp. 889-933

[150] Beck R, Englisch W and Gürs K, 1980: '*Table of Laser Lines in Gases and Vapors*', 3rd edn (Springer-Verlag, Berlin)

[151] Bloom A L, 1968: '*Gas Lasers*' (John Wiley & Sons, New York)

[152] Kogelnik H and Li T, 1966: 'Laser beams and resonators', *Appl. Opt.*, **5** (10) pp. 1550-1567

[153] Garrett C G B, 1967: '*Gas Lasers*' (McGraw-Hill Book Company, New York)

[154] Siegel P H, 2002: 'Terahertz technology', *IEEE Trans. Microwave Theory Tech.*, **50** (3) pp. 910-928